

https://dspace.org/

Effect of added vorticity on trailing vortices in the extended near wake

Wood, Andrew Robert

2013-07-23
http://hdl.handle.net/10539/12889

Downloaded from a DSpace repository. https://dspace.org/

EFFECT OF ADDED VORTICITY ON TRAILING VORTICES IN THE EXTENDED NEAR WAKE

Andrew Robert Wood

A dissertation submitted to the Faculty of Engineering and the Built Environment, University of the Witwatersrand, Johannesburg, in fulfilment of the requirements for the degree of Master of Science in Engineering.

Johannesburg, May 2013

Declaration

I declare that this dissertation is my own, unaided work, except where otherwise acknowledged. It is being submitted for the degree of Master of Science in Engineering in the University of the Witwatersrand, Johannesburg. It has not been submitted before for any degree or examination at any other university.

Signed this 23rd day of May 2013

_____

Andrew Robert Wood

Acknowledgements

The following people are thanked for playing a major role in the completion of this dissertation:

Dr. Craig Law : For his supervision and support. I am especially grateful for allowing me to shape the research to my own interest and for your willingness to assist; whether it was to secure funding for particular equipment, or to simply give advise and direction. I am also very grateful for the time and effort you have put in during the write-up and editing phase of the research.

Mr. Michael Boer : For his continuous support throughout my stay at Wits. Thank-you for always making time for me whenever I needed it. I also really appreciate the work that you put into my aluminum wing mould, and for the time and effort that went in to perfecting the wing foaming process before I had to build my own wing.

Mr. Randall Paton : For giving an incompressible flow student an office in the Flow Research Unit. For his support and willingness to help me get the best results out of my flow visualisation. For writing this LaTeX template.

Thanks to Shaun Riekart, Boetie, and the rest of the Mechanical Engineering Laboratory staff for manufacturing my test rig and countless other odds and ends.

Finally to my family. Thanks Dad and Mom for your unwavering support, both emotionally and financially. This dissertation would not have been possible without you. Thanks Pam for being such a large part of the process and being my support base here in Johannesburg.

Abstract

Wind Tunnel testing of a rectangular semi-span NACA0012 wing with an actuating trailing edge flap and two small oscillating tabs, affixed to the model's wingtip and flaptip, was undertaken with a view to introduce instabilities in the resulting wake. The tabs were oscillated sinusoidally at frequencies of 0.5, 1.0, and 2.0 Hz, both independently and together. The impact on the resulting wake was then studied; by examining the upper surface pressure distribution over the wing, and through images captured of the wake cross-section at three positions downstream of the model. Images were captured by seeding the flow with neutrally buoyant helium bubbles illuminated under a plane of light. Oscillation of the tabs at all frequencies was shown to impart instabilities in the near wake. The motion of the resulting vortex core under the oscillation of the tabs was mapped and shown to behave in a consistent manner through all angles of attack tested. An oscillation frequency of 2.0Hz showed the largest evidence of instabilities and greatest wake dispersion of the frequencies tested. A study into the transient pressure changes at the leading edge during oscillation of the tabs revealed a pressure oscillation equal to twice the frequency of the input tab oscillation. It was shown that synchronous oscillation of the two tabs at a frequency of 2.0 Hz, introduced sufficient instabilities into the flow to reduce the core diameter and wake extents of the primary wingtip vortex.

Contents

Declaration i

Acknowledgements ii

Abstract iii

Contents iv

List of Figures ix

List of Tables xv

List of Symbols xvii

1 Introduction 1

1.1 Vortex Movement and Dissipation 3

1.2 Modelling Wake Vortices 5

1.3 Trailing Vortex Interactions 9

1.3.1 Crow Instability 9

1.3.2 Interaction with a Turbulent Atmosphere 10

1.3.3 Interaction of the Flap and Tip Vortices 13

1.4 Miniature Trailing Edge Effectors 17

1.5 Wake Separation Standards 18

1.6 Motivation 19

2 Objectives **21**

3 Method **22**

3.1 Test Matrix 22

3.2 Pressure Measurement 24

3.3 Flow Visualisation 25

3.3.1 Helium Bubble Generator 25

3.3.2 Camera Setup 25

4 Draw Down Wind Tunnel **27**

4.1 Draw Down Tunnel Specifications 27

4.2 Coordinate System 28

5 Wind Tunnel Test Wing **29**

5.1 Experiment Overview 29

5.2 Preliminary Design and Placement 30

5.2.1 Geometry Optimisation 30

5.2.2 Airfoil Selection 37

5.3 Wing Manufacture 38

5.3.1 CNC Wing Moulds 39

5.3.2 Wing Skins 39

5.3.3 Wing Foaming 40

5.3.4 Flap Manufacture and Actuation 40
5.3.5 Pressure Tappings 41
5.3.6 Assembly 44
5.4 Oscillating Tabs 45
5.4.1 Position and Dimensions 45
5.4.2 Manufacture 46
5.4.3 Actuation 46
5.4.4 Control 47

6 Wind Tunnel Balance **52**
6.1 Position in the Tunnel 52
6.2 Design Overview 53
6.2.1 Operational Methodology 54
6.3 Loadcell Shortcomings 54

7 Data Acquisition **58**
7.1 Data Acquisition Hardware 58
7.2 LabVIEW Software 59
7.3 Pressure Measurement 59
7.3.1 Honeywell 24PC Series Sensors 59
7.3.2 Voltage Source 60
7.3.3 Constant Current Circuit 60
7.3.4 Instrument Amplifiers 62
7.3.5 Pressure Sensor Connection Diagrams 63

8 Calibration **65**

8.1 Honeywell Pressure Sensors 65

8.1.1 Sensor Response to Temperature 65

8.1.2 Pressure Calibration 67

8.2 Flap Angle Calibration 73

8.3 Wake Dimension Calibration 75

9 Data Processing **80**

9.1 Pressure Measurement 80

9.1.1 Procedure 80

9.1.2 Example of Pressure Data Processing 81

9.2 Image Processing 83

10 Results and Discussion **86**

10.1 Summary of Experimentation Performed 86

10.1.1 Pressure Measurement 86

10.1.2 Flow Visualisation 87

10.2 Baseline Tests 89

10.2.1 Pressure Measurements 89

10.2.2 Baseline Flow Visualisation 99

10.3 Tab Static Extension 104

10.4 Tab Oscillation Tests 106

10.4.1 Transient Response to Oscillating Tabs 108

10.4.2 Frequency Variation 111

10.4.3 Oscillation Scheme Variation 117

10.5 Summary of Discussion 129

11 Conclusions **138**

12 Recommendations for Further Work **141**

References **143**

A TE Flap Specifications **148**

B Faulhaber Motor and Controller Data Sheets **152**

C C# Motor Control Code **157**

D Sting Balance Dimensions & Drawings **162**

E Data Acquisition **166**

F Pressure Calibration **177**

G Pressure Sensor Uncertainty Calibration **182**

List of Figures

1.1 Trailing Vortex Shedding from a Conventional Wing 1

1.2 Starting Vortex Formation - Conservation of Angular Momentum 2

1.3 Chevalier Vortex Dissipation in Calm Air 3

1.4 Descent of Vortices shed from a Representative Airliner 4

1.5 Lateral Movement of Vortices Shed by a Low Flying Large Aircraft 4

1.6 Vortex Interaction on Parallel Runways with Separation less than 2500 ft . 5

1.7 Vortex Spacing Defined 8

1.8 Time Elapsed Capture of Vortex Dissipation showing the Crow Instability 10

1.9 Dimensionless Wake Lifespan τ as a Function of Turbulence Intensity η . 12

1.10 Wake Dissipation as a Function of Various Atmospheric Parameters 13

1.11 Effect of Physical Properties on the Stability of the Vortex System 14

1.12 Schematic of the Various Instability Modes Observed 15

1.13 Installation of MiTEs on Trailing Edge of a Rectangular Wing 17

1.14 Air passenger growth rate in United Kingdom, 1957-2007 19

3.1 Graphical Representation of Testing Completed 24

3.2 Flow Visualisation: Wingtip Tab Extended into the Freestream 26

3.3 Cross Section Stations along Tunnel Test Section 26

4.1 Photograph of the Wits Draw Down Wind Tunnel 27

4.2 Right-hand Coordinate System 28

5.1 Plot of Re vs. Chord Length 32

5.2 Plot of Available Downstream Spans against Semispan Length 33

5.3 Downstream Vortex Decay and Breakup 34

5.4 Plot of Aspect Ratio vs. Semispan for Various Chord Lengths 34

5.5 Plot of Available Downstream Spans vs. Aspect Ratio 35

5.6 Overview of Wing Geometry 36

5.7 Schematic Describing Crouch Ratio 37

5.8 Plot showing the Tab Dimensions 38

5.9 Photograph of the Wing Moulds Used in the Manufacture of the Test Wing 39

5.10 Layout of Trailing Edge Flap Actuation System 41

5.11 Overview of Pressure Tap Placement 43

5.12 Photograph of the Test Wing Upper Surface, Showing Pressure Tap Installation 44

5.13 Plan view of Gurney Flap Actuation System 47

5.14 Plan view of Test Wing Layout 48

5.15 Wiring Diagram for Controller Box 48

5.16 Front End Graphical User Interface, C# Control Programme 49

5.17 Sine Oscillation Control Input 51

6.1 Placement of Model in Wits DDT 52

6.2 Design overview, Wind Tunnel Vertical Balance 53

6.3 Rendering of Loadcell Base and Flexure 55

6.4 Non-Linearity and Hysteresis in Loadcell 56

6.5 Successful Loadcell Calibration - Away from Wind Tunnel 57

6.6 Zemic L6D Loadcell 57

7.1 Effect of a Voltage Regulator on Input Voltage Signal from PC Supply . . 61

7.2 Connection Diagram - LM117/317 Voltage Regulator [Appendix E] 61

7.3 Constant Current Wiring Diagram 24PC Series Pressure Sensor 62

7.4 AD627 In-Amp Circuit Diagram 63

7.5 Flow Chart Showing Pressure Measurement Components 63

7.6 Complete Circuit Diagram for One Pressure Sensor 64

8.1 Temperature and Sensor Zero Response over 24 Hr Test 66

8.2 Temperature Variation Calibration Sensor No. 14 68

8.3 Distribution of Pressure Sensor Output at a Constant Pressure Point . . . 70

8.4 Plot of Actual vs Theoretical Normal Cumulative Distribution 70

8.5 Raw Pressure Sensor Response to Ramped Pressure Inputs 71

8.6 Standard Deviation Variation, Pressure Sensor No. 1 72

8.7 Calibration Line for Pressure Sensor No. 1 73

8.8 Raw Pressure Data Scatter and Uncertainty: Sensor No. 1 74

8.9 Flap Angle Calibration Photograph 76

8.10 Trailing Edge Flap Calibration Line 76

8.11 Flow Visualisation Cross Section Stations 78

8.12 Plate Geometry for Skewness Calculation 78

8.13 Plot showing Pixel Conversion Factor as a Function of Downstream Position 79

9.1 Raw Cropped Image, $\alpha = 5°$, 0.37b 84

9.2 Inverted Image, $\alpha = 5°$, 0.37b 85

9.3 Rotated, Processed Image, $\alpha = 5°$, 0.37b 85

10.1 Dimensionless Chordwise Pressure Distribution, Experimental and Published Data, $\alpha = 10°$ 90

10.2 Dimensionless Chordwise Pressure Distribution, Experimental and Published Data, $\alpha = 15°$ 90

10.3 Chordwise Measured Pressure Distributions (Upper and Lower Surface) . . 93

10.4 Net Non-Dimensionalised Chordwise Pressure Plot. $Re : 2.56 \times 10^5$ 93

10.5 Upper Surface Streamlines, $\alpha = 5°$, Maximum Tab Extension 94

10.6 Upper Surface Streamlines, $\alpha = 15°$, Tab Retracted 94

10.7 Non-Dimensionalised Chordwise Pressure Data, α =10° 95

10.8 Non-Dimensionalised Upper and Lower Surface Spanwise Pressure Data. $Re : 2.56 \times 10^5$ 96

10.9 NACA0012 Spanwise Lifting Data. $Re : 43.6 \times 10^3$ 97

10.10Clean Wing Net Spanwise Pressure Distribution. $Re : 2.56 \times 10^5$ 98

10.11Photograph of Differing Vortex Diameter, 0.37b Downstream 100

10.12Non-dimensional Vortex Extent Growth, 0.37b 101

10.13Downstream Progression of Clean Wingtip Vortex. $\alpha = 15°$ 104

10.14Non-dimensional Vortex Growth with Downstream Propagation 105

10.15Chordwise Pressure Distribution, WT Tab Oscillate, Static Extension, $\alpha =$ 5° 106

10.16Vortex Extent, Static Gurney Tab Extension. $\alpha = 10°$, 0.37b 107

10.17Vortex Core Comparison; Static Extension and 2.0 Hz Oscillatory Scheme. $\alpha = 5°$, 2.0b 108

10.18Raw Pressure Data; $\alpha = 15°$, Both Tabs Oscillate, Varying Frequency . . . 110

10.19Transient Pressure Data Response; $\alpha = 15°$, Both Tabs Oscillate, 1.0Hz . . 112

10.20Fast Fourier Transform for Both Tabs Oscillating at 1.0Hz 112

10.21Fast Fourier Transform for Both Tabs Oscillating at 2.0Hz 113

10.22Chordwise Pressure Distribution due to Frequency Variation. Both Tabs Oscillated, $\alpha = 5°$ 113

10.23Chordwise Pressure Distribution due to Frequency Response. Both Tabs Oscillate, $\alpha = 10°$ 115

10.24Spanwise Pressure Distribution due to Frequency Response. Both Tabs Oscillate, $\alpha = 5°$ 116

10.25Vortex Extent and Core Properties at Differing Frequencies of Oscillation, 2.0b 117

10.26Chordwise Pressure Distribution, Various Oscillation Schemes, $\alpha = 5°$ . . 118

10.27Chordwise Pressure Distribution, Various Oscillation Schemes, $\alpha = 10°$. 118

10.28Spanwise Pressure Distribution, Various Oscillation Schemes, $\alpha = 5°$ . . . 120

10.29Spanwise Pressure Distribution, Various Oscillation Schemes, $\alpha = 15°$ . . . 121

10.30Spanwise Pressure Comparison, WT & FT 2.0 Hz Oscillation Schemes, $\alpha =$ 5 and 15° 122

10.31Vortex Core and Movement, $\alpha = 15°$, 1.0b 124

10.32Normalised Core Movement, $\alpha = 15°$, b:1.0 125

10.33Vortex Core and Movement, $\alpha = 15°$, 2.0b 126

10.34Effect of Oscillating Both Tabs on ΔC_P 127

10.35Vortex Core Comparison; $\alpha = 5°$, 0.37b 132

10.36Vortex Core Comparison; $\alpha = 5°$, 1.0b 133

10.37Vortex Core Comparison; $\alpha = 5°$, 1.0b, Flap: 30° 134

10.38Effect of Frequency on Vortex Disruption. $\alpha = 5°$, Flap: 30° 135

10.39Vortex Core Dispersion. $\alpha = 5°$, Flap: Retracted 136

10.40Vortex Core Dispersion. $\alpha = 5°$, Flap: 30° 136

10.41Sinusoidal Core Motion, WT & FT Tab Oscillate 2.0 Hz. $\alpha = 5°$ 137

List of Tables

1.1 FAA Minimum Separation Standards 18

5.1 Final Wing Geometry Selected 35

5.2 Pressure Tap Positions 43

7.1 Summary Data Acquisition Devices Purchased in Facilities Upgrade 58

7.2 Current Source Resistor Values 61

8.1 Temperature Calibration Gradients 68

8.2 Pressure Calibration Gradients 74

8.3 Pixel Width at Measured Downstream Locations 77

9.1 Sensor No. 5 Raw Data 81

9.2 Sensor No. 5 Zero Value Subtract 81

9.3 Sensor No. 5 Temperature Data 82

9.4 Sensor No. 5 Output Corrected for Temperature Variations 82

9.5 Sensor No. 5 Calibrated Pressure Output 82

10.1 Pressure Test Conditions 86

10.2 Nomenclature to Describe Tab Configurations 87

10.3 Minimum and Maximum Pressures - Transient Case 111

10.4 Change in C_P value at FT5 due to Frequency Variations, Both Tabs Oscillated 114

10.5 Change in C_P value at FT5 due to Oscillating Both Gurney Tabs, 2.0 Hz . 119

List of Symbols

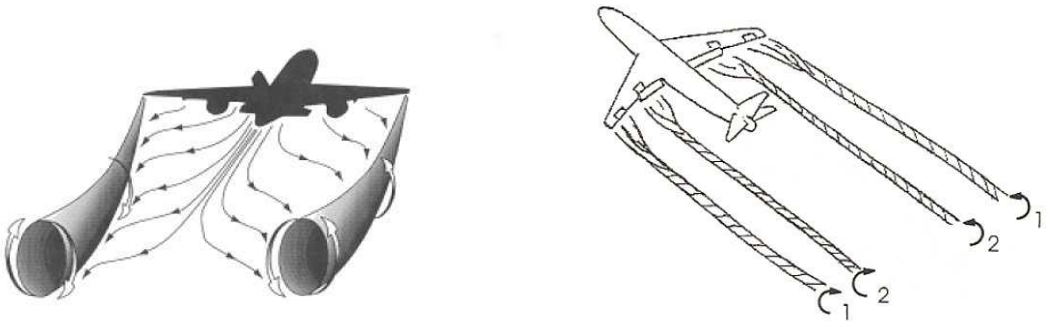
ρ	Fluid Density
U_∞	Free Stream Velocity $[m.s^{-1}]$
l	Lift Per Unit Span
Γ_0	Circulation at the Origin
b	Wing Span
y	Perpendicular Distance along the span of the wing from the centre line
C_L	Dimensionless Lift Coefficient
S_{Ref}	Reference Wing Area $[m^2]$
AR	Wing Aspect Ratio $\left(\frac{b^2}{S_{Ref}}\right)$
V_θ	Tangential Vortex Velocity
r	Radial Distance from Vortex Core
V_{Dec}	Vortex Descent Velocity
b_0	Vortex Core Spacing [m]
Γ	Circulation
C_{DI}	Induced Drag Coefficient
C_L	Lift Coefficient
AR	Wing Aspect Ratio

e	Oswald Correction Factor based on Apparent Wing Aspect Ratio
d_{cut}	Cutoff Distance in Self-induction Integral
c	Vortex Core Diameter
η	Dimensionless Turbulence Intensity
τ	Dimensionless Wake Lifespan
H	Dimensionless Wake Descent Distance
T	Dimensionless Time
NS	Dimensionless Stratification Parameter
QS	Dimensionless Turbulence Parameter
Γ_1	Wingtip Vortex Circulation
Γ_2	Flap Vortex Circulation
b_1	Wingtip Vortex Spacing
b_2	Flap Vortex Spacing
a_1	Wingtip Vortex Core Radius
a_2	Flap Vortex Core Radius
MAC	Mean Aerodynamic Chord [m]
μ	Dynamic Viscosity $[Pa.s]$
μ_0	Viscosity at STP
T_R	Air Temperature [°R]
T_{R0}	Rankine Temperature at STP: 518.6° R (15° C)
x^*	Normalised Downstream Distance
x	Tunnel Downstream Direction

δ	Crouch Ratio
d	Distance between Wingtip and Flap Tip Vortex Centroids
b	Distance between Wingtip Centroids
A	Amplitude
ω	Angular Frequency
$MaxPos$	Maximum Actuation Position ie +1100
$MinPos$	Minimum Actuation Position ie -750
$AmpPer$	Percentage of Maximum Amplitude Desired
f	Frequency of Oscillation [Hz]
T	Dimensionless Time
d_{ds}	Downstream Distance in x Direction
P	Gauge Pressure determined by Manometer [Pa]
ΔV	Pressure Sensor Voltage (Measured Voltage - Zero Voltage) [V]
C	Pressure/Voltage Slope
σ_c	Uncertainty in Slope
σ_P	Uncertainty in the Pressure Measurement
$\sigma_{\Delta V}$	Uncertainty in the Voltage Output

1 Introduction

Wingtip vortices are an inevitable consequence of the generation of lift by a lifting body. A large rotating mass of air trails an aircraft at any point where there is a finite discontinuity on the lifting surface, such as at a wingtip or the edge of a conventional trailing edge flap. An aircraft in a clean configuration (gear up, high lift devices retracted) produces two counter-rotating vortices; one at each wingtip. Figure 1.1 (a) depicts the conventional two vortex arrangement seen in the clean configuration. An aircraft with trailing edge flaps deployed trails four vortices, two along each semi-span as shown in Figure 1.1 (b). In reality, a third pair of counter-rotating vortices are shed off the horizontal stabiliser. However, these are shown to collide and merge as they move toward the centreline in the near wake and so are neglected when modeling the far wake [1]. The two vortices shed along each semi-span wing when trailing edge high lifting devices are deployed merge to form a single resultant vortex which propagates downstream of the aircraft eventually merging with the vortex shed on the opposite wingtip, dissipating into a harmless state after approximately 90 seconds [2].



(a) Two Vortex Arrangement [1] (b) Four Vortex Arrangement [3]

Figure 1.1: Trailing Vortex Shedding from a Conventional Wing

There are a number of physical explanations for the formation of the trailing vortex. One is that the wake forms as a result of the pressure difference between the upper and lower surface of the wing and the discontinuity of the wingtip. Air tends to

move in a spanwise direction, toward the tip on the lower surface and toward the wing root on the upper surface. Thus as one approaches the wingtip, the higher pressure air on the lower surface tends to roll up and over the tip onto the upper surface in an attempt to equalize the pressure gradient between the two. This rolling mass of air serves to hamper the motion of the aircraft. Thus the vortices are said to generate an 'induced drag' on the airframe. The name is derived from the fact that the drag force is induced as a result of the generation of a lifting force by the wing.

The trailing vortex can also be explained in terms of the conservation of angular momentum. A starting vortex is induced downstream of a wing due to the viscosity present in air, provided the wing is cambered or inclined at an angle of attack relative to the freestream. The formation of the starting vortex is shown in Figure 1.2. To satisfy the conservation of angular momentum, an equal but opposite circulation (Γ) must be set up on the wing to oppose this starting vortex. The velocity vectors induced by this circulation increase the velocity on the upper surface and reduce the velocity on the lower surface thus producing a negative pressure gradient and a corresponding lift force.

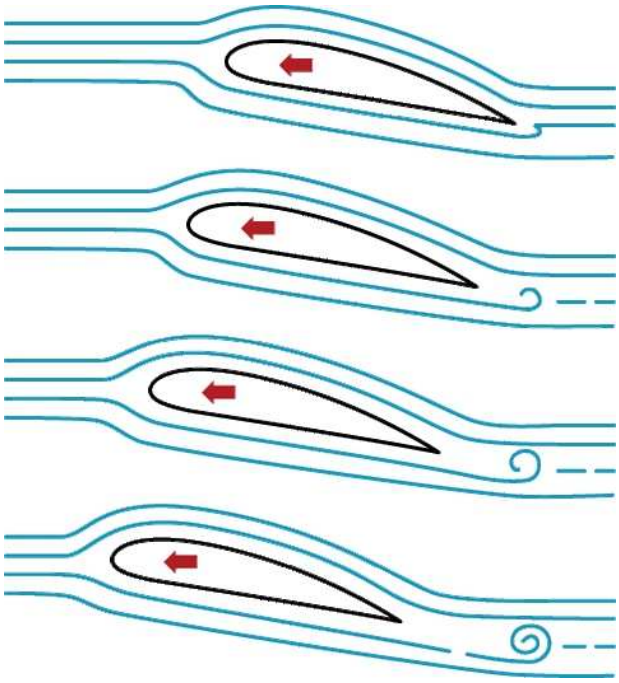
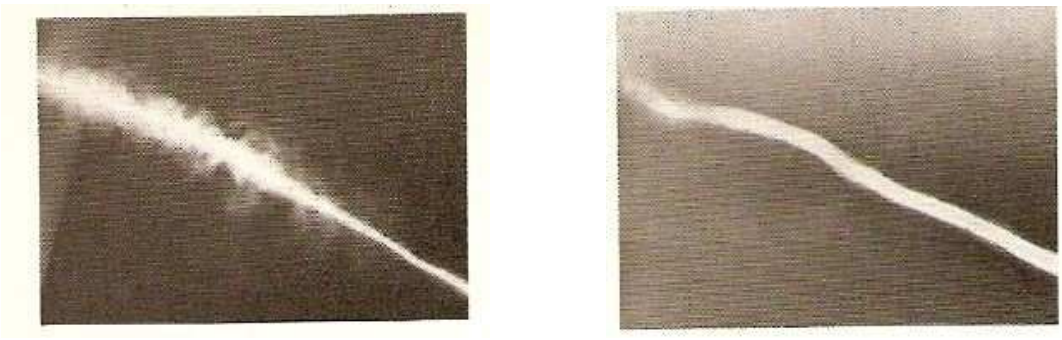


Figure 1.2: Starting Vortex Formation - Conservation of Angular Momentum [4]

1.1 Vortex Movement and Dissipation

Studies into the the movement of the wake trailed by an airliner began in the early 1970's as the danger of trailing behind ever larger aircraft became apparent. Crow [2] showed that wingtip vortices undergo a long period near sinusoidal instability until the two wingtip vortices join at intervals to form a train of vortex rings as seen in Figure 1.3. Chevalier [5] attempted to verify the instability noted by Crow by conducting flight tests where smoke was ejected at the wingtip of two light aircraft, and the resulting vortex pattern studied. Chevalier noted two vortex breakup patterns which occurred in calm air. The first appears as a bursting of the vortex core with a resulting dispersion into the surrounding atmosphere. The second appears as a simple stretching of the vortex core leading to dissipation. Photographs taken by Chevalier of these two dissipation phenomena are reproduced in Figure 1.3. Chevalier showed that the wavelength of the Crow-type instability and the wavelength of the vortex bursting instability are very similar, leading to the possible conclusion that the two instabilities are related.



(a) Core bursting Dissipation [5] (b) Chevalier Vortex Dissipation in Calm Air [5]

Figure 1.3: Chevalier Vortex Dissipation in Calm Air

Wake vortices produced by large transport aircraft have been shown to sink at a rate of several hundred feet per minute, diminishing in strength and rate of descent both with time and distance from the generating aircraft [3]. Figure 1.4 is a representation of the motion of the wake trailing a large airliner. The wake descends between 500 and 900 feet below the aircraft, levels off and dissipates to a safe level of turbulence approximately 5 NM behind the aircraft [3]. As a result, pilots trailing a landing aircraft are advised to always fly their approach at or above the flight path of the aircraft they trail. A vertical separation of 1000 ft may be considered safe for all cases [3].

Atmospheric conditions play an important role in the propagation of trailing vortices. Vortices at or near the ground tend to move laterally at a speed of 2-3 knots in a

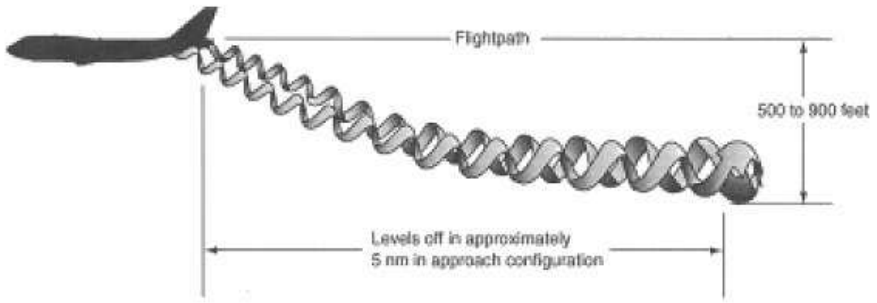


Figure 1.4: Descent of Vortices Shed from a Representative Airliner [3]

wind free situation (Figure 1.5). A crosswind will decrease the lateral movement of the upwind vortex and increase the propagation of the downwind vortex. In a situation where the wind speed matches the speed of lateral propagation of the upwind vortex, a situation can be reached where the vortex remains stationary in space for an extended period of time before dispersing. The situation could thus be reached where a vortex sits over a runway threshold for an extended period of time. Alternatively, the prevailing weather conditions may cause a vortex to stray onto the threshold of a parallel runway causing a wake encounter for an aircraft on a parallel approach (Figure 1.6). The ability to reduce the dissipation time of the vortex has the potential to reduce the risk of one aircraft straying into the path of another's wake. Understanding that the prevailing atmospheric conditions play a role in the movement and characteristics of the wake, the results generated by wind tunnel testing a wake attenuation scheme can be critically evaluated for the relevance in a real world situation.

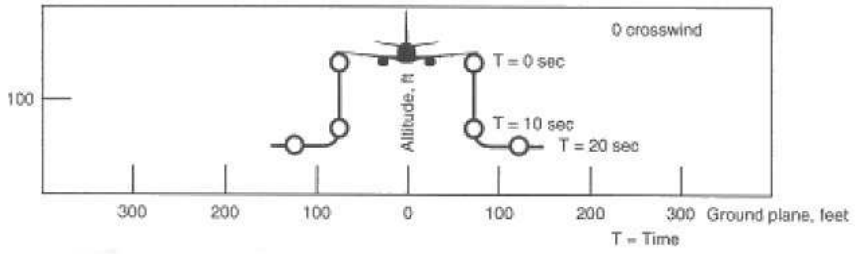


Figure 1.5: Lateral Movement of Vortices Shed by a Low Flying Large Aircraft [3]

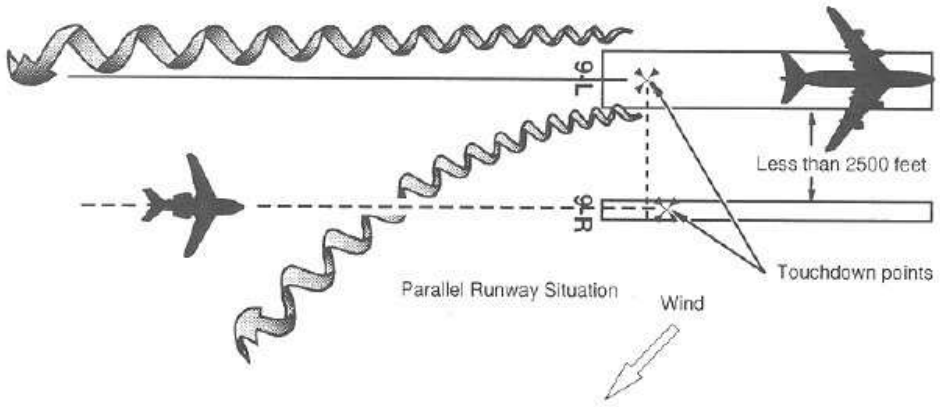


Figure 1.6: Vortex Interaction on Parallel Runways with Separation less than 2500 ft [3]

1.2 Modelling Wake Vortices

A mathematical model of the trailing vortex and its motion is presented now.

The Kutta-Joukowski theorem states that the lift per unit span in a two-dimensional inviscid flow field is expressed as the product of the fluid density, the speed of the body relative to the free stream, and the circulation about the wing.

$$l = \rho \cdot U_\infty \cdot \Gamma \tag{1.1}$$

Where:
ρ Fluid Density
U_∞ Free Stream Velocity $[m.s^{-1}]$
l Lift Per Unit Span

This definition was extended by Prandtl who developed the first practical theory for predicting the aerodynamic properties of a finite three-dimensional wing. Assuming the wing to have an elliptic spanwise circulation distribution, the circulation as a function of wing span position [6] is given by:

$$\Gamma(y) = \Gamma_0 \sqrt{1 - \left(\frac{2y}{b}\right)^2} \tag{1.2}$$

Where:
Γ_0 Circulation at the Origin
b Wing Span
y Perpendicular Distance along the span of the wing from the centre line

The total lift generated by a wing in a free stream is given by the following equation assuming incompressible flow.

$$L = \frac{1}{2}\rho U_\infty^2 S_{Ref} C_L \tag{1.3}$$

Where:
C_L Dimensionless Lift Coefficient
S_{Ref} Reference Wing Area $[m^2]$

By integrating the lift per unit span Eq(1.1) along the span of the wing and equating that to the fundamental lift equation Eq(1.3), an equation that defines the circulation at the origin as a function of aircraft geometry is defined.

$$\Gamma_0 = \frac{2C_L U_\infty b}{\pi AR} \tag{1.4}$$

Where:
AR Wing Aspect Ratio $\left(\frac{b^2}{S_{Ref}}\right)$

Equation 1.4 is of particular importance as it defines the initial circulation as a function of the wing geometry. A number of vortex properties, such as vortex tangential velocity and vertical descent rate, can be calculated directly from the circulation.

The tangential velocity of an irrotational vortex at any distance from the vortex core may be calculated using the following formula.

$$V_\theta = \frac{\Gamma}{2\pi r} \tag{1.5}$$

Where:
V_θ Tangential Vortex Velocity
r Radial Distance from Vortex Core

The vortex vertical descent rate as shown by Green [7] is calculated as follows. Here it is assumed that the vortices maintain a constant spacing as they descend.

$$V_{Dec} = \frac{\Gamma}{2\pi b_0} \tag{1.6}$$

Where:
V_{Dec} Vortex Descent Velocity
b_0 Vortex Core Spacing [m]
Γ Circulation

The vortex core spacing is defined as the distance between the centre of each wingtip vortex core. The vortex shed off a conventional square wingtip forms slightly inboard of the wingtip as shown in Figure 1.7. When calculating wingtip vortex spacing on a rectangular wing with a square wingtip, it is assumed that the spacing is a factor $\pi/4$ smaller than the aircraft wing span b [8]. That is:

$$b_0 = \frac{\pi b}{4} \tag{1.7}$$

The trailing vortex produced at the wingtip impedes the motion of the aircraft through the air. This impedance must be accounted for when calculating the total drag load produced by the aircraft. As trailing vortices are produced as a consequence to the creation of lift, the drag force is referred to as the induced drag generated by the wing. This induced drag can be modeled mathematically by applying Prandtl's lifting line theory to the case of a generally loaded wing [6]. The dimensionless induced drag coefficient is proportional to the square of the lift coefficient and inversely proportional to the aspect ratio of the wing. The simplified induced drag equation is shown in Eq 1.8

$$C_{DI} = \frac{{C_L}^2}{\pi ARe} \tag{1.8}$$

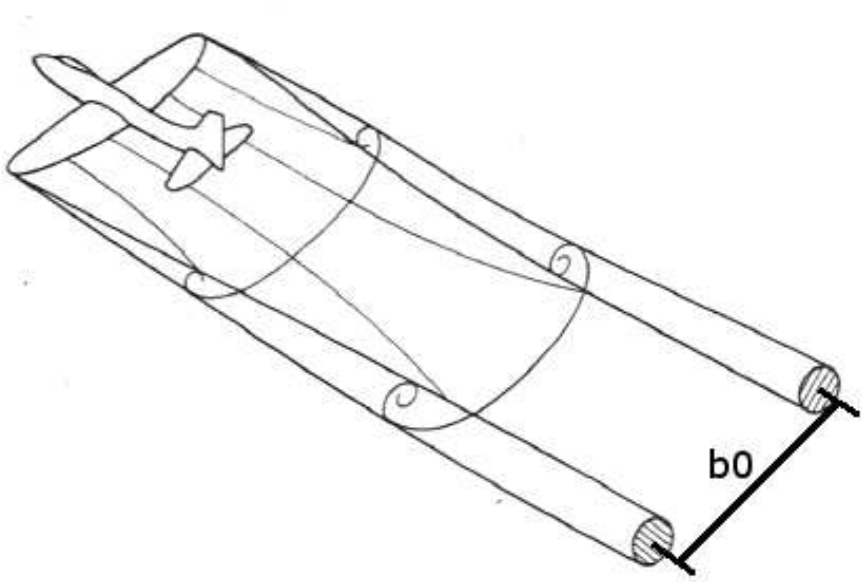


Figure 1.7: Vortex Spacing Defined [9]

Where:
C_{DI} Induced Drag Coefficient
C_L Lift Coefficient
AR Wing Aspect Ratio
e Oswald Correction Factor based on Apparent Wing Aspect Ratio

Equation 1.8 makes it apparent that the vortex shed at the wingtip is a maximum for a given aircraft at or near the stall condition where the lift coefficient is a maximum. This is most often seen during the takeoff and landing phase in a typical mission profile. During the approach to land phase, an aircraft typically has its trailing edge flaps partially or fully extended increasing the camber of the wing thereby increasing the resulting circulation. Four distinct vortices are thus formed as in the arrangement shown in Figure 1.1. It has been show through wind tunnel testing [10] and verified by flight tests [11] that the roll up centre forms around the outboard flap edge in this configuration.

1.3 Trailing Vortex Interactions

1.3.1 Crow Instability

The first to mathematically model trailing vortex behaviour with a degree of accuracy, Crow [2] showed that trailing vortices do not decay by simple diffusion but rather undergo a symmetric and nearly sinusoidal instability. The vortices produced at each wingtip eventually link up and join to form a train of vortex rings. Crow's model idealises the vortices as interacting lines with core diameters modelled by a cut-off in the line integral, representing self induction.

Figure 1.8 shows the vortex trail left by a B-47 Stratojet photographed with a stationary camera pointing vertically upward. The elapsed time after the fly-over is given under each slide. At thirty seconds, the vortices are still present as two distinct entities. At forty-five seconds, linking of the two vortices has already occured. By sixty seconds vortex breakup is evident. Once linking has occurred, the vortices dissipate relatively quickly into the harmless state shown at 75 and 90 seconds.

Crow related induced vortex velocity to vortex displacement in order to formulate an eigenvalue problem for the growth rate of the sinusoidal pertubations. Defining a cutoff distance to remove the singularity associated with defining the vortex as an interacting line, the stability of the system was found to depend on the products of vortex separation b_0 and the cutoff distance d_{cut}. The cutoff distance was found to be proportional to the diameter c of the vortex core. As a result, the following empirical formulae were constructed to describe the vortex geometry assuming an elliptical lift distribution.

$$\frac{d_{cut}}{c} = 0.3210 \tag{1.9}$$

Where:
d_{cut} Cutoff Distance in Self-induction Integral
c Vortex Core Diameter

$$\frac{d}{b_0} = 0.063 \tag{1.10}$$

A useful result, which verifies work undertaken by Spreiter and Sacks [12] is the relation between the vortex spacing and the size of the vortex core.

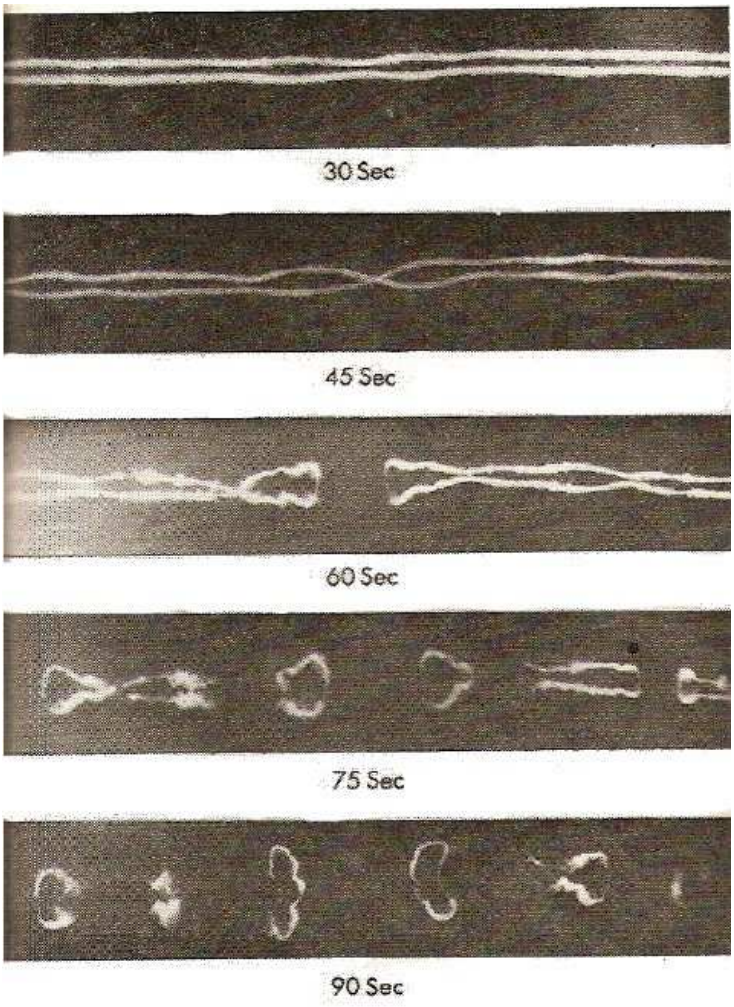


Figure 1.8: Time Elapsed Capture of Vortex Dissipation showing the Crow Instability [2]

$$c = 0.19626 b_0 \tag{1.11}$$

This result may be investigated during the course of testing to be undertaken, where the vortex core will be photographed and measured.

1.3.2 Interaction with a Turbulent Atmosphere

The nature of the vortex shedding and its subsequent dissipation has been shown to be a function of the local atmospheric conditions prevailing at the time of observation. Studies on the effect atmospheric conditions have on the dissipation time of the vortex pair was undertaken by Crow [9]. Crow built on his accepted model of vortex lifespan by attempting to incorporate the effects of atmospheric turbulence

into the model and thereby predict the wake lifespan for a range of meteorological conditions. Atmospheric turbulence was treated as a source of perturbations and enters the stability theory in the form of inhomogeneous forcing terms.

Crow [9] defined a dimensionless turbulence intensity factor η, normalising the downward velocity of the turbulent eddies with the downward velocity at which the vortex propagates. η is shown to be a function of the aircraft geometry through the vortex circulation, Γ, and the vortex spacing b. Separate models for high and low turbulence conditions were formulated by Crow [9].

For the case of strong turbulence, $\eta >> 1$, the dimensionless wake lifespan, τ was shown to be,

$$\tau = \frac{0.41}{\eta} \tag{1.12}$$

Where:
η Dimensionless Turbulence Intensity
τ Dimensionless Wake Lifespan

While Eq 1.12 was formulated for $\eta >> 1$ it was subsequently shown to be valid for any $\eta > 0.4$.

For the weak turbulence case, the induction between the vortices is at least as important as convection by atmospheric turbulence. Crow determined that the dimensionless turbulence intensity, η, and the dimensionless lifespan, τ, are related by the following expression.

$$\eta = 0.87\tau^{\frac{1}{4}} e^{-0.83\tau} \tag{1.13}$$

A plot of η against τ reveals that the two turbulent definitions coincide in the range $\eta = 0.22$ to 0.34 to produce a smooth curve of wake lifespan as a function of the turbulence intensity.

Increased turbulence clearly decreases the vortex dissipation time. While turbulence levels in the atmosphere can't be controlled, a method to simulate turbulence may equally lead to large reductions in the wake lifespan. Chevalier [5] showed that by porpoising (cycling through a range of angles of attack) an aircraft the Crow Instability could be induced, reducing the resulting wake lifespan. While this is not

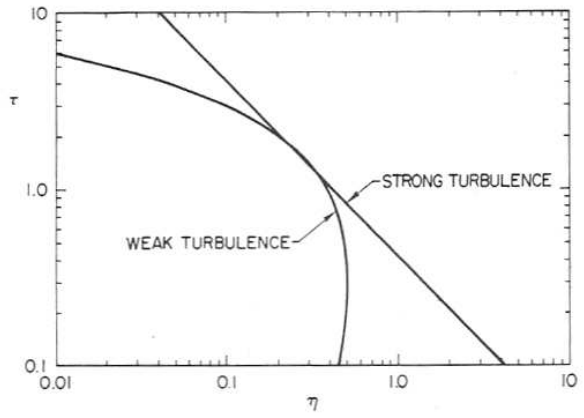


Figure 1.9: Dimensionless Wake Lifespan τ as a Function of Turbulence Intensity η [9]

a practical method to reduce the vortex danger, it was shown to be effective. Crow [9] suggests a more acceptable method. By wiring the aircraft controls such that symmetric oscillations of the lateral control surfaces are possible, the life distribution along the wing may be sloshed along the span while keeping the total lift constant. Crow postulated that by sloshing the lift distribution along the span of a Boeing 747, the lifespan of the trailing wake could be reduced by a factor of three.

Additional research into the area of vortex decay due to prevailing atmospheric conditions was undertake by Greene [7] in 1986. Greene included the effects of density stratification, turbulence and Reynolds number into a single model such that the relative importance of the above atmospheric effects to total wake decay time could be estimated.

Eq 1.6 characterises the flowfield as an ovular region of fluid descending at a velocity directly proportional to the circulation. As the wake descends through the atmosphere, it may experience viscous and buoyancy forces that reduce the impulse of the wake. If these forces are quantified, the rate of change of impulse may be determined which would result in a change in the circulation, velocity, and position of the wake.

Defining the following dimensionless parameters, plots of the wake behaviour due to varying atmospheric conditions can be made.

H Dimensionless Wake Descent Distance
T Dimensionless Time
NS Dimensionless Stratification Parameter

QS Dimensionless Turbulence Parameter

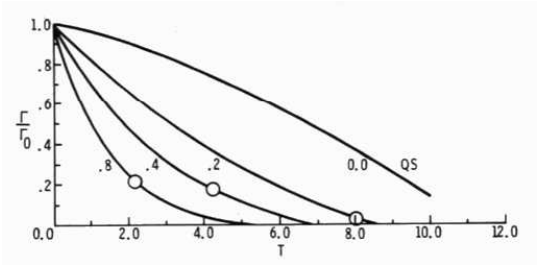
Each parameter is non-dimensionalised by vortex spacing, b_0, vortex descent velocity, V_{Dec}, or a combination of the two where appropriate. The various effects simplify into a second order ordinary differential equation (Eq 1.14) which can be solved to yield dimensionless descent velocity as a function of dimensionless time.

$$\frac{d^2H}{dT^2} + \frac{C_D L}{4\pi b}\left(\frac{dH}{dT}\right)^2 + 0.82QS\left(\frac{dH}{dT}\right) + \frac{A\,(NS)^2}{2\pi b^2}H = 0 \tag{1.14}$$

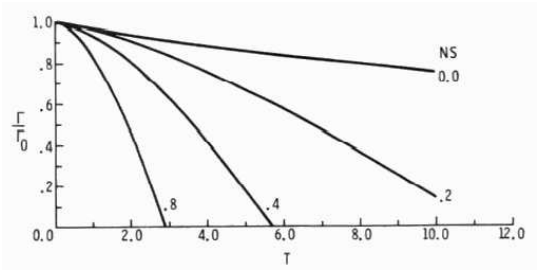
Greene also showed that

$$\frac{dH}{dT} = \frac{V}{V_{Dec}} = \frac{\Gamma}{\Gamma_0} \tag{1.15}$$

Thus a range of wake vortex properties can be investigated as the wake dissipates into the atmosphere. A number of plots are represented below (Figure 1.10) to give a brief overview of the effects of the various atmospheric parameters on the wake dissipation time.



(a) Circulation Degradation for Various Turbulence Values (NS=0.2)



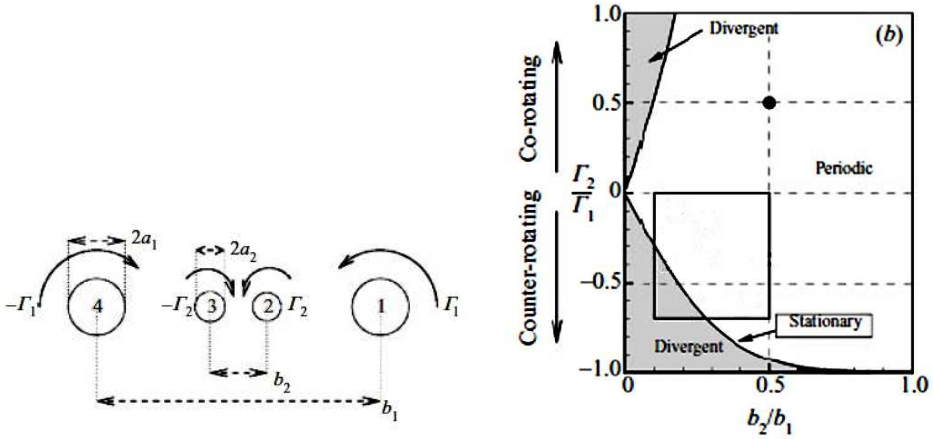
(b) Circulation Degradation for Various Stratification Values (QS=0)

Figure 1.10: Wake Dissipation as a Function of Various Atmospheric Parameters [7]

1.3.3 Interaction of the Flap and Tip Vortices

A commercial airliner during the approach and landing phase of flight, typically has leading edge slats and trailing edge flaps extended so as to fly the approach

at lower speeds and to assist in slowing the aircraft to landing speed. These flaps protrude into the free stream with the result that vortices are shed at the flap edges. A vortex shed on the outer portion of a trailing edge flap will produce an arrangement where the flap and wingtip vortex co-rotate with one another. A vortex shed on the inboard flap section produces a counter-rotating configuration. Both these configurations have been studied and modelled in some detail. Donaldson and Bilanin [13] produced a chart, reproduced as Figure 1.11, classifying the various configurations the wake could attain based on the physical properties of the aircraft.



(a) Four Vortex Nomenclature (b) Stability Classification Chart

Figure 1.11: Effect of Physical Properties on the Stability of the Vortex System [13]

The variables in Figure 1.11 take on the following definitions.
Γ_1 Wingtip Vortex Circulation
Γ_2 Flap Vortex Circulation
b_1 Wingtip Vortex Spacing
b_2 Flap Vortex Spacing
a_1 Wingtip Vortex Core Radius
a_2 Flap Vortex Core Radius

The bullet point and square in Figure 1.11 (b) show the regions in which studies have been undertaken. Crouch [14] looked at co-rotating configurations represented by the bullet point, while Fabre [15] studied counter-rotating configurations represented by the square region.

The rationale behind studying this four vortex arrangement is to determine if the deliberate interaction of these vortices could lead to an instability mode and hence an accelerated dissipation of the vortices into the atmosphere.

Crouch analysed the model analytically using the method of thin vortex filaments and solved the resulting stability equation using Floquet theory. In his model, he assumed that the two dominant vortex pairs on each semispan merge quickly as suggested by experiment ([16], [17]). A level flight path was assumed and the aircraft tracked a constant heading. Crouch's stability analysis identified three distinct growth mechanisms that could influence the break up of the vortex pairs.

The first is a long wavelength instability and is a generalisation of the Crow [2] instability discussed in Section 1.3.1. Unstable wavelengths greater than five times the vortex spacing (b_0) were shown. A Maximum growth rate non-dimensionalised by the total circulation, Γ, and vortex spacing, was calculated to be approximately 0.8. This is in close agreement with Crow's prediction for a single vortex pair. The position of the flap relative to the wingtip and the circulation ratio between the two provided only a small change to the non-dimensional growth rate. However, the physical growth rate was shown to vary by more than 50% with varying flap position and circulation ratio.

The second growth mechanism consists of short-wavelength instabilities. Both symmetric and antisymmetric instability modes were shown to exist. These instabilities are characterised by displacements about the vorticity centroids, with the centroid locations relatively unperturbed. Symmetric and antisymmetric modes refer to how the vortices rotate relative to one another. The various modes are shown in Figure 1.12

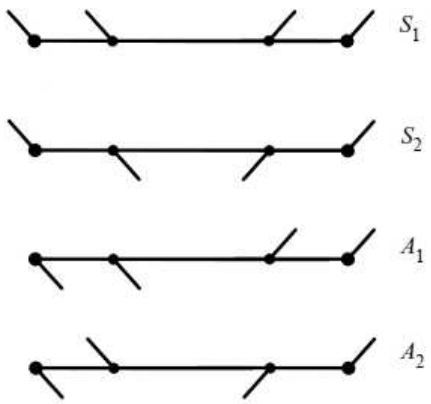


Figure 1.12: Schematic of the Various Instability Modes Observed [14]

The symmetric-mode wavelength lies between $1.5b_0$ and $4b_0$, while the antisymmetric wavelength was shown to exist in the range of $1.5b_0$ and $6b_0$. This instability mode was shown to produce non dimensional growth rates of approximately 1.3 for the

symmetric case and 1.6 for the antisymmetric case. This is significantly greater than the case of pure Crow Instability [2].

The last growth mechanism identified was one of transient growth. The amount of amplification seen dependened on the vortex pair's initial condition. If one vortex pair was excited by a perturbation, significant transient growth was observed. This was shown to amplify an initial disturbance by a factor of 10-15 over one period of rotation of the co-rotating pair. The greatest potential to exploit this transient growth occurs at the long wavelengths associated with the Crow type instability.

Crouch concentrated on the interactions of a pair of co-rotating vortices. Following his work, Fabre et al [15], extended the analysis to consider the instability of two vortex pairs in a counter-rotating configuration. Such a configuration is observed behind an aircraft with vortices produced at the inboard flap edges and on the wingtips.

Fabre's results showed similar trends to that of Crouch. Both optimal perturbations, corresponding to the largest amplification of the instability over all wavenumbers, and 'long wave optimal perturbations', defined as symmetrical perturbations leading to the largest amplification of the crow instability, were investigated. For periodic configurations very large growth rates were reached. However, this was achieved for large values of $b_2/b_1 (> 0.4)$ which corresponds to very high loading at the wingtips. The subsequent analysis was thus limited to a more realistic value of $b_2/b_1 = 0.3$. At a downstream position of 30 spans, growth rates of between 10^3 and 10^4 were noted for the optimal perturbation case, and long-wave optimal growth rates of between 10 and 100 were shown.

A large initial amplitude is required to force the optimal perturbation case. Similar results were obtained by Crouch [14] for the co-rotating case. Crouch demonstrated a growth factor of 10 at 30 spans for the long wave transient growth mechanism and at 45 spans for the short-wave instability mechanism. This is a large improvement over single pair vortex Crow instability mechanisms which have been shown to reach an amplification factor of 10 at a downstream position of 100 spans.

Crouch [14] showed that amplifications of the instabilities inherent in the roll-up and propagation of wingtip vortices can be achieved, leading to a more rapid dissipation of the trailing wake. These instabilities have been introduced by 'sloshing' control surfaces, or by manipulating the shedding of the vortex off the wingtip and flap tip.

Tabs have been used on the trailing edges of airfoils in the past, most notably the use of Gurney flaps to increase downforce on racing cars or to aid in keeping the flow over a helicopter stabiliser attached at high angles of attack.

This body of work looks to extend this area of study by looking at the effect of introducing vorticity into the vortex shedding region using a pair of small tabs which will oscillate at the wing's trailing edge.

1.4 Miniature Trailing Edge Effectors

Research undertaken at Stanford University by Matalanis and Eaton [18, 19] investigated the use of segmented Gurney flaps attached to a conventional trailing edge which can be rapidly actuated and oscillated in a bid to disrupt and dissipate the trailing vortex formed behind the wing. The results of their experimentation and computational work showed that a row of segmented Gurney flaps, so named Miniature Trailing-edge Effectors (MiTEs), could indeed be used to excite vortex instability and thus form a possible solution to the wake vortex hazard. MiTEs were also used to excite a four vortex arrangement as would be seen when an aircraft lowers its flaps during approach to land. MiTE perturbations were shown capable of exciting a variety of instabilities of both long and short wavelengths in this configuration. A rectangular wing with a NACA 0012 profile was used and is pictured in Figure 1.13 where the installation of MiTEs along the trailing edge are clearly visible.

1.5 Wake Separation Standards

Current airport throughput is constrained primarily by the number of arrivals and departures a given runway can handle in a given time. The FAA state that average runway occupancy time for an aircraft 50 seconds [20]. For a trailing airliner approaching the runway at 160 kts, the ideal aircraft separation would then be 2.2 nautical miles (nm). In reality, separations of between 4 and 6 nm are enforced at present due to the necessity to space arriving airliners such that the wake induced behind the landing aircraft does not interact negatively on any aircraft following.

These separations are issued by the Federal Aviation Authority (FAA), have been adopted by all the regulatory bodies, and are applicable for all aircraft on approach

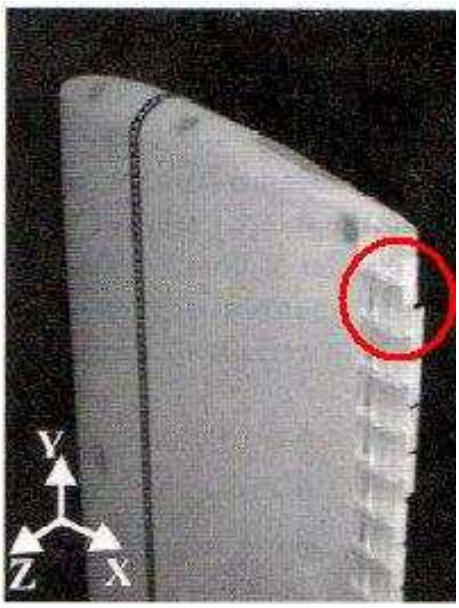


Figure 1.13: Installation of MiTEs on Trailing Edge of Rectangular Wing. [18]

to land in Instrument Meteorological Conditions (IMC) [20]. These standards dictate the minimum trailing distance of an aircraft relative to that of the aircraft ahead. All aircraft are categorized as either 'Small', 'Large', or 'Heavy' based on their maximum takeoff weight. Generally, widebody intercontinental passenger aircraft (B747, A340) fit into the 'Heavy' category while smaller domestic airliners such as the Boeing 737 or the Airbus A320 family are classified as 'large'. The B757 is placed in a category of its own due to the relatively larger vortices shed by it when compared to similar sized aircraft and the number of wake incidents reported by aircraft trailing the B757. Current FAA standards (as of June 2012) are shown in Table 1.1.

Table 1.1: FAA Minimum Separation Standards [20, 21]

Generating Aircraft	Separation Distance for Following Aircraft (nm)		
	Small(<41k lbs)	Large (41-300k lbs)	Heavy (>300k lbs)
Small	2.5	2.5	2.5
Large	4	2.5	2.5
B757	5	4	4
Heavy	6	5	4
Superheavy (A380)	8	7	6

Wake vortex limitations primarily restrict arrival capacity at an airport; however departure capacity can also be affected to a lesser extent. The degree of restriction is not independent of airport layout and thus will vary from airport to airport. Studies undertaken estimate an increase in capacity of between 5-15% could be expected in the simplest case of reducing separation distances for aircraft landing on a single runway [22]. Even greater increases would be noted in the case where closely spaced parallel runways are operated. If it could be shown that the wake produced by a landing aircraft would not interact on an aircraft flying a parallel approach, one could effectively decouple the runways thus increasing airport capacity anywhere from 20-50% [23–26].

In order to achieve an improvement in throughput efficiency, the minimum separations shown in Table 1.1 would need to be relaxed. In order to realise this, the time taken for a trailing vortex to dissipate to a level of turbulence safe for an aircraft to pass through would need to be decreased.

1.6 Motivation

Air traffic movements and passenger numbers are on the rise all over the world. Demand for air transportation in the United States is projected to double or even triple from present numbers by 2025 [22]. Statistics compiled in the United Kingdom show that passenger numbers in that country have increased from 7 million in 1957 to 241 million in 2007 [27]. This exponential growth is illustrated in Figure 1.14.



Figure 1.14: Air passenger growth rate in United Kingdom, 1957-2007 [27]

The World's current airport infrastructure does not have the capacity to deal with this large influx of air traffic. The United States have acknowledged this and set

up a Joint Planning and Development Office (JPDO) consisting of among others representatives from the National Aeronautics and Space Administration (NASA), the Federal Aviation Administration (FAA), and the Department of Homeland Security (DHS). JPDO is tasked with finding a solution to the looming problem by making major changes to the air transportation system. Called the Next Generation Air Transportation System or "NextGen" the aim of the program is to meet the increased air traffic demand projected for 2025 [22].

One of the primary constraints to the number of arrivals and departures a given airport can handle, is the need to space aircraft sufficiently on the final approach to land. This constraint is not imposed to allow sufficient time for the landing aircraft to vacate the runway, but rather as a response to the wake vortex danger posed when one aircraft follows another. The strength of the wake shed is proportional to the amount of lift produced by the wing and is thus particularly severe for large, heavily laden aircraft flying slowly in high lift situations such as takeoff and landing.

There have been a number of accidents and incidents where an aircraft trailing too close to another on approach to land, has inadvertently strayed into the wake of the leading aircraft. In 1998, a Cessna 152 and a Boeing 757 were cleared on approaches to two parallel runways. The B757 landed first and then the C152 at approximately 150 feet AGL, pitched up sharply and rolled inverted, slamming into the ground [28]. In another wake turbulence incident, an Israel Aircraft Industries Westwind business jet encountered wake turbulence behind a United Airlines B757 on approach to John Wayne International Airport in California. The ensuing crash killed all five people on board [29]. These wake encounter accidents are not isolated incidents; between 1982 and 1998, 56 accidents were reported and directly linked to wake turbulence encounters [28].

This body of research looks at ways to reduce the hazard posed by one aircraft flying into the wake of another. Crouch [14] and Fabre [15] showed that co-rotating and counter-rotating vortices shed off a wing may interact and induce early vortex dissipation. Thus a study is undertaken to chracterise the wake shed by a wing where vorticity is introduced at two points along the span. Vortex lifespan has been well documented by the likes of Crow [2], [9] and Chevalier [5], who have modeled the wake and shown that it is possible to induce instabilities which reduce the lifespan of the wake. It is hoped that the introduction of vorticity into the wake by oscillating tabs on the trailing edge of a test wing will induce instabilities in the vortex field and lead to the early dissipation of the resulting vortex.

2 Objectives

The following set of objectives are to be addressed during the course of this investigation.

1. Model the wake flow behind a lifting surface with a trailing edge flap and variable incidence sinusoidally oscillating tabs.
2. Examine the effect of added vorticity on the stability of trailing vortices.
3. Validate and verify the modeling methods applied.

3 Method

A wind tunnel investigation was undertaken to ascertain the effect of adding vorticity to the near wake by oscillating two tabs on the trailing edge of a test wing. One tab was affixed to the wingtip, the other to the trailing edge of a plain flap. By periodically introducing additional vorticity at these two locations, it was hypothesised that instabilities created in the flow field would accelerate the breakup of the trailing vortex, leading to earlier dissipation of the powerful trailing vortices.

In order to model and characterise the near wake, two sets of measurements were taken; upper surface pressure tests to examine the effect of tab oscillation on the upper wing surface, and flow visualisation tests which examined the physical dimensions of the resulting wake vortex. A baseline case was established for the wing in a clean configuration, that is tabs and the plain flap retracted, after which the effect of periodically introducing vorticity into the near-wake could be established. The test wing made use of a NACA 0012 airfoil section. This was selected primarily due to the large quantity of published aerodynamic data available for this profile and served as a means to validate and verify the modeling methods applied.

3.1 Test Matrix

A comprehensive test matrix was developed to incorporate both the pressure measurement and flow visualisation components of the experiment. The two areas were tested individually, the data processed, and further testing completed where necessary. The following variables were monitored and varied during the test process.

- Test Model Angle of Attack (0, $\pm 5, \pm 10, \pm 15^{\circ}$)
- Wind Tunnel Test Velocity (7 - 16 $m.s^{-1}$)
- Trailing Edge Flap Angle (0 - 50°)

- Tab Oscillation Scheme
- Tab Oscillation Frequency (0.5 - 2.0 Hz)

A test schedule was compiled for one angle of attack (α) and then repeated for each subsequent α tested. The negative angles of attack were used when compiling baseline pressure data only as only the wing upper surface was tapped. This allowed for net pressure distributions to be established for the clean wing where the negative angle of attack simulated the lower surface of the wing at its corresponding positive angle. This was only possible due to the symmetry of the NACA 0012 profile used. Net pressure distributions could not be obtained for cases where the tabs were extended or oscillated as this configuration breaks the symmetry of the wing.

A trailing edge flap was built into the wing which could be controlled from outside the tunnel and extended to any angle between 0 and 50° . Vortex attenuation would be of most benefit in the approach and landing phase of flight where a trailing edge high lift device is used to increase the camber of the wing and reduce the stall speed of the aircraft. Thus tests were performed with the flap extended to 30° in order to mimic an aircraft as it commences its landing phase.

The two tabs affixed to the wing were built such that they could remain parallel to the chord or be extended normal to the freestream. By oscillating the tabs in a sinusoidal manner, vorticity was introduced into the near wake; the effects of which were studied and characterised. Both static and oscillating tab configurations were examined. In both cases, three variations in tab scheme was studied; the case where only the wingtip (WT) tab was extended/oscillated, extension/oscillation of just the flap tip tab (FT), and the case where both were extended/oscillated (WT & FT). For all cases where the tabs were oscillated, three sinusoidal oscillation frequencies were examined; 0.5, 1.0, 2.0 Hz. A synchronous oscillation scheme was used for cases where both tabs were oscillated.

Figure 3.1 graphically illustrates a sample test matrix for which flow visualisation tests performed at a speed of $7.2 m.s^{-1}$; the resulting speed attained with the tunnel's manual speed controller set to 0.3mA. These same tests were then repeated to obtain pressure measurements for the wing in the same configurations. Figure 3.1 shows the three basic configurations tested (Baseline, Static Extension and Oscillating Tabs) and the specific cases tested within that as lower members on the organisational structure.

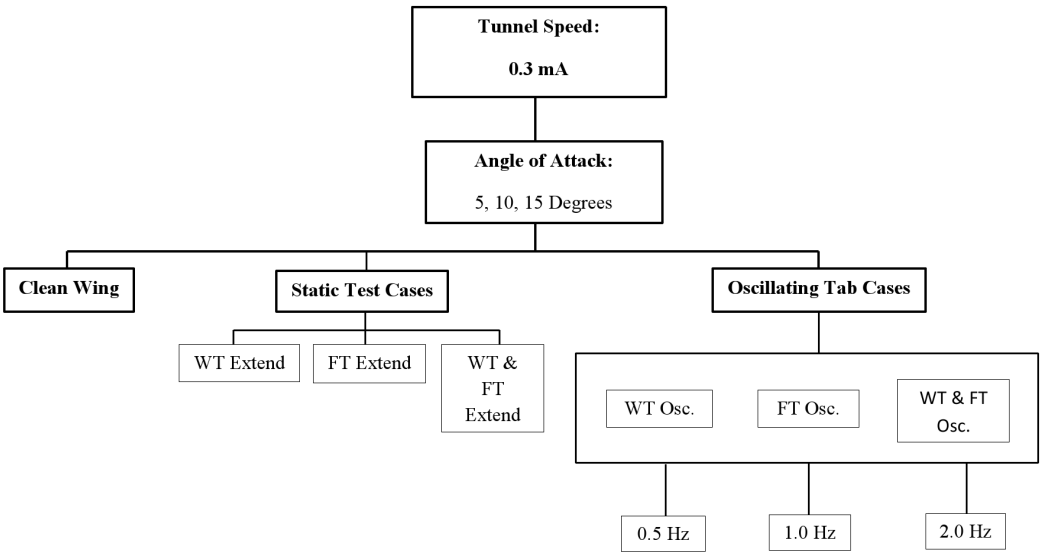


Figure 3.1: Graphical Representation of Testing Completed

3.2 Pressure Measurement

Pressure tests formed an important component in the investigation as the upper surface curvature is primarily responsible for the generation of lift. By installing pressure taps in the upper surface, a good indication as to the increase in lifting capability of the wing achieved by oscillation and extension of the two tabs was had. Twenty-five pressure taps were installed on the wing upper surface both in a spanwise and chordwise arrangement. Two chordwise locations were measured; one at the wingtip and one at approximately 60% along the span. Spanwise taps were installed at approximately 0.33c and 0.73c. The installation and positioning of the taps is covered in more detail in subsection 5.3.5.

Pressure data was gathered using hand built electronic pressure transducers and a *National Instruments* digital data acquisition system. Pressure data was automatically written to a file which was subsequently opened in Excel and processed. The design and build of the transducers is covered in chapter 7 along with the data acquisition hardware and software acquired. Information pertaining to the calibration of the transducers is covered in chapter 8.

3.3 Flow Visualisation

Flow visualisation formed the second aspect of the experimental testing undertaken. Visualisation of the resulting airflow and associated streamlines were shown using a helium bubble generator to seed the airflow with a constant stream of neutrally buoyant soap bubbles illuminated by a continuous light-source directed on the region of interest. All images were captured using a Nikon D90 SLR camera.

Images were collected both of the chordwise distribution of flow over the wing for the various tab oscillation schemes as well as cross-section images of the resulting wake, measured at three distinct downstream regions. Images were obtained of the wake from roll-up and tracked the vortex centre and extents under the oscillation of the tabs to give insight into the motion of the resulting wake. Images were used in conjunction with pressure plots to characterise the wake.

3.3.1 Helium Bubble Generator

Flow visualisation was completed using a *Sage Action* Helium Bubble Generator. The bubble generator works by creating neutrally buoyant helium filled soap bubbles and injecting them into the test section freestream. The bubbles entrain in the flow, highlighting the streamlines in their area of application. The bubble generator allows the operator to vary the bubble diameter between $\frac{1}{32}''$ and $\frac{3}{16}''$ to suit the particular application. The bubbles are ideally suited to capturing flow patterns at speeds below $30fps$ ($9m.s^{-1}$) although bubbles will remain intact at speeds up to $60m.s^{-1}$. Small bubbles of approximately $\frac{1}{32}''$ were produced and used for all testing to give the best resolution possible when calculating vortex extent and core diameter. A tunnel speed of $7.2m.s^{-1}$ was used for all flow visualisation performed in this body of work. This allowed clear photographs of the vortex cross-section to be taken as the wake propagated downstream.

3.3.2 Camera Setup

The test wing was mounted vertically in the tunnel allowing flow visualisation photographs to be captured in two planes; chordwise images of the flow over the wing taken from directly above the model, and vortex cross-section images taken at three distinct downstream locations normal to the flow. The chordwise images were taken by cutting a window into the roof of the windtunnel and enclosing the hole in

pexiglass. A camera mount was constructed from wood which allowed the camera to be precisely located normal to the window looking directly down at the chord. Figure 3.2 serves as an example of the type of photograph captured from the vertical camera mount. The image shows the resulting airflow at the trailing edge of the wing at 10° angle of attack with the wingtip tab extended.

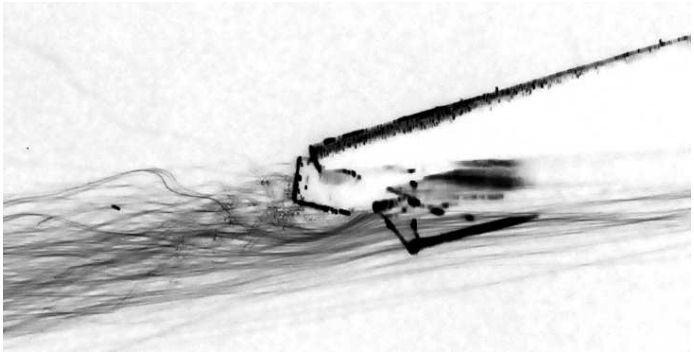


Figure 3.2: Flow Visualisation: Wingtip Tab Extended into the Freestream

Images of the resulting vortex cross-section at different downstream locations formed the bulk of the experimental data gathered. Cross-section images gave a clear insight into the ability of the various tab schemes to impart vortical instabilities into the wake. This was achieved by looking at the vortex extent, the size and position of the core, and the movement of the wake as the tabs were oscillated. Three distinct downstream locations, referenced relative to the full span of the wing (twice the semispan model) were selected from which to capture images; namely 0.37b, 1.0b, and 2.0b. Figure 3.3 shows the location of the three downstream positions relative to the model. The position of the Nikon D90 camera mounted to a tripod is also shown at the rear of the tunnel.

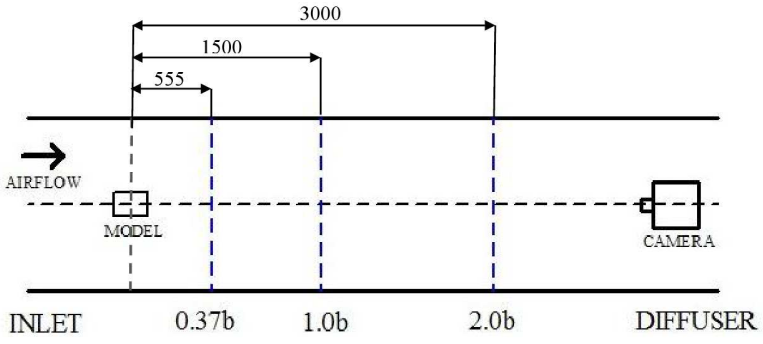


Figure 3.3: Cross Section Stations along Tunnel Test Section

4 Draw Down Wind Tunnel

4.1 Draw Down Tunnel Specifications

Wind Tunnel testing was completed in order to model the wake propagation behind a lifting body with a view to examine and exploit instabilities in the wake. While Computational Fluid Dynamics packages are suitable as a preliminary investigation into the wake properties of a lifting body, wind tunnel testing is necessary in order to fully map the behaviour and interactions of complex wake structures. The Wits low speed Draw Down Tunnel was selected as the most appropriate facility in which to perform the experimentation. A photograph of the Wits Draw Down Tunnel (DDT) is shown in Figure 4.1.



Figure 4.1: Photograph of the Wits Draw Down Wind Tunnel

The tunnel is driven by a 25 kW DC electric motor turning a six blade, Howden CT6 10ft diameter fan. This is capable of accelerating the air in the 1.5 $\times$ 1.5m test section to a maximum speed of approximately $17m.s^{-1}$. The tunnel's draw-down

configuration and flow straightening honeycomb inlet ensures low flow turbulence is present in the test section.

The tunnel was chosen primarily as a result of its long 9m test section which is critical when examining the wake flow downstream of the model. The long test section and low turbulence properties lends itself very nicely to flow visualisation methods for determining the resulting vortex position and downstream propagation.

4.2 Coordinate System

It is necessary to standardise the coordinate system to be used for all experimental work. A right hand coordinate system has been employed with body fixed axes. Figure 4.2 shows the vertical semispan model in the tunnel with the coordinate system shown. The downstream direction designated x, the spanwise direction toward the right wingtip y, and the lift direction z. The coordinate system selected is common across the majority of work in this field, and as such has been adopted here.

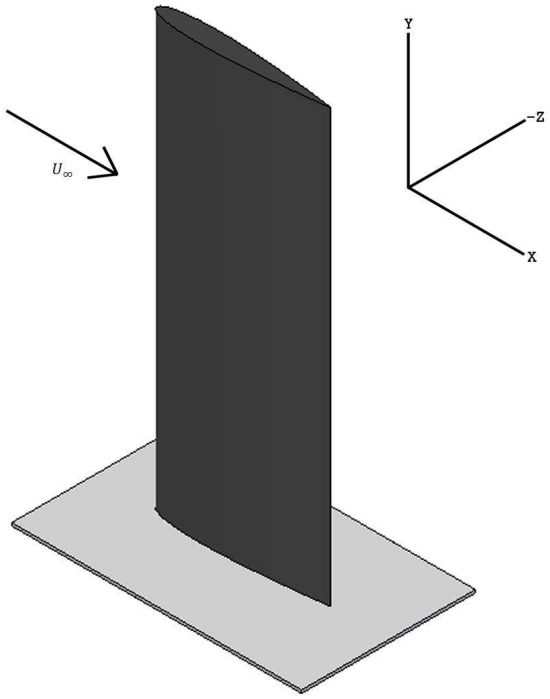


Figure 4.2: Right-hand Coordinate System

5 Wind Tunnel Test Wing

5.1 Experiment Overview

A brief overview of the work to be undertaken is given now to familiarise the reader with the basic layout of the tests completed before describing the necessary equipment in more detail. A semispan NACA 0012 wing was constructed and mounted vertically in the forward section of the tunnel. The wing has an electronically driven trailing edge flap which is able to deflect into the freestream flow to a maximum angle of 48°. Embedded into both the flap tip and wingtip are small tabs which are controlled by external Faulhaber Minimotors and have the ability to be oscillated in a sinusoidal scheme or extended to a static position. These tabs introduce vorticity and perturbations into the flow in order to induce instabilities in the near wake.

Twenty-five pressure taps are installed both spanwise and chordwise along the upper surface of the wing. This allows a detailed pressure investigation to be undertaken looking at the effect the tabs have on the resulting flow properties.

Flow visualisation in the form of photographing the resulting wake seeded with neutrally buoyant helium bubbles was used in conjunction with the pressure data to characterise the flow field.

The semispan model is mounted vertically on a purpose designed sting balance, bolted to the tunnel floor.

5.2 Preliminary Design and Placement

5.2.1 Geometry Optimisation

A number of important design criteria had to be taken into consideration when designing the semispan wing. Most notably, the geometry selected formed a trade-off between maximising Reynolds number while at the same time maintaining an aspect ratio representative of the type of aircraft to benefit from wake alleviation. It is common practice to represent downstream wake distance as a multiple of wing span and too great an aspect ratio would result in a situation where the available downstream distance at which the wake could be quantified would become too short. The various criteria are discussed below from which the best design given the tunnel constraints was determined.

Reynolds Number

Reynolds number is an important dimensionless quantity that must be considered when performing tunnel testing. It is defined as the dimensionless ratio between inertial and viscous forces experienced by the model in the freestream. Reynolds numbers allow the classification the flow type as either laminar or turbulent. The accepted minimum for testing wings in a wing tunnel is 40 000. Below this Reynolds number the flow will not be turbulent. [30] Ideally the Reynolds number over the test piece's characteristic length should match that of the intended fullscale design; although this is seldom possible due to wind tunnel speed constraints. Fully turbulent flow with a Reynolds number of approximately 200×10^3 is necessary to allow a comparison to be drawn with existing literature. The Reynolds number is defined as follows:

$$R_e = \frac{\rho U_\infty MAC}{\mu} \tag{5.1}$$

Where:
MAC Mean Aerodynamic Chord [m]
μ Dynamic Viscosity $[Pa.s]$

The dynamic viscosity of air varies with temperature and can either be looked up from a table or calculated using the following method as outlined by Pope [30]. The viscosity is calculated first in imperial units ($lb - s/ft^2$), then converted to the

more familiar SI convention. Sutherlands Law (not shown here) to define viscosity in terms of SI units can also be used and both methods will yield the same final value.

$$\mu_{IMP} = \mu_0 \frac{T_R}{T_{R0}}^{0.76} \tag{5.2}$$

$$\mu_{SI} = 47.88038 \times \mu_{IMP} \tag{5.3}$$

Where:
μ_0 Viscosity at STP
T_R Air Temperature [°R]
T_{R0} Rankine Temperature at STP: 518.6° R (15° C)

A rectangular wing section was deemed most appropriate for the testing to be undertaken. This allowed the wing geometry to be simplified and a more direct comparison with existing results to be made. The rectangular wing means the test Reynolds number obtained is simply a function of the chosen chord length. Figure 5.1 shows the variation of Reynolds number with chord length at a number of attainable tunnel speeds. The density used is $0.983kg/m^3$, an average density as calculated on a typical Johannesburg day.

Research undertaken by Breitsamter et al [10] into the turbulent vortex flow behind a large transport aircraft made use of a semispan model in a wind tunnel of similar dimensions to the Wits Draw Down Tunnel. Testing was conducted at a freestream velocity of $25m.s^{-1}$ corresponding to a Reynolds number of 0.471×10^6.

The work carried out by Matalanis et al [18], [19] forms another example where similar work has been carried out by completing a set of low speed wind tunnel tests. In this case a NACA 0012 wing with a chordwise Reynolds number 0.350×10^6 was used for all testing.

After considering the various literature available, a chord length of $300mm$ was selected corresponding to a Reynolds number of 0.285×10^6 at $17m.s^{-1}$ and 0.335×10^6 at $20m.s^{-1}$.

Test Section Length

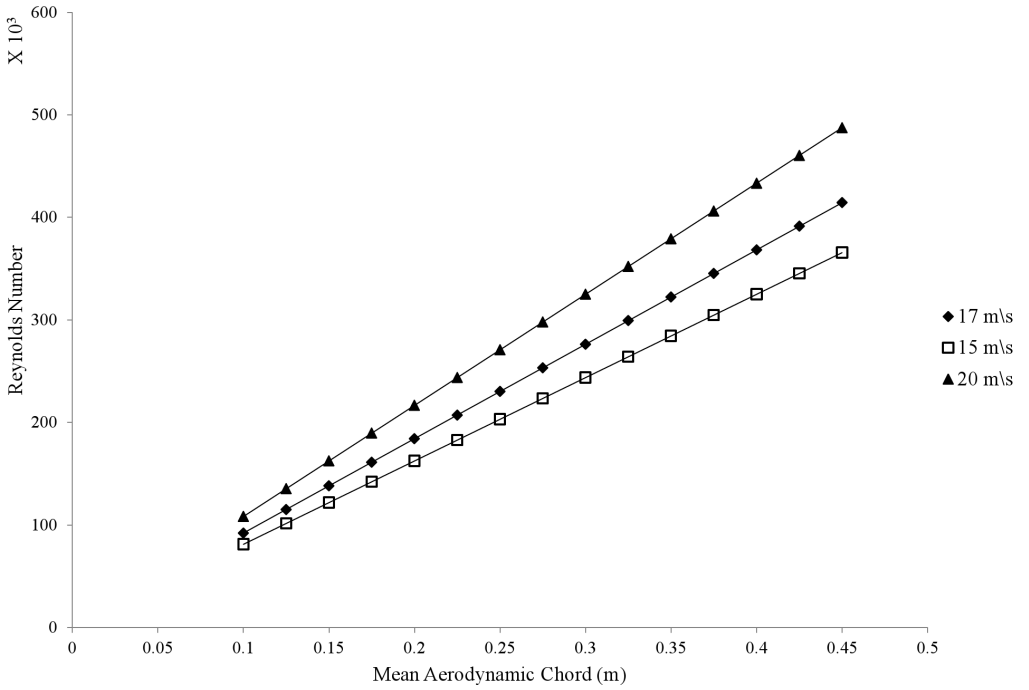


Figure 5.1: Plot of Re vs. Chord Length

The available downstream distance available behind the model is another important consideration when specifying the geometry of the semispan wing. Similar work carried out to quantify and map the downstream progression of the trailing vortex has resulted in an adoption of a standard convention for non dimensional downstream wake distance, normalised with respect to the wingspan of the model. [10]

$$x^* = \frac{x}{b} \tag{5.4}$$

Where:
x^* Normalised Downstream Distance
x Tunnel Downstream Direction

It is important to note that the wingspan here would refer to the entire span of the aircraft and so in the case of the semi-span being tested, the value of b is effectively twice the semi-span length. In order to select the most appropriate semi-span, a plot of semi-span length against the maximum number of downstream spans available due to the tunnel geometry was drawn up and plotted as Figure 5.2

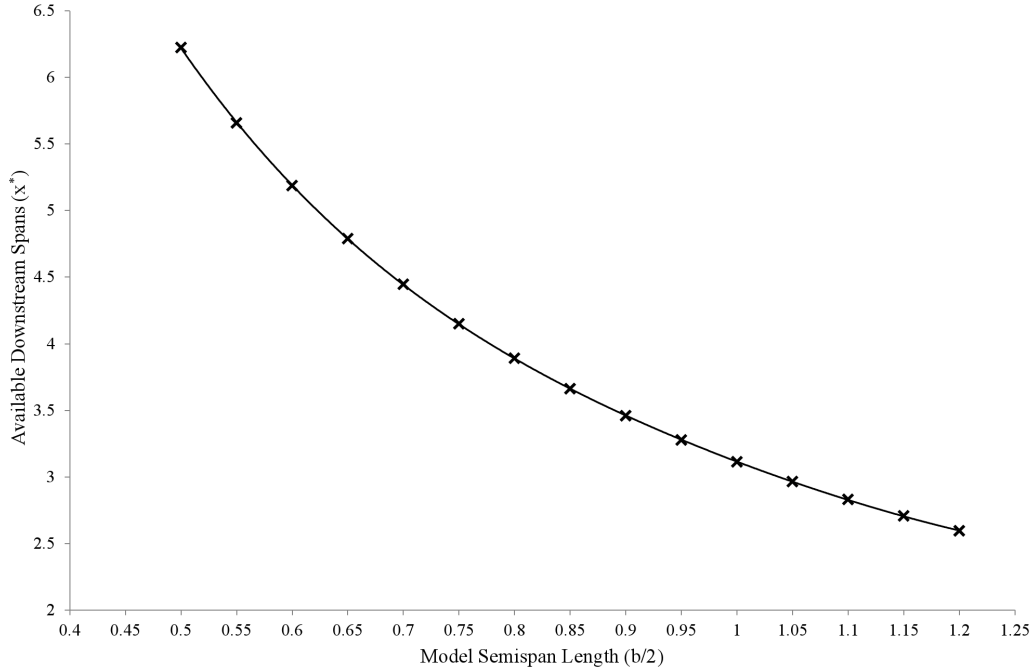


Figure 5.2: Plot of Available Downstream Spans against Semispan Length

Previous work examined has categorised the downstream development of the wake into a number of distinct regions. [10] The near field exists from the wing trailing edge to $\frac{x}{MAC} = 1$. This region is characterised by the formation of highly concentrated vortices shed at all discontinuities. The extended near field exists where $x^* \leq 10$. This is the region where the roll up and merging of the dominant vortices take place, leading to the formation of two counter-rotating vortices propagating downstream of the wing. The far field is characterised by the wake descending in the atmosphere and emerging linear instabilities between $10 \leq x^* \leq 100$. Finally the dispersion region is classified as $x^* \geq 100$ where instabilities cause strong interactions between the two vortices resulting in their collapse. Figure 5.3 is reproduced from [31] and graphically illustrates the above explanation.

The physical dimensions of the tunnel mean that only the extended near field can be examined. It is advantageous to maximise the number of downstream spans at which vortex behaviour can be analysed - this is possible when one minimises the span. However, decreasing the span results in a corresponding decrease in aspect ratio. A balance between the number of available downstream spans and an aspect ratio representative of the type of aircraft that would use small tab type trailing edge devices was sought. Figure 5.4 shows the effect a changing semispan length has on the aspect ratio, while Figure 5.5 plots the available downstream distance with aspect ratio.

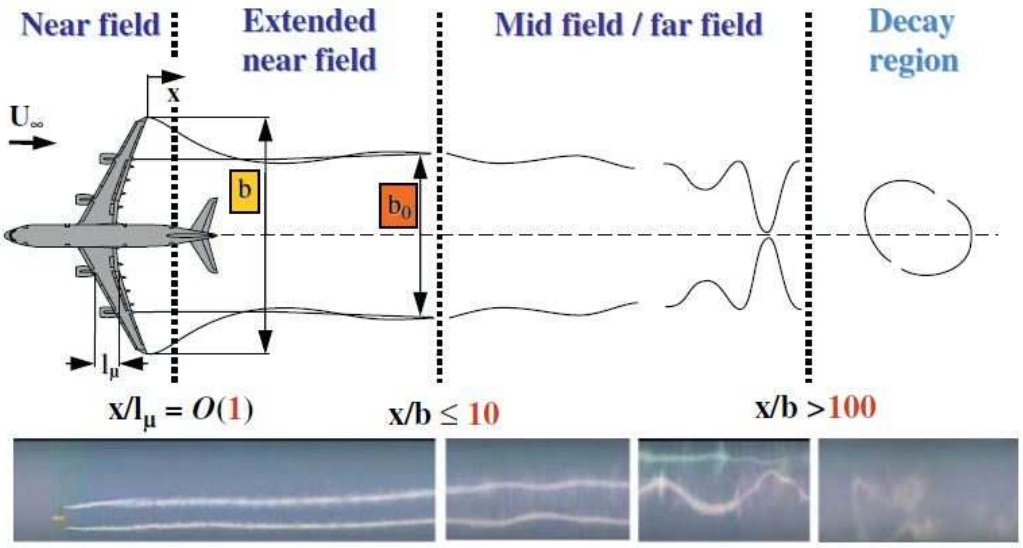


Figure 5.3: Downstream Vortex Decay and Breakup [31]

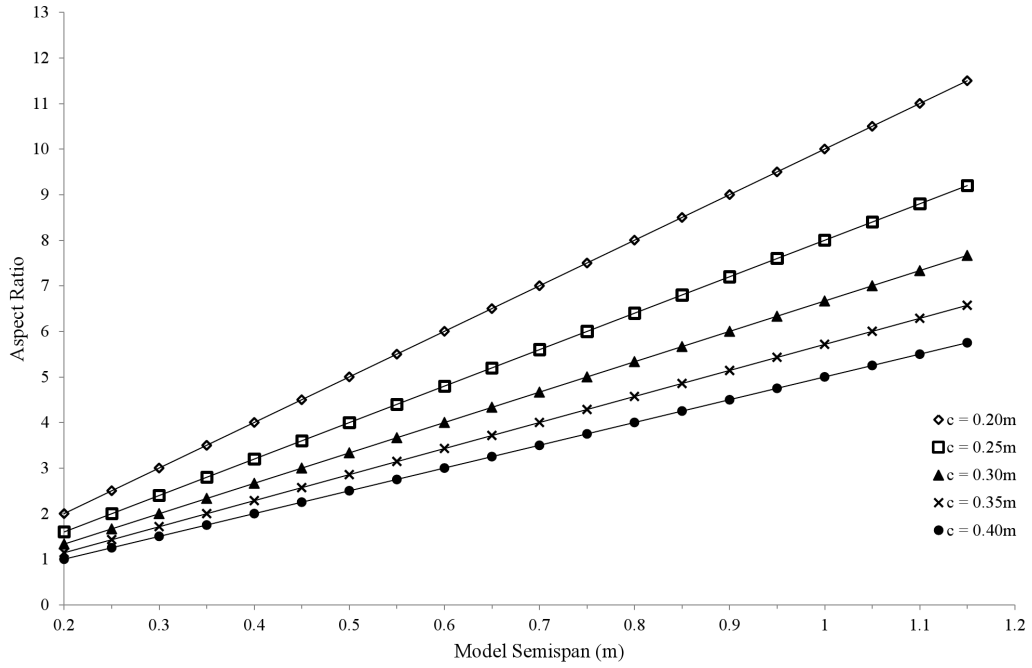


Figure 5.4: Plot of Aspect Ratio vs. Semispan for Various Chord Lengths

Test Wing Frozen Geometry

The geometry of the semispan test model was frozen after taking the above mentioned considerations into account. The result is shown in plan view in Figure 5.6 and tabulated in Table 5.1. This configuration is considered the best compromise in Reynolds number, downstream span distance and aspect ratio.

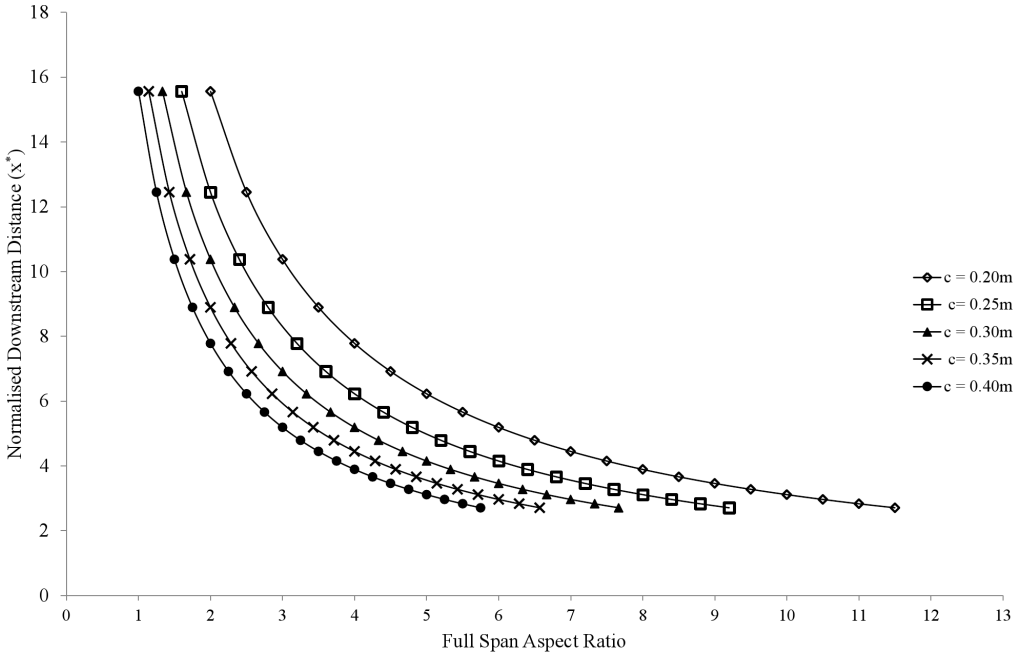


Figure 5.5: Plot of Available Downstream Spans vs. Aspect Ratio

Table 5.1: Final Wing Geometry Selected

Wing Area	0.255 (m^2)
Full Span Aspect Ratio	5
Wing semi-span	0.75 (m)
Chord	0.300 (m)
Taper	0
Sweep	0°
Crouch Ratio	0.19

Figure 5.6 and Table 5.1 makes reference to a term designated the Crouch Ratio. This non-dimensional term stems from work completed by Crouch on the instability and transient growth of a pair of co-rotating vortex pairs [14]. The ratio is defined as the distance between the wingtip and flaptip vortex centroids on one semispan, divided by the distance between the wingtip vortex centroids across the full wingspan. This is more clearly seen Figure 5.7.

$$\delta = \frac{\tilde{d}}{\tilde{b}} \tag{5.5}$$

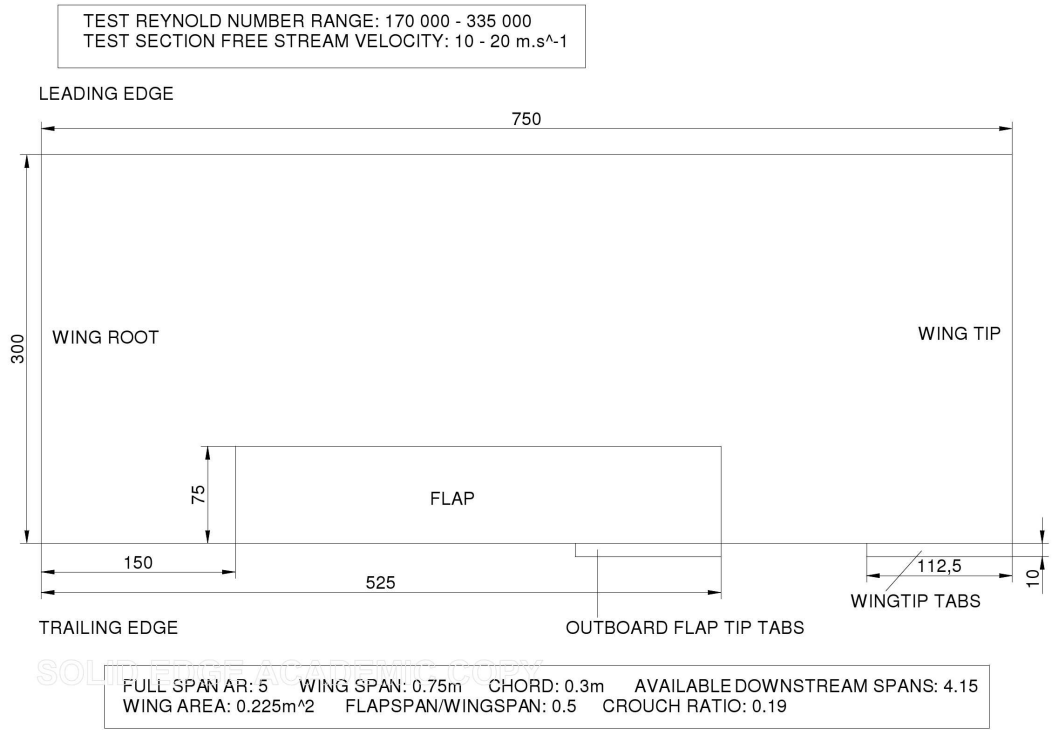


Figure 5.6: Overview of Wing Geometry

Where:
δ Crouch Ratio
d Distance between Wingtip and Flap Tip Vortex Centroids
b Distance between Wingtip Centroids

The Crouch ratio gives an indication as to the tendency of the flap and wingtip vortices to merge. Typical values for commercial aircraft range from $0.3 \leq \delta \leq 0.4$. The smaller the ratio, the more likely vortex merger becomes [14]. The Crouch ratio of the selected semispan geometry is 0.19. Thus an early merger is expected within approximately one span downstream of the model. This is essential due to the limited space available in the tunnel to observe the vortex propagation as it moves downstream of the model.

Tabs are installed on both the wingtip and outer flap tip of the model as a means to introduce perturbations into the wake flow. The tabs installed on the model protrude approximately $10mm$ into the freestream or 3.33% of the chord length. Liebeck [32] showed that the best lift to drag ratios are obtained for cases when the tab protrudes less that 0.0125c. Larger protrusions produce a greater increase in lift coefficient but with a correspondingly larger increase in drag. However, it is

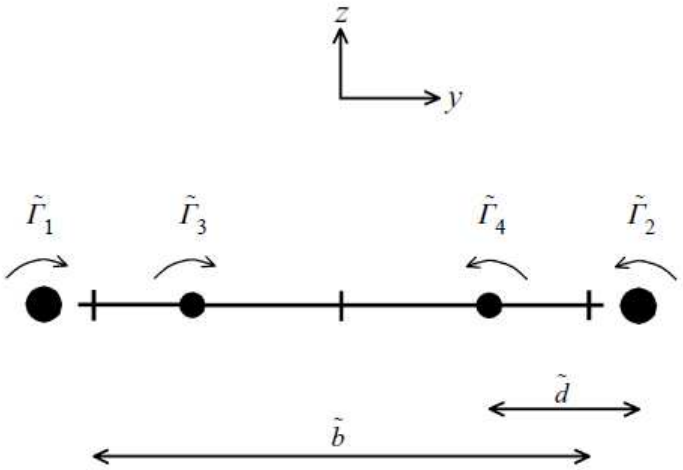


Figure 5.7: Schematic Describing Crouch Ratio

envisioned that the tabs only be actuated during the approach and landing phase of flight where the increase in drag is useful in slowing the aircraft and small relative to the drag increase of deploying the trailing edge flaps in the landing configuration.

Tab Dimensions and Placement

Tabs were installed on both the wingtip trailing edge and flap tip trailing edge. Both sets extend 15% of the wing semispan or 112.5mm. The dimensions are represented pictorially in Figure 5.8

Actuation of the tabs were completed using *Faulhaber* Linear Actuators and their oscillation scheme controlled using software written in Microsoft Visual C# 2010 Express. Both the mechanical actuation scheme and the software control are discussed in more detail in section 5.4.

5.2.2 Airfoil Selection

A symmetrical NACA 0012 profile was selected as the airfoil to be used for all testing. This was selected primarily due to the large quantity of aerodynamic data available for this profile, which can be used as a means to compare the data obtained from tunnel tests. Additionally, a number of researchers have selected this profile

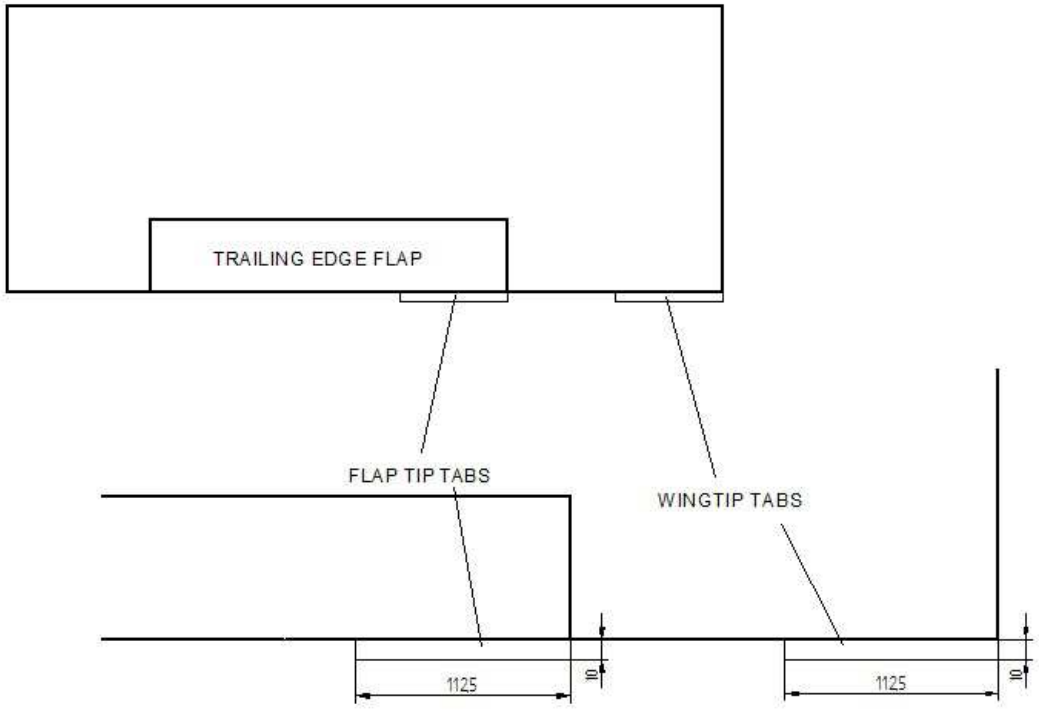


Figure 5.8: Plot showing the Tab Dimensions

as a basis from which to perform tests in the field of wake alleviation. Thus similarities and differences can be drawn between the various alleviation methods and conclusions made regarding the suitability of the apparatus as a means to reduce the vortices trailing an aircraft.

5.3 Wing Manufacture

Composite wings were manufactured for wind tunnel testing. The wings consisted of glass fibre wing skins which were manufactured in specially machined and polished aluminium moulds. The space between the two skins was then filled using two-component foam to form a rigid wing. The wing was constructed in full chord sections 500mm wide, and moulded as a separate top and bottom section split along the chord line. Four 500mm wing half sections were manufactured and then cut to size to construct the 750mm wing. Detailed instructions in manufacturing the wing appear in the subsections following this introduction.

5.3.1 CNC Wing Moulds

Aluminium wing moulds were CNC machined in the Wits Mechanical Engineering Laboratory. The mould consisted of two halves; an upper and lower surface section, to allow a complete NACA 0012 wing profile to be foamed at once. In the case of the wing manufactured for tunnel testing, one mould was inverted to form one half surface of the complete profile with a flat surface on one side corresponding to the wing's chord position. A photograph of one wing mould as used is shown below in Figure 5.9.



Figure 5.9: Photograph of the Wing Moulds Used in the Manufacture of the Test Wing

5.3.2 Wing Skins

Glass Fibre wing skins with a 300mm chord length were manufactured in 500mm spans. 163 gsm 0/90 e-glass was used and cut into 600mm x 400mm rectangular pieces, which formed one layer of the wing skins. Two pieces of cloth were used per surface to create a complete wing skin.

To form the adhesive, 150g AMT epolam epoxy resin was mixed with 50g hardener. This formed enough liquid to coat one full wing skin. Adjacent layers of cloth were coated in resin and smoothed by a 40mm hair brush. After applying two sheets of cloth and resin, the composite skin was allowed to cure for three hours and then baked in front of a heater for an additional hour.

5.3.3 Wing Foaming

Once wing skins had been manufactured, two part component expanding foam was used to give the wing its internal structure. AMT Composites manufacture the foam under the product name PU 38. The liquid foam consists of two parts mixed in a 1:1 ratio. Once mixed, the foam remains liquid for approximately one minute before reaction occurs and the foam begins to expand and harden. The method adopted for ensuring the foam completely filled the wing inner structure is outlined below.

1. The inner surface of the aluminium mould was thoroughly cleaned with acetone to ensure a dust free surface.
2. Ram wax was applied as a release agent to the mould surface to allow the wing skin to be removed once foaming had occurred.
3. A single wing skin was placed in the mould and adjusted such that it sat flush to the mould surface.
4. Two part expanding foam was mixed in a 1:1 ratio and stirred until the liquid resembled a uniform cappuccino colour. Care was taken to mix enough to completely fill the mould.
5. The liquid foam was poured onto the wing skin in an even manner at the approximate quarter chord position. This position was found to best distribute the foam over the entire section of the wing once expansion began to occur.
6. Once the foam began to react and expand, wax paper was placed over the top of the wing half section. This was done to stop the foam from sticking onto the flat section of the top mould when this was installed.
7. The top section of the mould was placed flat side down onto on top of the wax paper and bolted in place to ensure that the foam expanded into the entire half wing profile without any discontinuities.
8. The moulds and foam were left for a day to ensure that the foam had completely hardened before being reopened, at which point a well formed half section of a NACA 0012 wing was popped out the lower mould.

5.3.4 Flap Manufacture and Actuation

The trailing edge flap was only built once the complete wing was moulded as described above. The section of the wing that forms the flap was cut away from the

upper and lower wing surface, bonded together and reinstalled into the wing. The flap is mechanically driven by a geared DC motor attached directly to a shaft running through the approximate quarter chord position of the flap. Accurate flap position control is realised using a 5k linear potentiometer connected in a full bridge circuit which outputs a voltage based on the resistance setting of the potentiometer. The potentiometer is connected to the DC motor via a common shaft. The resistance of the potentiometer varies linearly as the motor rotates the flap. This provides an accurate indication as to the position of the flap relative to the chord line of the wing. A sketch of the flap actuation layout is given in Figure 5.10 For additional specifications on the motor, gearbox, and potentiometer refer to Appendix A.

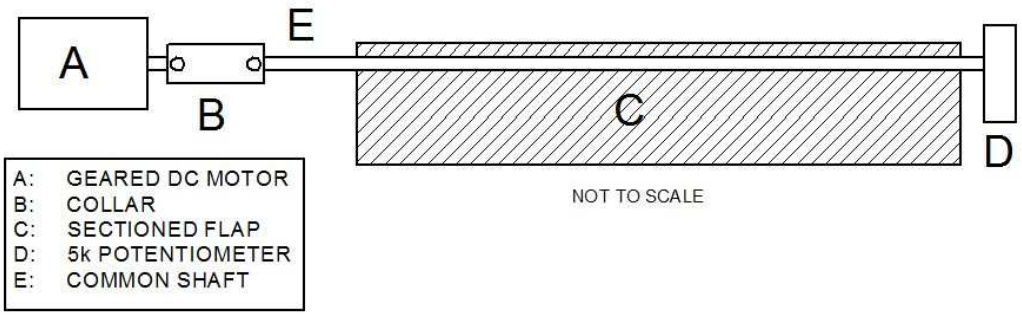


Figure 5.10: Layout of Trailing Edge Flap Actuation System

5.3.5 Pressure Tappings

Pressure tappings were installed on the wing upper surface as a means to map the resulting pressure distribution as the tabs were oscillated. Only the upper surface was tapped primarily due to the internal space constraints of the wing. The wing profile is symmetrical, thus rotating the wing through the corresponding negative angle of attack effectively allows the lower surface pressure distribution to be calculated for a given angle of attack. This is only valid when the wing is in its clean or baseline configuration (tabs retracted). Every effort was made to ensure the taps were installed perpendicular to and flush with the wing surface to avoid any unwanted flow disturbances.

Two sets of spanwise pressure taps were installed, the first at $0.33c$, the second at $0.727c$. The addition of the tabs are expected to shift the pressure centre towards the trailing edge due to the increase in camber they provide. Thus the decision to place the forward set of spanwise taps at $0.33c$ rather than the more traditional quarter chord.

Two sets of chordwise taps were embedded into the wing; one set at the wingtip, the other at the outer flaptip edge. These were placed in positions where it was expected the effect of oscillating the tabs would be visible in the resulting pressure distributions. The set of chordwise taps placed near the outer section of the trailing edge flap were sufficiently far away from the wingtip to approximate two-dimensional flow. While two-dimensional flow would only be possible by the addition of a large end-plate to the wingtip, a pressure distribution along this set of taps could still be compared to published two-dimensional pressure data as a means of calibration verification.

Each set of chordwise taps was offset in the spanwise direction at a constant angle from trailing edge to leading edge. The offset serves to ensure that flow interaction between taps is minimised as any protrusion of the tap above the surface of the wing would result in the shedding of a small vortex which could potentially interact with a downstream tap [33] & [34]. Hand et al states that it is not always necessary to offset the taps in the spanwise direction provided the taps are installed flush to the surface [34]. However, as the taps were installed by hand and presfit into the foam surface it was deemed prudent to apply a small offset to the taps. The positions of all the taps, their respective labels, and their positions relative to an origin selected as the root leading edge are given in Figure 5.11 and Table 5.2 respectively.

It should be noted that the offset angle of the midchord set of chordwise pressure taps (8°) is larger than that at the wingtip (3°). This larger offset was unavoidable in order to ensure adequate clearance between taps and the linear actuator used to drive the flap tip oscillating tab. A photograph of the wing upper surface showing the position of the taps appears in Figure 5.12 for clarity. This larger offset angle has a small impact on the chordwise results as the spanwise lift distribution decreases from root to tip. The net result is that the taps near the trailing edge (closer to the tip) may slightly underestimate the pressure relative to the taps near the leading edge. However, the majority of the upper surface suction is generated by the leading edge curvature and as such the effects on the lifting capability of the wing should be minimal. This will be further investigated once baseline pressure tests are complete.

The taps were installed into the wing in the following manner:

1. A dremmel tool was used to drill through the fibreglass skin at each pre-determined tap location.

2. A hypodermic needle was then pressfit through the hole and bonded to the soft foam.

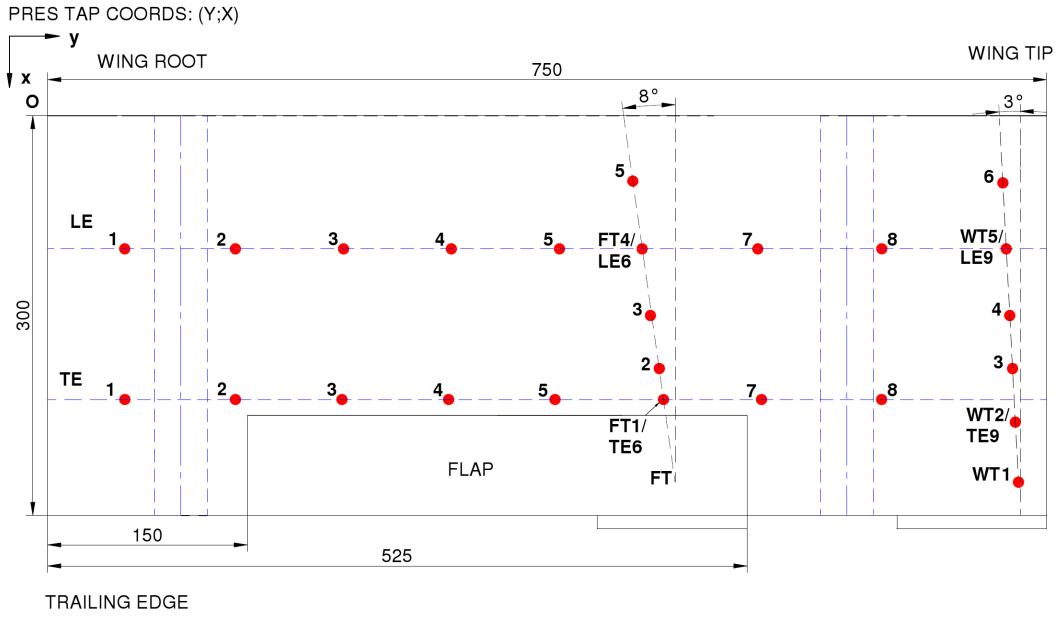


Figure 5.11: Overview of Pressure Tap Placement

Table 5.2: Pressure Tap Positions

LE 1	(57,100)	TE 1	(57,218)	WT 1	(734,271.5)	FT 1	(568,218)
LE 2	(135,100)	TE 2	(135,218)	WT 2	(731,225)	FT 2	(461,179)
LE 3	(215,100)	TE 3	(215,218)	WT 3	(729,186)	FT 3	(456,151)
LE 4	(295,100)	TE 4	(295,218)	WT 4	(726,146.5)	FT 4	(440,100)
LE 5	(375,100)	TE 5	(375,218)	WT 5	(716,98)	FT 5	(432,48)
LE 6	(440,100)	TE 6	(568,218)	WT 6	(721,47)		
LE7	(524,100)	TE 7	(524,218)				
LE8	(616,100)	TE 8	(616,218)				
LE9	(716,98)	TE 9	(731,225)				

3. The foam around each tap was milled away to allow narrow silicon tubing to be pushed over to the end of each needle.

4. Channels were cut in the foam to allow the tubing to be ducted from each tap to a central point at the root where the tubing could exit the wing.

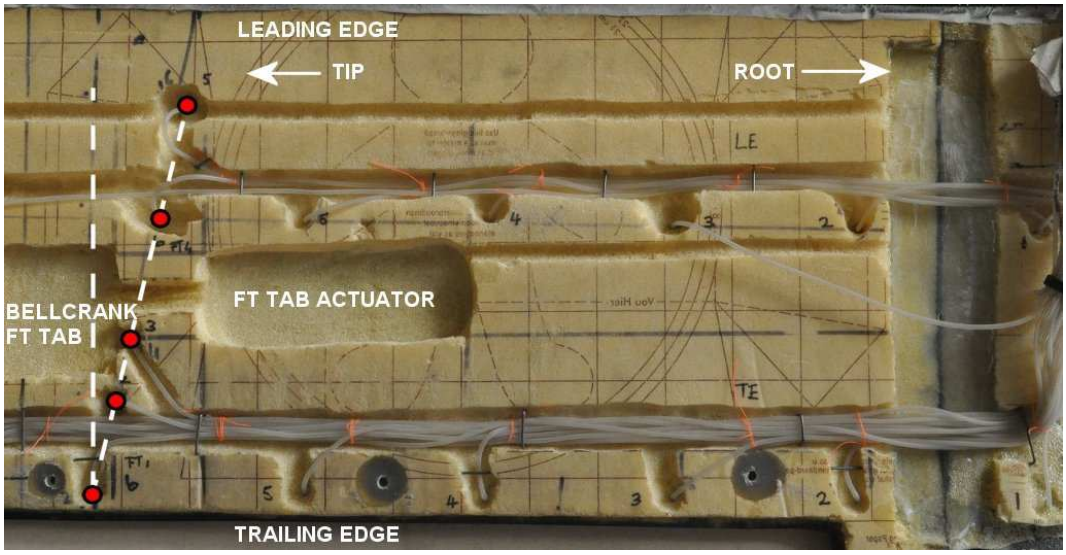


Figure 5.12: Photograph of the Test Wing Upper Surface, Showing Pressure Tap Installation

5.3.6 Assembly

A number of criteria had to be met concerning the wing assembly. It was imperative that the wing allow access to the linear actuators embedded in the wing. The final wing consisted of six distinct pieces; three upper and three lower surface sections. The wing moulds used to lay up the wing skins have a span of 500mm, thus making it impossible to manufacture the wing as a single section. The decision was made to divide the wing into three sections along the span, primarily so as to incorporate the entire trailing edge flap section as a single 500mm piece.

The upper and lower sections of the wing were bonded independent of one another to form a single upper and lower wing section. The two sections were then attached to each other with fasteners which allowed access to the internals of the wing. Two cutouts were made in the foam on the wing lower surface to accommodate wide wooden ribs at the two wing joints. These ribs were manufactured by hand and the foam cut away to ensure a precise fit. The wooden ribs were placed in the wing and then bathed in resin to bond the ribs to the foam. Cutouts were made in the upper sections of the ribs to allow the electric cables connecting the linear actuators to their external controllers to pass through. A larger section NACA 0012 mould formed the jig into which the moulds were placed to ensure the correct profile was maintained along the span of the wing. Bonding was accomplished by bathing the joints in resin after coating the mould surface and outer wing skins in release agent allowing easy removal of the wing after bonding.

The upper and lower wing surface were fastened together with wood screws countersunk into the upper surface and secured into hardened sections on the lower wing. Hardening was acomplished by milling out the necessary foam and filling the void with automotive body-filler. The fastener locations were determined by placing the two wing surfaces together, pressing them together, and determining the points that would ensure the wing best maintained its NACA0012 profile. The countersunk holes on the upper surface were filled in using melted bees-wax which was then scraped down to ensure a seamless profile or covered with insulation tape.

A rounded leading edge was created using a section of aluminum tubing specified to the correct diameter based on the calculation by Abbott & Von Doenhoff [35]. The calculation is based on the profile series of the wing and the chord length.

Body-filler was used in order to create a seamless joint at the leading edge where the upper and lower surface meet. All voids were were filled in order to maintain the desired profile. The lower section was filled such the the filler bonded permanently onto the foam while the upper surface was filled such that the filler bonded to the upper surface while remaining detached from the lower surface. This was accomplished using wax paper as a release agent and ensured that the wing could be disassembled into two distinct pieces. Any additional voids were filled with bees-wax once the wing had been fastened together.

5.4 Oscillating Tabs

5.4.1 Position and Dimensions

Figure 5.6 shows the placement and dimensions of the two tab installed on the trailing edge of the wing. Both tabs were installed at discontinuities; one at the wing tip, the other at the flap tip. Their position along the span section corresponded to the regions where the wingtip and flap tip vortices were shed. This ensured the tabs introduced vorticity into the wake, and as such influenced the position and motion of the vortices as they were oscillated.

Each tab spanned 112.5mm or 15% of the total wing semispan. Chordwise pressure taps were installed in the region of both tabs so as to characterise their influence in altering the chordwise pressure distribution. The tabs were built with a 10mm chord, corresponding to a tab-to-wing chord ratio of 3.33%. While this is larger than the ideal (1.25%) as noted by Liebeck [32], the physical design constraints

imposed by the hinges selected meant that this was the smallest size tab that could be installed.

5.4.2 Manufacture

The tabs were manufactured from 3mm thick glass fibre composite which ensured that the flaps were both light and strong and could easily be actuated by the *Faulhaber* Linear Actuators. Two hinges per tab were used to secure them to the model, the hinges being standard model aircraft hinges. The hinges were bonded to both the model and the flap using *Pratley's* epoxy resin. The wingtip tab was bonded to the upper surface of the lower wing half section, while the tab on the trailing edge flap was bonded to the flap lower surface.

5.4.3 Actuation

Faulhaber Controllers

The tabs are oscillated using linear actuators and controllers manufactured by *Faulhaber*. LM 1247-020-01 Linear DC Servomotors make use of Hall sensors to accurately position the tab in the desired location or oscillate the tab at the desired frequency. The servomomotors' motion is controlled by Series MCLM 3003S motion controllers. Each servomotor requires its own controller; therefore two linear actuators and two controllers were purchased. The LM1246-020-01 Series Linear Servomotor gives a usable stroke of 20mm, a precision of $120\mu m$ and a repeatability of $40\mu m$. For more information on the *Faulhaber* components, see the company data sheets placed in Appendix B.

Mechanical Actuation Scheme

A simple mechanical actuation system was designed in order for the tabs to actuate reliably and with a high repeatability. The seating position of the Linear Servomotors was a major design constraint as they had to fit completely within the wing and not protrude or disrupt the NACA 0012 profile in any way. Figure 5.13 shows a plan view of the wing lower surface with the motors and actuation system installed. Foam was milled out of the profile to accommodate the various actuation components. The Faulhaber motors were screwed into blocks of plywood that had

been resined into the wing to ensure that the motors remained fixed throughout the duration of their motion. Threaded M2 rods were used to connect the Faulhaber Mini-Motors to the flaps. Micro Control horns as used in radio controlled models were purchased, bonded to the tabs, and connected to the control rods to complete the actuation scheme. The tab that attached to the trailing edge flap tip made use of a flexible plastic control arm to connect the bellcrank to the flap control horn. This allowed some play in the actuation system to compensate for the varying length of the control rod required as the trailing edge flap was extended and retracted. This setup was shown to work well, and allowed the tab to actuate at all tested trailing edge flap angles of extension. The flexibility in the plastic control arm was shown not to affect the vorticity input as the tab oscillated at the same frequency when the trailing edge flap was extended. A photograph of the lower half of the wing is presented below in Figure 5.14 where the layout is clearly shown.

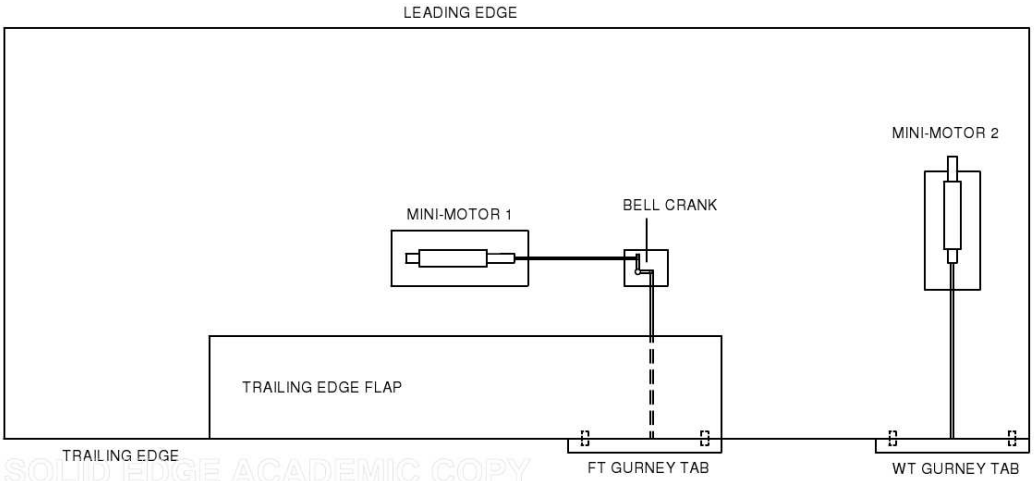


Figure 5.13: Plan view of Gurney Flap Actuation System

5.4.4 Control

Each linear actuator made use of its own controller to accurately position and move the tab. Due to the geometry constraints of the wing test piece, the actuators were installed in the wing while the controllers were built into a box and placed underneath the wing on the base of the wing mount. RS232 Serial ports connected each wing mounted linear actuator to the controllers inside the box. The box was built to accept a 24V input supply to power the controllers as well as an additional serial port input as a means to connect the controllers to a PC. The PC connection allowed for control of the actuators and their various schemes to be made directly

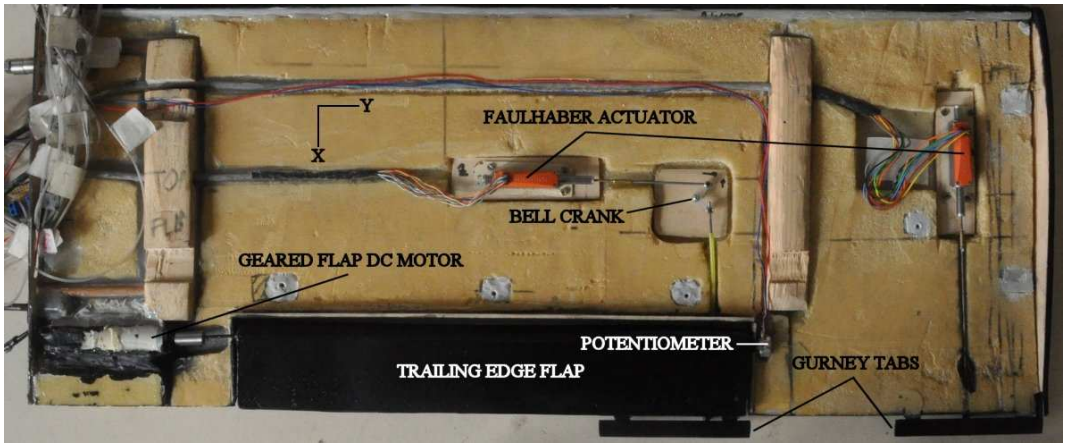


Figure 5.14: Plan view of Test Wing Layout

from within the Windows environment. A control program was written in Microsoft C# to allow static control as well as sinusoidal oscillation of the tabs. Figure 5.15 shows the wiring schematic of the controller box.

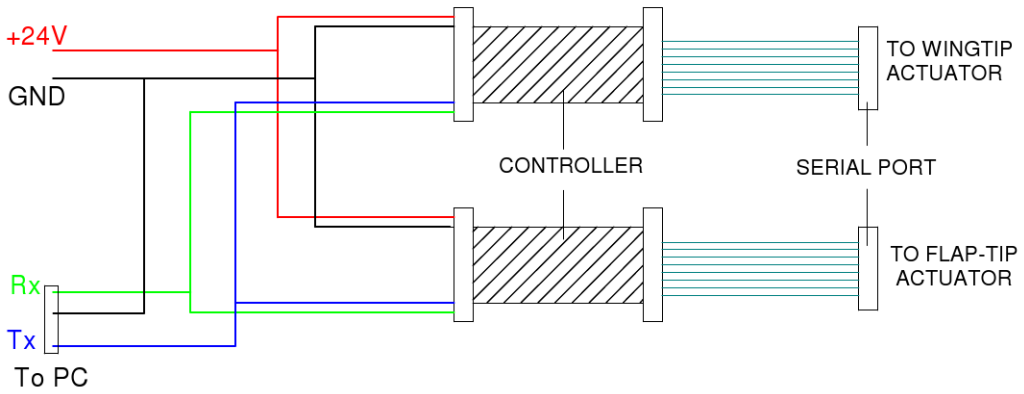


Figure 5.15: Wiring Diagram for Controller Box

Microsoft C# Control Programme

The Faulhaber linear actuators make use of an RS232 interface which allows connection to a PC to be made for external control. The controller comes with an extensive set of ASCII commands which allow the motors to be controlled either from the Faulhaber Motion Manager PC software or any stand alone software where ASCII commands can be specified and sent to the motor controllers via the RS232 serial port.

The Motion Manager software available from Faulhaber was not adequate to allow for precise oscillation control of the motors. Thus software was coded in Microsoft Visual C# 2010 Express to control the tabs as desired. The motor control programme was run in a Windows GUI and allowed the tabs to be controlled both simultaneously or independent of one another. The tabs could be positioned statically in any position between fully retracted and fully extended, or oscillated between these positions at the desired frequency. Figure 5.16 depicts the GUI window that provides the front end to the programme. A brief overview of the operation of the GUI is given, whereafter a description of the mathematical model used to oscillate the tabs is presented. A copy of the fully commented control code appears in Appendix C and is not included here due to space constraints.

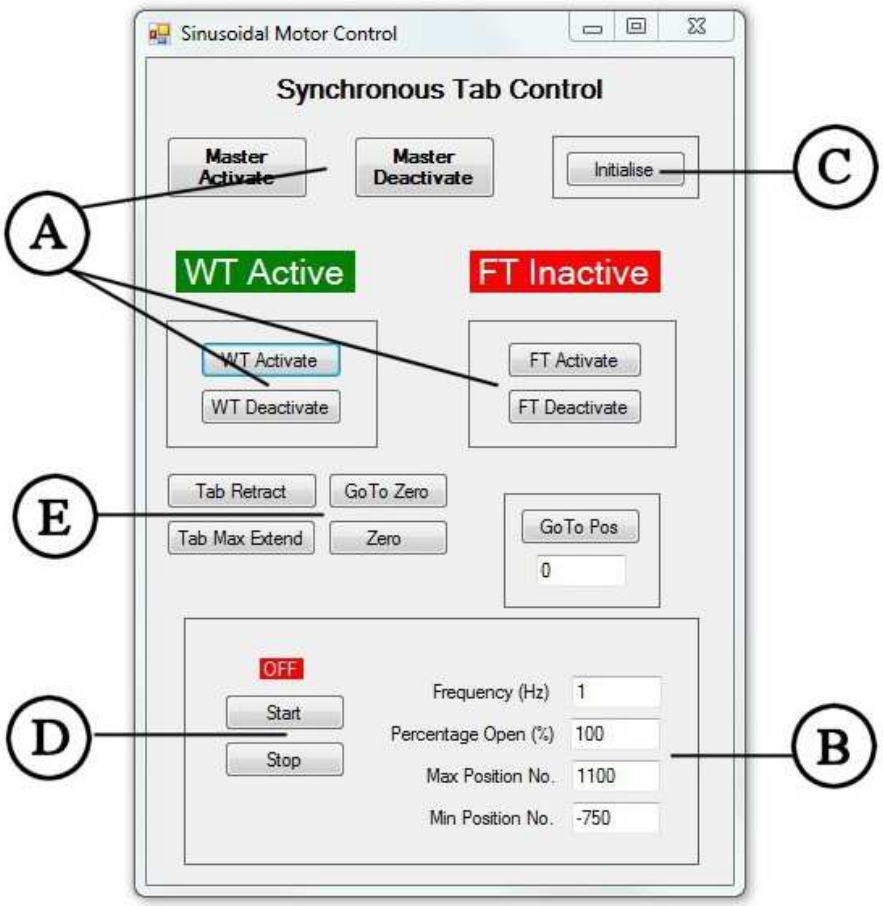


Figure 5.16: Front End Graphical User Interface, C# Control Programme

Labels A - E in Figure 5.16 represent the various steps that are taken when operating the programme. A brief description of the operational methodology follows here.

(A) Activation Buttons: Here one selects the tabs that are required to operate. The Master selection turns both motors on, while individual motors can be selected by their respective activation buttons. Tabs can also be deactivated here.

(B) Sinusoid Properties: If sinusoidal oscillation is required one can specify the oscillation properties here. The max and min position values are defined later. The frequency of oscillation is also entered here.

(C) Initialise Button: In order to apply the changes made in B, the Initialise button is pressed before oscillation is commenced.

(D) Oscillation Start/Stop: This starts or stops the selected sinusoidal oscillation scheme.

(E) Static Extension Buttons: These buttons control the static extention of the tabs. Either fully retraced or fully extended positions can be selected as well as any intermediate position using the 'Go To Pos' button.

The linear actuators make use of Hall Sensors to specify discrete points along the stroke of the actuator. The total stroke (20mm here) is broken up into 3332 discrete points, each position being assigned a value between -1666 and +1666. Thus the actuator can be moved to any one of these points using the C# programme described above. In order to introduce sinusoidal motion into the system, the variation of the actuator position with time necessary to produce a sinusoidal displacement was determined.

Once the actuators were installed into the wing, the range of position values between fully retracted and fully extended were shown to lie between +1100 and -750 respectively for both tabs. A mathematical model was constructed such that the tab position with time for any frequency could be calculated and sent to the actuators. Figure 5.17 shows the required sinusoidal input for 0.5, 1.0, and 2.0 Hz. As is shown in the figure, the tab moves from its retracted position (+1100) to the position of maximum extension (-750) in the frequency specified. The mathematical equation used to produce this motion is given below. A timer function was used in the C# environment to send the required real-time position to the actuator. After testing various timing intervals 15ms was selected as the time between position outputs. This gave smooth sinusoidal motion to the tabs without saturating the controllers.

$$y = \left(-Asin\left(\omega t - \frac{\pi}{2}\right) + (MaxPos - A)\right) \times \frac{AmpPer}{100} \tag{5.6}$$

Where:

$$\omega = 2\pi f \tag{5.7}$$

$$A = \frac{MaxPos - MinPos}{2} \tag{5.8}$$

A Amplitude

ω Angular Frequency

$MaxPos$ Maximum Actuation Position ie +1100

$MinPos$ Minimum Actuation Position ie -750

$AmpPer$ Percentage of Maximum Amplitude Desired

f Frequency of Oscillation [Hz]

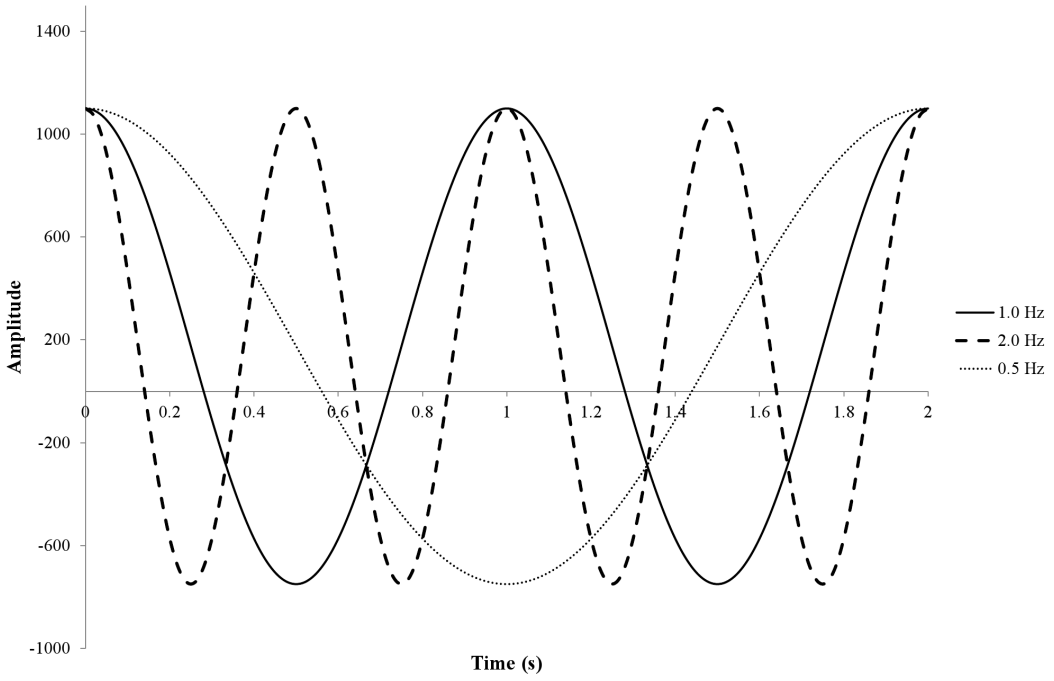


Figure 5.17: Sine Oscillation Control Input

6 Wind Tunnel Balance

6.1 Position in the Tunnel

The manufactured wing was mounted vertically through the floor in the forward section of the Wits DDT. Placement was selected such that the air entering the tunnel had propagated sufficient distance from the honeycomb inlet to transition to smooth flowing air, while also being placed sufficiently close to the tunnel inlet to permit a downstream length equal to four full spans along which to take wake measurements. Figure 6.1 shows the placement of the wing in the tunnel and the number of downstream spans available for wake interaction measurements to be taken.

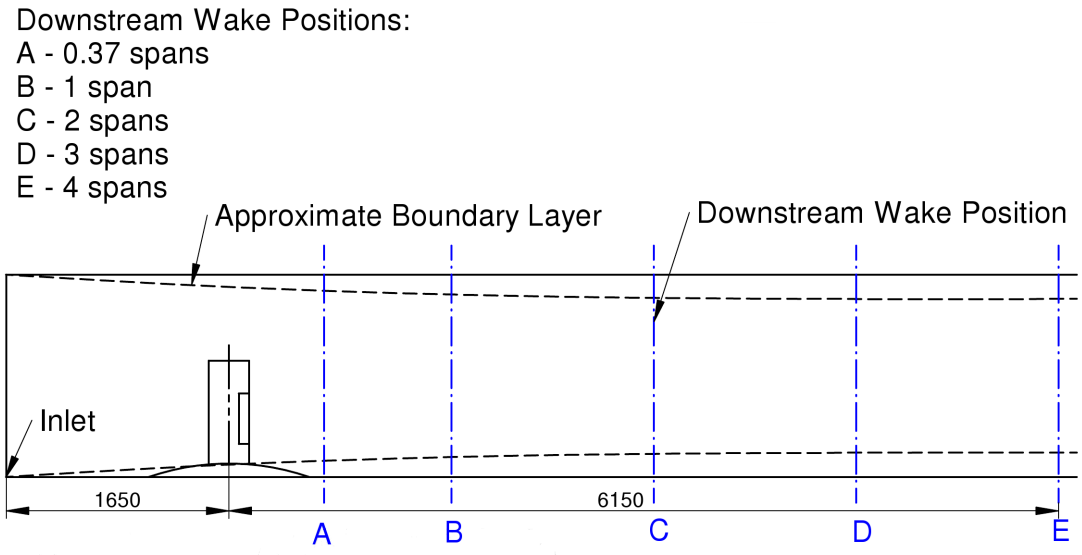


Figure 6.1: Placement of Model in Wits DDT

6.2 Design Overview

Once the decision to mount the wing vertically in the tunnel was taken, it became apparent that no existing tunnel balance or sting would suitably accept the wing's intended dimensions. Thus a mount and flexure configuration was designed to accommodate the wing with provision made to readily accept a large range of models of varying shapes and dimensions for future work.

A cage-like frame was proposed as this would yield rigidity in all planes, and reduce the chances of the mount flexing due to aerodynamic loading. The cage was designed such that all existing tunnel floor structure and support beams could be left unmodified. For this reason the frame is not square but rectangular so as to accommodate a horizontal support beam on the tunnel floor. Detailed frame dimensions and engineering drawings appear in Appendix D, while a rendered view of the complete balance design is given in Figure 6.2.

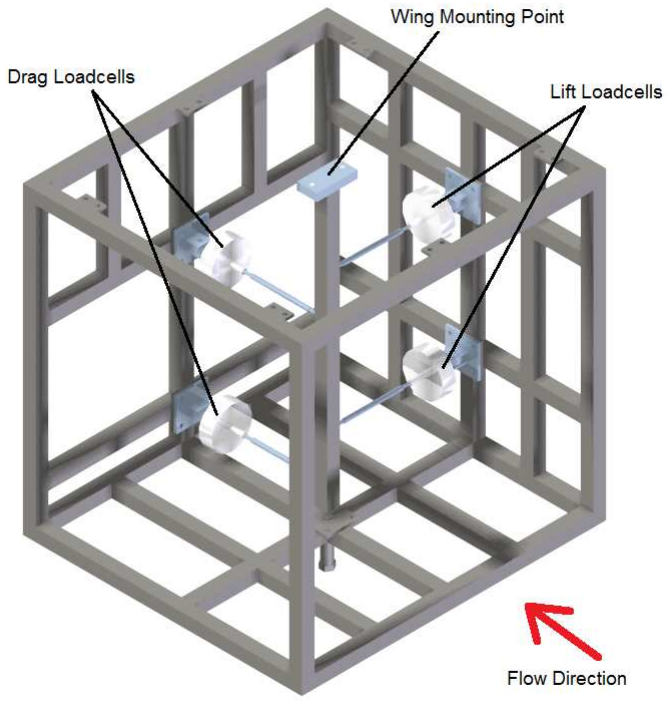


Figure 6.2: Design overview, Wind Tunnel Vertical Balance

6.2.1 Operational Methodology

It was intended that the mount provide force measurement in both the lift and drag direction so the effect of the various oscillating tab configurations on the aerodynamic forces produced could be investigated. However, the load cells used were unable to adequately handle the out of plane loading that arose as a result of the balance design and thus did not yield repeatable data and had to be discarded. A brief description of the design methodology of the balance system follows as well as the known shortcomings of the loadcells used for measurement.

The balance design made use of four custom built loadcells, arranged with two loadcells in each force component direction. Tie rod ends were used to connect each loadcell to the steel cage in a bid to decouple the strain response to the lift and drag forces produced by the wing. This allows each pair to resolve their respective forces without any cross-coupling in the system and simplifies the force calculation matrix be removing cross-coupling terms.

Custom designed Loadcells for the balance were manufactured in house by the School's workshop staff. An existing cylindrical aluminium body used in a previous failed axial loadcell design formed the departure point for the new design. Flexures were made from tool steel and heat treated so as to relieve any residual stresses set up during the machining process. Rather than fastening the flexures to the loadcell base, the flexures were clamped in place by bolting the two sections of the loadcell together thus forming a press-fit for the flexure.

Each loadcell was designed to operate in axial loading; that is, the flexure was designed such that it would deform from the application of an axial force. Strain gauges arranged in a full bridge configuration were installed into the flexure such that temperature compensation would be maintained for all load cases. An exploded view of the loadcell base and flexure is given in Figure 6.3.

6.3 Loadcell Shortcomings

Calibration of each loadcell was completed on a custom rig away from the windtunnel balance. This was done so as to test each loadcell for linearity and repeatability before being installed onto the balance. Calibration weights were hung from a hanger attached to the loadcell, loaded up to a maximum of 6kg and unloaded back down to zero. During testing it quickly became apparent that while the loadcells showed good

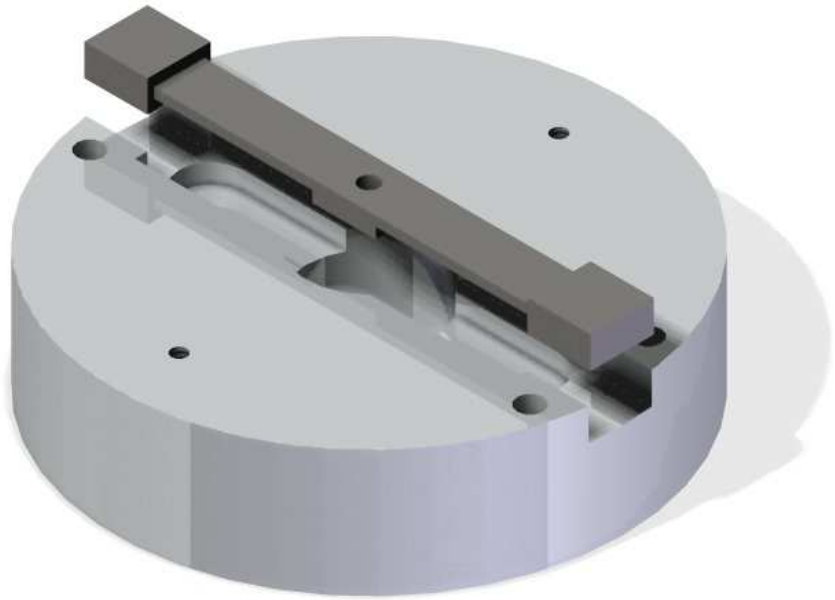


Figure 6.3: Rendering of Loadcell Base and Flexure

linearity if left to stabalise at each loadcase for at least two minutes, the response to successive runs were never identical. Figure 6.4 shows an early calibration effort where both the non-linearity of the system, as well as the hysteresis is clearly seen. This was improved by torquing up the bolts that press the flexure into the loadcell. Over tightening the loadcell set up stress concentrations around the strain gauges and so an optimum torque was sought where the loadcell gave a linear response but was also sensitive enough to pick up small changes in strain. Figure 6.5 shows a later calibration where the linearity is much improved as is the hysteresis in the system.

An offset in the zero load value was shown in every calibration test. Careful examination showed the loadcells to be very sensitive to off axis loading which was unavoidable even though the weights were suspended vertically from the flexure. The slightest side force caused warping of the flexure, with a corresponding distortion and deformation that was not as a response to the design axial load. The flexures could not be made thicker to combat this off-axis loading as this would render them too insensitive to pick up the drag force changes at low angles of attack.

A situation was reached where it was concluded that while the theory behind the flexure design was sound, and a near linear calibration could be had in laboratory conditions, in practice the loadcells were not suitable to be used for accurate force

measurement in the wind tunnel - principally as a result of the inevitable off-axis loading generated as a result of the balance configuration. The design of the flexures were completely dictated by the geometry of the original loadcell housing which was inherited from an earlier failed project. If custom built loadcells were to be manufactured to give a suitably accurate response, a complete redesign of the loadcell and flexure arrangement would be needed.

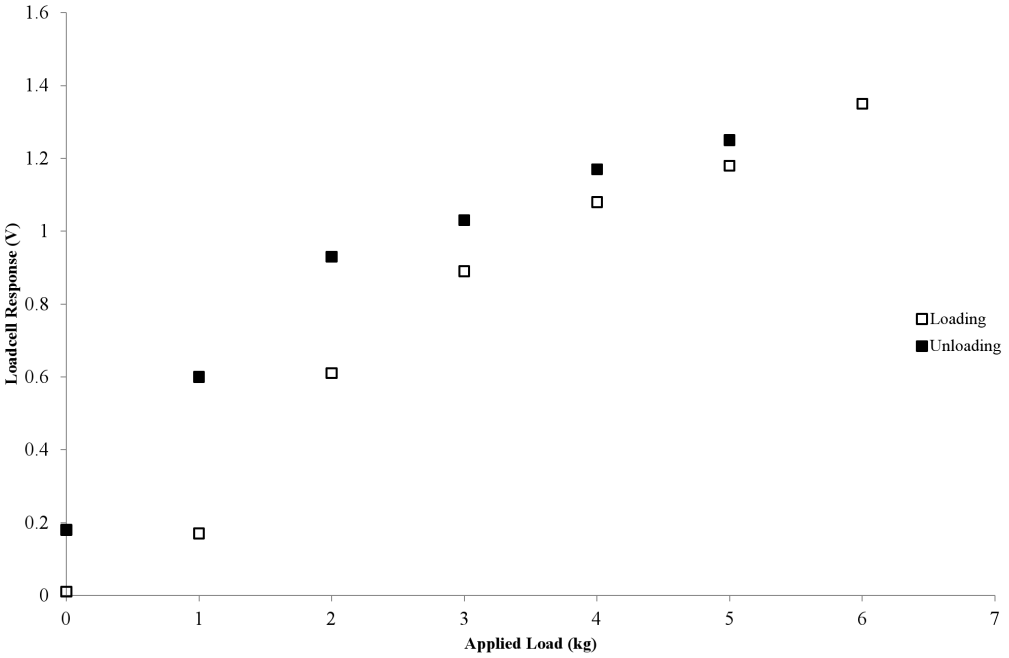


Figure 6.4: Non-Linearity and Hysteresis in Loadcell

Commercial loadcells were investigated as replacements for the failed ones manufactured. A 0-6kg Zemic L6D loadcell pictured in Figure 6.6 has been examined as a possible replacement. For this loadcell to be incorporated into the balance design a number of modifications would be needed which fall outside the timeframe allotted to this body of work. At the time of writing, the balance has not yet been modified and so no meaningful force data has yet been extracted. However, the balance did form a sturdy mount from which pressure data and flow visualisation could be completed; which together gave a suitable picture as to the response of the near wake to the introduction of perturbations of different kinds.

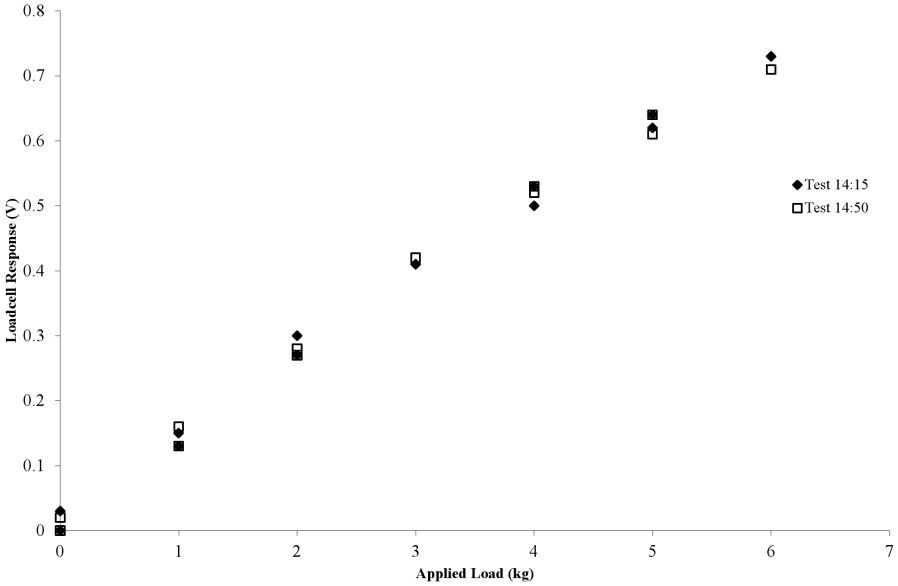


Figure 6.5: Successful Loadcell Calibration - Away from Wind Tunnel

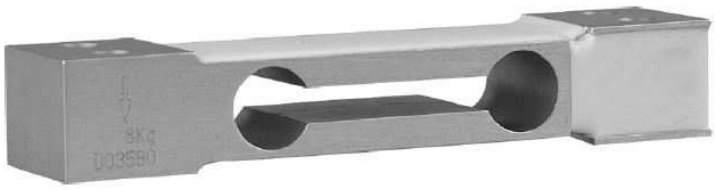


Figure 6.6: Zemic L6D Loadcell

7 Data Acquisition

In order for reliable accurate test data to be obtained, a substantial upgrade of the Wits Wind Tunnel Facilities was undertaken with a view to install a modern digital data acquisition system in both the Wits DDT and the Wits Closed Circuit Continuous Tunnel. This Chapter documents these upgrades.

7.1 Data Acquisition Hardware

A digital data acquisition system capable of processing and recording a large quantity of data was required to meet the needs of this research and future work undertaken in the Wind Tunnel Facilities. After careful review, a set of *National Instruments* (NI) Data Acquisition (DAQ) Devices were purchased. A large primary DAQ was procured and supplemented by two additional smaller devices. Table 7.1 summarises the hardware purchased from NI as well as the fundamental capabilities of each DAQ. All DAQ's purchased were capable of high speed bi-directional data transfer, a necessity when using the system to both record measurements and output control commands to the wing.

Table 7.1: Summary Data Acquisition Devices Purchased in Facilities Upgrade

Model	USB6225	USB6211
Devices Purchased	1	2
Analogue Input Channels	80	16
Analogue Output Channels	2	2
Digital I/O Channels	24	8
Resolution	16-bit	16-bit
Maximum Voltage Range	- 10V to 10V	-10V to 10V
Sample Rate	250 kS/s	250 kS/s

The range of DAQ's purchased are designed to be connected to a PC via a USB connection. This ensures portability and ease of setup for a variety of different test cases. Furthermore, by standardising the channel inputs into each DAQ, true plug-and-play capability is realised. The data sheets as supplied by National Instruments for both the USB6211 and USB6225 appear in Appendix E.

7.2 LabVIEW Software

In order to realise the full benefit that could be gained from using the NI Data Acquisition System, the software suite that accompanies the hardware was purchased. LabVIEW allows a user tailored real-time representation of the test data to be displayed, processed, and written to a text file that can be viewed once testing is complete. The text file can be specified to write directly into a format that Microsoft Excel can interpret, which makes for efficient post processing of data and results. LabVIEW works with an intuitive GUI that allows custom Virtual Instruments (VI) to be created and displayed on a computer monitor. Full computer control of the test piece can be had by careful design of the VI. In the case of the research undertaken, LabVIEW was used to monitor the pressure distribution over the wing, monitor the ambient temperature at the wind tunnel, and control the retraction angle of the trailing edge flap during tests.

7.3 Pressure Measurement

In order to obtain highly accurate real-time pressure measurements, a set of pressure sensors, regulators, and instrument amplifiers were purchased and constructed. The amplified signal was then output to the USB6225 DAQ where the measurements were recorded. The various components making up the pressure measurement system are detailed in the subsections that follow.

7.3.1 Honeywell 24PC Series Sensors

A set of 36 0-0.5psi gauge pressure sensors were acquired for the purpose of pressure measurement at the various positions on the test wing. The sensors are manufactured by Honeywell and form a part of the 24PC Series. The 24PCEFA6G sensors purchased respond linearally to pressure variation are typically excited by a 10V DC source. A response time of $1.0ms$ is specified by the manufacturer. The sensors, if

excited by a constant current, exhibit temperature compensation along their operating span. When driven by a constant current, the sensors' terminal voltage will rise with increased temperature, allowing for an indication of sensor temperature to be had. The sensors' follow a PCB layout, meaning that they can be soldered to vero-board along with the various resistors and capacitors needed to control them. The relevant data sheets concerning the sensors may be found in Appendix E. Information pertaining to the calibration of the pressure sensors may be found in the chapter entitled Calibration.

7.3.2 Voltage Source

A 350W PC voltage supply was used to power the pressure sensors. Each sensor required a 10V DC input supply. The voltage signal output by the PC supply was characterised by large noise signals; thought to be a result of both the AC signal feeding the PC Supply as well as the internals of the rectifying supply itself. To smooth the voltage fed to the pressure transducers, the PC supply was regulated down from 17V to 10V using an LM317 Three Terminal Adjustable Voltage Regulator. This had a considerable impact on the signal noise. Figure 7.1 shows the effect of the regulator on the supply voltage. The bottom line shows the unregulated voltage. The signal is staggered and noise within the sinusoidal form is evident. The top line shows the regulated voltage output. The output is still sinusoidal but the noise within the sinusoid is much reduced. The sinusoid shows a voltage difference of +-0.0025V. This equates to a variation of 0.05% over the mean voltage output range, adequate for the purposes of the tests undertaken. The connection diagram for the LM317 circuit is shown in Figure 7.2. A 5k 25 turn adjustable trimpot was used to regulate the voltage to the precise 10V DC required by the sensors.

7.3.3 Constant Current Circuit

Each pressure sensor was given its own constant current circuit to provide compensation for temperature effects. A LM334Z constant current source was used to set the output current to 2.0mA. The circuit used for each transducer is given below in Figure 7.3. Two parallel banks of resistors were used to regulate the current to the required amperage. The resistor values are shown in Table 7.2. It would have been preferable to replace one of the resistors in the full bridge with a variable resistor which would have allowed for fine tuning of the current supplied to exactly 2.0mA. Using resistors only meant that the current outputs varied between 1.97 and 2.07mA

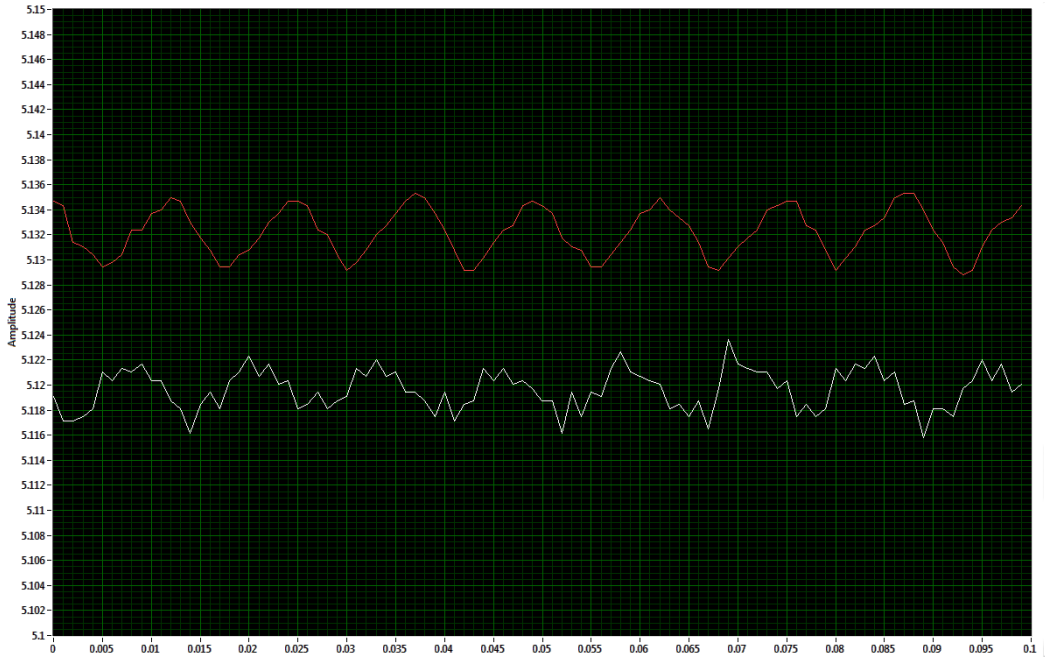


Figure 7.1: Effect of a Voltage Regulator on Input Voltage Signal from PC Supply

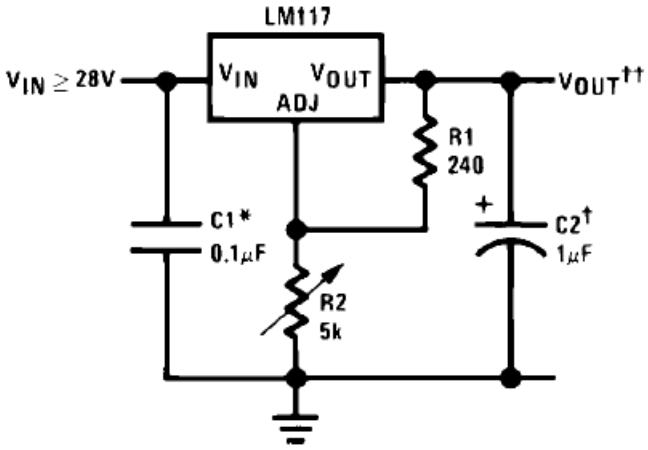


Figure 7.2: Connection Diagram - LM117/317 Voltage Regulator [Appendix E]

across the pressure sensors. The data sheet used to spec the LM334 may be found in Appendix E.

Table 7.2: Current Source Resistor Values

R1	56 Ω
R2	11 Ω
R3	560 Ω
R4	110 Ω

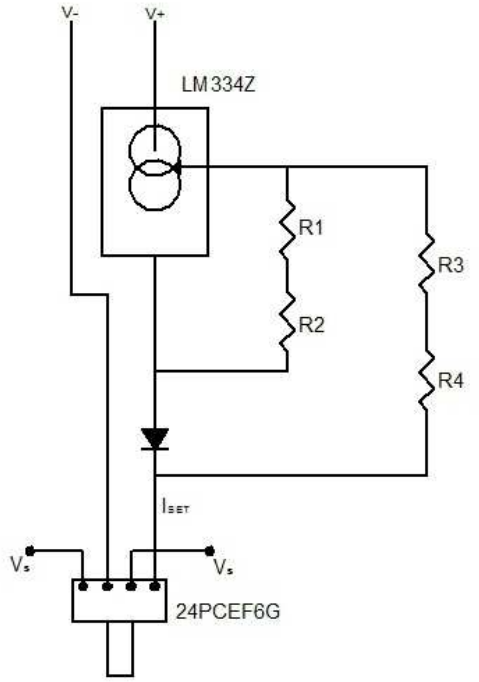


Figure 7.3: Constant Current Wiring Diagram 24PC Series Pressure Sensor

7.3.4 Instrument Amplifiers

It was shown while testing the pressure sensors that even though the DAQ was happy to output pressure changes in the mV range, the output signals were very susceptible to spikes and outliers; an indication of electrical noise within the system. On consultation with members of the electrical engineering department, it was recommended that instrument amplifiers be constructed for each pressure sensor channel to mitigate this. The primary role of an instrument amplifier (In-Amp) is to amplify the difference between the two input signals (measured value), while rejecting any signals that are common to both inputs. Thus an In-Amp is able to extract small signals from transducers, while rejecting the noise signal present on both input signals. An Analog Devices AD627 Instrument Amplifier was selected to amplify the pressure signals as it allows gains of up to 1000 to be set as well as a Common Mode Rejection Ratio (CMRR) of up to 77db. This ensure that much of the noise present in the unamplified signal is rejected, and a smoother signal is fed into the DAQ. A circuit diagram showing the various inputs and outputs to the AD627 is shown below in Figure 7.4.

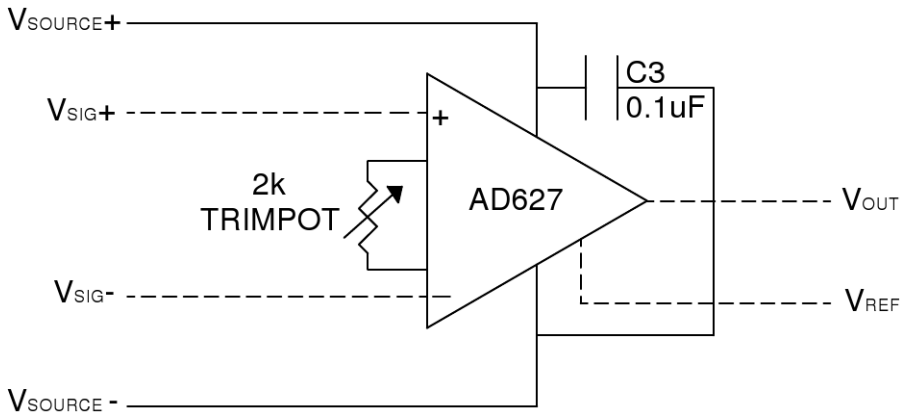


Figure 7.4: AD627 In-Amp Circuit Diagram

7.3.5 Pressure Sensor Connection Diagrams

A flow diagram showing the position of each electrical component relative to the pressure sensor is given in Figure 7.5. The complete circuit diagram for one pressure sensor is shown in Figure 7.6. One voltage regulator was used to power 24 sensors in a parallel configuration and each sensor was given its own constant current source and Instrument Amplifier. This was done so as to isolate each pressure sensor such that any noise signal found on on sensor would not be transferred to the other sensors. Each sensor was also grounded separately for the same reason.

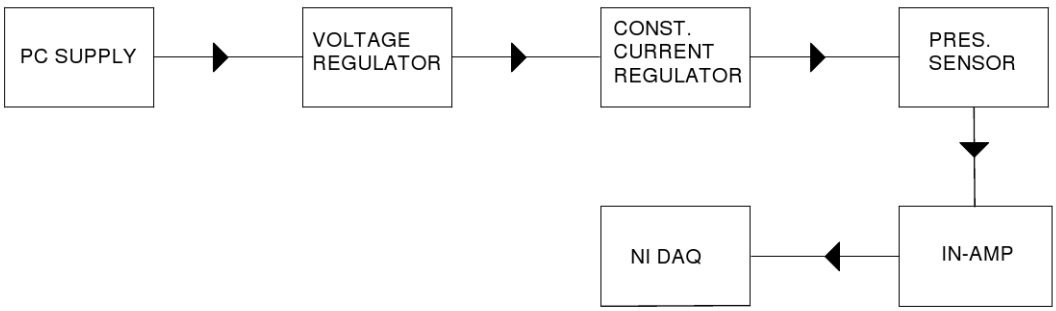


Figure 7.5: Flow Chart Showing Pressure Measurement Components

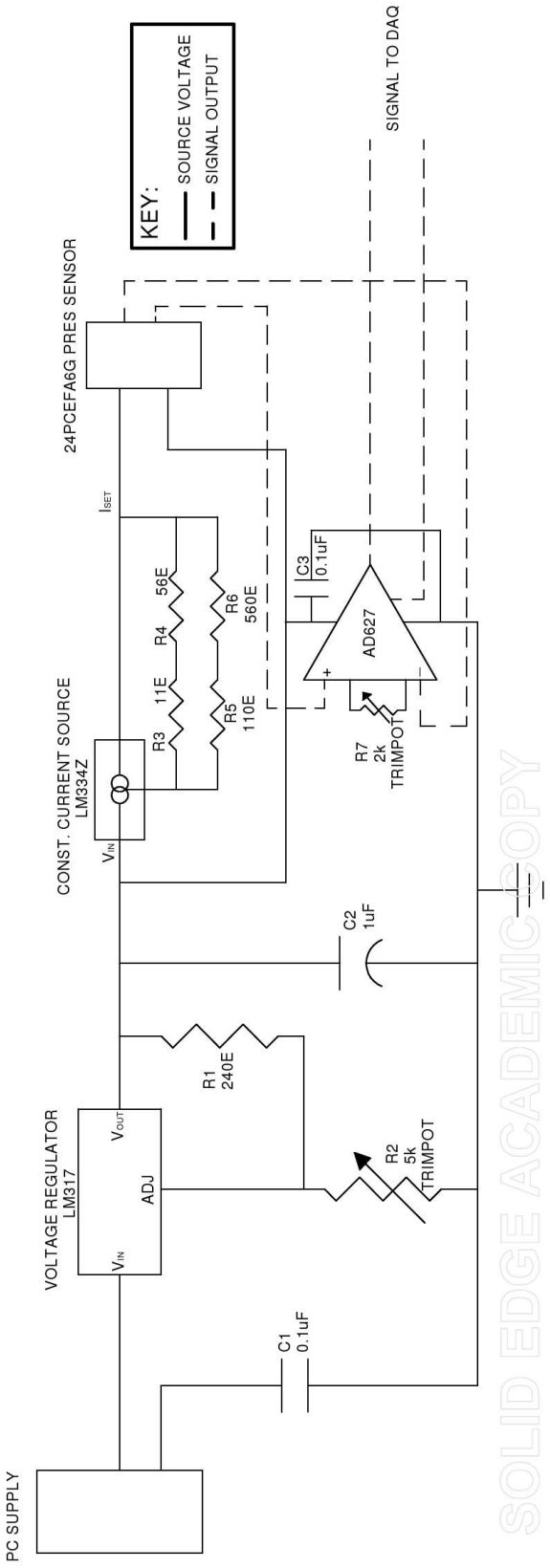


Figure 7.6: Complete Circuit Diagram for One Pressure Sensor

8 Calibration

A thorough calibration of the various instruments used during testing allows for uncertainties to be accounted for, and gives an indication as to the accuracy and repeatability of the experimental data gathered. Calibrations were performed on the Pressure Sensors, the Flap Angle Sensor, and the Flow Visualisation Measurements.

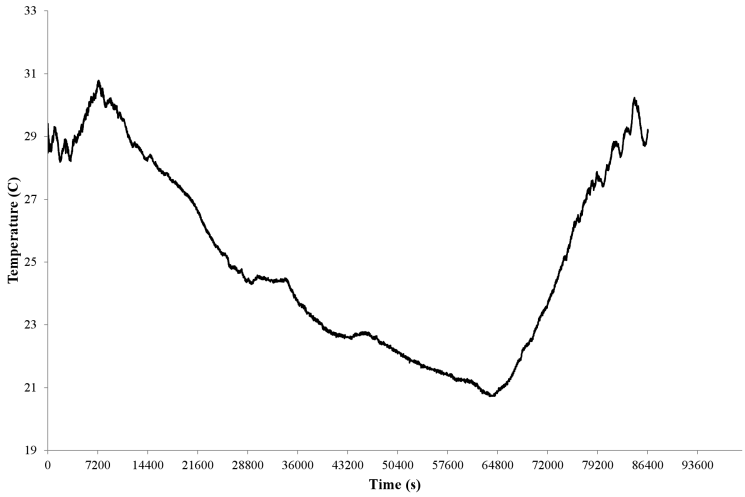
8.1 Honeywell Pressure Sensors

A detailed study into the behaviour of the Honeywell 24PCEFA6G Pressure Sensors was necessary in order to characterise the sensors' response to varying pressure conditions. Following this, a once off calibration could to be performed to relate the sensor voltage output to the measured pressure. A number of operating intricacies were found while studying the sensors' responses; most notably the sensors' dependency on ambient temperature.

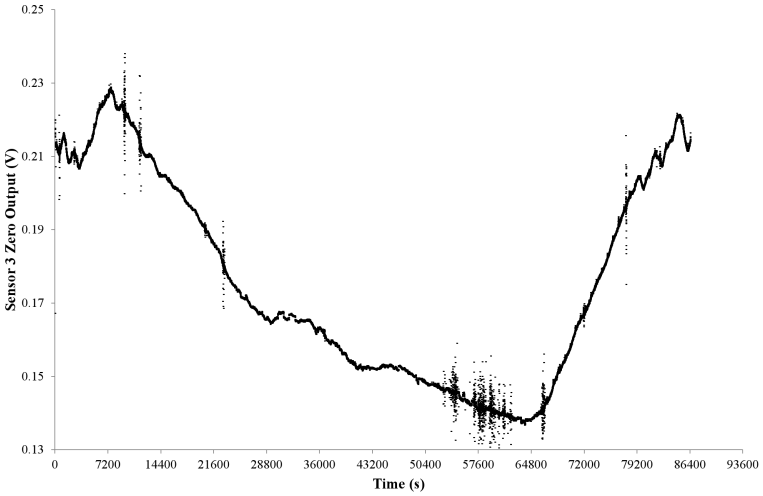
8.1.1 Sensor Response to Temperature

While testing the sensors, it became apparent that the zero offset of each sensor connected to the same power supply would fluctuate between tests. Upon investigation, it was shown that the sensors' offset was tracking the changing ambient temperature of the room in which they were installed. The variation in offset was significant as the sensor box was placed on the platform of the Wits Draw Down Windtunnel where the temperature was shown to vary appreciably during the course of a day. Figure 8.1 (a) shows the variation of the temperature at the sensor box over a 24 hr test period performed in February 2012. Temperature measurements were gathered using a NI USB-TC01 Thermocouple and a Moving Air Type K Probe, and output to a text file for analysis. The test was started at 12:39pm and ended at the same time the following day. The temperature peaked at 30.8°C at 14:40 and reached its

low point of 20.7°C at 06:20 the following morning. This temperature range was found to be representative of the typical range of temperatures that would be encountered during the duration of testing which took place in late summer and early autumn 2012. Figure 8.1 (b) shows a typical sensor's response to the changing temperature over the same 24 Hr period. Note how closely the sensor response matches the changing temperature. Studying Figure 8.1 (b),there appears to be some disturbance or ambient noise in the sensor output signal. There is a particularly noticeable band of noise in the early hours of the morning where the temperature is reaching its lowest levels. The cause of this disturbance is not known, but it is easy to pick up during the course of a test where outliers in the data could be readily compensated for.



(a) 24 Hr Temperature Log at Wits DDT



(b) Sensor Response to Temperature over 24 Hrs

Figure 8.1: Temperature and Sensor Zero Response over 24 Hr Test

A linear relationship between the sensor output and temperature was shown for each of the 24 sensors. A linear regression yielded a temperature correction gradient for each numbered sensor and a corresponding regression coefficient which gives an indication of the quality of the linear fit. This is shown in Table 8.1.

Figure 8.2 shows the calibration line created for Sensor No. 14, the sensor showing the greatest linearity. MATLAB code (available in the electronic appendix) was written which sorted the sensor output voltage by temperature. The mean sensor output and standard deviation was calculated at each temperature for each sensor. A conservative approach to the uncertainty in the measurement was followed where the maximum standard deviation obtained through the range of temperatures measured was used in the uncertainty calculation. The voltage error was calculated at two standard deviations and applied as upper and lower bounds in the error analysis.

Generally the sensor response showed a reasonable correlation to temperature; however, Sensors 5,8 and 10 showed considerable scatter in the dataset obtained. Sensor 8 and 10 were therefore attached to non-critical pressure taps such as those near the root of the wing or on the trailing edge set of spanwise taps. The pressures at these taps were shown not to vary considerably upon oscillation of the tabs nor to be of interest or much use in the analysis of the pressure distributions across the wing model. Sensor 5 showed very little drift with changing temperature, evident by the slope of the regression line obtained being a full order of magnitude less then a number of the other sensors. Thus the scatter and lack or correlation inherent in Sensor 5 is understandable as the voltage changes output from the sensor are so slight.

The overall effect of the temperature calibration was often not critical in the determination of the sensor pressure. That is, looking at the gradients obtained in Table 8.1, and correcting for the temperature change during the course of a typical short test, the correction was oftentimes shown to be less than the uncertainty in the pressure measurement itself. Thus the scatter of data and poor linearity of the fit seen in a number of sensors was deemed non-critical to the overall accuracy of the pressure data obtained. The resulting temperature calibration curves obtained for the remainder of the sensors can be found in the electronic appendix.

8.1.2 Pressure Calibration

Calibration of the pressure sensors were completed away from the Draw Down Wind Tunnel in a room specifically set up for calibration. The room naturally maintains

Table 8.1: Temperature Calibration Gradients

Sensor No.	Gradient	R^2 Value	Sensor No.	Gradient	R^2 Value
1	0.0079	0.9666	13	0.0058	0.9800
2	0.0062	0.9473	14	0.0080	0.9957
3	0.0082	0.9786	15	0.0138	0.9360
4	0.0047	0.9574	16	0.0066	0.9831
5	0.00084	0.5620	17	0.0055	0.9862
6	0.0046	0.9761	18	0.0084	0.9760
7	0.0049	0.9563	19	0.0059	0.9898
8	0.0031	0.3432	20	0.0080	0.9862
9	0.0075	0.8711	21	0.0047	0.9724
10	0.0058	0.5444	22	0.0056	0.9721
11	0.0084	0.9255	23	0.0087	0.9865
12	0.0079	0.9523	24	0.0060	0.9851

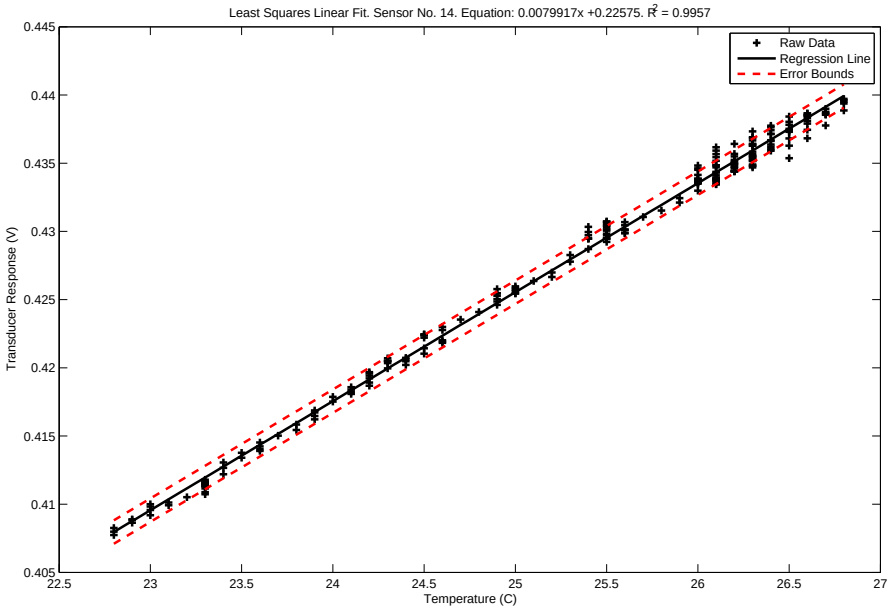


Figure 8.2: Temperature Variation Calibration Sensor No. 14

a near constant temperature over a 24 hr period, with large periods of constant temperature, ideal for calibration. On a typical summers day the room varies in ambient temperature by approximately 0.7°C. This is contrasted by the temperature variation at the Wits DDT, where the temperature was shown to typically vary in the region of 10°C.

Calibration was completed by exerting a series of known pressures on each sensor for a period of two minutes, then determining the electrical response of the transducer at each known pressure point using ensamble averaging. The pressure was varied by periodically ramping up the speed of a small calibration wind tunnel, and measuring the pressure head on a pitot tube located in the tunnel free stream. The pressure was simultaneously read by a calibrated manometer, and the twenty-four pressure sensors to be calibrated.

Calibration Tunnel

All calibration was performed in a purpose built calibration tunnel. The tunnel is manufactured by Airflow Developments LTD and is a small draw down tunnel powered by a 10A 2.0 HP DC electric motor manufactured by Normand Electrical Co. The tunnel speed is varied by a Varic Thyristor which allows for accurate speed changes to be made.

During the calibration, the tunnel was ramped up in 5% intevals to 50% of the total available motor speed, with a final jump from 50% to a maximum of 60%. The speed was then reduced back to zero in the same intevals. This was performed in order to examine the effects of hysteresis in the system. The maximum speed to which the tunnel was run corresponds to a pressure head of 544Pa. This is a factor of two greater than the maximum anticipated gauge pressure the sensors will measure during the course of wind tunnel testing. At higher speeds, the natural turbulence in the calibration tunnel caused too great a variation in the output of the sensor and the calibrated manometer to give a reading sufficiantly accurate for calibration purposes.

The digital data acquisition system was set to measure the pressure sensor voltage output at a frequency of 10 Hz. Thus at each measured pressure point, approximately 600 observations were taken. The scatter of data acquired was then investigated to determine if the measured pressure output was normally distributed about a mean value. Figure 8.3 is a histogram of Pressure Sensor No.5's voltage output at a constant pressure of $89Pa$ taken during testing. This is a typical data set and representative of the full set of pressure sensors. The scatter in the voltage output appears to follow a normal distribution by inspection; this was verified by plotting the theoretical normal distribution for the data and comparing it to the actual distribution (show in Figure 8.3). The actual cumulative distribution was plotted against the theoretical distribution in Figure 8.4 and the resulting regression analysis showed sufficient linearity to confirm the hypothesised normality of the

distribution [36]. Uncertainty calculations based on the statistical normality of the data could thus be undertaken.

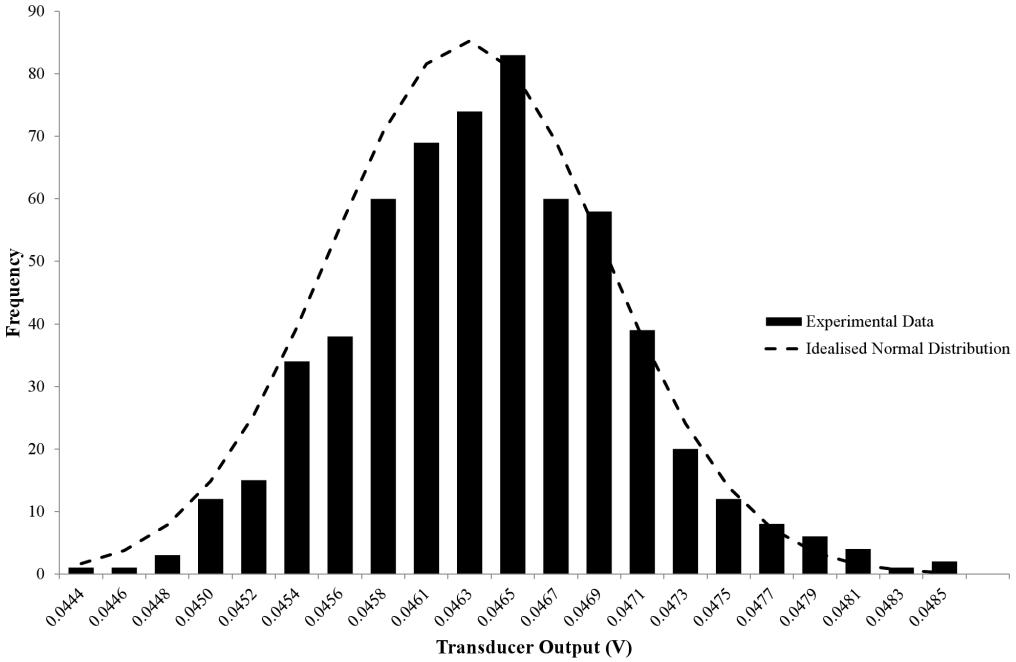


Figure 8.3: Distribution of Pressure Sensor Output at a Constant Pressure Point

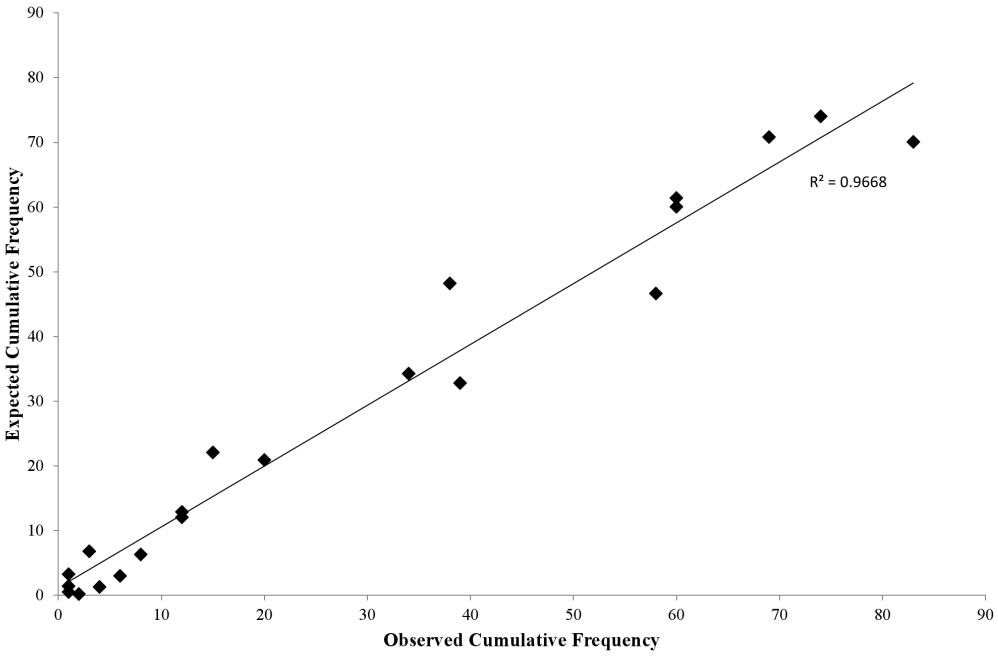


Figure 8.4: Plot of Actual vs Theoretical Normal Cumulative Distribution

Figure 8.5 plots the raw sensor output of Sensor 1 for the duration of the calibration test. Figure 8.6 plots the standard deviation of the mean at each pressure point tested as the motor was ramped up and down. The increasing noise inherent to the signal as the pressure (tunnel speed) is increased is shown clearly in the plot of the standard deviation. At higher speeds where the turbulence in the tunnel becomes significant, the standard deviation is approximately five times greater than the sensor's natural deviation when measuring zero gauge pressure. The increasing standard deviation at higher pressures due to the calibration tunnel constraints is accounted for in the calibration.

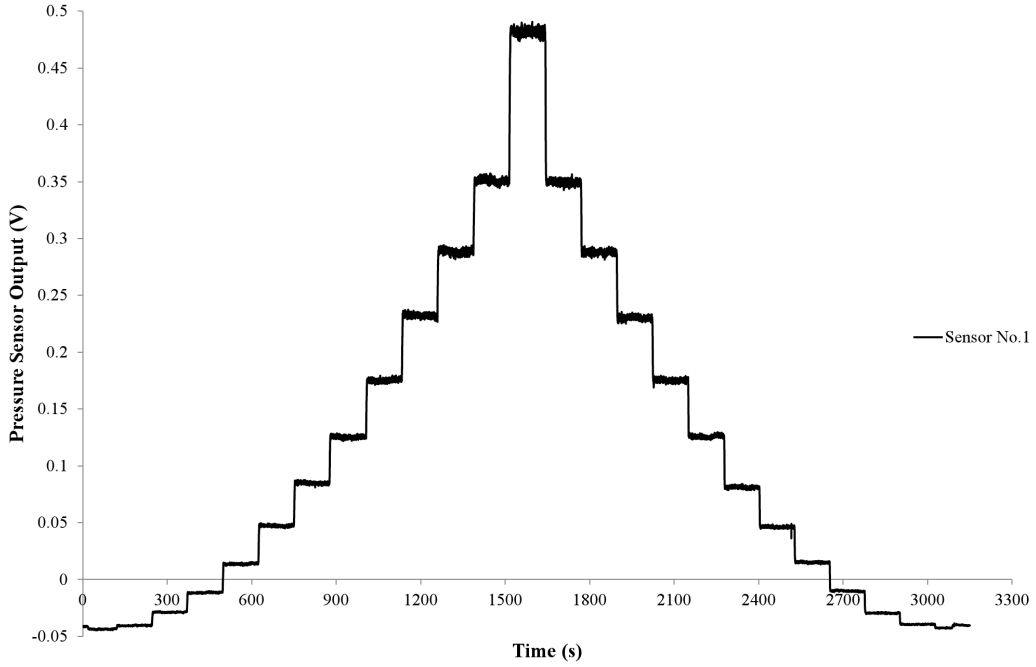


Figure 8.5: Raw Pressure Sensor Response to Ramped Pressure Inputs

Digital Manometer

A DMP ST6 Series Digital Pocket Manometer was used to correlate each sensor output to a known pressure. The manometer was calibrated by DP Measurement and a calibration certificate for the instrument was granted on 11/01/2012 valid for a year. A copy of the certificate may be found in Appendix F. The manometer was set up to output a pressure reading in Pa for the duration of testing.

Calibration Results

Plotting the known pressure readings against the sensor voltage outputs yielded a set of 24 unique calibration lines; one for each sensor. The calibration lines all show

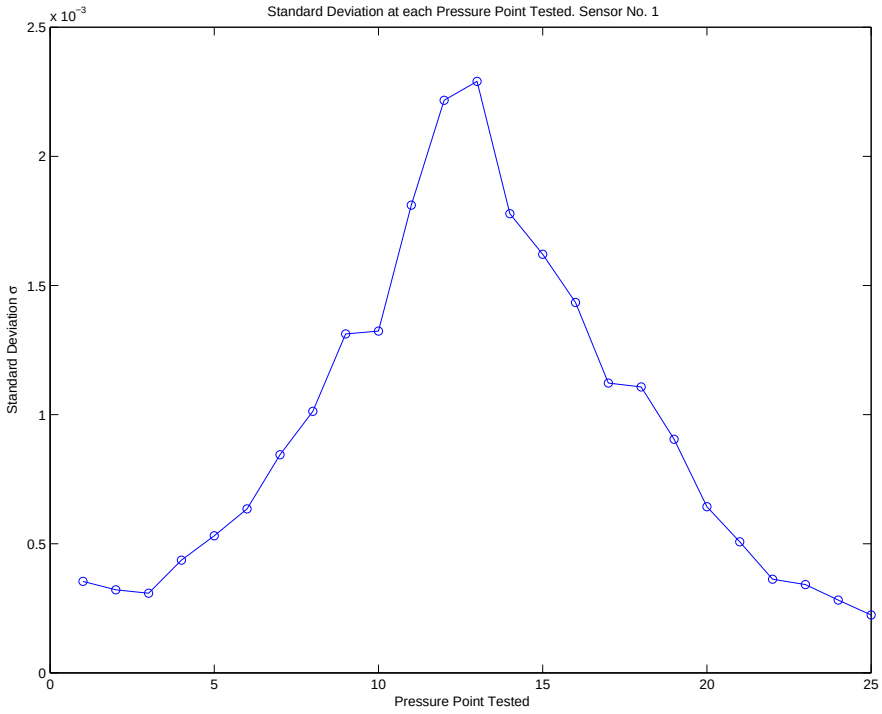


Figure 8.6: Standard Deviation Variation, Pressure Sensor No. 1

high levels of linearity with the linear regression correlation coefficient (R^2) shown to lie between 0.9988 and 1.0 for each sensor. Figure 8.7 shows the calibration line obtained for Sensor 1. The data has very good repeatability with almost no Hysteresis present when increasing and decreasing pressures. This is largely as a result of the time spent building voltage regulators and making use of Instrument Amplifiers to smooth the input signal to the transducers. The red dotted lines that follow the regression curve indicate pressure variation due to the uncertainty in the sensor's voltage output based on a 95% confidence inteval ($\pm 2\sigma$) of the measured data. That is, there is a 95% certainty that any measured transducer voltage will lie inside the area bounded by the confidence limits.

As mentioned when discussing the Calibration Tunnel, the uncertainty increases as the pressure is increased due to increased levels of turbulence in the calibration tunnel. However, the transducers are still able to resolve the pressure measurement to within 4Pa at the estimated maximum pressure difference expected during testing. This is plotted in Figure 8.8 where the scatter of the data about the mean may also be seen.

An uncertainty analysis based on the interaction of the uncertainty in the pressure measurement read by the digital manometer and the voltage output of the pressure sensor showed a 1% uncertainty in the measurement through the expected typical operating range during tunnel testing. The calculation is shown in Appendix G and the variation in slope of the calibrated pressure sensor based on this uncertainty is included in Figure 8.7.

The results presented here indicate that the pressure sensors will be capable of picking up small changes in pressure, thus being able to differentiate between small pressure differences as the trailing edge tabs are oscillated during testing. The calibration lines for the additional 23 sensors can be found in Appendix F. Of particular importance is the gradient of each calibration line as this is what is used to determine the measured pressure in Pa. The intercept is done away with in the data processing by subtracting the zero pressure voltage from the measured voltage at each pressure point. Table 8.2 lists each sensor and its corresponding calibration gradient along with the correlation coefficient (R^2 value).

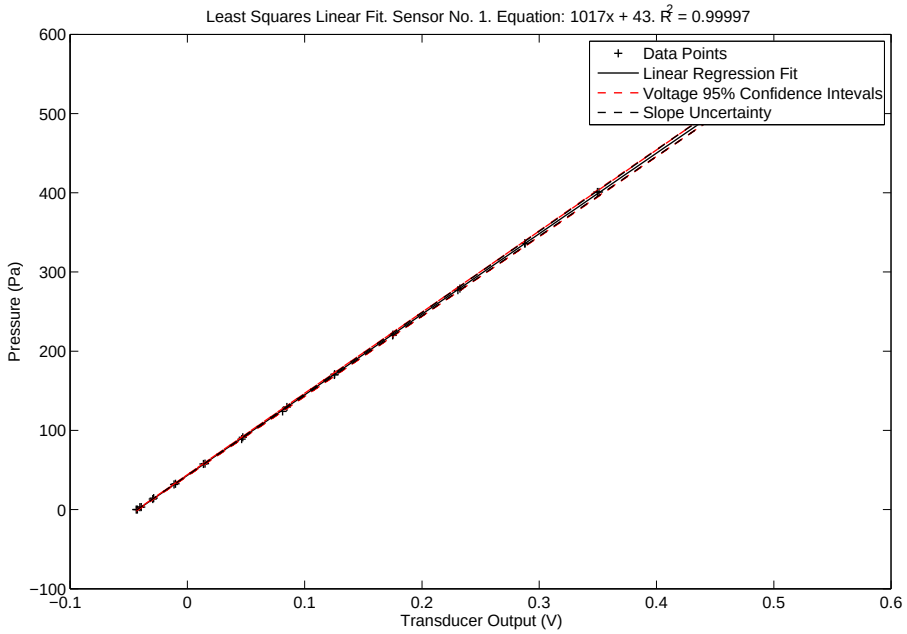


Figure 8.7: Calibration Line for Pressure Sensor No. 1

8.2 Flap Angle Calibration

Calibration of the trailing edge flap was performed in order to relate the output of a rotary potentiometer fixed to the flap shaft, to the flap extension angle relative to

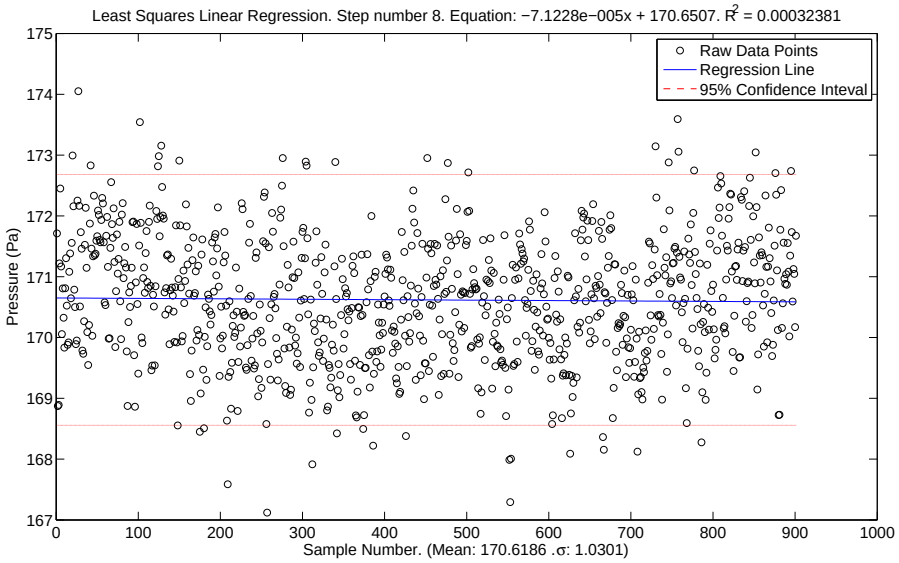


Figure 8.8: Raw Pressure Data Scatter and Uncertainty: Sensor No. 1

Table 8.2: Pressure Calibration Gradients

Sensor No.	Gradient (±1%)	R^2 Value	Sensor No.	Gradient (±1%)	R^2 Value
1	1017	1.0000	13	1049	0.9988
2	971	0.9998	14	1115	0.9998
3	1059	0.9995	15	1104	0.9996
4	1200	0.9999	16	1049	0.9997
5	1242	0.9998	17	1067	0.9998
6	985	0.9960	18	995	0.9999
7	1017	0.9999	19	1043	0.9999
8	2918	0.9940	20	987	0.9999
9	936	0.9990	21	1005	0.9999
10	1049	0.9999	22	940	0.9997
11	966	0.9999	23	1133	0.9998
12	1020	0.9999	24	1040	0.9992

the wing chordline. The potentiometer forms one arm of a full bridge arrangement. As the flap extends or retracts, the resistance of the potentiometer varies linearly resulting in a change in the full bridge output voltage. The output signal from the bridge is connected to the digital data acquisition system and recorded in LabVIEW. To ensure that the voltage input to the bridge remained constant, a voltage regulator

as used to regulate the voltage in the pressure transducer box (Figure 7.2) was installed downstream of the lab supply used to power the system. This ensured a constant 5V was maintained at all times. A balancing half bridge on the full bridge allowed for a fine tuning of the voltage output of the flap when fully retracted. This compensated for any drift during the course of testing and meant that the flap in the retracted position could always be set to the same zero voltage.

To determine the flap angle during calibration, digital photographs were taken of the wing by a camera mounted vertically above the wing and aligned with the chordline. The wing and flap chordlines were both marked on the wing before calibration commenced, allowing for accurate flap angle measurements to be made. The full bridge output was written to a tab delimited file, which was then compared to photographs taken at twelve discrete flap angles; from fully retracted, to an extension angle of 48° , and back to the fully retracted state.

Figure 8.9 shows the wing with the trailing edge flap extended at one of the twelve discrete angles. The flap chordline is visible but faint in the photograph and as such, has been darkened in the post processing. The extension angle was then measured making use of trigonometry and a protractor to verify results. The uncertainty in the flap angle measurement came from the protractor used to measure the flap angle from the photographs, which has a resolution of $\pm 0.5^\circ$. The resulting distortion from the camera used to photograph the images was deemed negligible in comparison to the size of the uncertainty in the protractor measurment.

The uncertainty in the voltage reading was determined using a statistical analysis of the raw data as it is normally distributed. The corresponding error bounds were plotted at intervals calculated at two standard deviations and shown on the graph. This was deemed sufficient for the purposes of testing the oscillating tab response to a trailing edge flap extension. The resulting calibration line is given in Figure 8.10.

8.3 Wake Dimension Calibration

Cross section images of the resulting wake were photographed at three distinct downstream locations while oscillating the tabs. Refer to Figure 3.3 for the position of the camera relative to the downstream positions of interest. In order to draw meaningful data from the images such as vortex extent and core diameter, a means to measure distances on the each photograph was sought. Calibration of the images was completed at each downstream location by photographing a machined aluminium plate

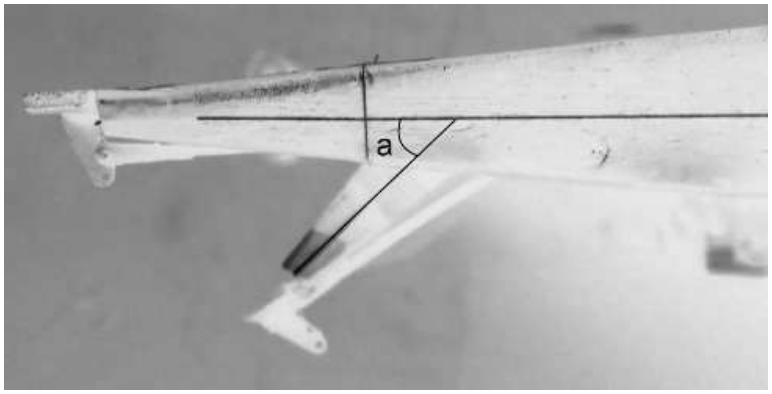


Figure 8.9: Flap Angle Calibration Photograph

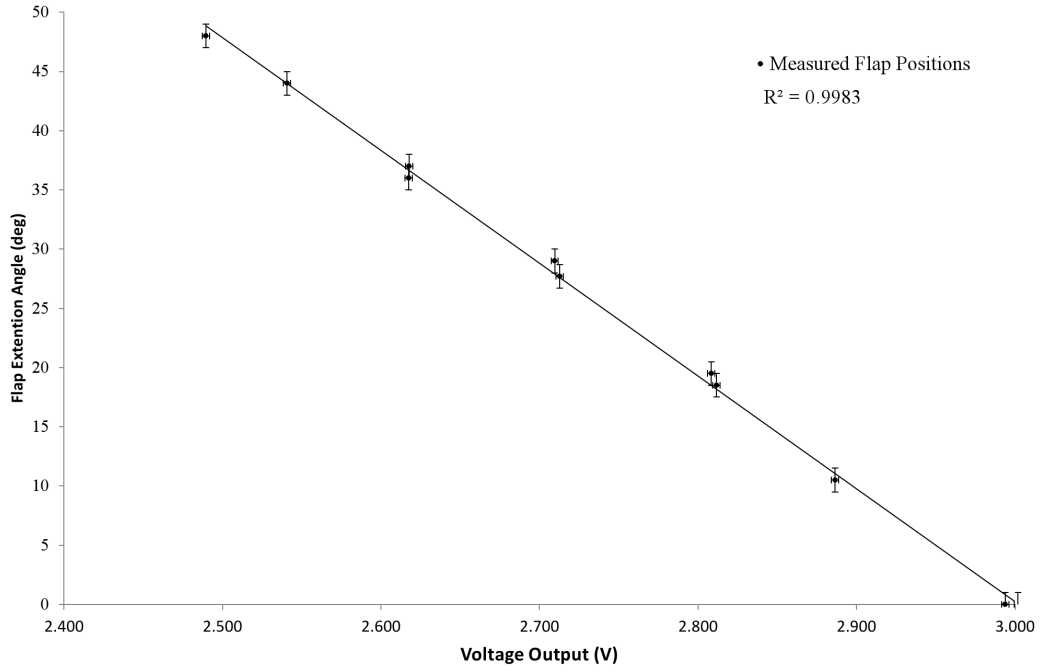


Figure 8.10: Trailing Edge Flap Calibration Line

of known dimension and relating the number of pixels across the image to the known length of the plate. The camera was carefully aligned such that the centre of each photograph would coincide with central holes machined into the calibration rig. This was accomplished using a laser attached to the camera. Figure 8.11 shows the calibration rig placed in the tunnel at a downstream position of 1.0b. Calibration was completed each time the camera was moved so as to ensure accurate measurements could be attained.

GIMP 2.6.9 was used to measure the number of pixels along the calibration rig's know dimension. Thus the known dimension could be related to the number of pixels across that part of the image to give the pixel width. This was then used in subsequent images with the camera in the same location to measure vortex wake phenomena. All focusing of the camera was handled manually to ensure repeatability in the photographs taken. Table 8.3 gives the width of a single pixel at each of the locations tested.

Table 8.3: Pixel Width at Measured Downstream Locations

Location	Pixel Width [mm]
0b (Wing TE)	0.541
0.37b	0.473
1.0b	0.367
2.0b	0.193

Figure 8.13 plots the relationship between pixel dimension and downstream location in the tunnel. The uncertainty in the measurement arises from the fact that the camera may distort the image slightly. This was considered by measuring the skewness of the calibration plate, measured as the angle that the width and breadth of the plate make (μ) as described in Figure 8.12.

The angle μ as determined in the calibration images (Figure 8.11) was found to differ from the actual geometry measured by a vernier scale in the Wits Laboratory. The largest distortion was found at the 2.0b location, the location nearest the camera. Here the distortion was determined to be 1.87%; this has been used throughout the range of downstream locations and forms a conservative estimation of the error in the measurement for the calibration line generated in Figure 8.13. The error in the measurment at 0.37b was determined to be four time less than that at 2.0b.

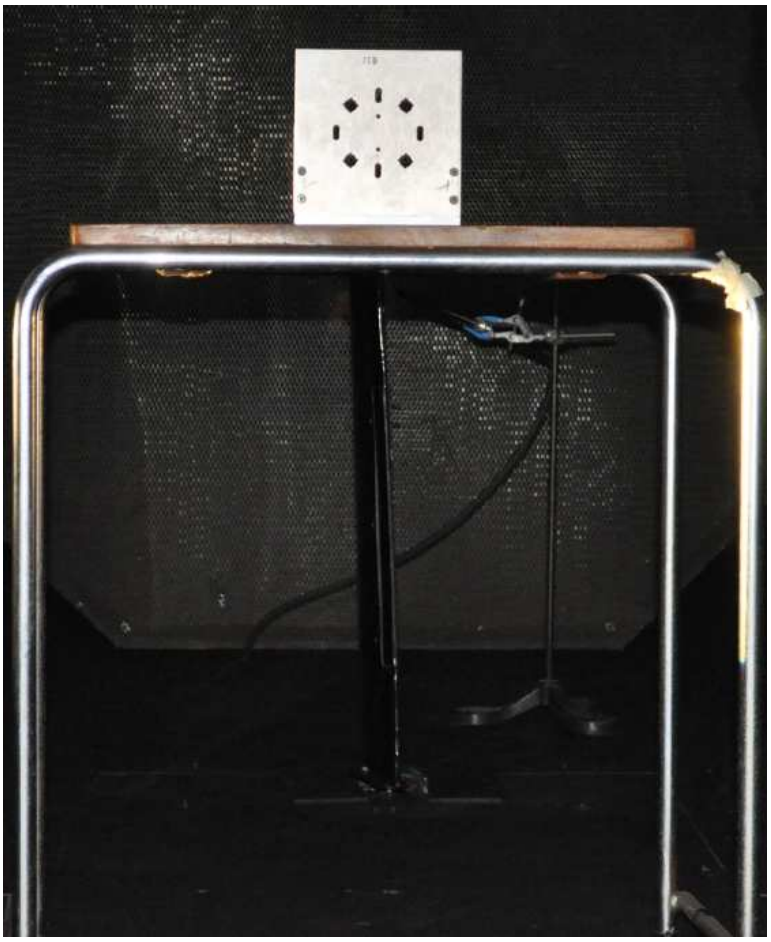


Figure 8.11: Flow Visualisation Cross Section Stations

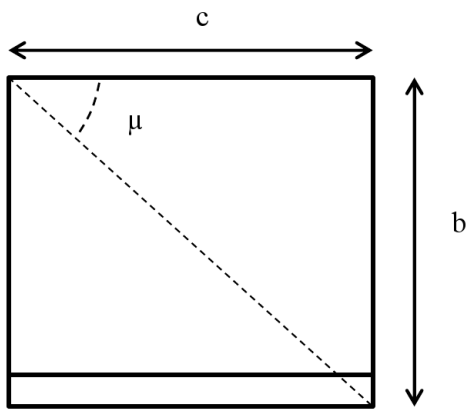


Figure 8.12: Plate Geometry for Skewness Calculation

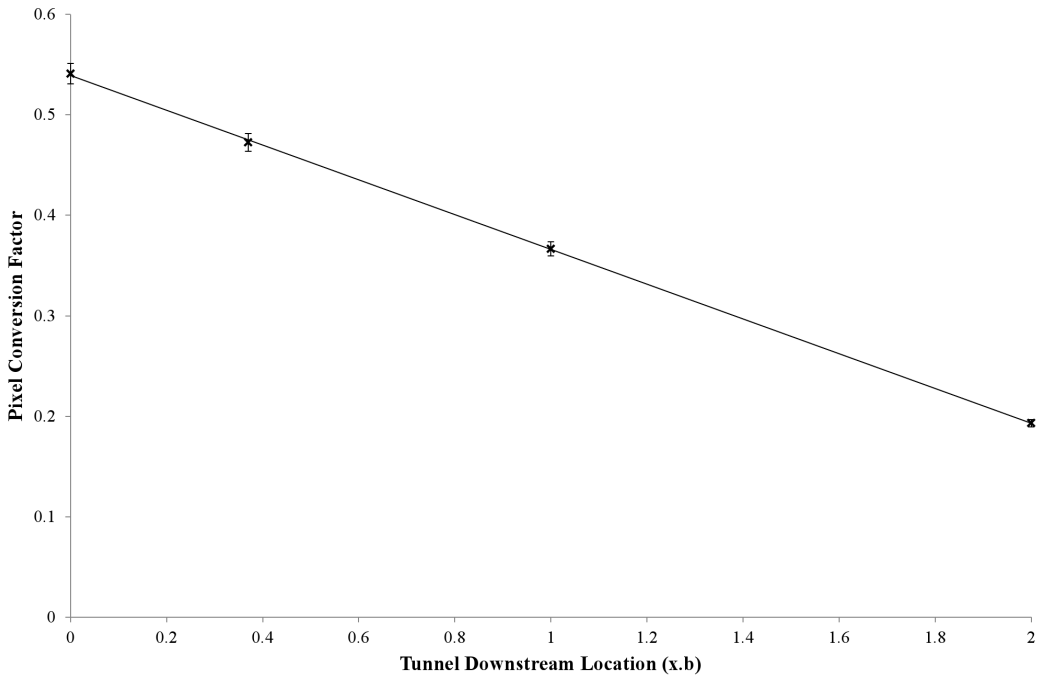


Figure 8.13: Plot showing Pixel Conversion Factor as a Function of Downstream Position

9 Data Processing

9.1 Pressure Measurement

9.1.1 Procedure

The following is an outline of the method followed to process the raw data obtained from the pressure sensors into know pressures.

1. On the commencement of each test, zero readings were recorded for each sensor. Zero readings were required primarily due to the sensor drift experienced as the ambient temperature at the Draw-down Tunnel varied. This required running the sensor box under zero gauge pressure conditions for two minutes and outputting the resulting averaged zero readings to a text file via the 'Write to Measurement File' output in Labview.

2. A test was then performed, writing all the raw data obtained to a text file for later processing. For each new test performed, a new set of zero values were taken. Data obtained included voltage outputs from each pressure sensor as well as the measured ambient temperature.

3. The zero values measured for each sensor were then subtracted from each subsequent data point obtained. This has the effect of shifting the data to intercept the origin, thus negating the need to apply a constant offset to each point, and therefore relating the modified raw output to the gradient of the measured calibration line only.

4. The data was then corrected for temperature variation during the course of the test. As shown in Chapter 8.1.1, the temperature variation at the Wits DDT during the course of a test has an impact on the output of each sensor. The temperature through out the course of each test was measured and recorded.

The initial ambient temperature was subtracted from the measured temperature at each data point, and multiplied by the relevant temperature variation gradient as shown in Table 8.1 to obtain the shift in the sensor output due to temperature changes.

5. The temperature shift factor was then subtracted from the sensor output. The sensor output had thus been corrected for initial output as well as temperature variation.

6. Finally, the output data was multiplied by the respective pressure gradient calibration factor shown in Table 8.2 to convert the sensor output to a measured pressure given in Pascals (Pa).

9.1.2 Example of Pressure Data Processing

Table 9.1 shows a set of averaged raw data collected by Sensor 5 at three different speeds, with the wing at an angle of attack of 5°.

Table 9.1: Sensor No. 5 Raw Data

Speed ($m.s^{-1}$)	Output (V±0.0005)
0	-0.2982
10.3	-0.3790
13.2	-0.4358
15.8	-0.4976

Subtracting the zero value from each data point negates the zero offset. The result is given in Table 9.2

Table 9.2: Sensor No. 5 Zero Value Subtract

Speed ($m.s^{-1}$)	Output
0	0
10.3	-0.0808
13.2	-0.1376
15.8	-0.1995

Table 9.3 shows the temperature at each data point and the change in temperature relative to when the test began. The change in temperature (dT) is multiplied

by the temperature variation gradient taken from Table 8.1, which results in the temperature correction factor for each data point.

Table 9.3: Sensor No. 5 Temperature Data

Speed ($m.s^{-1}$)	Temperature	dT
0	30.9	0
10.3	31.2	0.3
13.2	31.4	0.5
15.8	31.6	0.6

The Temperature Variation Gradient calculated for Sensor 5 is 0.0008. Table 9.4 gives the correction factors as well as the corrected data.

Table 9.4: Sensor No. 5 Output Corrected for Temperature Variations

Speed ($m.s^{-1}$)	Temp Factor	Corrected Data
0	0	0
10.3	0.00024	-0.0811
13.2	0.00045	-0.1381
15.8	0.00058	-0.2000

The results from Table 9.4 are finally multiplied by the Pressure Calibration Gradient, calculated for Sensor 5 to be 1242 to convert from a voltage output to a pressure in Pa. The final pressure values are shown in Table 9.5.

Table 9.5: Sensor No. 5 Calibrated Pressure Output

Speed ($m.s^{-1}$)	Pressure (Pa)
0	0
10.3	-100
13.2	-171
15.8	-248

9.2 Image Processing

Raw images of the vortex cross section as captured in the wind tunnel were cropped, inverted, and their colour levels modified before being used to determine the effect that the tabs have on the resulting wake. All processing was completed in GIMP 2.6.9, a freeware image manipulation tool.

Figure 9.1 shows a cropped raw image taken of the resulting vortex at a downstream position of 0.37b with the wing at an angle of attack of 5° and no oscillation of the tabs. The photograph has an exposure time of 10sec at f5.6 and ISO 3200. This image is unmodified aside from cropping to fit on the page and the addition of labels to show the position of the apparatus in the tunnel. The image was taken from directly behind the vertically mounted wing with the airflow out of the page. It should be noted that images of the wake with a 5sec exposure were predominantly used in the Flow Visualisation section but the image processing undertaken was identical.

Figure 9.2 shows the same photograph but now with the colours inverted. The colour inversion was used as it was deemed more practical to include images with a white background than a dark one in the report. In order to distinguish the various properties of the vortex more clearly, the colour levels in each photograph were modified post inversion.

Figure 9.3 show the final image, where the input levels on all three colour channels were reduced to improve the contrast between the white background body of the test piece. The images were also rotated clockwise 90° so as to provide the reader with a more intuitive image of a horizontal wing with the wingtip at the right-most extent of the image and flow toward the observer(out of the page). The lift vector is vertical in the image.

A clear image of the resulting vortex is thus produced which can be used in the analysis of the near wake under the oscillation of the installed tabs.

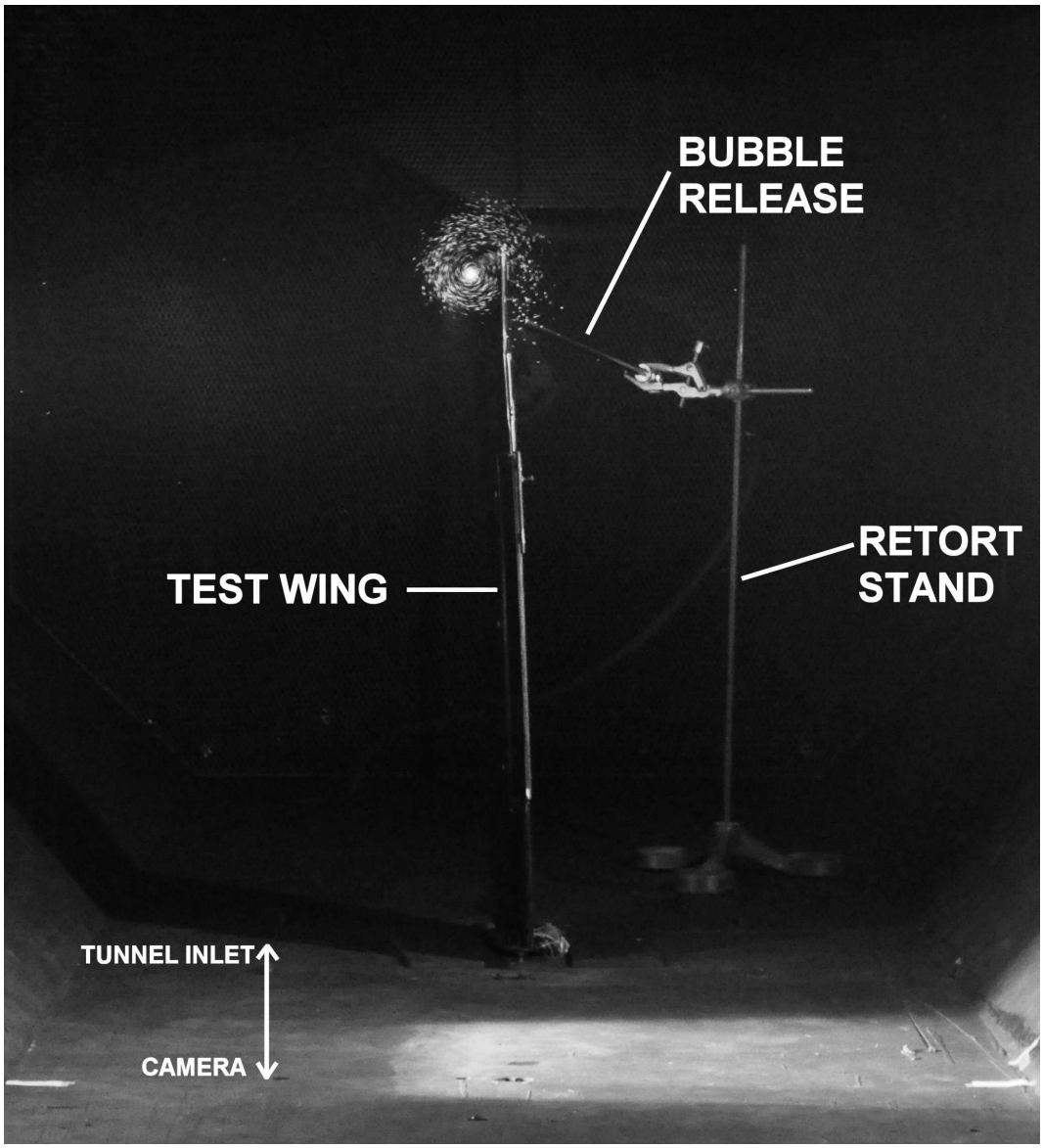


Figure 9.1: Raw Cropped Image, $\alpha = 5^\circ$, 0.37b

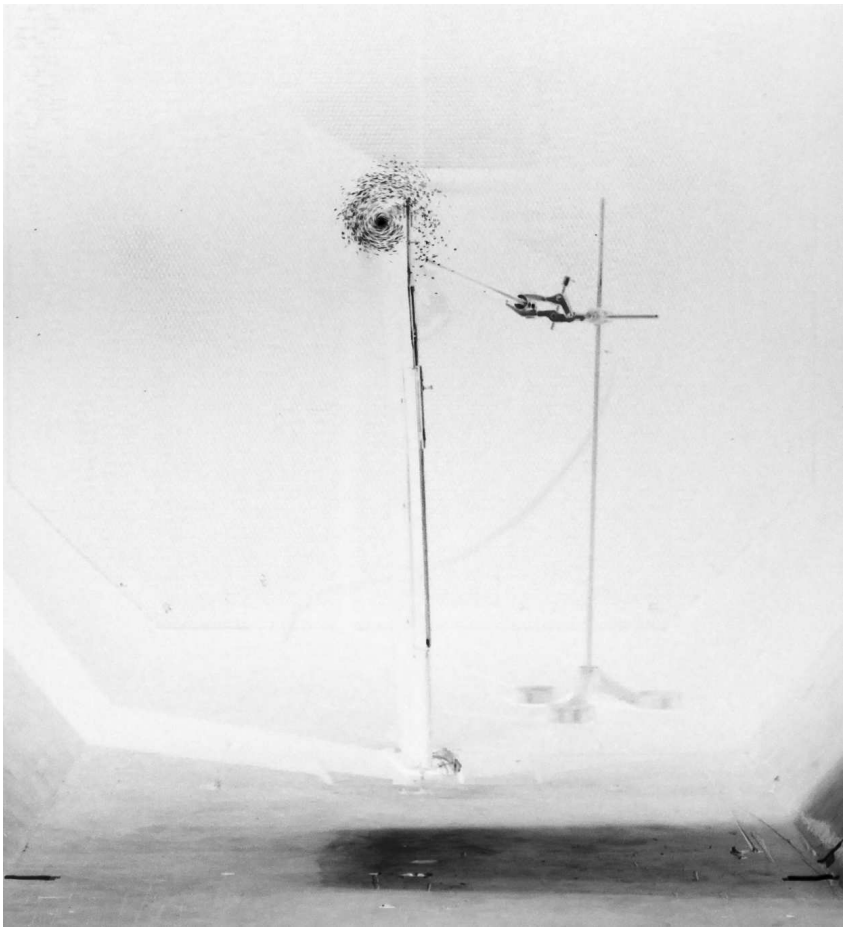


Figure 9.2: Inverted Image, $\alpha = 5^\circ$, 0.37b

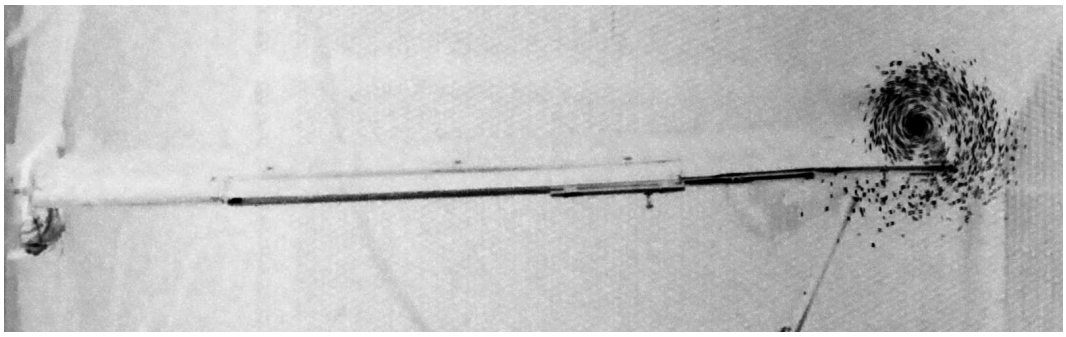


Figure 9.3: Rotated, Processed Image, $\alpha = 5^\circ$, 0.37b

10 Results and Discussion

10.1 Summary of Experimentation Performed

The experimental phase comprised of Pressure Measurement and Flow Visualisation Tests to investigate the feasibility of introducing vorticity into the near wake of a wing as a means to excite instabilities in the wake and hence reduce the time taken for vortices to link, merge, and dissipate. This added vorticity was introduced through the use of oscillating trailing edge tabs placed at the wing and flap tip ends. A short summary of the various tests performed is given now.

10.1.1 Pressure Measurement

Pressure tests were completed for the wing at three tunnel velocities; namely 10.3, 13.2, and $15.8 \pm 0.1 m.s^{-1}$ with corresponding Reynolds numbers over the mid-chord of the test wing of 167.2×10^3, 215.0×10^3, and 256.1×10^3 respectively. The highest speed tested represents the upper limit of test speeds possible in the Wits DDT. The conditions, test velocities, and Reynolds numbers are summarised in Table 10.1.

Table 10.1: Pressure Test Conditions

Speed Setting	0.4	0.5	0.6	mA
ΔP (dyn)	52	86	122	Pa
ρ	0.9839	0.9839	0.9839	kg/m^3
Velocity	10.3 $\pm$0.1	13.3 $\pm$0.1	15.8 $\pm$0.1	$m.s^{-1}$
Reynolds No.	167.2×10^3	215.0×10^3	256.1×10^3	

At each speed, the wing was tested in a clean or baseline configuration (no trailing flap extension, all tabs retracted) at angles of attack of $0, \pm 5, \pm 10, \pm 15$ ° . Pressure taps were built into the upper surface of the wing as per the configuration shown

in Figure 5.11. The symmetrical nature of the NACA 0012 profile used allowed net pressure distributions to be calculated by testing at the negative angles of attack which would represent the lower surface of the wing at the corresponding positive attitude. Using this method, a set of pressure data for the wing in a clean configuration at $5, 10$, and 15° was completed. The clean configuration provided a baseline set of results to which the results obtained for the various oscillation schemes could be compared. Due to the asymmetrical nature of the wing when the tabs are extended, pressure tests in these configurations were only completed for the upper wing surface.

Pressure tests were then performed with the tabs statically extended to their maximum position. Two tabs were built into the wing resulting in three possible static configurations which were tested once the baseline case had been established. The nomenclature used to describe the three additional configurations is presented in Table 10.2 and is carried through to the sections that follow.

Table 10.2: Nomenclature to Describe Tab Configurations

Abbreviation	Configuration
WT	Tab situated at Wingtip
FT	Tab situated at Trailing Edge Flap Tip
WT and FT	Refers to Both Tabs Deployed/Oscillating

Finally, pressure measurements were taken while oscillating the tabs in the various schemes presented in Table 10.2. Tests were performed for all positive angles of attack and at tab oscillation frequencies of 0.5, 1.0, and 2.0 Hz. Only synchronous oscillation schemes were investigated here.

10.1.2 Flow Visualisation

Flow visualisation formed a major component of the testing completed. All visualisation was completed by illuminating the area of interest in light and then injecting neutrally buoyant helium filled bubbles upstream of the model. The bubbles follow the resulting streamlines exactly and provide valuable insight as to how the flow is behaving, specifically the effect that adding vorticity into the near wake has have on the resulting vortex formed. The bubbles were introduced approximately one chordlength ahead of the wing from a steel tube of approximately 10mm diameter

connected to the externally located bubble generator. The tube was positioned using a retort stand placed at the tunnel wall so as to keep flow interference effects to a minimum. The effect of the interference in the flow between the tube and the wing was determined by examining the resulting surface pressure trace for the wing with and without the tube and stand in the tunnel. No difference was seen in the resulting pressure plots and therefore the effect of the tube in the freestream was deemed negligible.

The bubbles were photographed using a Nikon D90 camera with exposures ranging from 1-10 seconds. Two primary camera orientations were used; the camera was mounted directly above the vertically mounted wing to photograph the resulting flow patterns across the chord, and at the rear of the tunnel directly behind the wing to photograph the resulting vortex cross-section. Refer to section 3.3 for additional detail pertaining to the set up of the flow visualisation equipment used.

Cross sectional photographs were taken at three distinct positions: 0.37b, 1.0b, and 2.0b downstream of the wing as defined in Figure 6.1. In order to illuminate only the plane in question, a planer lens was fitted to the lightsource and blackout curtains were hung over the tunnel windows. Ambient light was a problem, entering the tunnel through the inlet and obscuring the resulting vortex. To avoid this, testing was completed at night when the laboratory could be completely darkened.

All flow visualisation took place at a tunnel speed of $7.2 \pm 0.1 m.s^{-1}$ corresponding to a Reynolds number of 116.0×10^3. The slow speed allowed one to position oneself in the back of the tunnel with the camera when taking photographs. Tests were conducted at higher speeds but the resulting images were of a poorer quality than those at the lower speed.

Flow visualisation was completed at wing angles of attack of 0, 5, 10, and 15° for both the statically extended case as well as oscillating cases as described in Table 10.2. Three test frequencies were selected when oscillating the tabs; 0.5, 1.0, and 2.0 Hz. As with the pressure testing completed, only synchronous oscillation schemes were considered in this body of research.

The cross-section tests as described above were repeated with the wing's trailing edge flap extended at an angle of 30°. This was done to test the effectiveness of the oscillating tabs in such a configuration that would be common of an aircraft on a final approach to land.

The Test Results and accompanying Discussion has been broken into three sections; namely the Baseline Case, the Static Extension Case, and the case where the Tabs are Oscillated to introduce vorticity into the near wake.

10.2 Baseline Tests

10.2.1 Pressure Measurements

Chordwise Data

In order to characterise the data being gathered from the wing, baseline pressure tests of the wing at all angles of attack in a clean configuration were completed. The pressure results are non-dimensionalised in order for a comparison with published data to be made. Published chordwise pressure data was obtained from the work carried out by Gregory et al. [37] which is seen as a reliable set of data for a NACA 0012 profile. Gregory's C_P data is most widely used as a means to validate CFD results and is listed as part of NASA's Turbulence Modeling Resource on their website [38]. The data is essentially 2D, not taking the formation of the wingtip vortex into account. It is for this reason that the experimental data used in the comparison was obtained from the chordwise set of pressure taps labelled FT1 - FT5 (see Figure 5.11) away from the wingtip. Figures 10.1 and 10.2 plot the results of the comparison for 10 and 15° respectively, the two angles at which data is available.

The results follow the published data for both angles of attack shown. In both cases, the experimental data sits just below the published for all pressure points tapped. Interesting to note is the drop-off of the experimental data near the trailing edge. This was predicted in subsection 5.3.5 based on the spanwise positions of the rear taps relative to those at the leading edge. The pressure coefficient at the rear most two taps is close to zero and as described in subsection 5.3.5 has little impact when determining the overall lifting capability of the wing. The uncertainty analysis completed on the pressure sensors in the Calibration Chapter show a very small uncertainty in the measurement. See Figure 8.7 for the calibration curve of Sensor No.1. Appendix F contains the remaining sensor uncertainties. Error bars were plotted for the experimental data gathered in Figures 10.1 and 10.2; however, the size of the vertical error bar is smaller than the size of each data point and thus is not clearly visible. The data obtained by Gregory [37] was completed at a Reynolds number of 3.0 million, an order of magnitude greater than what is possible in the Wits DDT. Both the data obtained experimentally and that obtained by

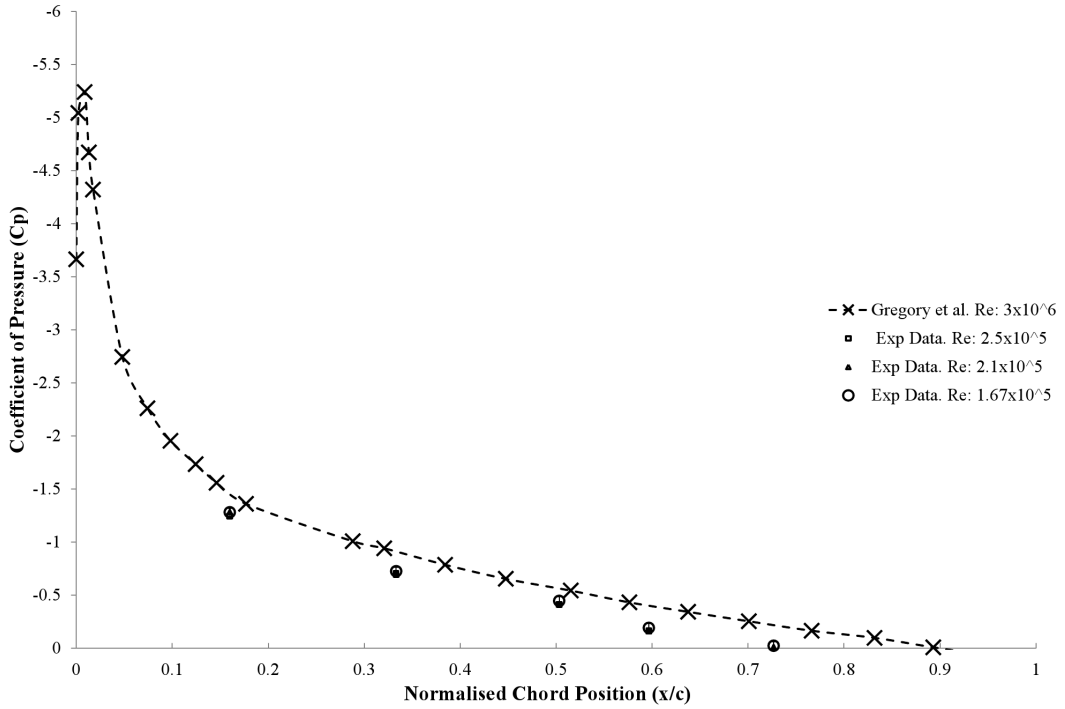


Figure 10.1: Dimensionless Chordwise Pressure Distribution, Experimental and Published Data, $\alpha = 10°$

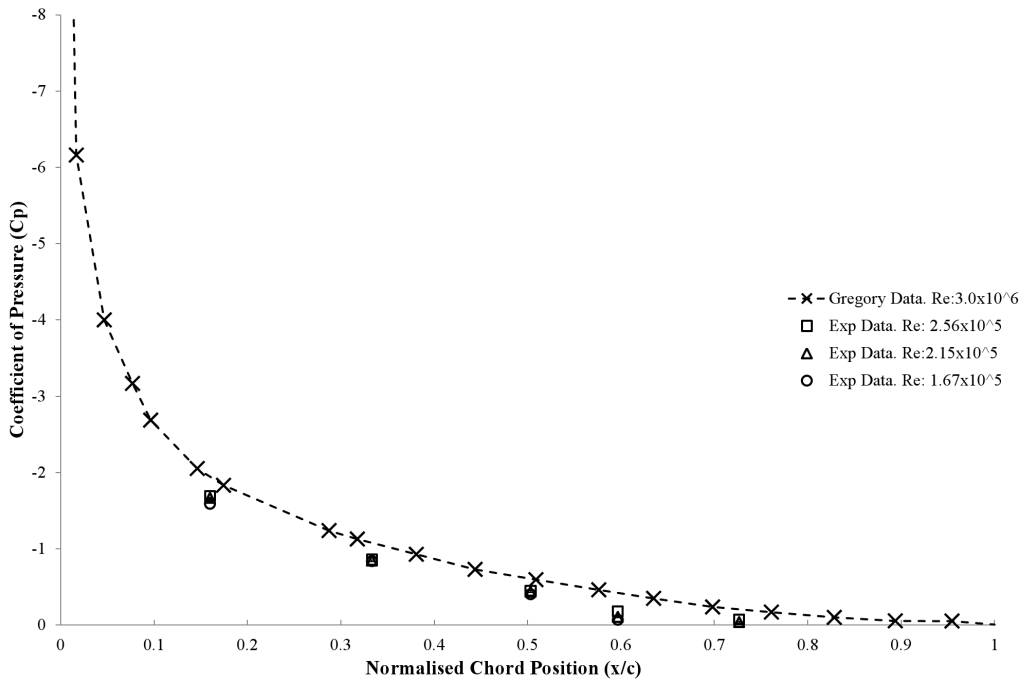


Figure 10.2: Dimensionless Chordwise Pressure Distribution, Experimental and Published Data, $\alpha = 15°$

Gregory were tripped so as to ensure turbulent flow over the entire chord. Tripping of the flow over the test wing was achieved by affixing a narrow strip of sand paper along the length of the span just downstream of the leading edge. Other external differences between the two tests include the addition of a trailing edge flap and tab on the chord section immediately downstream of the most aft pressure tap. While every effort was made to ensure that the flap and tab were always flush with the wing body to follow the wing's chord line, very small movements, especially of the tabs may have occurred as the test progressed which could have potentially altered the desired wing profile. The flap and wing tip areas where the tabs were installed would also then have a slightly longer chord length as a result of the tabs being positioned so as to not disturb the resulting airflow. The sections where the chord length has been increased would then show a higher Reynolds test number, but this small increase in chord length will not significantly alter the pressure distribution as the flow is tripped at the leading edge. The relatively low aspect ratio of the wing may also contribute to the slight variation between the test and published data as the lift curve slope reduces with aspect ratio.

The comparison between the two sets of data shows the experimental data to be of an acceptable accuracy and thus validates the data capturing method and allows for meaningful data to be extracted from the test facility. It is important to note that the number of chordwise pressure taps installed on the wing are not sufficient to transform the pressure data into lifting data with much accuracy. As is evidenced from Gregory's results [37], there is a non-linear drop in surface pressure near the leading edge. The bulk of the lifting force is produced by this pressure drop on the upper surface leading edge as the free stream is accelerated over the leading edge curvature. The C_P value at 0.2c is approximately half that at 0.05c. As such, finding the lift force from the experimental data by integrating the pressure distribution over the chord will greatly underestimate the total lift force produced by the wing as the pressure tap nearest the leading edge is only situated at 0.16c. Even though it is not possible to accurately resolve the total lift force from the pressure data, the chordwise data still proves invaluable in distinguishing between the various oscillation schemes and frequencies at which the tabs are oscillated.

Figure 10.3 compares the chordwise surface pressure distribution for the wing in the baseline configuration over the range of angles of attack tested. Both the upper and lower surface plots have been included. An increase in the angle of attack produces a change both in the magnitudes of the surface pressures as well as the pressure difference between the upper and lower surface at each angle of attack. Also clear from the plot is the fact that the upper surface is primarily responsible for the

increase in lift with angle of attack. Since the addition of oscillating tabs on the trailing edge will increase both the chord and camber of the upper surface, the tabs are expected to increase the resulting lift force significantly in addition to introducing vorticity into the near flow. Figure 10.4 plots the net pressure distribution of the clean wing at angles of 5, 10, and 15° at the maximum Reynolds number tested. The net distribution is found by subtracting the lower surface pressure from the upper. The relative importance of the leading edge section of the wing in generating lift is clearly visible on the plot. The pressure tap nearest the leading edge (FT5) produced substantially greater pressure differences between tested angles of attack when compared to the taps closer to the trailing edge. When doubling the angle of attack from 5 to 10°, the C_P value at FT5 doubles from approximately -0.6 to over -1.2. When moving from 10 to 15°, the relative increase between taps at the same position decreases but the largest increases are still found at the leading edge. Thus the effect that the tabs have on the leading edge of the wing will be of great importance as it will give an idea as to the change in the lift produced as a result of the oscillation scheme applied. It should also be noted that the tap closest to the trailing edge, FT1, shows net pressure coefficients close to zero. One can thus conclude that the trailing edge region of the wing downstream of 0.7c has little effect on the lifting properties of the uncambered wing. As with the results comparing the experimental data to that of Gregory [37], the uncertainty in the measurement is smaller than the data points used to represent the pressure at each tap. Error bars are therefore not included on all subsequent pressure plots.

The fact that only the upper surface pressure distribution can be measured during tab tests will not negatively affect the results and conclusions drawn as the upper surface leading edge is shown to dominate the net pressure distribution and hence is a direct indication of the wing's ability to generate lift.

As a means to validate the pressure results presented in Figures 10.3 and 10.4, compare Figures 10.5 and 10.6 which are photographs taken of the streamlines near the upper surface of the chord at 5 and 15 degrees angle of attack respectively. The angle through which the air has to bend at 15° to remain attached is considerably greater than that of the 5° case. The streamlines in Figure 10.6 (15° case) are more densely packed than in the 5° case, indicating the far higher pressure gradients developed over the upper surface at the higher angle of attack. As the air moves down the chord toward the trailing edge, the difference in surface pressure between the various angle of attack cases decrease; evidenced both in the pressure plot (Figure 10.3) and the photographs described above.

Data Collapsibility

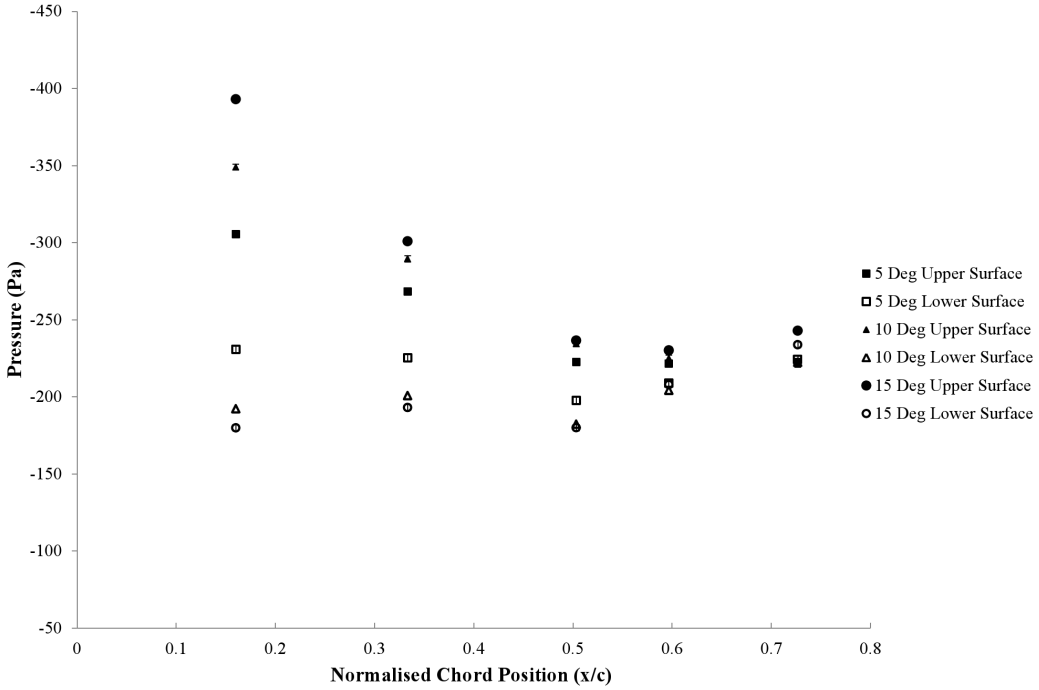


Figure 10.3: Chordwise Measured Pressure Distributions (Upper and Lower Surface)

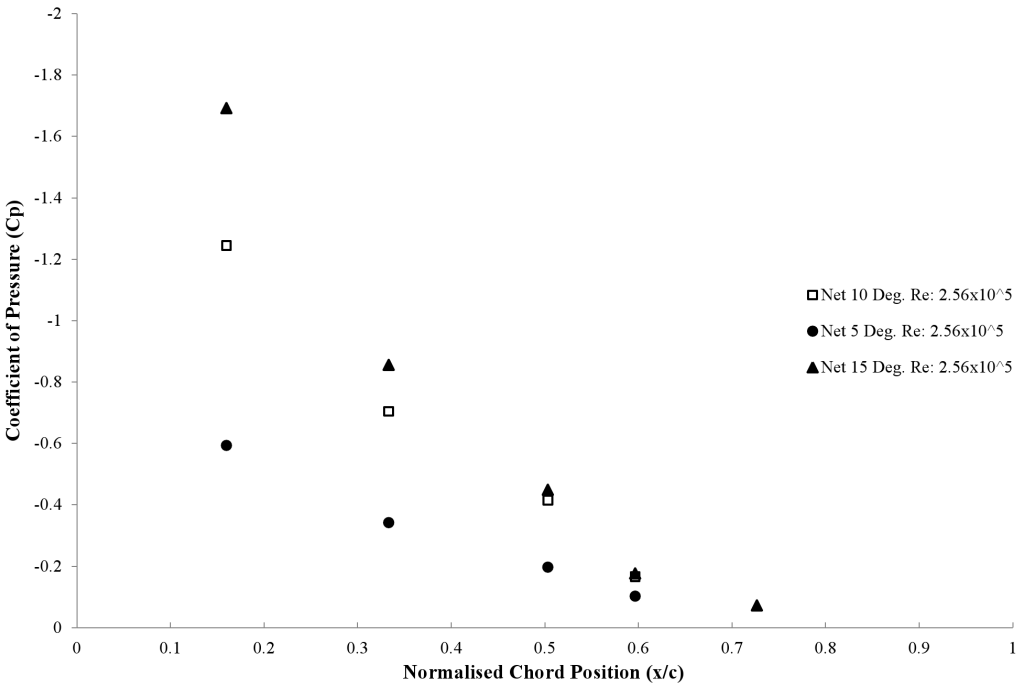


Figure 10.4: Net Non-Dimensionalised Chordwise Pressure Plot. $Re : 2.56 \times 10^5$

An important consideration when testing at various Reynolds numbers is the collapsibility of the data from dimensional to non-dimensional units. Ideally, when

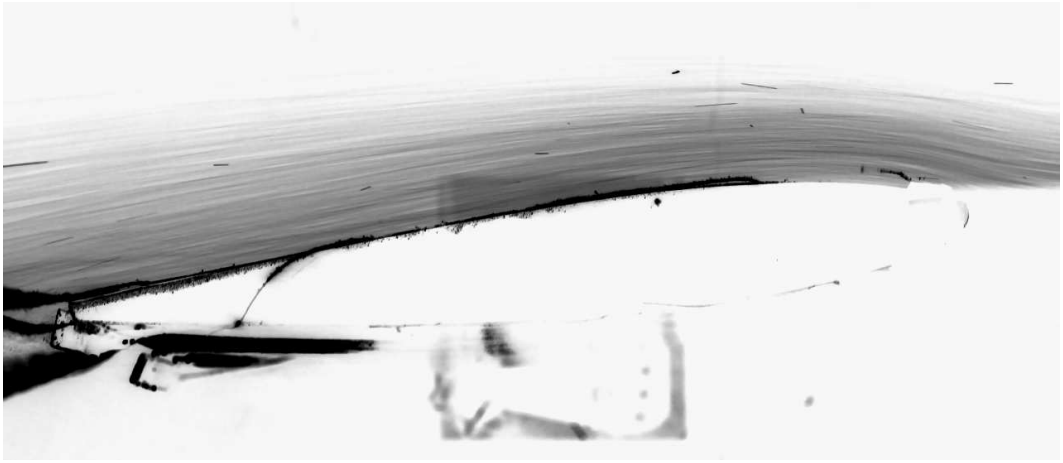


Figure 10.5: Upper Surface Streamlines, $\alpha = 5°$, Maximum Tab Extension

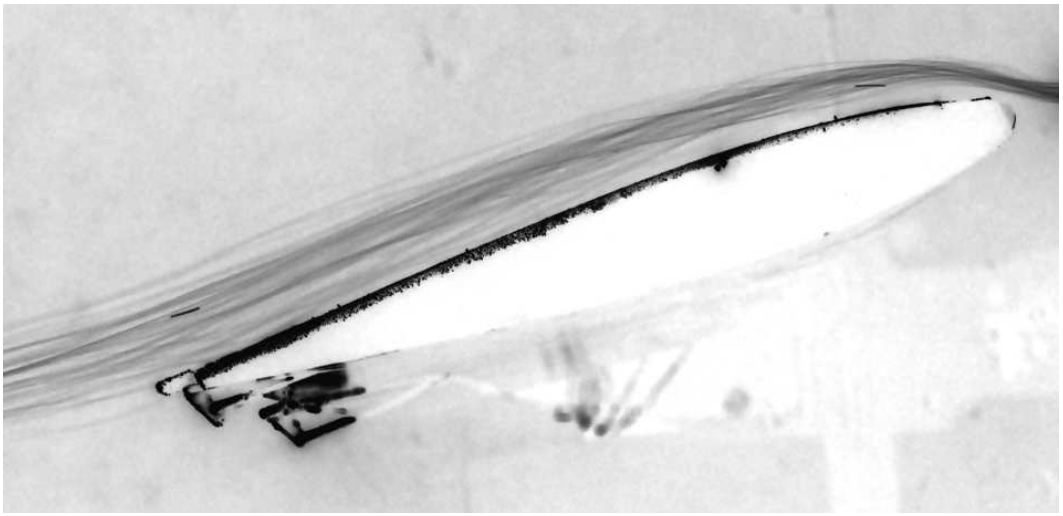


Figure 10.6: Upper Surface Streamlines, $\alpha = 15°$, Tab Retracted

non-dimensionalised, the data for each test speed should coalesce into a single correlation curve. This allows for tests carried out at various speeds to be directly compared to one another. Figure 10.7 shows the collapsibility of the net pressure distribution at the three different test speeds for the wing at an angle of attack of 10°. As is evident in Figure 10.7, the results when non-dimensionalised collapse well onto a single line. It can be concluded therefore, that the speed at which testing took place does not largely affect the results presented for the range of Reynolds numbers achievable in the Wits DDT. Figures 10.1 and 10.2, the chord plots comparing the experimental data gathered to that published by Gregory [37], further demonstrate the collapsibility of the data. This result allowed for the flow visualisation component of the testing to be completed at lower speeds than that at which pressure data

was attained and a direct comparison between identical cases to be made in spite of the differing Reynolds numbers.

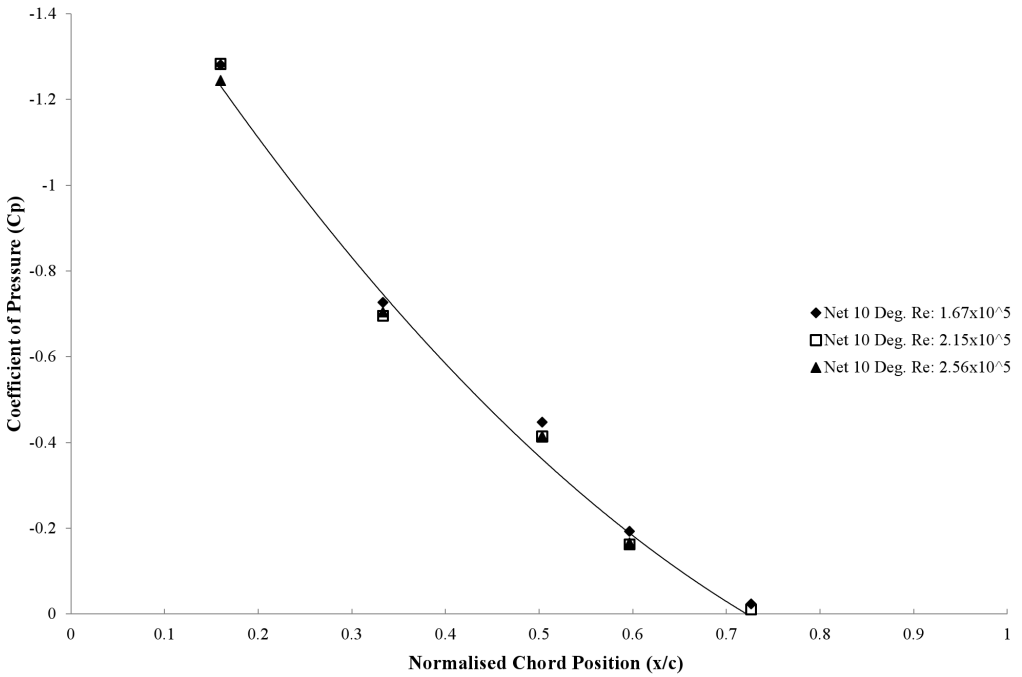


Figure 10.7: Non-Dimensionalised Chordwise Pressure Data, α =10°

Spanwise Pressure Data

Two sets of spanwise pressure taps were installed in the test wing as shown in Figure 5.11. They are designated as the Leading Edge span set (labelled as LE1-LE9) and Trailing Edge span set (TE1-TE9). The leading edge span set is situated at a position of $\frac{1}{3}c$ while the trailing edge sits at 0.727c. As evidenced by the chordwise plots presented previously, the leading edge spanwise distribution should be more sensitive to pressure changes than the trailing edge span due to the greater magnitude of the pressures developed close to the leading edge as the angle of attack is increased. Pressure tap LE1 was not considered in the spanwise analysis as the tap sits close to the wing root and as such is influenced by the boundary layer formed on the wind tunnel floor. The tap closest to the root was also influenced by the small gap present between the tunnel floor and the wing mount, which was impossible to completely close due to the tubing exiting the wing at the root and running out the wing into the transducer box outside the tunnel. The pressure distribution from the mid-span to the wing tip is of primary interest as this is where the largest influence of the tabs will be seen; particularly near the wingtip where the largest vortex is shed.

Figure 10.8 plots the upper and lower surface pressure distribution along the wingspan for the three tested angles of attack. The data mirrors that of the chordwise plot (Figure 10.3) in that the magnitude of the upper surface pressures all sit above that of the lower surface. Also the difference between upper and lower span surface pressures increases in magnitude as angle of attack is increased. The highest surface pressures occur on the lower surface of the clean wing at 15°, the highest angle of attack. These pressures decrease (move toward the corresponding upper surface pressures) as the angle of attack is reduced. This is an expected result; as the angle of attack is increased, the stagnation point on the wing drops further onto the lower surface of the wing, thus increasing the pressure on the leading edge portion of lower surface and reducing the velocity of the air as it transits the lower surface. As a means of comparison, a spanwise lift distribution for a finite width NACA0012 wing is published as Figure 10.9 [39]. In the case of Figure 10.9, the drop in pressure is represented by an increase in the lift coefficient.

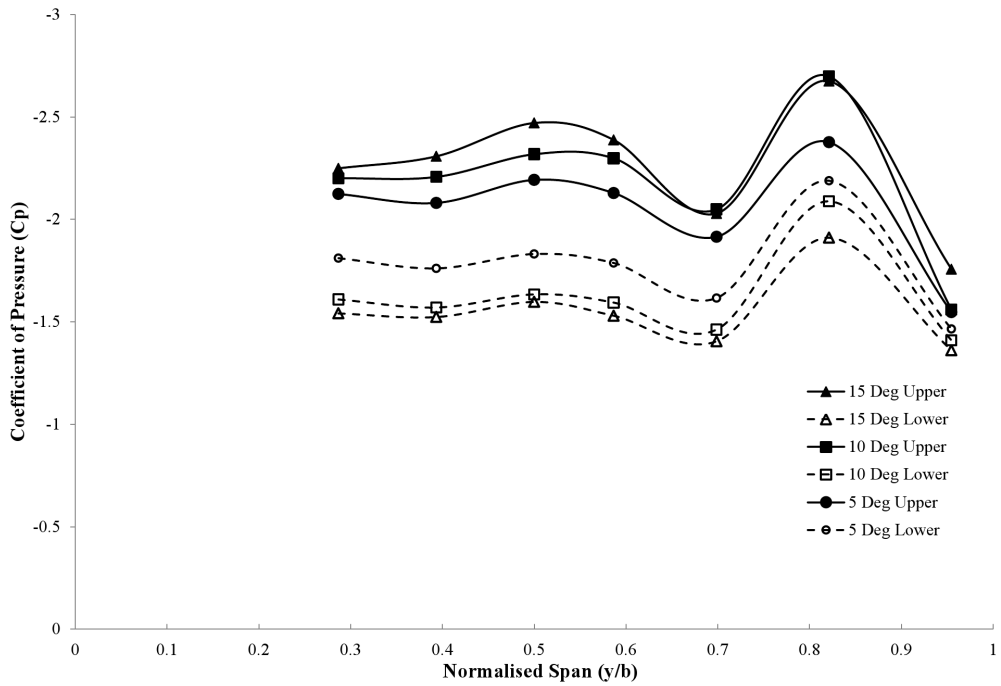


Figure 10.8: Non-Dimensionalised Upper and Lower Surface Spanwise Pressure Data. Re : 2.56×10^5

Of particular interest in Figure 10.8 is the portion of the span from 0.7b to the wingtip. Pressure Tap LE8 shows a spike in $-C_P$ for all angles of attack tested. This corresponds to a large drop in the surface pressure over this region and is a direct indication of the influence of the vortex being shed at the wingtip. Air is moving from the lower surface at the wingtip discontinuity and wrapping itself up and over the tip to form the primary wingtip vortex. The point where the lowest

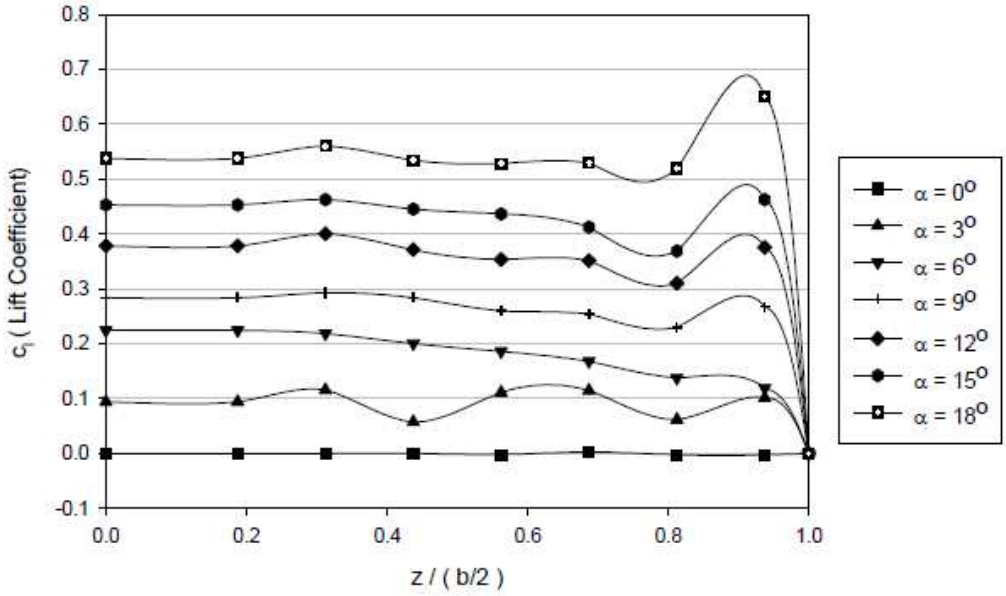


Figure 10.9: NACA0012 Spanwise Lifting Data. $Re : 43.6 \times 10^3$ [39]

pressure is found would then correspond to the centre of the vortex core. The adverse pressure gradient set-up from the vortex core moving out to the vortex extents is visible when examining Figure 10.8. This is seen by the peak in negative C_P shown at LE8, and the pressure recovery at the two adjacent pressure taps LE7 and LE9.

Greene [7] states that the wingtip vortex is shed at approximately $\frac{\pi}{4}b$ or 0.785b for an elliptical wing. A conclusion as to the precise location of the vortex centre cannot be drawn based on the results of the span plot in Figure 10.8 as there are too few pressure taps in the region between 0.75b and 1.0b to accurately determine the low pressure peak. However, the results presented do show the influence of the wingtip vortex in the region under investigation and clearly demonstrates that the pressure in the vortex core drops as the angle of attack is increased. The pressures at LE7 and LE9 which can be considered to mark the extents of the vortex are approximately equal through the range of angles of attack tested. This implies that the pressure gradient $\frac{dP}{dr}$ is greater at higher angles of attack, leading to a more powerful vortex shed at the wingtip. This results in a stronger wake vortex region at high angles of attack and corresponds to a greater wake threat for a trailing aircraft that comes into contact with the wake being shed.

Subtracting the lower surface pressure distribution from that of the upper surface yields the net pressure distribution for the wing in its baseline configuration, shown in Figure 10.10. The taps near the root are influenced by the boundary layer on

the tunnel floor and are not shown. It is clear that the middle third of the wing is producing the majority of the lifting force, and that as the angle of attack is increased, the amount of lift produced by the wing increases as well. The pressure distribution at the wingtip is also of interest. There is no discernible spike in the data at 5° to indicate the presence of a wingtip vortex. This may be attributed to the fact that the vortex core and associated spike is expected to lie in the region between the two pressure taps between 0.7b and 0.8b. This is consistent with the findings of Crow [9], predicting the core at 0.785b for an elliptical distribution. At $\alpha = 5°$ the vortex shed is also weaker than at the higher angles tested, hence the lack of evidence of the vortex when examining the net spanwise pressure distribution. Another interesting trend to notice is the apparent movement of the vortex core toward the wingtip as the angle of attack is increased.

The phenomena shown revealed by the pressure tests are backed up and discussed in relation to the flow visualisation tests completed for the wing in the baseline configuration. This is expanded upon in the proceeding section.

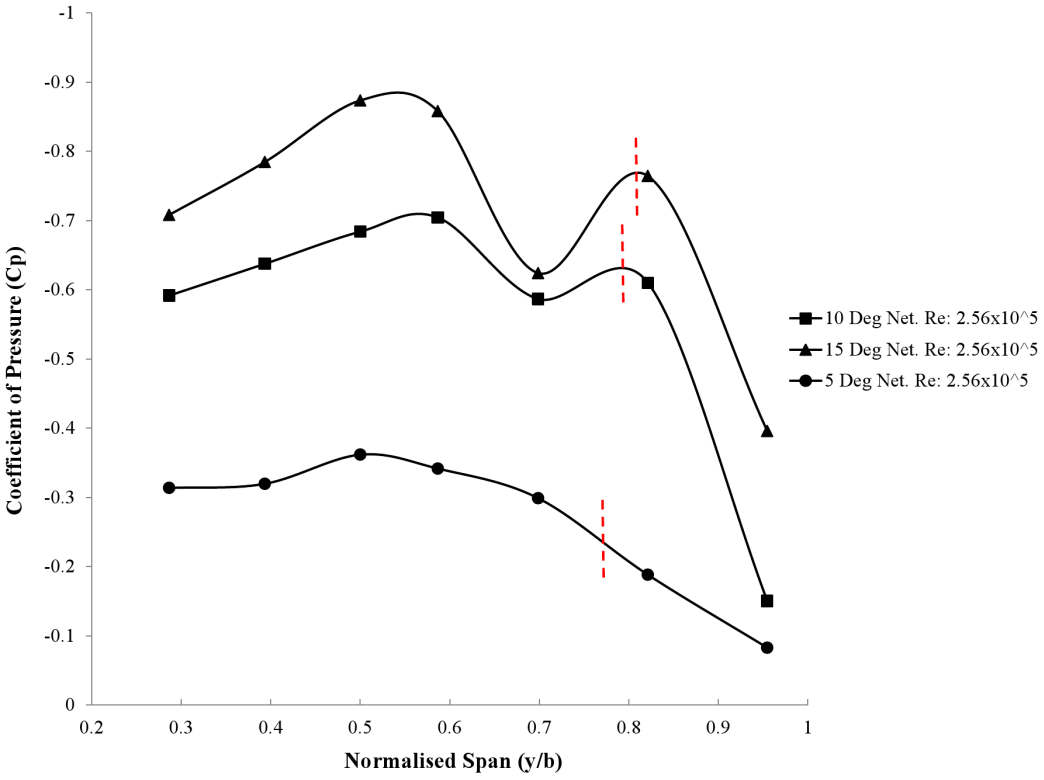


Figure 10.10: Clean Wing Net Spanwise Pressure Distribution. $Re : 2.56 \times 10^5$

10.2.2 Baseline Flow Visualisation

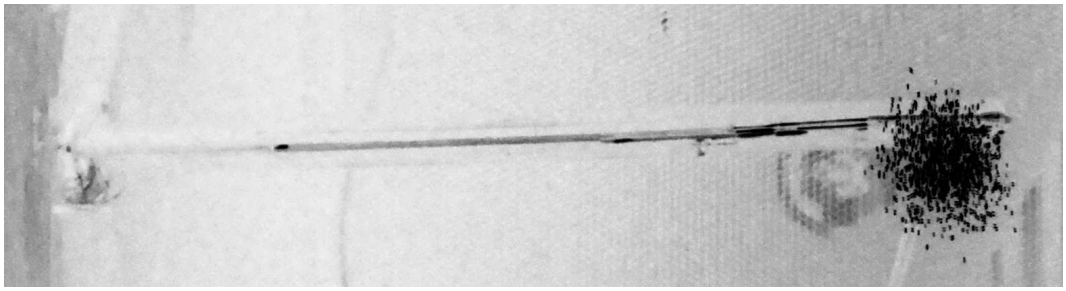
Flow visualisation formed an integral component of the testing undertaken. Both chordwise and downstream cross section images were collected as a means to quantify the behaviour of the wingtip vortex as it propagated downstream. Detailed instructions pertaining to the set up, capture and subsequent processing of the images taken can be found in chapter 3 of this report. Images of the vortex cross section were collected at three distinct downstream locations; namely $0.37b$, $1.0b$, and $2.0b$. Refer to section 10.1 for a summary of the testing undertaken. The test matrix detailing the experimental configurations tested is shown in Figure 3.1.

Vortex Variation with Increasing Angle of Attack

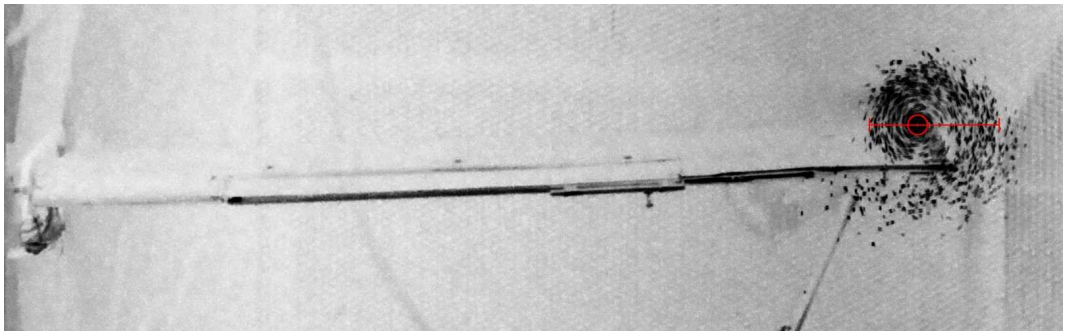
In order to quantify the effect that oscillation of the tabs has on the wingtip vortex, a clear understanding of the vortex shed by the wing in a clean configuration had to be demonstrated. Figure 10.11 consists of a series of four photographs showing the resulting vortex cross section shed at the wingtip at a downstream position of $0.37b$ as the angle of attack of the wing is varied from 0° to 15° . The bubbles are introduced upstream of the wingtip in a stream in order to best capture the vortex roll-up. Due to the symmetry of the NACA 0012 profile, no vortex roll-up is present with the wing at $\alpha = 0^\circ$ as the wing is producing zero net lift.

As the angle of attack is increased, a well defined vortex is shed, indicating that the wing is producing lift and therefore an associated circulation. At 5° angle of attack the resulting vortex extents are contained to a small region either side of the clearly visible core. Increasing the angle of attack produces a linear increase in the extent of the vortex (Figure 10.12), indicating an increase in the lift force produced and subsequent strengthening of the resulting vortex. Figure 10.12 was compiled by measuring the extents of the wake region in Figure 10.11 as the angle of attack was increased, and non-dimensionalising the diameter with respect to the wing semi-span (b). The increase in lift and strengthening of the resulting vortex is verified when examining the pressure plots for the wing in this baseline configuration. Net chordwise and spanwise data (Figures 10.4 and 10.10 respectively) both show an increase in the lift and hence circulation produced as the angle of attack is increased provided the wing is kept below the stall angle.

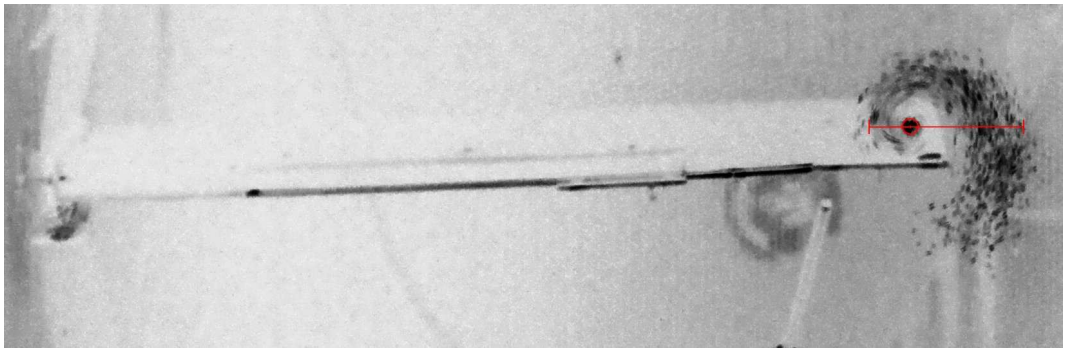
This linear relationship shown experimentally is derived mathematically as follows:



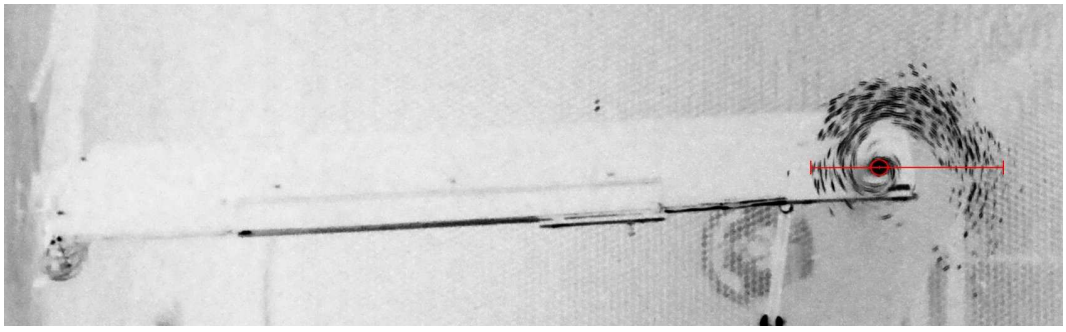
(a) $\alpha = 0°$



(b) $\alpha = 5°$



(c) $\alpha = 10°$



(d) $\alpha = 15°$

Figure 10.11: Photograph of Differing Vortex Diameter, 0.37b Downstream

Crow [9] showed the total circulation produced by a wing in the free stream to be related to the Lift Coefficient and the physical geometry of the wing. Equation 1.4 is repeated here for convenience.

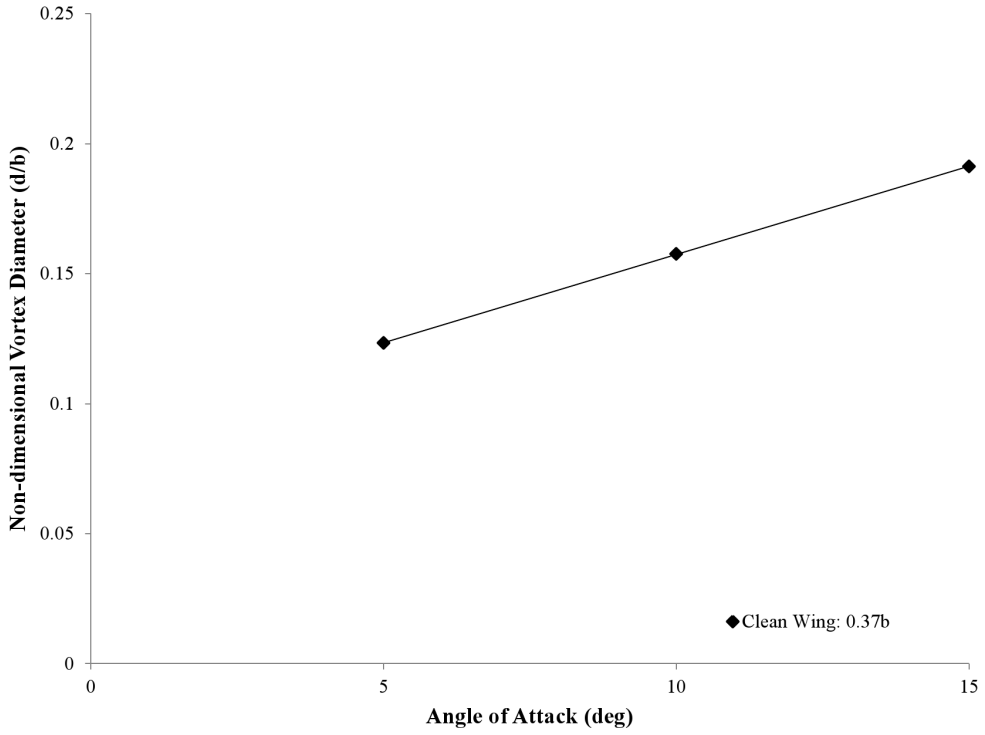


Figure 10.12: Non-dimensional Vortex Extent Growth, 0.37b

$$\Gamma = \frac{2C_L U_\infty b}{\pi AR} \tag{10.1}$$

The wake tangential velocity is shown in Section section 1.2 to be equal to the quotient of circulation and radial distance from the vortex core. Equation 1.5 is repeated below.

$$V_\theta = \frac{\Gamma}{2\pi r} \tag{10.2}$$

This may be rearranged in terms of circulation,

$$\Gamma = 2\pi r V_\theta \tag{10.3}$$

Equating Equation 1.5 and Equation 10.3 one can solve for the vortex radius as a function of the flow conditions and wing geometry.

$$2\pi r V_\theta = \frac{2C_L U_\infty b}{\pi AR} \tag{10.4}$$

$$r = \frac{C_L U_\infty b}{\pi^2 A R V_\theta} \tag{10.5}$$

In the linear region below stall, $C_L = C_{L\alpha}\alpha$ Thus:

$$r = \alpha \left(\frac{C_{L\alpha} U_\infty b}{\pi^2 A R V_\theta} \right) \tag{10.6}$$

The extents of the vortex are defined by the points where the tangential velocity reduces to zero. Having shown that circulation increases with increasing angle of attack, and decreases with downstream propagation; it thus follows that the higher the wing angle of attack, the larger the wake diameter. This is confirmed by Figure 10.12 and the linear relationship between non-dimensional diameter and angle of attack derived from the mathematical model presented above.

$\lim_{V_\theta \to 0} r \to \infty$

Therefore: as
$r \to \infty : \alpha \to \infty$

Vortex Variation with Downstream Propagation

Greene [7] examined wingtip vortex decay in the atmosphere and showed that the wingtip circulation decreases as the vortex propagates downstream away from the wingtip. Figure 1.10 shows the results obtained by Greene where the degradation in circulation value for various stratification and turbulence values are shown. The x-axis value on Greene's plots, non-dimensional time (T) as a function of the lifting properties of the wing and its associated geometry is placed here as Equation 10.7.

$$T = \frac{16 C_L d_{ds}}{\pi^4 A R} \tag{10.7}$$

Where:
T Dimensionless Time
d_{ds} Downstream Distance in x Direction

Using equation 10.7 and estimating the maximum lift coefficient that the wing produces during testing in the baseline configuration, one can show that the maximum

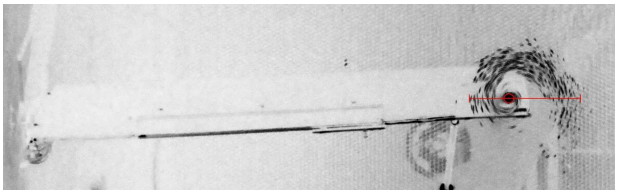
non-dimensional time (T) reached in the tunnel is of the order of 0.15. Thus circulation degradation has begun to occur but not to too great an extent. Circulation at 2.0b is estimated to be at least 80% what it is at the wing based off the plots in Figure 1.10.

The size and shape of the vortex as it propagates downstream is investigated for the wing in the baseline configuration. Figure 10.13 shows the wingtip vortex formed with the wing at an angle of attack of 15° at the three measured downstream locations, 0.37b, 1.0b, and 2.0b. As the wake moves downstream, degradation of the vortex occurs, the circulation decreases, and as a result, the tangential streamlines move further apart. This is evident when examining Figure 10.13 where the streamlines at 0.37b and 1.0b are noticeably closer together than at 2.0b. This indicates a reduction in the tangential velocity of those streamines as they move further away from the vortex core.

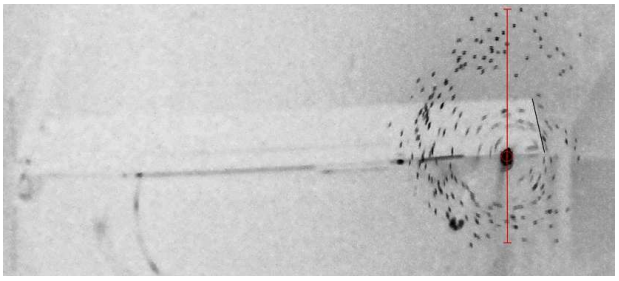
Figure 10.14 plots the measured vortex extent at each downstream position for the various angles of attack tested. All three tested angles show the same sharp increase in extent from 0.37b to 1.0b, before tapering off slightly as one reaches 2.0b downstream. The vortex increase in extent is expected between 0.37b and 1.0b as the vortex roll up is ongoing in this region. At 2.0b, the small decrease in circulation results in slower tangential velocities at the vortex extents with a corresponding drop in angular momentum. The neutrally buoyant bubbles injected in the free stream will then naturally coalesce in regions of lower pressure closer where the wake tangential velocities are higher; hence the slight decrease in vortex diameter.

Looking at the baseline case as a whole, the system is shown to be both predictable and stable at all angles of attack below stall. Chordwise pressure distributions show the curvature at the leading edge portion of the wing is primarily responsible for the generation of lift and thus also circulation. The rearward 30% of the chord does little to generate lift for all angles of attack. Increasing the angle of attack of the wing, and hence the angle through which the air has to bend around the leading edge has the effect of introducing much larger pressure gradients on the forward portion of the wing with a resulting increase in the total lift produced and a corresponding increase in induced drag - evidenced by the increase in the vortex extents shown in Figure 10.13.

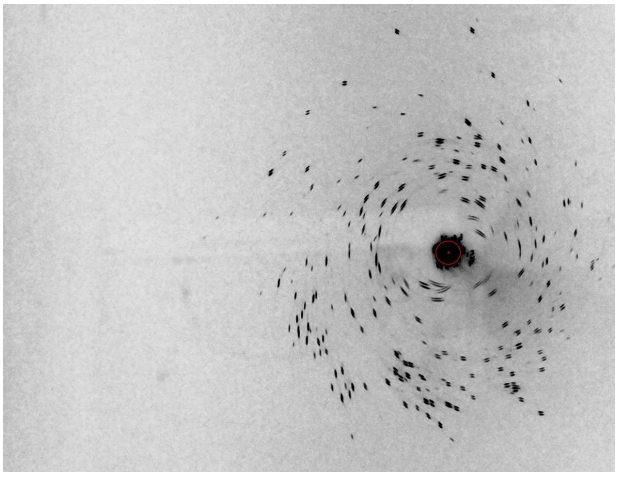
Spanwise pressure plots of the wing showed larger pressure gradients through the vortex at higher angles of attack. The influence of the wingtip vortex on the spanwise pressure distribution is clearly seen in Figures 10.8 and 10.10.



(a) 0.37b



(b) 1.0b



(c) 2.0b

Figure 10.13: Downstream Progression of Clean Wingtip Vortex. $\alpha = 15°$

Characterising the wing in the baseline configuration allows the effect of introducing vorticity into the near wake by oscillating tabs on the trailing edge to be studied. By imparting vorticity into the stable wake, it is thought that instabilities may be introduced which will alter the stability shown in the baseline case and ultimately result in a situation where breakup of the core may be seen earlier into the downward propagation of the near wake.

10.3 Tab Static Extension

Static extension of the two tabs in their maximum position (near perpendicular to the trailing edge) were investigated both with pressure measurments and flow visualisation completed. Figure 10.15 plots the chordwise pressure distribution with

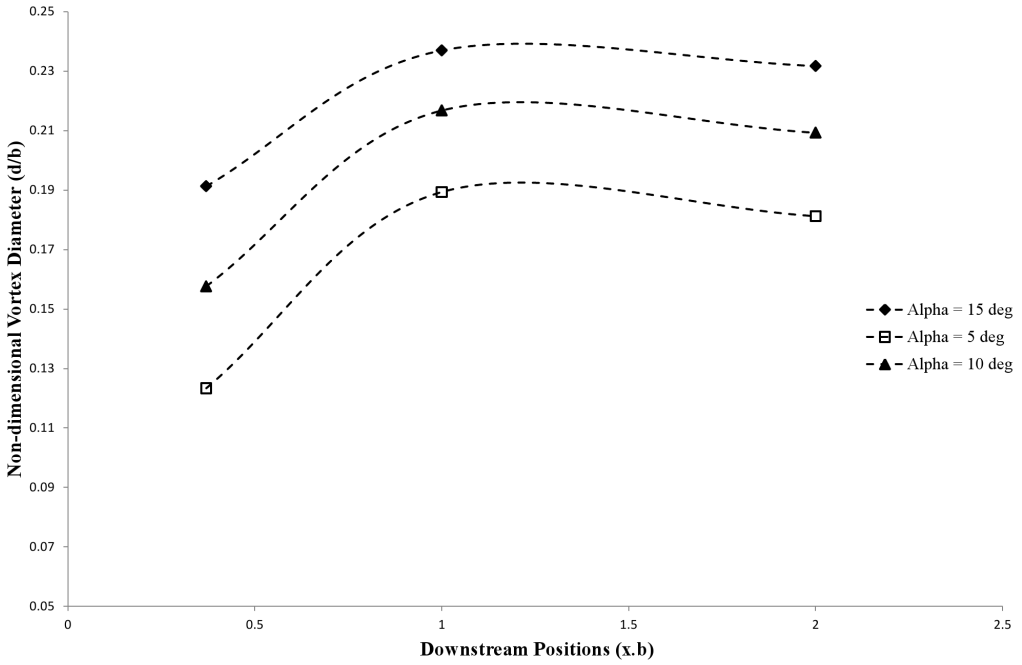


Figure 10.14: Non-dimensional Vortex Growth with Downstream Propagation

the wing at an angle of attack of 5° where the lifting potential of the wing can be seen both for the case where the wingtip tab is oscillated at 2.0 Hz and left statically extended. Unsurprisingly, the statically extended case is shown to produce the greatest drop in surface pressure over the entire chord. The influence of the wingtip in determining the lifting capacity of the wing can be seen by the fact that there is considerable change in the pressure distribution even though this was measured away from the wingtip at taps FT1-FT5.

Figure 10.16 provides confirmation of the pressure results by examining photographs taken of the wing at 10° angle of attack for the various static extension schemes tested. The photographs are displayed with the wing vertical in the tunnel. The static extension of the wingtip tab provides the greatest relative change to the vortex, increasing the tangential streamline density, and introducing greater vorticity into the resultant vortex. Extending both the WT and FT tab only strengthens the vortex. This configuration provides the largest increase in pressure coefficient and subsequent increase in lifting capability of the wing. The effect of extending the FT tab only can be seen by comparing Figure 10.16 (a) and (d). The FT extension provides an increase in vortex strength at the wingtip albeit to a lesser extent than the configuration in (c) or (d). The same trends noted in Figure 10.16 with regards to the effect of statically extending the tabs were for all static configurations tested.

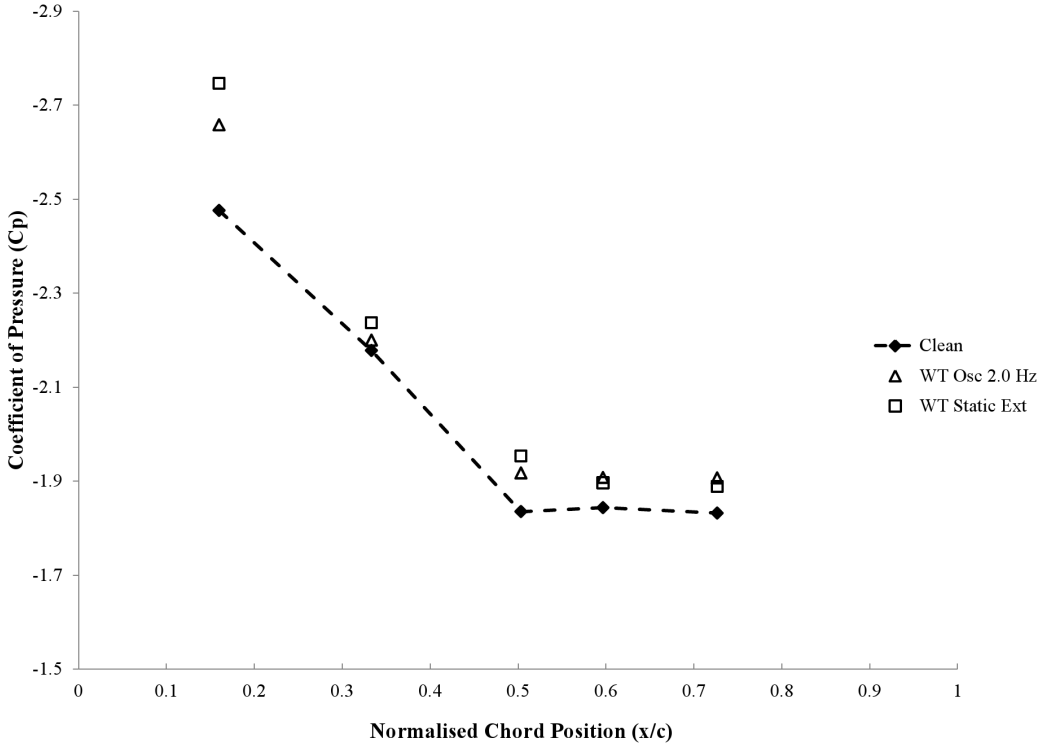
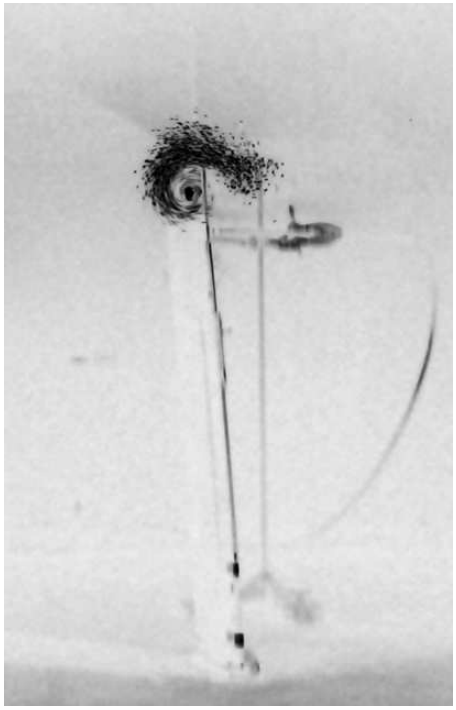


Figure 10.15: Chordwise Pressure Distribution, WT Tab Oscillate, Static Extension, $\alpha = 5°$

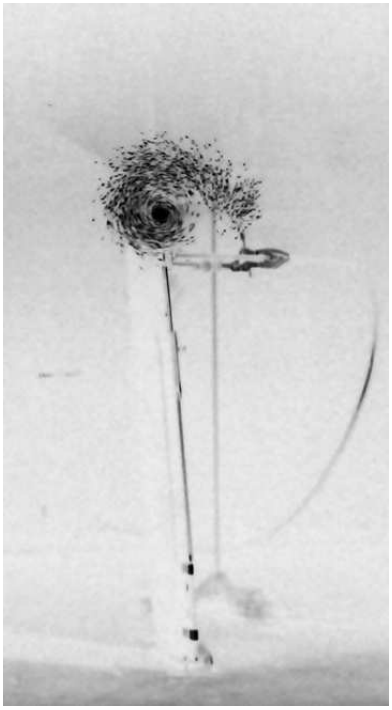
Static extension of the tabs does not seed the vortex with the instabilities necessary to facilitate early breakup and dissipation of the wake. This is clearly shown in Figure 10.17 where the resulting vortex core at position $2.0b$ is compared for a static tab extension (a) and that where both tabs are oscillated at 2.0Hz (b). Both images were taken with the wing at an angle of attack of five degrees. It is clear that vortex core motion and elongation will not be induced by a static configuration and will thus not be discussed further.

10.4 Tab Oscillation Tests

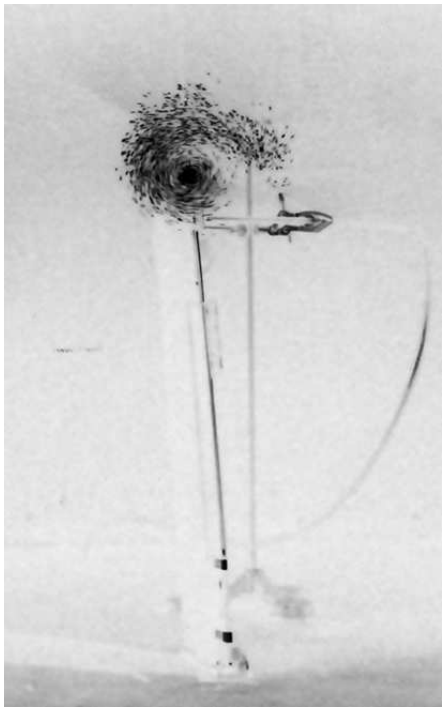
In order to seed the near wake with the instabilities necessary to induce early vortex breakup and dissipation, two tabs affixed to the trailing edge of the test wing were oscillated sinusoidally at frequencies ranging from 0.5Hz to 2.0 Hz. Each tab could be oscillated independently, or both oscillated together. Table 10.2 lists the nomenclature used to differentiate between the two tabs and their associated schemes, and will be used extensively here.



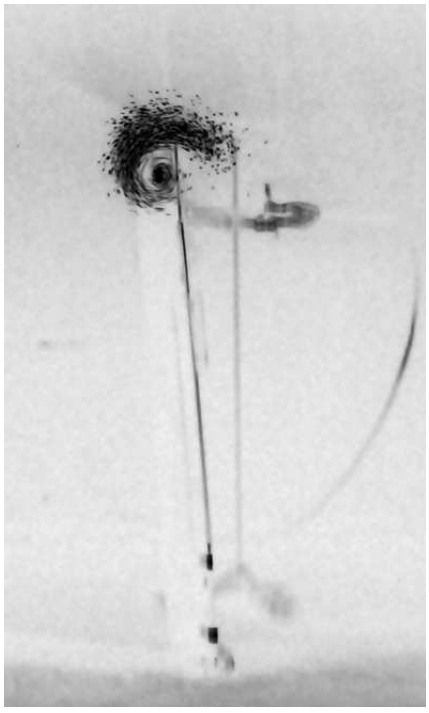
(a) Clean Configuration



(b) WT Static Extension



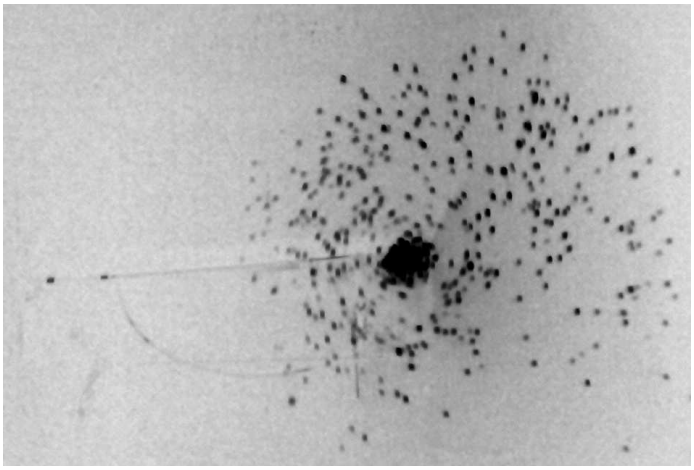
(c) WT & FT Static Extension



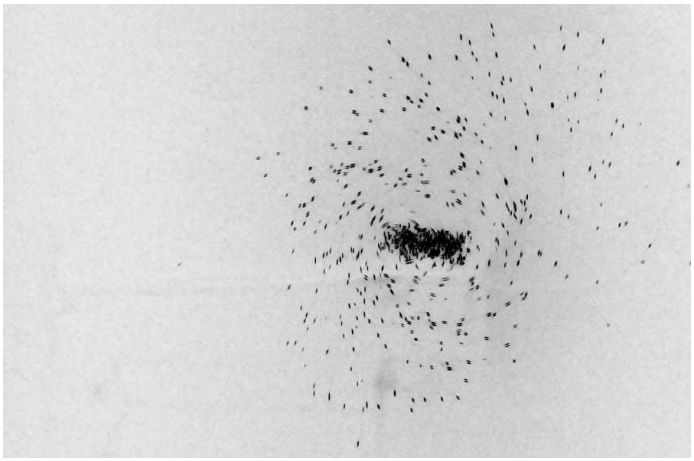
(d) FT Static Extension

Figure 10.16: Vortex Extent, Static Gurney Tab Extension. $\alpha = 10^{\circ}$, 0.37b

The effect that varying the frequency of tab oscillation had on the ability to induce instability formed the starting point of the oscillation tests. In order to use time averaged pressure data from the pressure sensors, the response had to be shown to



(a) Resultant Vortex Both Gurney Tabs Statically Extended



(b) Resultant Vortex Both Gurney Tabs Oscillate 2.0 Hz

Figure 10.17: Vortex Core Comparison; Static Extension and 2.0 Hz Oscillatory Scheme. $\alpha = 5^\circ$, 2.0b

be time invariant. A study was thus completed to investigate the transient pressure response during oscillation.

10.4.1 Transient Response to Oscillating Tabs

All surface pressures examined during baseline and static tests were calculated based on the time averaged pressure at each tap. However, the assumption that the pressure response is time invariant may not hold true for the case where the tabs are oscillated. The largest angle of attack tested, 15° , is examined here with the assumption that if the response is time invariant for this case then it will hold true for cases of lower α.

Figure 10.18 shows the raw output for two pressure sensors during a test performed at $\alpha = 15^{\circ}$, where the effect of varying frequency was investigated while oscillating both tabs. A significant variation in pressure response is seen across the pressure taps. Two taps, one near the leading edge and one near the trailing edge are compared. The upper line in Figure 10.18, plots the response of tap FT1 situated slightly upstream of the trailing edge flap hinge and forms the rearmost pressure tap used when examining the chordwise pressure response. The lower line in the plot, WT6, is situated nearest the leading edge at a position of 0.16c and forms part of the wingtip set of chordwise taps. Refer to Figure 5.11 to see the placement of the taps. Pressure data for these two cases were obtained simultaneously by the data acquisition system.
The test ran as follows:

- The tunnel was kept off so a zero value could be taken (0-45 sec)
- The tunnel was then turned on and the fan accelerated to the test speed. (45-60 sec)
- Thirty seconds of data for the wing in a clean configuration was taken. (60-90 sec)
- The test was then performed. Both tabs were oscillated at 0.5 Hz, 1.0 Hz, and 2.0 Hz for approximately 30 seconds with a 30 second gap between tests where the wing was in a clean configuration. (90-270 sec)

Immediately apparent in the raw data output is the much greater effect that the tab oscillation has on the pressure fluctuation at or near the leading edge (WT6). This is represented by the greater displacement from the clean configuration pressure trace that this tap sees. For the case of the tap at the trailing edge (TE6), the three regions where the tabs were oscillated can be clearly seen, but the magnitude of the pressure variation is considerably smaller than the tap at WT6. It is also evident from the plot that the tab oscillating at 2.0 Hz produces smaller pressure fluctuations at the leading edge than the lower frequencies of oscillation. That is, the amplitude of pressure fluctuations at WT6 appears to decrease as the tab oscillation frequency is increased. It follows that the most accurate time averaged pressure response would be had for the for the highest frequency tested.

In order to better investigate the magnitude of these oscillations, clean data taken between 60 and 90 seconds from WT6 (as seen in Figure 10.18) has been superimposed onto data captured of both tabs oscillating at 1.0 Hz. The result, shown

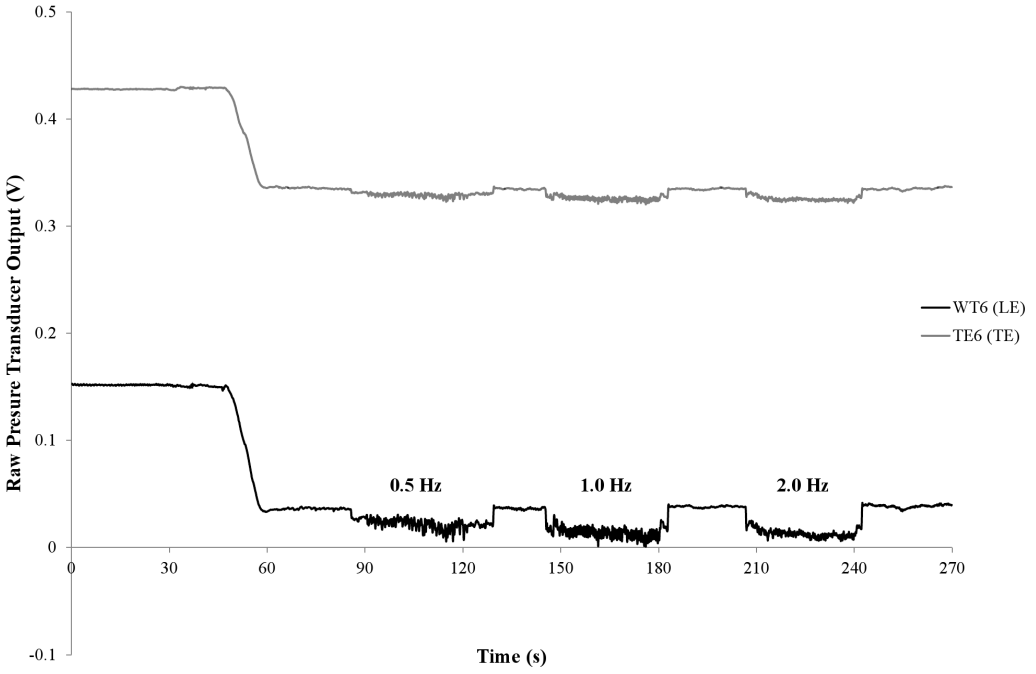


Figure 10.18: Raw Pressure Data; $\alpha = 15°$, Both Tabs Oscillate, Varying Frequency

in Figure 10.19, allows one to clearly see the effect that the oscillation has on the pressure values at the leading edge. The clean data shows no definable oscillation or period, with a maximum variation of approximately 5 Pa between peak and trough. The data for the oscillating tabs however show a clear sinusoidal oscillation. The variation in pressure from peak to trough for this case is 21 Pa, four times the variation in the clean case. The minimum and maximum values, and variation appear in Table 10.3. Uncertainties in the pressure measurement were shown to be approximately $\pm 4Pa$ which is demonstrated in the clean data and reinforces the claim of the larger pressure variation when the tabs are oscillated. The pressure oscillation seen in Figure 10.19 is predictable and approximately constant with time which allows for the mean pressure to be used when examining subsequent oscillation pressure plots. Images taken of the resulting vortex were taken with a five second exposure time as detailed previously, and thus captures the transient response shown here.

In order to further investigate this inherent sinusoidal oscillation a Fast Fourier Transform (FFT) was performed on the 1.0Hz oscillating data. The results were transferred into the frequency domain and appear in Figure 10.20. It is clear that a steady oscillation of 1.94Hz is present in the output. This is an oscillation of twice the input frequency that of the oscillating tabs (0.97Hz). The input frequency is visible as a smaller spike. The FFT also shows that there is a slight lag present

Table 10.3: Minimum and Maximum Pressures - Transient Case

Test Scheme	Max Pressure (Pa)	Min Pressure (Pa)	Difference (Pa)
Clean	-121	-126	5
WT & FT Osc.1.0 Hz	-140	-161	21

in the system (0.97Hz input rather than 1.0Hz) due to the software and smoothing filters used to produce the sinusoidal tab oscillation.

The inherent sinusoidal oscillation in the pressure response was investigated further by looking at the case where the tabs were oscillated at 2.0Hz. Figure 10.21 plots the FFT response where the tabs were oscillated at 2.0Hz. Here, as in Figure 10.20, there are two spikes present; one at the frequency of tab oscillation (1.92Hz) and a second spike at 3.84Hz; twice the input frequency. It is thus concluded that oscillation of the tabs set up a pressure oscillation equal to twice the input frequency.

It was seen during flow visualisation tests that oscillating the tabs at higher frequencies appeared to produce a more rapid movement of the vortex core and greater dispersion through the wake extents. The FFT result above gives an indication as to why the 2.0Hz frequency was shown to be most effective (of the tested frequencies) in disrupting the vortex. The greater the frequency of oscillation, the greater the transient pressure oscillation. This pressure oscillation of twice the tab frequency thereby introduces a greater disturbance into the near wake with the result that the wake is more unstable.

10.4.2 Frequency Variation

After showing that the transient pressure response to the tab oscillation was predictable, average surface pressures were extracted from the wing at the three frequencies tested. This was completed in order to determine the effect frequency has on the tab's ability to induce vortex instability. Figure 10.22 is a plot of the chordwise pressure distribution (FT1-FT5) at a 5° angle of attack where both tabs were oscillated simultaneously at 0.5, 1.0, and 2.0 Hz before being statically extended to their maximum position in the freestream. The results show mean pressure changes at each tap with the static case causing the greatest pressure drop when compared to the baseline case. This is followed by the 0.5 Hz oscillation scheme, the 1.0 Hz

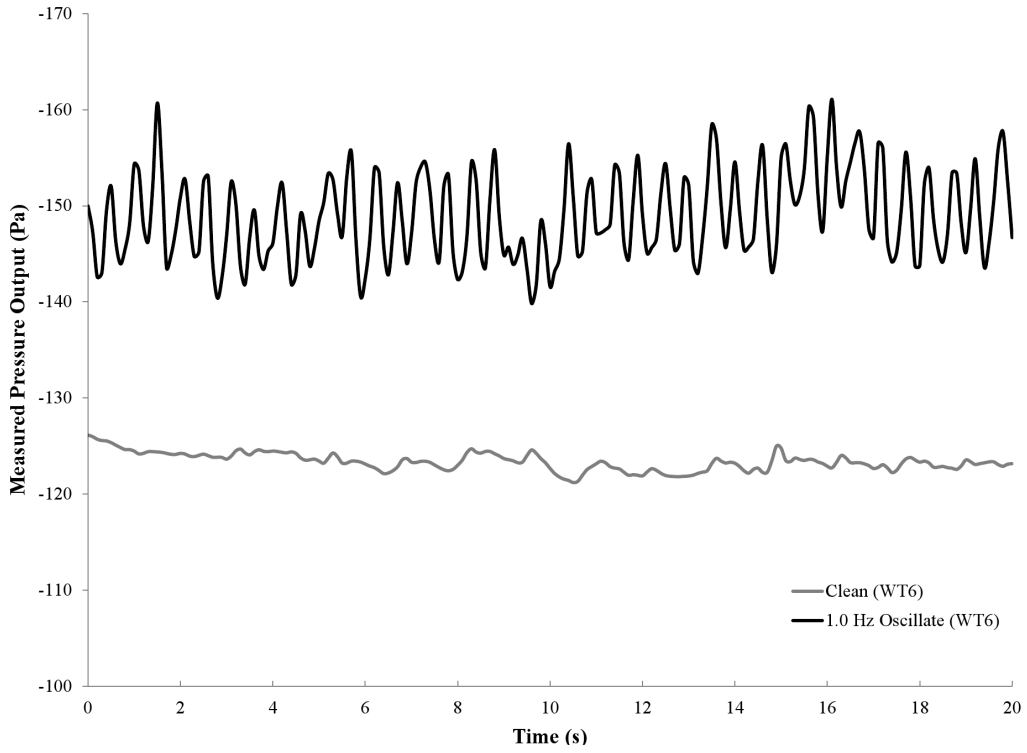


Figure 10.19: Transient Pressure Data Response; α =15°, Both Tabs Oscillate, 1.0Hz

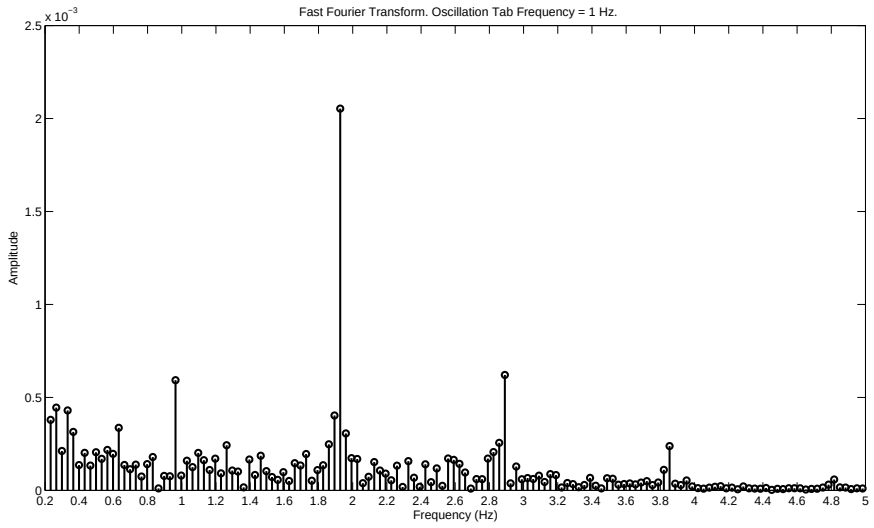


Figure 10.20: Fast Fourier Transform for Both Tabs Oscillating at 1.0Hz

scheme and finally 2.0 Hz case. The pressure drop at the leading edge (FT5) changes significantly through the different oscillation frequencies and appears in Table 10.4. As shown in subsection 10.2.1, the leading edge static pressure gives a good indication as to the lifting capability of the wing.

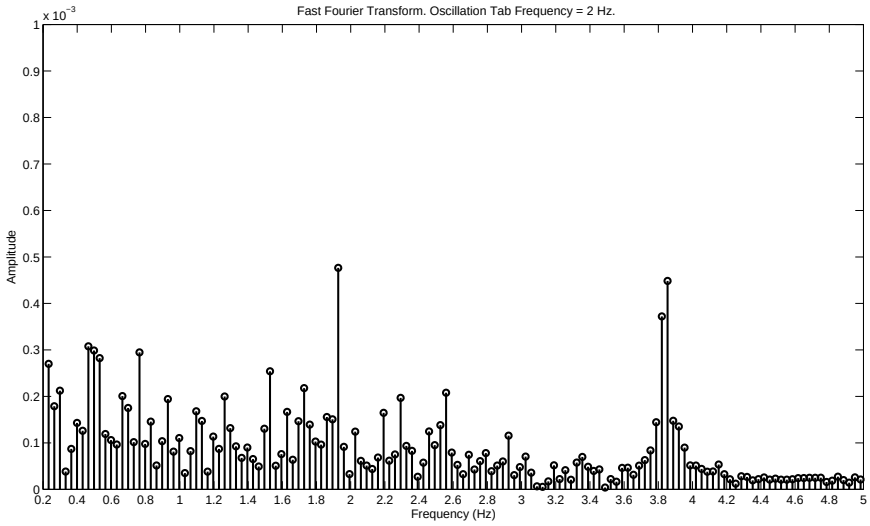


Figure 10.21: Fast Fourier Transform for Both Tabs Oscillating at 2.0Hz

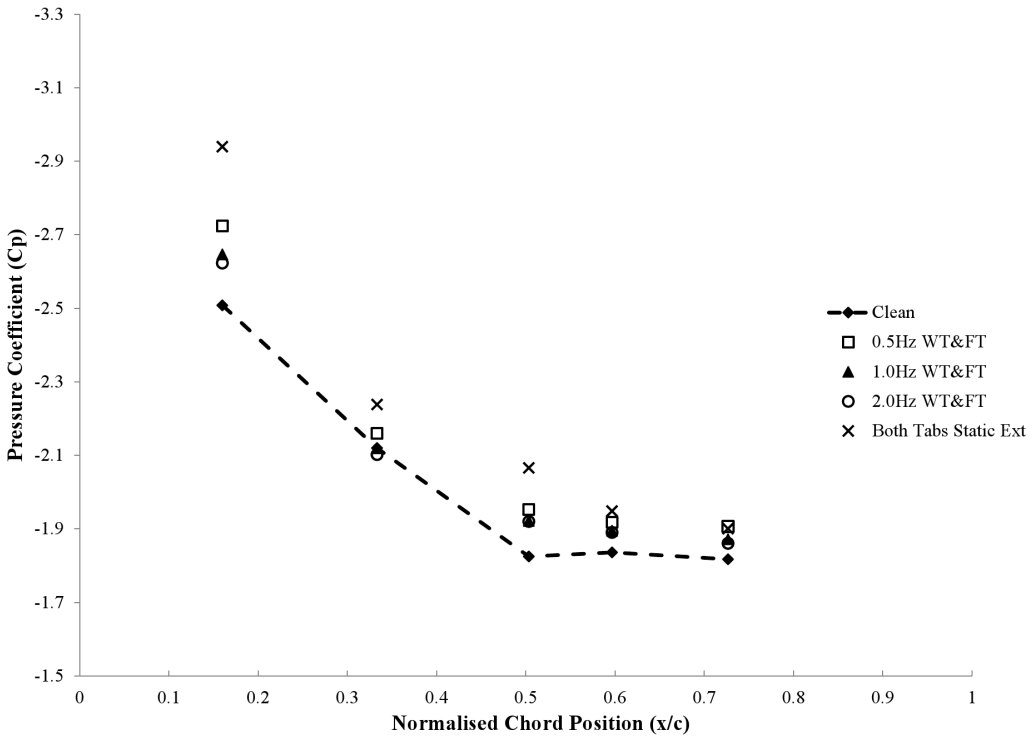


Figure 10.22: Chordwise Pressure Distribution due to Frequency Variation. Both Tabs Oscillated, $\alpha = 5°$

Figure 10.22 and Table 10.4 show that the tab oscillation scheme can have a significant effect on the lifting properties of the wing. The static case shows the greatest

Table 10.4: Change in C_P value at FT5 due to Frequency Variations, Both Tabs Oscillated

Oscillation Scheme	$\Delta CP(FT5)$	% Change
Clean	0	0
2.0 Hz	0.115	4.6
1.0 Hz	0.138	5.5
0.5 Hz	0.216	8.6
Static Extension	0.431	17.2

increase in the lift capability which can be explained by the fact that the tab increases the effective camber of the wing while extended. As this configuration keeps the tab extended indefinitely it follows that the largest increase will be had for this case. For the oscillation schemes tested, the lower the frequency of oscillation, the greater the net increase in lift produced.

As described in the transient analysis, flow visualisation tests revealed that higher frequencies tended to produce a more rapid movement of the vortex core. The motion of the vortex core followed the frequency of oscillation; the more rapidly the tabs were oscillated, the greater the "sloshing" of the wake downstream of the wing. This may explain why the net lift produced by the wing increases as the tab frequency is decreased. The wing is able to reach a more stable equilibrium while the frequency is low, but the higher frequencies produce a greater disruption (pressure oscillation) with a resulting decrease in lifting capability of the wing. It is not necessarily the case that one would prefer a large increase in the lifting capabilities over a small one. The associated rise in the lift coefficient with tab application would almost certainly increase the drag signature left behind by the wing as it moves through the air; especially for the case where the tabs are statically extended and so do not induce vortex movement or pressure oscillation of any kind.

Figure 10.23 is a chordwise plot taken at 10° angle of attack and compares the various oscillation frequencies to the statically extended case. One can immediately see a difference between the results shown here and those gathered for the 5° case (Figure 10.22). Looking at the 5° case there is a clear decrease in the C_P value as the frequency of oscillation is slowed; at the higher angle of attack the relative change in C_P for each configuration is markedly less. The statically extended case still produces the greatest drop in pressure over the leading edge but there appears no real lift advantage to be gained from the static extension.

A spanwise plot showing the variation in C_P as the oscillation frequency was varied is given in Figure 10.24 with the wing at a 5° angle of attack. A clear decrease in surface pressure is shown with a corresponding decrease in the frequency of oscillation. This is most clear at tap LE8, nearest which the wingtip vortex core is situated. Also visible is the greater increase in lift or drop in surface pressure created when the tabs are left statically extended.

The pressure tap nearest the wingtip, LE9, gives near identical pressures for the baseline and all oscillation cases. However, there is a noticeable drop off in this pressure point for the statically extended case; that is the pressure gradient ($\frac{dP}{dr}$) is much steeper through the vortex cross-section when the tab is left statically extended. This steep pressure gradient indicates a more powerful vortex shed for the statically extended case which would indicate that the drag in this configuration is the greatest of those tested. This is expected as the pressure drag generated is induced by the lifting force generated by the wing, which has been shown to be the greatest for the statically extended case (Figure 10.22).

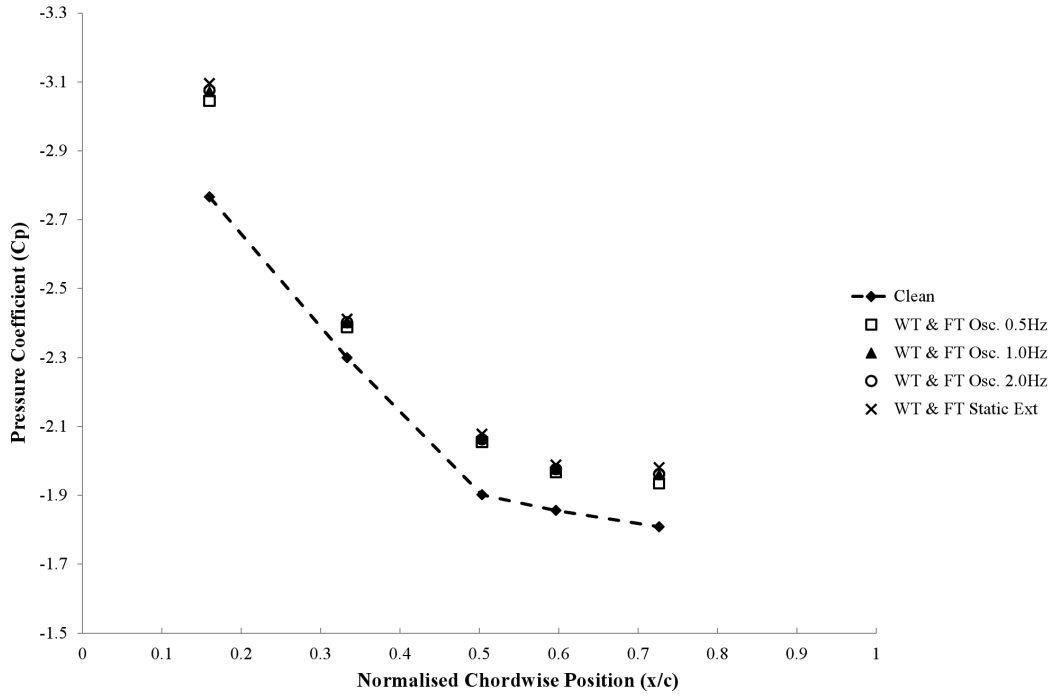


Figure 10.23: Chordwise Pressure Distribution due to Frequency Response. Both Tabs Oscillate, $\alpha = 10°$

Looking at the flow visualisation pictures for these two cases helps to interpret the differing flow dynamics at the two angles of attack. Figure 10.25 is a set of four images, taken with the both tabs oscillating first at 0.5Hz and then at 2.0 Hz for an angle of attack of 5° ((a) and (b)) and 10° ((c) and (d)). The images were captured

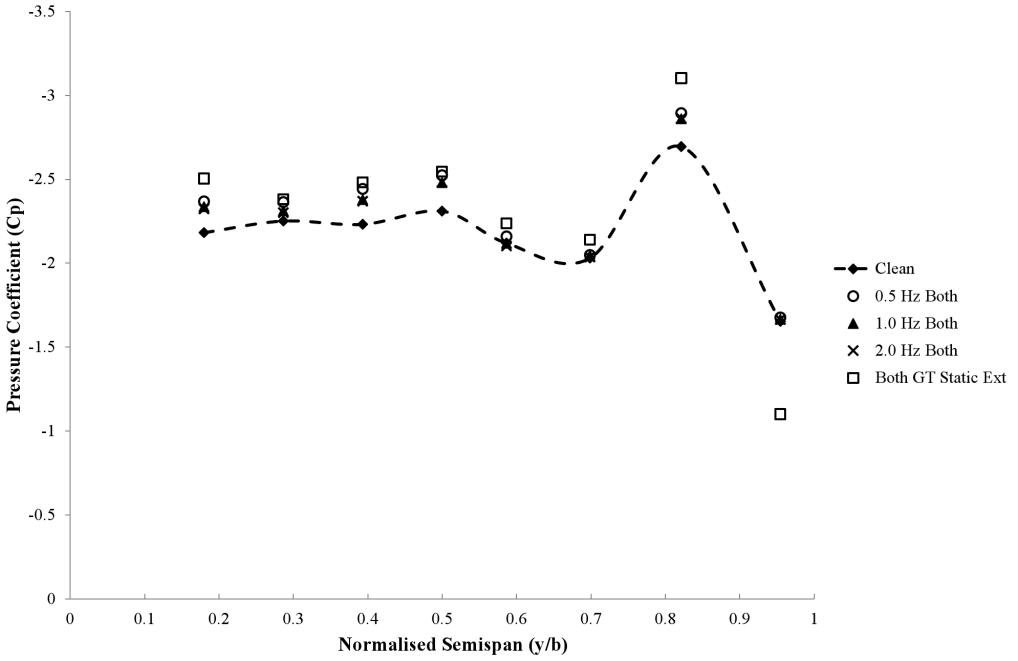
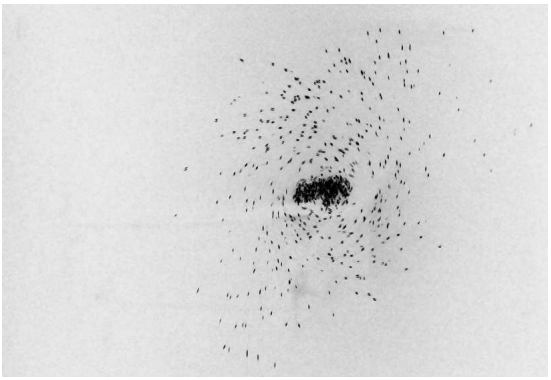


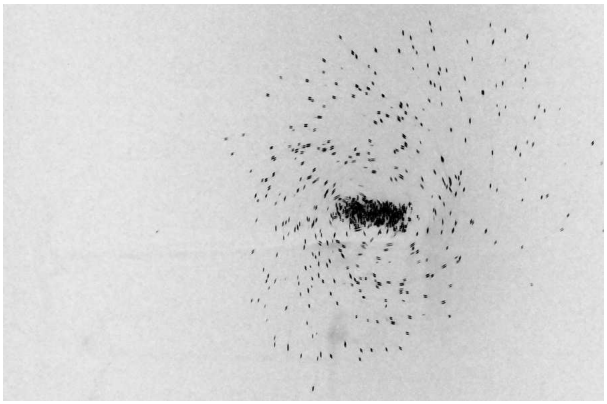
Figure 10.24: Spanwise Pressure Distribution due to Frequency Response. Both Tabs Oscillate, $\alpha = 5°$

at a downstream position of 2.0b, the furthest downstream position tested. The lower angle of attack shows a large elongation of the vortex core for both frequencies tested. However, when oscillating at 2.0 Hz (b) the core appears more elongated and less dense than the 0.5 Hz (a) case. When the angle of attack is increased to 10° , the core appears far more compacted for both oscillation frequencies, showing less tendency for dispersion. It is thus noted that the angle of attack of the wing has a crucial influence on both the lift produced at the various frequencies (pressure plots) and the tendency for the oscillating tabs to introduce instabilities into the near wake (seen from the flow visualisation).

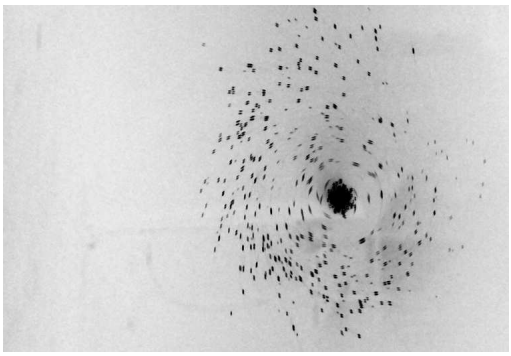
After investigating both the transient response and averaged pressure results obtained by varying the tab oscillation frequency, it was concluded that a frequency of 2.0 Hz is most effective of those tested to introduce instabilities into the near wake. However, it was shown that oscillating the tabs at 0.5 Hz and 1.0 Hz also produced instabilities. The largest dispersion of the vortex core was seen at 5° angle of attack. Higher angles of attack tended to concentrate the vortex core, specifically when looking at the core at the furthest downstream position tested (2.0b) as seen in Figure 10.25. A tab oscillation frequency of 2.0Hz was thus used in subsequent tests to determine the effect that differing tab oscillation schemes had on the ability to induce early vortex breakup.



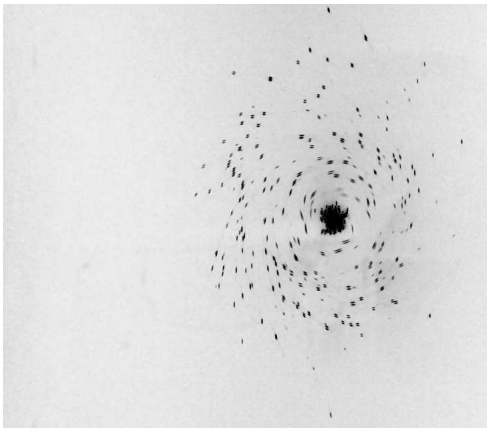
(a) $\alpha = 5^\circ$, $2.0b, 0.5HzOscillation$



(b) $\alpha = 5^\circ$, $2.0b, 2.0HzOscillation$



(c) $\alpha = 10^\circ$, $2.0b, 0.5HzOscillation$



(d) $\alpha = 10^\circ$, $2.0b, 2.0HzOscillation$

Figure 10.25: Vortex Extent and Core Properties at Differing Frequencies of Oscillation, 2.0b

10.4.3 Oscillation Scheme Variation

Tests were conducted at four angles of attack; 0, 5, 10, and 15° to ascertain the effectiveness of the various tab oscillation schemes in imparting the necessary vorticity into the near wake to disrupt the resulting vortex. Upper surface pressure plots provide an insight into the effect that oscillating the tabs have on the wing and were used in conjunction with flow visualisation results to model the flow properties of the wing.

Figure 10.26 is a mid-span chordwise plot of the wing at 5° at the three tab oscillation schemes. Figure 10.27 is the same plot but with the wing at 10° angle of attack. Refer to Table 10.2 for the nomenclature used to describe the three oscillation schemes considered.

As expected, all three schemes have an influence on the pressure and thus the chordwise lift distribution produced by the wing. In the same way that increasing the

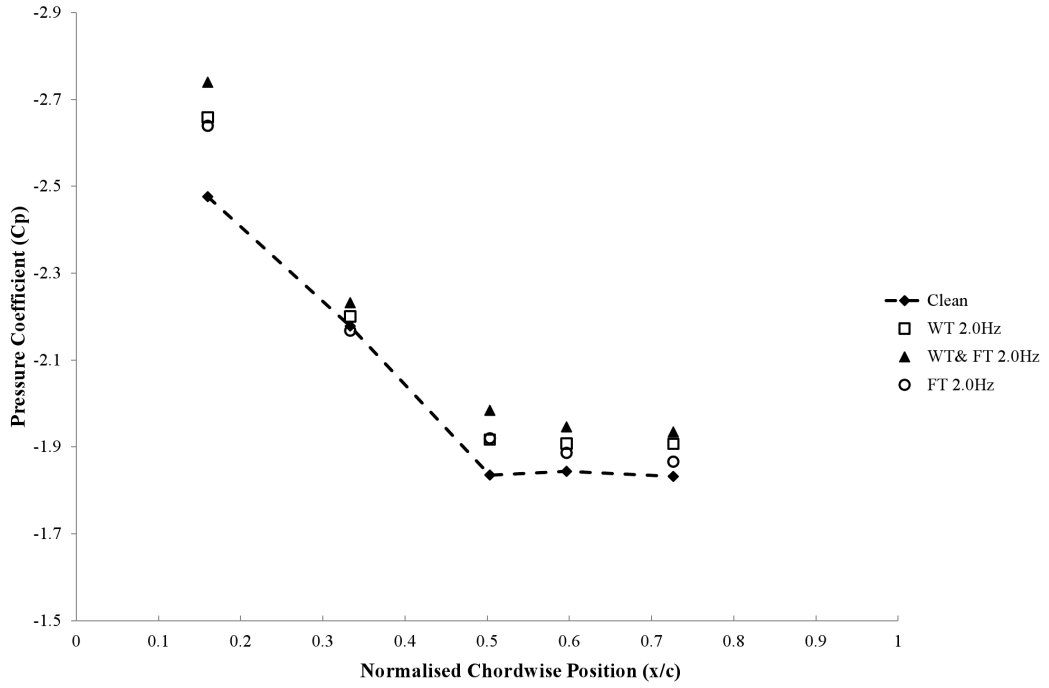


Figure 10.26: Chordwise Pressure Distribution, Various Oscillation Schemes, $\alpha = 5°$

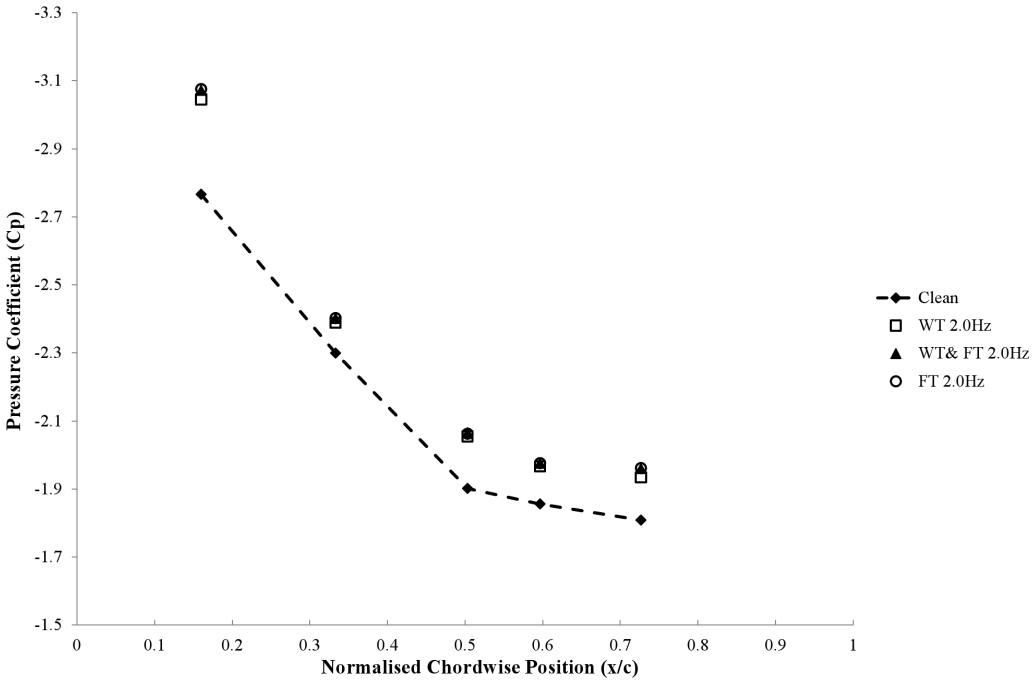


Figure 10.27: Chordwise Pressure Distribution, Various Oscillation Schemes, $\alpha = 10°$

angle of attack of the baseline configuration had the largest effect on the leading edge portion of the wing, the same is shown true when oscillating the tabs. Extending

the tabs has been shown to increase the effective camber of the wing, which in turn increases the lift produced by the wing and hence the circulation at a given angle of attack. While the pressure gradients are greatest at the leading edge tap (FT5), the trend of sharper pressure drops (increasing $|C_P|$) with tab oscillation is evident at all points along the chord.

In both Figure 10.26 and 10.27, the ability of the various schemes to influence the total lift that the wing produces is roughly the same. The most effective scheme is one where both tabs are oscillated. Next most effective is the scheme where only the wingtip (WT) tab is oscillated. And the least effective in producing additional lift is the case where only the flaptip (FT) tab is oscillated. This is an entirely intuitive result; extending both tabs into the free stream will increase the effective camber of the wing over the largest span, and oscillating the wingtip tab will have a marked effect at the wingtip, where effective span is being "lost" as the wingtip vortex sheds inboard of the tip as demonstrated in Figure 10.8. It is also interesting to consider that oscillating the wingtip tab has a greater effect on the pressure distribution at the leading edge of the Flap Tip set of pressure taps than the FT tab which is located immediately downstream of the FT set of taps. This demonstrates the dominance of the wingtip vortex on the lifting properties of the wing. The amount by which the pressure coefficient changes at the tap nearest the leading edge when both tabs are oscillated is of the same order regardless of the angle of attack. The changing C_P with Angle of Attack appears in Table 10.5.

Table 10.5: Change in C_P value at FT5 due to Oscillating Both Gurney Tabs, 2.0 Hz

Angle of Attack (°)	$\Delta CP(FT5)$
5	0.265
10	0.214
15	0.224

Figure 10.28 and Figure 10.29 are spanwise plots with oscillations at 2.0 Hz at an angle of attack of 5° and 15° respectively. As with the chord plots presented above, a vertical shift in the C_P value corresponding to a drop in pressure is noted for all configurations with the largest drop in pressure (largest lifting force) being attributed to the WT & FT simultaneous oscillation scheme. The same trend in the relative magnitudes of the pressure displacements is also noted where the most effective scheme consists of both tabs oscillating and the least effective scheme where only the FT tab is oscillated. Here though the differences between the displacements caused by the different schemes is smaller than those measured along the chord.

There is a clear peak in C_P at tap LE8 corresponding to the position of the wingtip vortex core being shed near the wingtip. In this case where both tabs are oscillating the pressure is at the lowest, which implies that the vortex core is at its strongest in this configuration. It should be noted that the resolution of the pressure taps is not sufficient to conclusively state that the scheme where both tabs oscillate produces the largest or strongest vortex based on the pressure data alone. It is possible that the pressure peaks in one of the areas adjacent LE8 before dropping to the values recorded at LE7 and LE9 for any of the schemes tested. These spanwise plots do not allow for one to make any comment on the motion of the vortex core as the tabs are oscillated; only what the time averaged response to the oscillation scheme does to the lifting properties of the wing. It should also be noted that these plots are for the upper surface of the wing only and do not take into account the lower surface response to the tab oscillation.

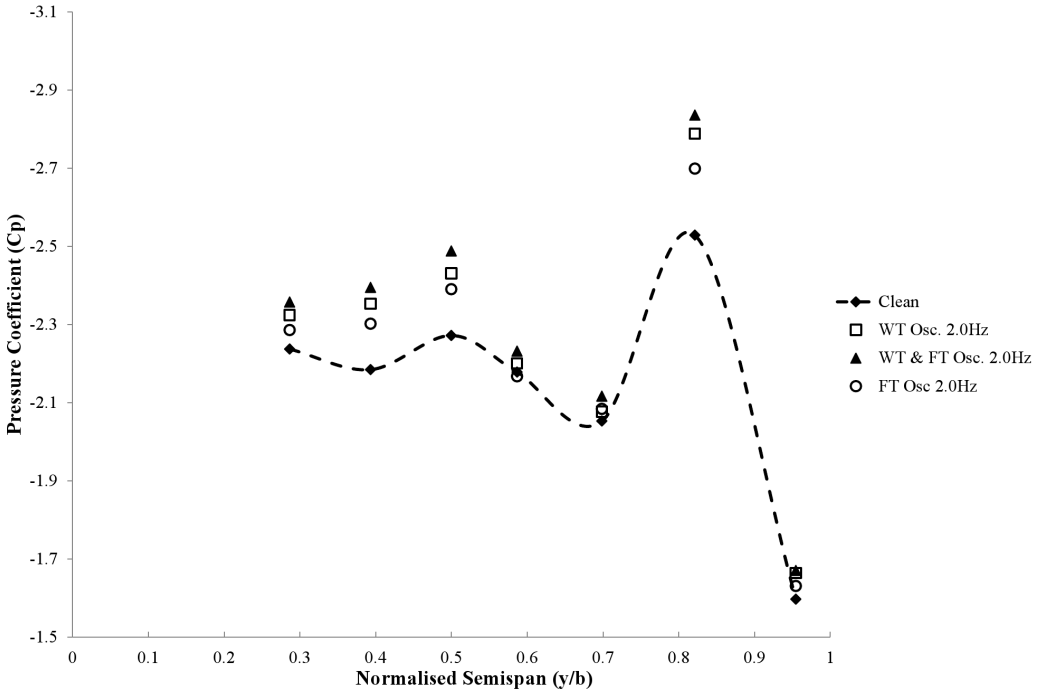


Figure 10.28: Spanwise Pressure Distribution, Various Oscillation Schemes, $\alpha = 5°$

Figure 10.30 allows for a comparison to be made between the 5° and 15° case in both the clean configuration and the configuration where both tabs are oscillated at 2.0 Hz. In both cases the oscillation of the tabs offset the C_P values by a near equal amount at each pressure tap. This would suggest that the shape of the spanwise loading distribution is not significantly affected by the addition of the tab but that the lifting capacity of the wing would increase as the tab causes lower pressures over the upper surface of the wingtip. The pressure tap LE8, situated in the vortex

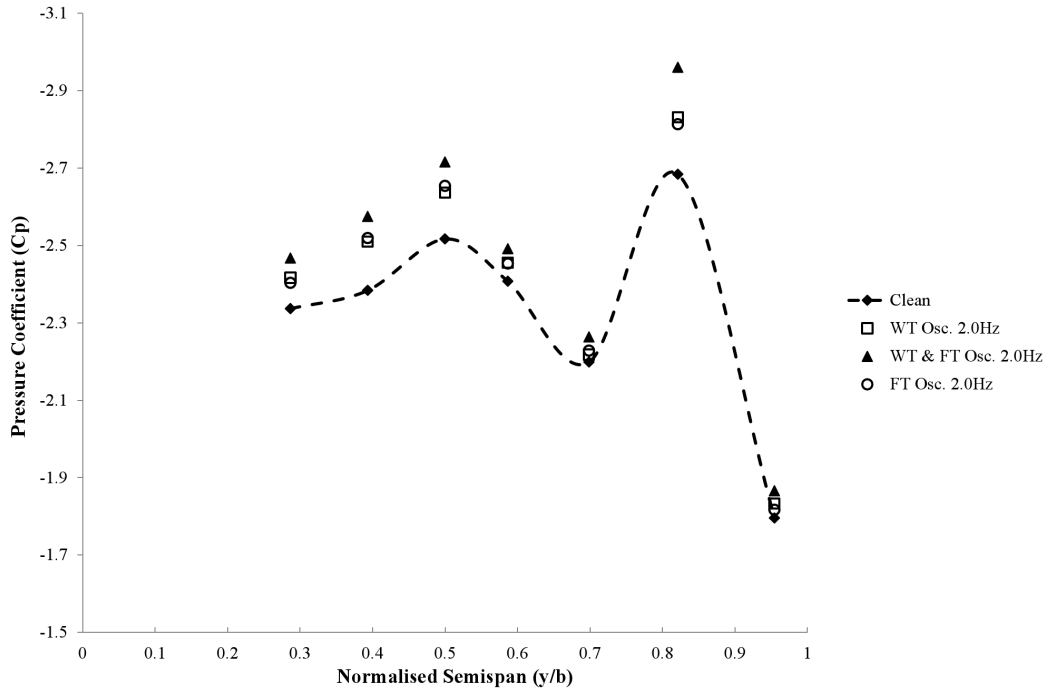


Figure 10.29: Spanwise Pressure Distribution, Various Oscillation Schemes, $\alpha = 15°$

shedding region of the wing is particularly interesting as the plot shows that the addition of the tab oscillation at 5° induces a greater drop in the pressure at that point than merely increasing the wing angle of attack to 15° .

Images of the resulting vortex shed as the various oscillation schemes were tested give a physical description to the flow fields which are set up. Photographs were captured for the three cross-section positions, 0.37b, 1.0b, and 2.0b and at angles of attack of 0, 5, 10, and 15° . Each tab was first oscillated independently and then simultaneously at frequencies of 0.5, 1.0, and 2.0 Hz. A complete set of images were taken with the trailing edge flap in the retracted position as well as extended into the freestream at an angle of 30° . Photographs were taken at two exposure times, 5 and 10 seconds. In all, approximately 460 photographs were taken and processed to ascertain the behaviour of the wake as it is subjected to tab oscillation. A typical data set and the results where the greatest vortex motion was observed is presented here. Additional cases and images appear on the electronic Appendix that accompanies this report if further study into a particular case is desired.

Movement of the Vortex Core

By studying the photographs taken and comparing these to the surface pressure plots obtained, patterns emerge as to how the wake moves as it is subjected to the

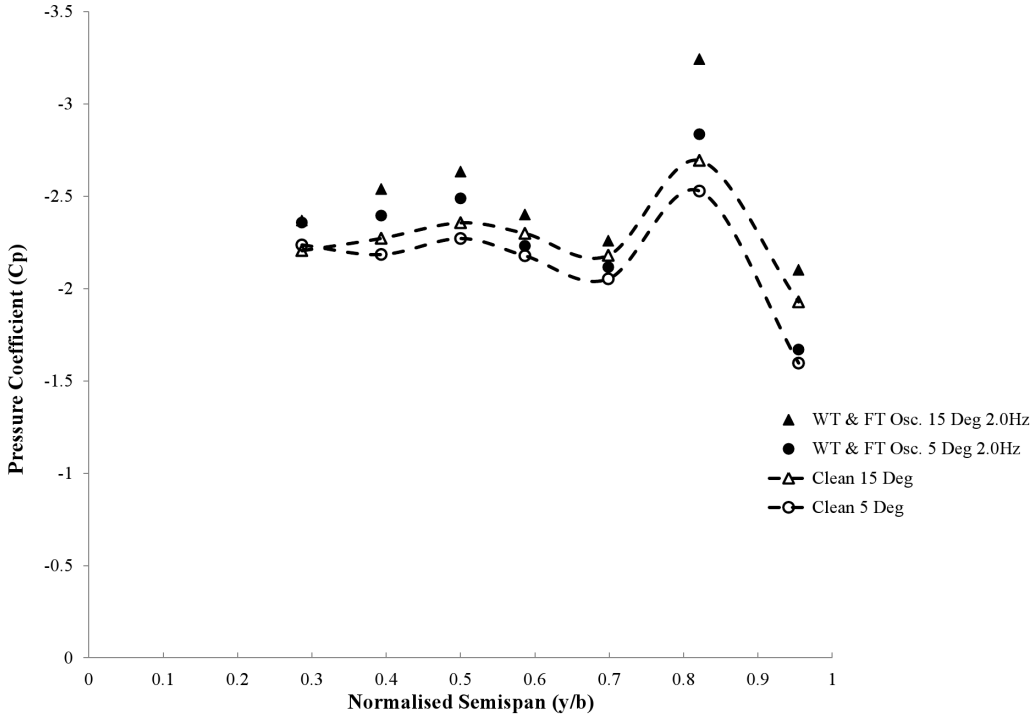


Figure 10.30: Spanwise Pressure Comparison, WT & FT 2.0 Hz Oscillation Schemes, $\alpha =$ 5 and 15°

various oscillation schemes tested. The easiest way to plot the movement of the vortex is to look at how the core moves. As the core moves, so the extents of the vortex move with it. Figure 10.31 shows the vortex core at a downstream position of 1.0b with the wing at an angle of attack of 15° . The labels (a) - (d) refer to the configurations shown below.

(a) Clean Configuration
(b) WT Tab Oscillated
(c) FT Tab Oscillated
(d) WT & FT Tabs Oscillated

Figure 10.31 (a) shows the wingtip vortex in a clean configuration. The elongation of the core arises from the fact that the wing is close to the stall angle and thus experiences a fair amount of buffeting. The position of the core relative to the wingtip is made clearer with a black line drawn along the chord of the wingtip during post processing. In (b) the wingtip tab is being oscillated in a sinusoidal manner at 2.0 Hz. There is a clear motion of the core down and across towards the wingtip in this configuration. The numbers 1 and 2 on each photograph refer to the core position when the tab is in its retracted and fully extended position

respectively. This vertical and spanwise shift is shown to occur for all cases where the wingtip tab is oscillated. The tab in the extended position increases the camber of the wing, increasing the total lift produced and subsequently shifts the vortex core downwards and further outboard. This is confirmed by the pressure data presented above (Refer to Figure 10.8 and Figures 10.26 and 10.27).

Liebeck [32] showed that a Gurney tab in the order of 1.25% chord length both increases the lift produced by the wing while simultaneously increasing the overall aerodynamic efficiency. While the tabs tested in this body of work are large and produce a significant increase in drag, the movement of the vortex core toward the wingtip suggests that one of the reasons for the reduction in lift induced drag as described by Liebeck [32] may be the increase in the Oswald Efficiency Term 'e' seen when examining the classic induced drag formula (eqn 1.8). Increasing this term has the effect of increasing the effective aspect ratio of the wing, and with it a corresponding drop in induced drag is seen.

Figure 10.31 (c) shows the effect on the core of oscillating only the flap tip tab. It is shown here, and reinforced by additional images found in the electronic Appendix, that oscillation of the flap tip tab has the effect of drawing the vortex core inboard in a spanwise direction towards itself. The effect is not as pronounced as is the case for pure wingtip tab oscillation; the wingtip tab is consistently shown to have the largest effect on the flow properties of the wing, both in flow visualisation and pressure measurements (Figures 10.26 and 10.27)

Thus it is not unexpected that case (d) (WT & FT Oscillation) is a superposition of the two cases described above with precedence of the overall core movement taken by the WT tab. The spanwise movement inboard caused by the FT tab is seen in (d) by the pulling down of the core away from the wingtip. Thus the vortex core extent moves further away from the wingtip when compared to the oscillation of only the WT tab.

Figure 10.32 is a plot of the relative motion of the core for each of the four oscillation schemes discussed. The co-ordinate $(0, 0)$ refers to the centre of the core in the clean configuration. The extents of each core were taken off the original photographs shown in Figure 10.31 and non-dimensionalised with respect to the wing chord. This comparison clearly demonstrates the effect of both tabs on the resultant movement of the core as well as the relative importance of the WT tab over the FT in causing a shift in the vortex core. The largest spanwise movement occurs when only the WT tab is oscillated. Oscillation of both tabs in conjunction causes a decrease the overall extents of the vortex core and confines the motion to a smaller area. The

motion of the vortex core can also be related to the force changes on the wing during oscillation. A downward movement of the core as the tab extends occurs as a result of the increased circulation due to the additional camber the tab affords. Motions toward the wingtip indicate an increase in the effective wingspan and a corresponding reduction in induced drag.

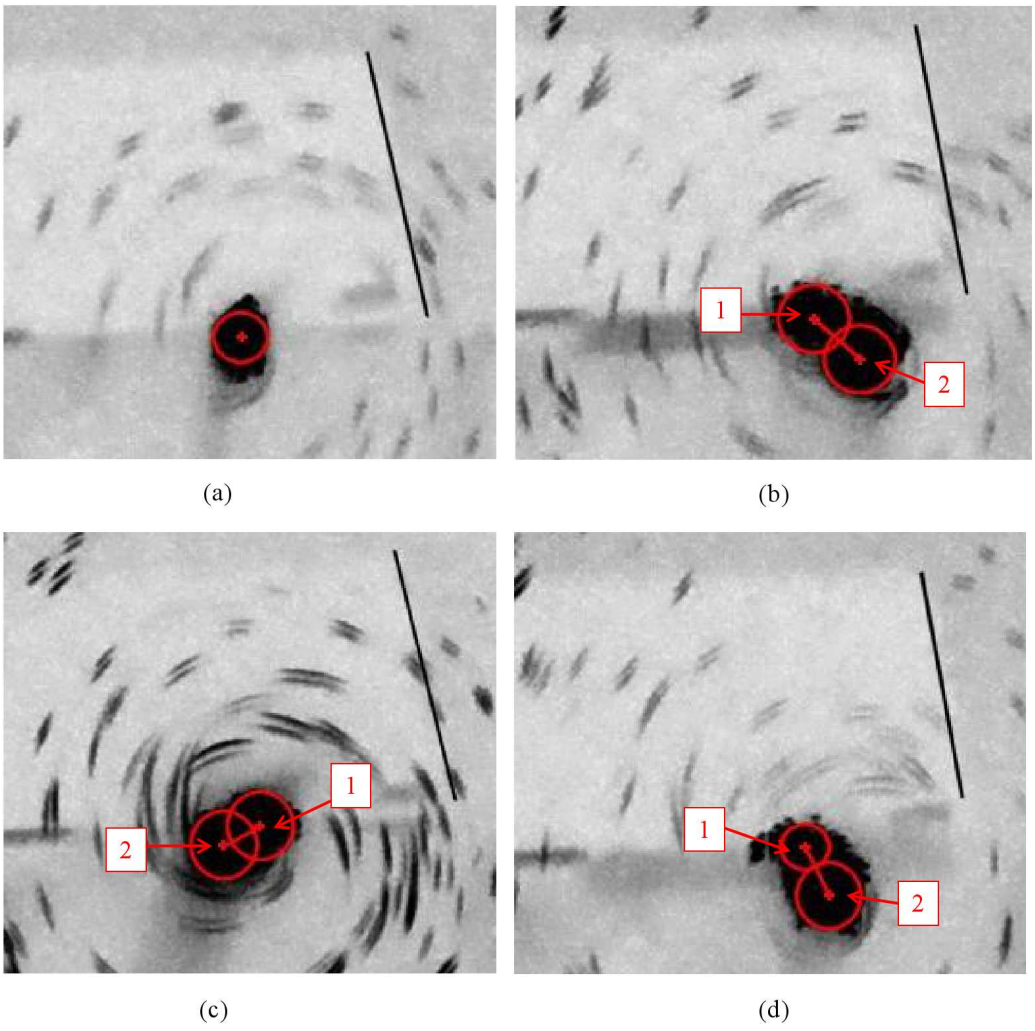


Figure 10.31: Vortex Core and Movement, $\alpha = 15°$, 1.0b

Continuing with the investigation of the movement of the vortex core, Figure 10.33 shows the core at a downstream position of 2.0*b*. The test configuration is identical to that discussed above (Figure 10.31). For the clean case (a), the core is well defined, and densely packed in a near circular cross-section.

(c) and (d) show the identical motions as described upstream at 1.0*b* albeit with more dispersion in the vortex core at this downstream position. This is a crucial result; breakup in the vortex core is really only visible from the 2.0*b* position. As

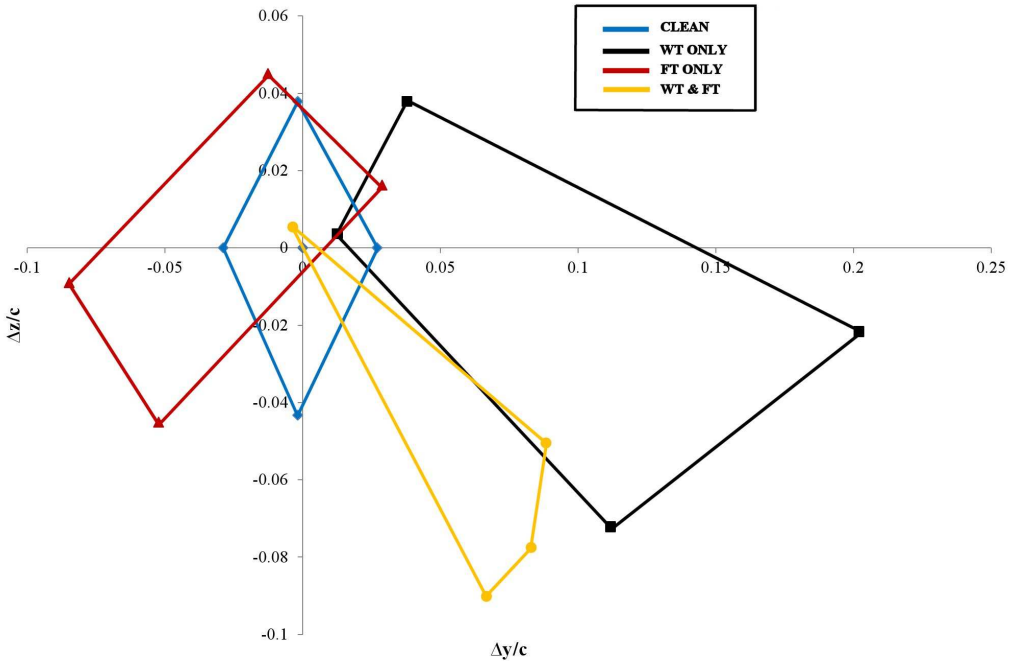


Figure 10.32: Normalised Core Movement, $\alpha = 15°$, b:1.0

the core propagates downstream, the instabilities induced by the motion of the tabs result in a more chaotic motion of the core with greater movement and subsequent dispersion clearly visible.

Relating this result back to the spanwise pressure plot in Figure 10.29, the largest drop in pressure at LE8 (vortex shedding region) occurs for the case where both tabs are oscillated. This would indicate that on the wing upper surface, the strongest vortex core is formed in this configuration. However, as the core propagates downstream away from the trailing edge, the addition of vorticity into the wake from the flap and wing tip serves increase the dispersion of the vortex core as seen by the images presented in Figure 10.33. The case where both the wingtip and flap tip tabs oscillate in unison is seen as the scheme that offers the most potential in inducing early vortex breakup.

The pressure changes over the wing due to the synchronous oscillation of both tabs is sufficient to drastically alter the lifting properties of the wing. Figure 10.34 plots the chordwise distribution of the wing at three different configurations; the clean wing at 5 and 10° angle of attack, and the wing at 5° with both tabs oscillating at 2.0 Hz. The peak pressure points at the tap closest to the leading edge (FT5) differ by less than 1% between the 10° clean data and the 5° oscillation case presented here, while the tap at 0.3c (FT4) also shows a close correlation of data with the C_P

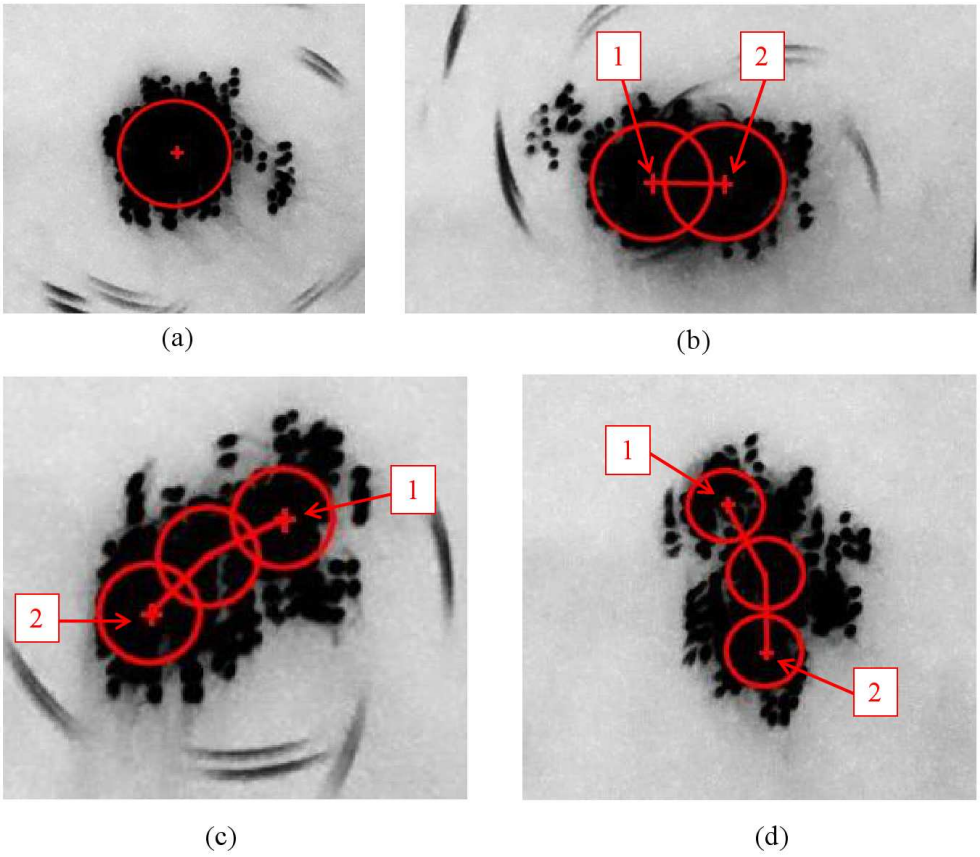


Figure 10.33: Vortex Core and Movement, $\alpha = 15°$, 2.0b

at 10° only slightly more negative than the 5° oscillation case. Interesting to note is the elevation of the 5° data above that at 10° for the three taps closest to the trailing edge (FT1-3). Oscillating both tabs results in an increase in the effective camber of the wing resulting in a vertical shift in C_P on the graph. This shift is greater at FT1 through 3 than the corresponding shift at those taps as the angle of attack is increased from 5 to 10° for the baseline case depicted in Figure 10.34.

Results at $\alpha = 5°$

The analysis undertaken above is now extended to a case where the vortex shed off the wingtip is less severe, at a 5° angle of attack. This is a typical configuration for an aircraft on approach to land and as such the vortex behaviour at this attitude is of interest. The analysis begins with Figure 10.35 which shows the resulting vortex at 0.37b for the three oscillating cases at 2.0Hz. The images were photographed consecutively with the bubble mixture held constant such that a clear insight into the vortex response could be ascertained. The immediate observation made is the

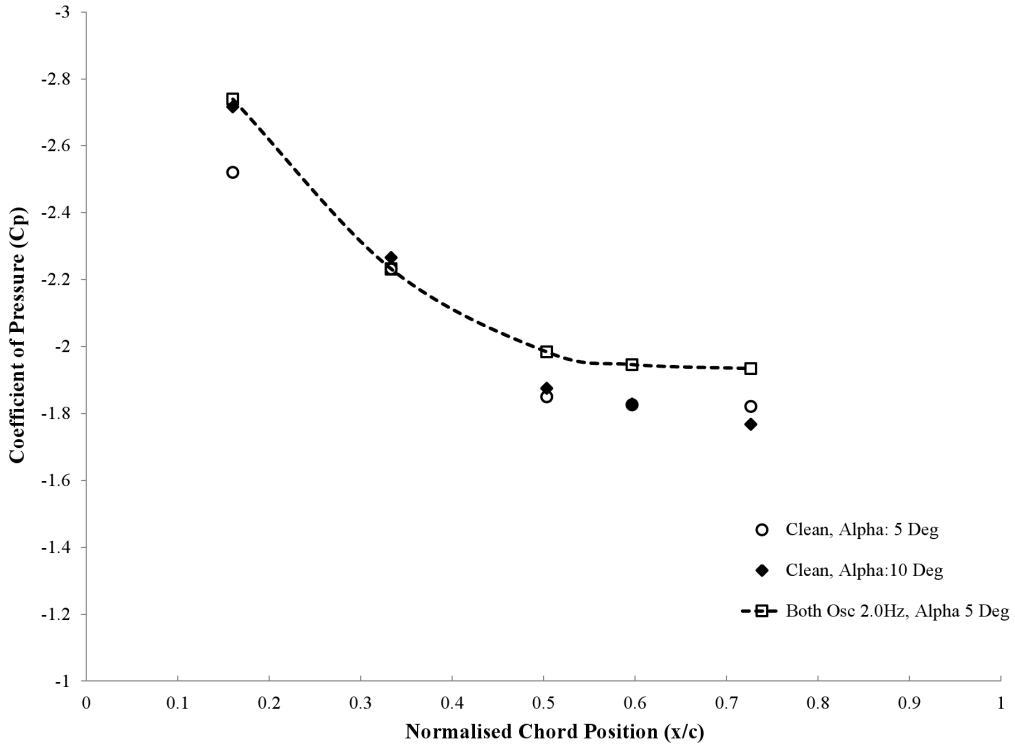


Figure 10.34: Effect of Oscillating Both Tabs on ΔC_P

difference in the vortex extents and dispersion between the clean case and those where the tabs are oscillated. The clean vortex is far tighter, and more densely packed, indicating regions of higher tangential velocity. Figure 10.35 (b) and (c) provide another confirmation of the effect that the FT tab has on the movement of the vortex core; forcing the core downward and away from the wingtip.

Figure 10.36 shows the vortex further downstream at 1.0b. The images shown depict the wingtip tab oscillating (a) and both tabs oscillating (b). For the case where both tabs are oscillating, the cores form two distinct regions rather than a locus as the core moves. This is not the case where the frequency of oscillation is lower. The cores are also noticeably smaller, with greater dispersion throughout the vortex extent. The only difference between the two configurations is the oscillation of the flap tip tab. Thus the conclusion has to be drawn that the motion of the flap tip tab produces an interaction with the wingtip vortex which increases the dispersion within the vortex field and reduces the size of the vortex core. While it is difficult to quantify the extent of the interaction, it is very apparent that interaction does occur.

To show that this result is not just a product of a fluctuation in the bubble stream produced, Figure 10.37 is presented for the same two cases but with the trailing edge

flap extended 30° from the chordline into the free stream. Here again, the effect of oscillation of the FT tab is clearly demonstrated. A larger core and a denser rotating mass of air is shown for the case where only the wingtip is oscillated, as opposed to two distinct vortex cores, and greater dispersion within the vortex when both tabs are oscillated.

Decreasing the frequency of oscillation of the tabs reduces the effectiveness of the tabs in dispersing the resulting wingtip vortex as seen in Figure 10.38. The 0.5 Hz oscillation case is less effective than the 1.0 Hz case which in turn is less effective than oscillation at 2.0 Hz. In all the cases where the trailing edge flap is extended to 30° , the vortex core and associated vortex extents are larger than when the flap is retracted. This gives a physical interpretation of the greater lifting force, increased circulation, and corresponding drag increase produced by the wing when the flap is extended.

The shape and density of the vortex core offers good insight into the effectiveness of the various oscillation schemes in introducing instabilities into the proceeding wake. Examining the results of oscillation scheme and frequency at 2.0b where the wake is furthest progressed confirms the effectiveness of the wingtip tab in inducing vortex instability.

Figure 10.39 and Figure 10.40 plot the vortex core at the various oscillation schemes for the cases where the trailing edge flap is retracted and extended to 30° respectively. Immediately apparent is the large effect the wingtip tab has on the resulting core shape and extent. A near horizontal motion is induced in the resulting core as the wingtip tab is oscillated. This is compared to the core movement further upstream, where movement is still toward the wingtip but vertically downward as well. Figure 10.35 (b) shows the wing in the same configuration at 0.37b where only the WT tab is oscillated at 2.0 Hz. The resulting core motion is primarily vertical as the core is pulled down by the increase in downwash that the tab provides. The transition from primarily vertical movement close to the wing to horizontal displacements as one moves further downstream can be explained by both the reduction in circulation as the wake progresses downstream (increased circulation pulls the vortex core downward) and the tenancy for the wingtip tab to push the vortex core further outboard (introduced instabilities into the near wake reducing induced drag).

The effect of oscillating the FT tab in conjunction with the WT tab is markedly different at 2.0b to that at 1.0b. At 1.0b, the addition of the FT tab noticeably reduces the size of the resulting core as evidenced in Figure 10.36 as well as increasing the dispersion of the vortex extents. However, at 2.0b, the resulting core shows the

largest evidence of breakup and dispersion for the case where only the WT tab is oscillated. This is shown to be true for both the case with the trailing edge flap retracted and that where it is extended (Figures 10.39 and 10.40 respectively). It has been discussed previously how the flap extension increases the size and extents of the vortex as the lifting potential of the wing is increased. Thus it is noted here that the dispersion of the core is more pronounced for the case where the trailing edge flap is retracted.

For the case where both tabs are oscillated the core appears to remain more densely packed, although there is still a far greater distortion of the core than in the clean configuration. There is evidence in both cores of a sinusoidal core motion consistent with the sinusoidal oscillation scheme imparted on the tabs. Figure 10.41 plots the cores with both tabs oscillating at the two trailing edge flap configurations. The sinusoidal motion of the core has been indicated by a red line and was determined by looking at the areas of the core where the bubble density is the greatest.

10.5 Summary of Discussion

Surface pressure tests and flow visualisation of the near wake shed by the rectangular NACA 0012 semispan model were conducted in a bid to characterise the flow and lifting properties upon oscillation of the two trailing edge tabs affixed to to the wingtip and flap tip of the model.

Baseline Tests

Chordwise pressure distributions obtained using the calibrated pressure sensors were shown to correspond to those obtained by Gregory [37] (see Figures 10.1 and 10.2). This baseline set of tests were used to validate the accuracy of the sensors and establish a baseline set of data from which the effect of oscillating the two tabs could be ascertained. The net pressure distribution for the wing in a clean configuration matched published data with the leading edge providing the largest contributor to the total lifting force produced by the wing. Accurate lifting data by integration of the chordwise pressure variation at the various angles of attack could not be obtained due to insufficient resolution of the pressure distribution at the leading edge. The chordwise static pressure drops significantly as the leading edge is approached. Without a sufficiently fine resolution between taps, the lifting coefficient predicted would be substantially lower than the actual value. Spanwise pressure plots of the wing in a clean configuration clearly showed the influence of the vortex shed at the

wingtip as a drop in the local static pressure with the largest drop corresponding to the position of the vortex core. This was backed up by the flow visualisation images obtained for the baseline case in Figure 10.11.

The vortex radius extent was shown to increase linearly with increasing angle of attack when observing the resulting vortex cross-section at a constant downstream position (Figure 10.12). Degradation of the vortex circulation as the wake propagated downstream was shown qualitatively by analysis of the photographs captured. This was seen both in the density of the streamlines in the vortex as well as the physical dimensions of the wake extents. Static extension of the tabs in all schemes were shown not to be effective in introducing the instabilities necessary to affect vortex breakup, but did show the largest increase in the lifting capability of the test wing as the effective camber of the wing was the greatest with the tabs statically extended.

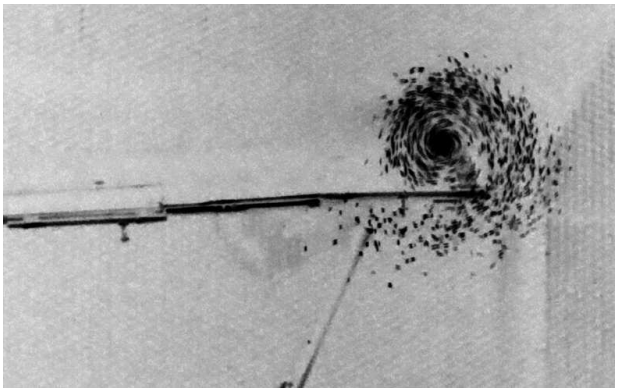
Tab Oscillation and Associated Vortex Break-up

The two tabs affixed to the wingtip and flap tip trailing edge of the test wing were oscillated at frequencies of 0.5, 1.0, and 2.0 Hz in a bid to introduce instabilities into the near wake by a point introduction of vorticity. An oscillation frequency of 2.0 Hz was shown to be the most effective in introducing instabilities into the wake, evidenced primarily by the flow visualisation images of the resulting vortex formed downstream of the wing. A frequency analysis of the transient pressure response showed a clear pressure oscillation of frequency twice the tab oscillation frequency, thought to be a driver in the introduction of instabilities into the near wake. Oscillation of the tabs were shown to introduce movement of the vortex core and associated vortex extents. The movement of the core was not random, but clearly observed for the various oscillation schemes tested.

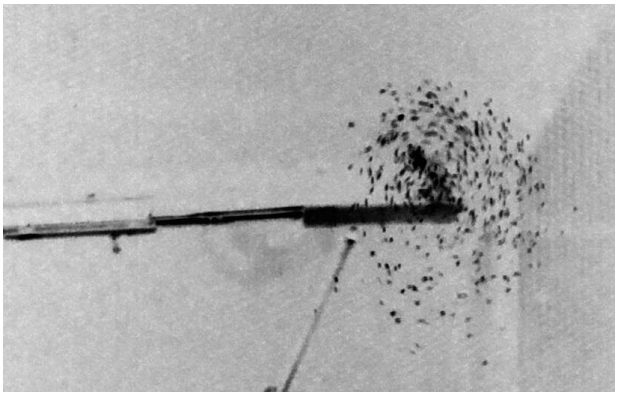
In all cases where tabs were oscillated, extension of the tab towards the high pressure side of the airfoil caused the resulting vortex core to move towards that oscillating tab. The Wingtip tab was shown to dominate the resulting motion of the vortex core when both tabs were oscillated together, and the resulting core movement when both tabs were oscillated simultaneously was shown to be a superposition of the motions of the core under independent oscillation of the individual tabs.

Break-up in the vortex core was not seen before the 2.0b downstream position. Thus the beginning stages of vortex break-up is said to occur between 1.0b and 2.0b. As the wake propagates downstream,the instabilities induced by the motion of the tabs result in a greater movement of the core with dispersion clearly visible. A clear

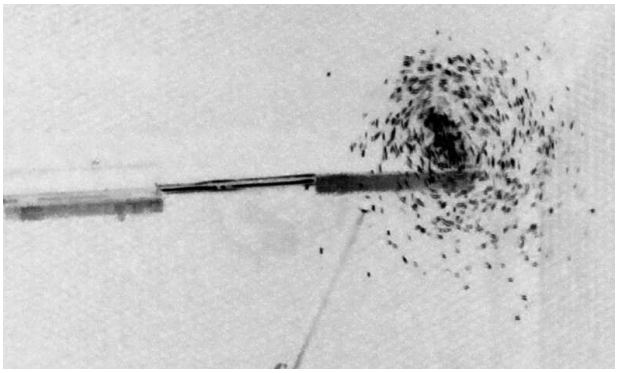
reduction of the resultant wake core and vortex extents at 1.0b were noted for the case of the Wingtip and Flap Tip Tabs oscillating at 2.0 Hz in a synchronous scheme. Thus it is said that the motion of the Flap Tip Tab produces an interaction with the Wingtip vortex which increases the dispersion within the vortex field and reduces the size of the vortex core.



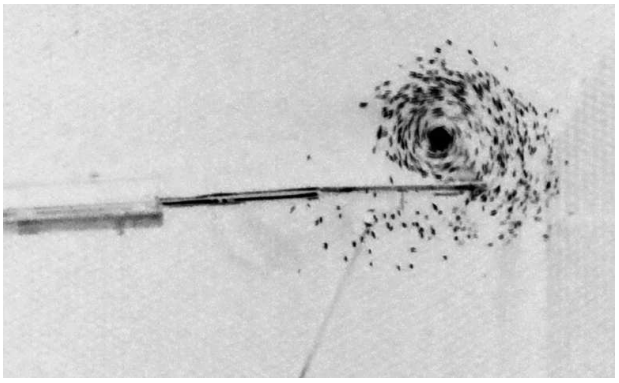
(a) Resultant Vortex Clean Configuration



(b) Resultant Vortex Wingtip Tab Oscillate 2.0 Hz

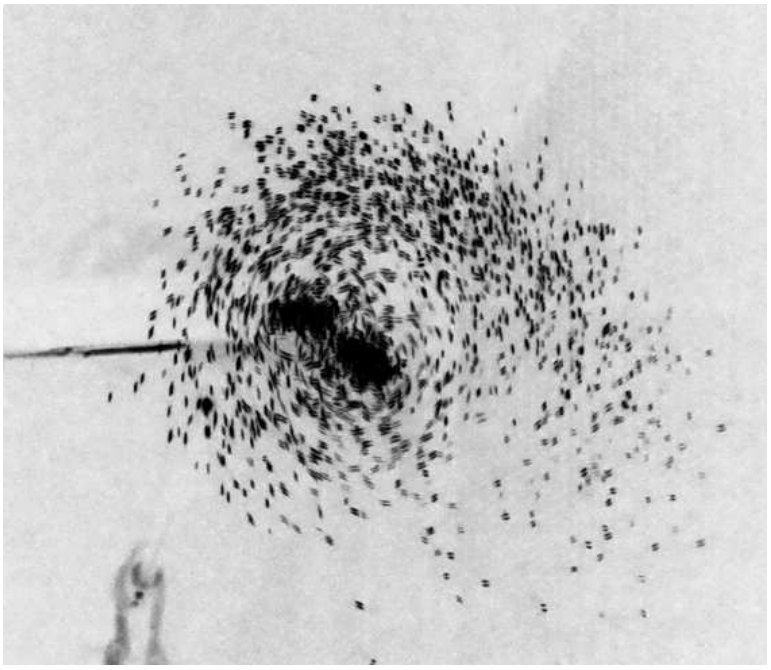


(c) Resultant Vortex Both Tabs Oscillate 2.0 Hz

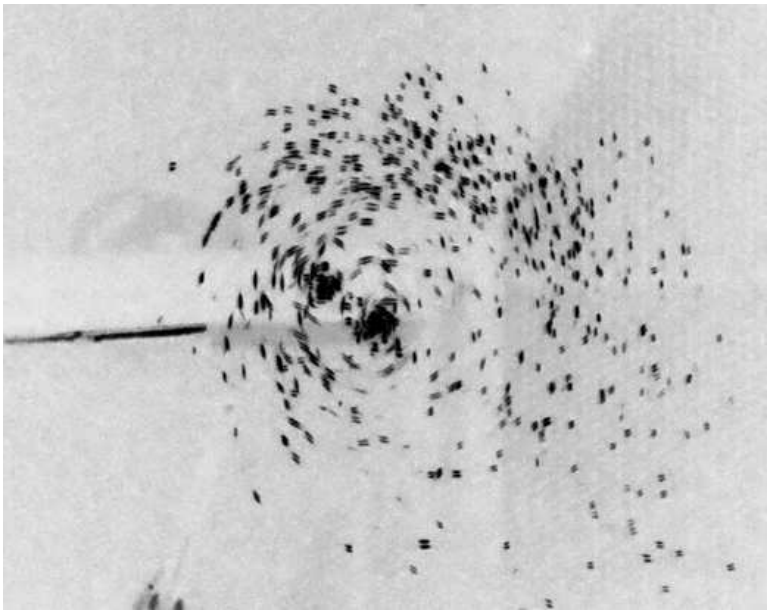


(d) Resultant Vortex Flap Tip Tab Oscillate 2.0 Hz

Figure 10.35: Vortex Core Comparison; $\alpha = 5°$, 0.37b

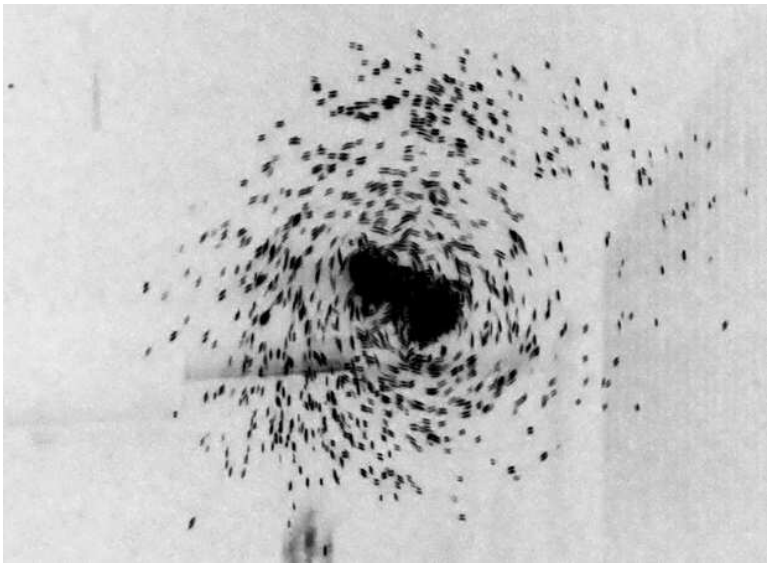


(a) Vortex Close-up, Wingtip Tab Oscillate 2.0 Hz

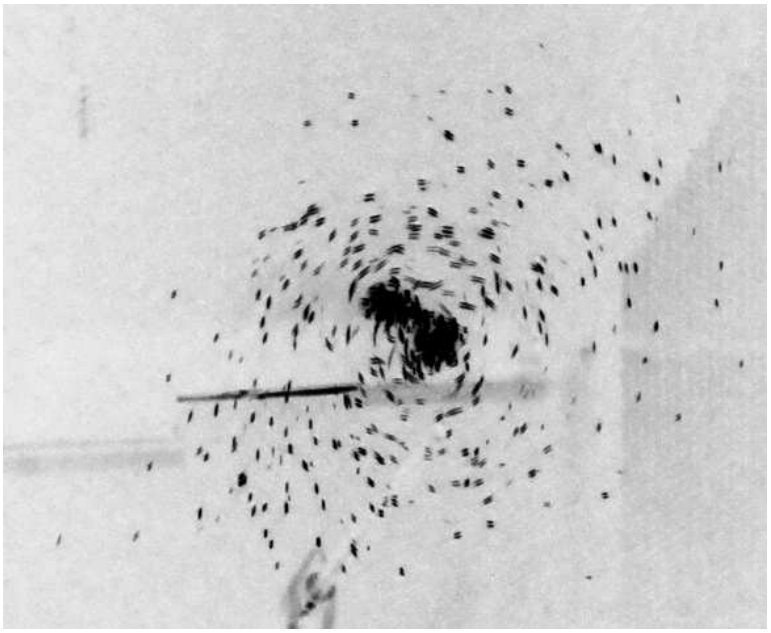


(b) Vortex Close-up, Both Tabs Oscillate 2.0 Hz

Figure 10.36: Vortex Core Comparison; $\alpha = 5^\circ$, 1.0b

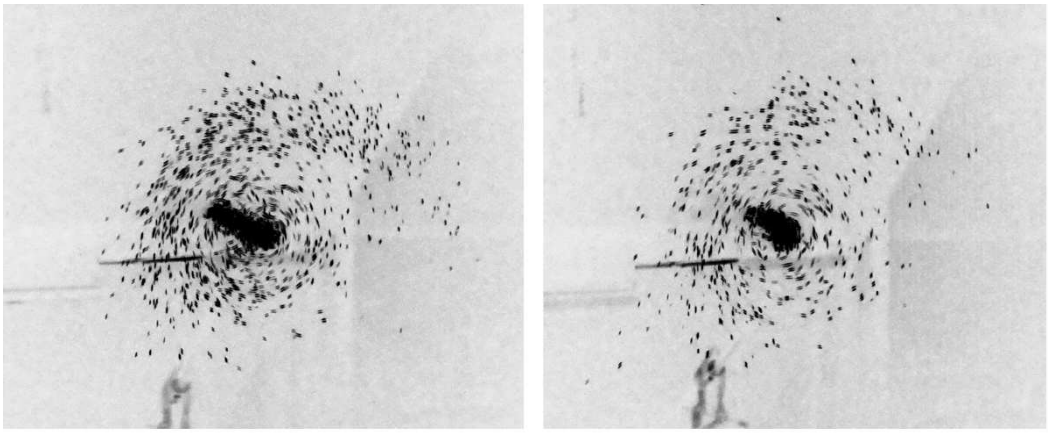


(a) Vortex Close-up, Wingtip Tab Oscillate 2.0 Hz, Flap: 30°

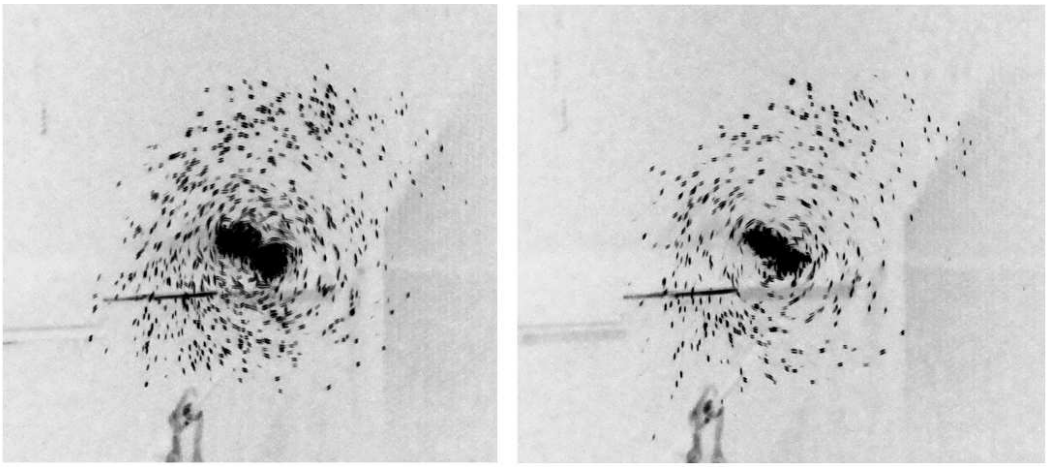


(b) Vortex Close-up, Both Tabs Oscillate 2.0 Hz, Flap: 30°

Figure 10.37: Vortex Core Comparison; $\alpha = 5°$, 1.0b, Flap: 30°

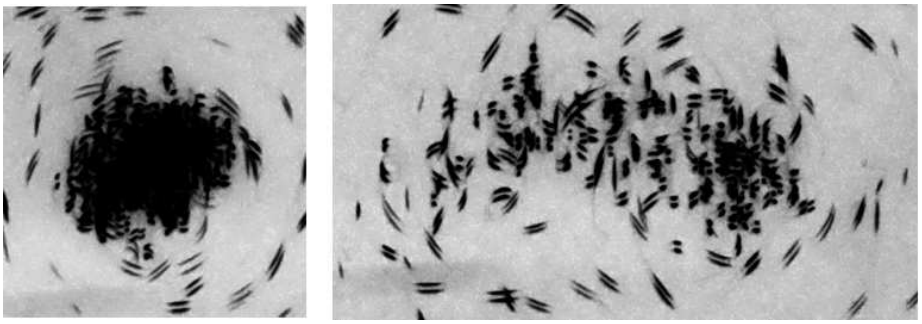


(a) WT Tab Oscillate 0.5 Hz (L) Both Tabs Oscillate 0.5 Hz (R)

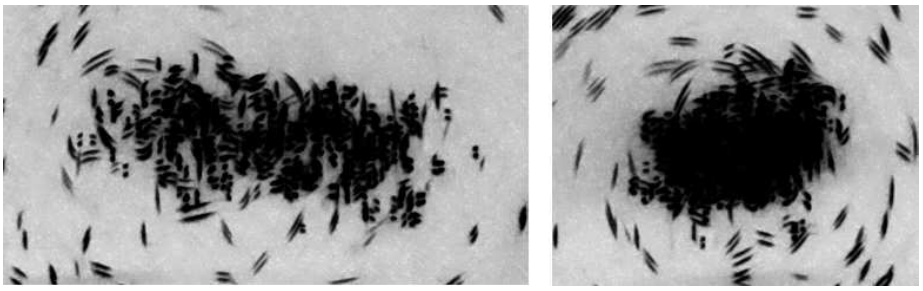


(b) WT Tab Oscillate 1.0 Hz (L) Both Tabs Oscillate 1.0 Hz (R)

Figure 10.38: Effect of Frequency on Vortex Disruption. $\alpha = 5°$, Flap: 30°

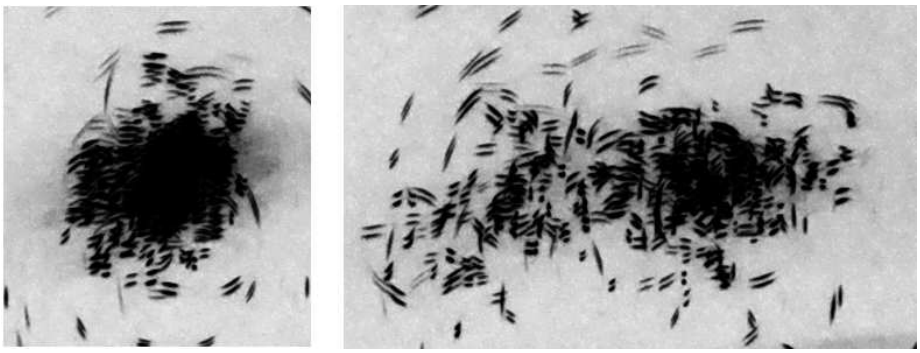


(a) Clean Core (b) WT Tab Oscillate 2.0 Hz

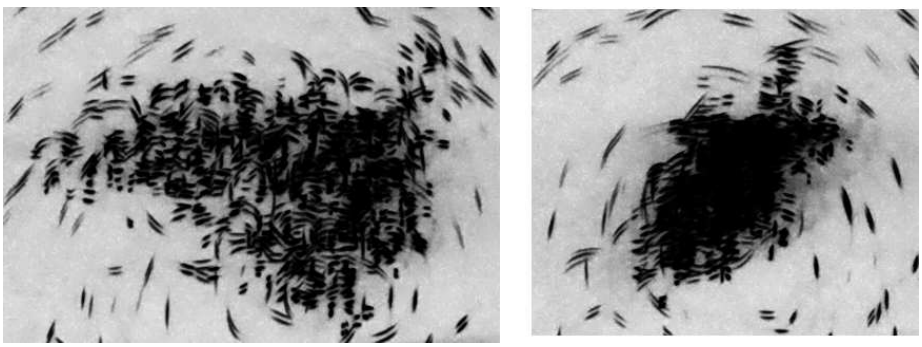


(c) WT & FT Tab Oscillate 2.0 Hz (d) FT Tab Oscillate 2.0 Hz

Figure 10.39: Vortex Core Dispersion. $\alpha = 5°$, Flap: Retracted

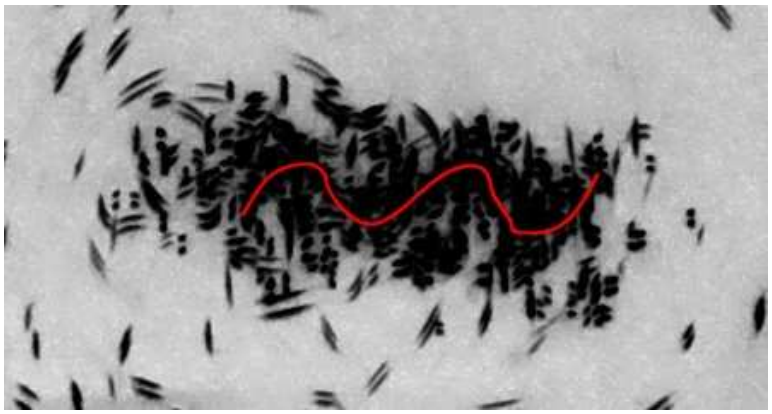


(a) Clean Core (b) WT Tab Oscillate 2.0 Hz

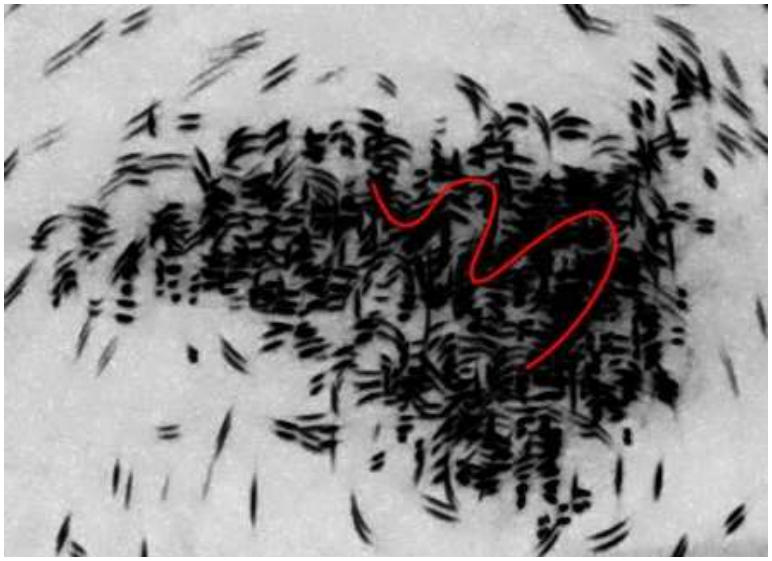


(c) WT & FT Tab Oscillate 2.0 Hz (d) FT Tab Oscillate 2.0 Hz

Figure 10.40: Vortex Core Dispersion. $\alpha = 5°$, Flap: $30°$



(a) Flap Retracted



(b) Flap Extended 30°

Figure 10.41: Sinusoidal Core Motion, WT & FT Tab Oscillate 2.0 Hz. $\alpha = 5°$

11 Conclusions

The design and manufacture of a vertically mounted NACA 0012 test wing with an electrically operated trailing edge flap and two oscillating tabs was completed and tested in the Wits Draw Down Wind Tunnel. Large tabs (0.0333c) affixed to the wingtip and flap tip trailing edge were sinusoidally oscillated at three frequencies, 0.5, 1.0 and 2.0 Hz, with a view to induce vortex instability in the resulting near wake. Chordwise and spanwise pressure measurements were taken on the upper surface of the model so as to ascertain the resulting pressure distributions of the various oscillation schemes tested. Flow visualisation in the form of photographs of the resulting wake cross-section at three downstream positions in the tunnel formed the bulk of the test data gathered and was used to capture and model the differing trailing vortex behaviour as oscillation schemes were varied.

Calibration of the pressure sensors took place in a calibration room away from the tunnel using a small calibration wind tunnel and a factory calibrated manometer. Results obtained during calibration showed each of the twenty-four sensors built to exhibit near perfect linearity along the range tested with no discernible hysteresis effects. The uncertainty analysis used to generate the error bounds for each sensor showed a slope uncertainty of 1% through the pressure range seen by the the wind tunnel model during testing in the Wits Draw Down Tunnel.

The pressure sensor data was validated using NACA 0012 data obtained by Gregory [37] and showed a good correlation to the published data, albeit the Reynolds number of the data in the current study being an order of magnitude below that published.

To compliment the pressure measurements obtained, flow visualisation was completed using a helium bubble generator. The neutrally buoyant, helium filled soap bubbles entrained themselves to the flow over the wing with the result that high quality vortex cross-section images were obtained at three downstream positions in the tunnel; namely 0.37b, 1.0b, and 2.0b. The resulting images allowed for a clear

insight into the effect of adding vorticity to the near wake through the use of oscillating tabs at various frequencies and with various schemes. Flow visualisation images were combined with pressure results to model the flow over the wing surface and resulting wake. The investigation included testing the model at four angles of attack (0, 5, 10, 15°) as well as with a trailing edge plain flap extended to 30° .

Introducing vorticity into the aircraft wake was shown to cause a clear movement of the vortex core and associated wake extent. The spanwise position of the introduced vorticity (flap tip or wing tip) determined the behaviour of the resulting wake. Movement of the vortex core could be characterised by the particular tab being oscillated. Extension of either tab towards the lower surface of the airfoil caused the resulting vortex core to move towards that oscillating tab. The resulting core movement when both tabs were oscillated simultaneously was shown to be a superposition of the motions of the core under independent oscillation of the individual tabs, with the Wingtip tab shown to dominate the resulting motion of the vortex core.

It was shown by oscillating two tabs sinusoidally at 2.0 Hz that a reduction in the vortex core diameter and wake extents was seen at a downstream position one full span from the wing. The oscillating tabs were shown to impart a motion onto the vortex core, pulling the core downward and toward the tab as the tab extended. The wingtip tab was shown to dominate the overall wake properties and motion of the core, but it was the addition of vorticity introduced into the flow at the flap tip by a tab that showed the interference necessary to reduce the wake extents.

A frequency based investigation of the transient pressure effects on the leading edge of the wing revealed that a pressure oscillation equal to twice the input tab frequency was present at the three frequencies tested. This may explain why of the three frequencies tested, the highest tab oscillation frequency (2.0Hz) was shown to introduce the greatest instability into the downstream wake; as the largest pressure oscillation frequency was seen for this case.

Pressure tests conducted on the upper surface of the wing showed that the oscillation of the tabs induced an increase in the wing's lifting capability due to the increase in effective camber of the wing. Oscillation of the tabs was shown to produce a greater lifting increase then merely increasing the angle of attack of the wing. The large dimension of each tab was responsible for this; however the increase in drag associated with the extension of the tabs mean that this method of wake alleviation could only be considered for high drag applications, such as the approach to land. This is not seen as limiting as the approach phase is the section of a typical mission

profile where wake encounters most commonly occur. As such, it is thought that the pursuit of wake vortex attenuation using oscillating tabs or any means to introduce vorticity shows promise and thus it is recommended that further work in this field be undertaken.

12 Recommendations for Further Work

The results obtained when introducing vorticity into the near wake showed that the associated resulting instabilities have the potential to influence the wake and that vortex attenuation may be possible with such a scheme. The following work is recommended in the continuation of this field of research:

1. Force and Moment measurements should be taken of the wing, both in the baseline case and where the tabs are oscillating. This will give a quantitative value to the lift and drag increase seen upon oscillation of the tabs. By measuring the lift produced by the wing, initial circulation could be calculated from the geometry of the model, and the associated downstream circulation degradation quantified as a result of introducing vorticity into the near wake.

2. The change in pitching moment with tab extension should also be quantified and an investigation undertaken to assess any potential controllability issues were this scheme were to be used on an aircraft.

3. The setup of the pressure taps in the upper surface of the model meant that net pressure distributions could only be sought where the tabs were parallel to the chordline (baseline configuration). Further work to include net pressure distributions while the tabs are oscillated is recommended.

4. Further study into the effect of tab oscillation on the lift distribution across the whole wing would assist in characterising the effect the tabs have on the lifting capacity of the wing.

5. Further investigation into the transient pressure effects of oscillating the tabs could yield insight into the mechanism by which instability is introduced into the wake. Further study into the relationship between the input oscillation frequency and the resulting pressure oscillation frequency may result in the determination of an optimum tab oscillation frequency with which to introduce instability and early break-up in the wake.

6. Cross section velocity plots of the wake at the various downstream positions would further substantiate the claims made as to the destructive nature of vorticity introduction on the near wake.

7. The work presented here only looked at synchronous oscillation of the two tabs. Further investigation into out of phase or asynchronous oscillation schemes is recommended.

References

[1] JD Crouch, GD Miller, and PR Spalart. Active-control system for breakup of airplane trailing vortices. *AIAA journal*, 39(12):2374–2401, 2001.
Referenced on page: 1, 1

[2] S.C. Crow. Stability theory for a pair of trailing vortices. *AIAA Journal*, 8(12):2172–2179, 1970.
Referenced on page: 1, 3, 9, 10, 15, 16, 20

[3] J.J Ballough. FAA Advisory Circular AC No. 90-23F: Aircraft Wake Turbulence, 2002.
Referenced on page: 1, 3, 3, 3, 4, 4, 5

[4] Dr Peter Walley. http://weblab.open.ac.uk/firstflight/images/vortex/vortex_formation.gif. Accessed 05-01-13.
Referenced on page: 2

[5] H Chevalier. Flight test studies of the formation and dissipation of trailing vortices. *Journal of Aircraft*, (730295), 1973.
Referenced on page: 3, 3, 3, 11, 20

[6] J D Anderson. *Fundamentals of aerodynamics*, volume 1984. McGraw-Hill New York, 4th edition, 2007.
Referenced on page: 5, 7

[7] G C Greene. An approximate model of vortex decay in the atmosphere. *Journal of Aircraft*, 23(7):566–573, 1986.
Referenced on page: 7, 12, 13, 97, 102

[8] R E Robins, D P Delisi, United States. National Aeronautics, Space Administration, Langley Research Center, and Inc Northwest Research Associates. *Wake vortex algorithm scoring results*. Citeseer, 2002.
Referenced on page: 7

[9] S C Crow and E R Bate. Lifespan of trailing vortices in a turbulent atmosphere. *Journal of Aircraft*, 13:476–482, 1976.
Referenced on page: 8, 10, 11, 11, 12, 12, 20, 98, 100

[10] C Bellastrada, C Breitsamter, and B Laschka. Investigation of turbulent wake vortex originating from a large transport aircraft in landing configuration. In *Proc. CEAS Aerospace Aerodynamics Research Conference*, page 31, 2002.
Referenced on page: 8, 31, 32, 32

[11] C.D Donaldson, R.S Snedeker, and R.D Sullivan. Calculation of Aircraft Wake Velocity Profiles and Comparison with Experimental Data. *Journal of Aircraft*, 11(9):547–555, 1974.
Referenced on page: 8

[12] J R Spreiter and A H Sacks. The rolling up of the trailing vortex sheet and its effect on the downwash behind wings. *Jour. Aero. Sci*, 18(1):21–32, 1951.
Referenced on page: 9

[13] C P Donaldson, A J Bilanin, and O D T De L'Atlantique. *Vortex wakes of conventional aircraft*. Technical editing and reproduction, 1975.
Referenced on page: 14, 14

[14] J D CROUCH. Instability and transient growth for two trailing-vortex pairs. *Journal of Fluid Mechanics*, 350(-1):311–330, 1997.
Referenced on page: 14, 15, 16, 16, 20, 35, 36

[15] D Fabre, L Jacquin, and A Loof. Optimal perturbations in a four-vortex aircraft wake in counter-rotating configuration. *JOURNAL OF FLUID MECHANICS*, 451:319–328, January 2002.
Referenced on page: 14, 16, 20

[16] B Caiger and D G Gould. An analysis of flight measurements in the wake of a jet transport aircraft. *Aircraft wake turbulence and its detection: proceedings*, page 125, 1971.
Referenced on page: 15

[17] R E Dunham Jr. Model tests of various vortex dissipation techniques in a water towing tank. *NASA LWP-1146, January*, 1974.
Referenced on page: 15

[18] CG Matalanis and JK Eaton. Wake vortex control using static segmented Gurney flaps. *AIAA journal*, 45(2):321–328, 2007.
Referenced on page: 17, 17, 31

[19] CG Matalanis and JK Eaton. Wake vortex alleviation using rapidly actuated segmented Gurney flaps. *AIAA journal*, 45(8):1874–1884, 2007.
Referenced on page: 17, 31

[20] U.S. Dept Of Transportation. Order JO 7110.65S, Air Traffic Control.
Referenced on page: 18, 18, 18

[21] U.S. Dept Of Transportation. Air Traffic Organisation Policy, Appendix A, Aircraft Information Fixed -Wing Aircraft.
Referenced on page: 18

[22] S Plan, S Committees, P Committees, and HSR. Wake Turbulence: An Obstacle to Increased Air Traffic Capacity. *Transportation*, 2008.
Referenced on page: 19, 19, 20

[23] S. Lang, A.D. Mundra, WW Cooper, B.S. Levy, C.R. Lunsford, AP Smith, and J. Tittsworth. A Phased Approach to Increase Airport Capacity Through Safe Reduction of Existing Wake Turbulence Constraints. *Air Traffic Control Quarterly*, 11(4):331–356, 2003.
Referenced on page: 19

[24] S. Lang, DA Domino, A. Mundra, and C. Bodoh. ATC feasibility of potential near-term wake turbulence procedures. In *Digital Avionics Systems Conference, 2004. DASC 04. The 23rd*, volume 1, 2004.
Referenced on page: 19

[25] J.E. Lebron. Estimates of Potential Increases in Airport Capacity Through ATC System Improvements in the Airport and Terminal Areas. *McLean, Virginia: Prepared for the Federal Aviation Administration by The MITRE Corporation*, 1987.
Referenced on page: 19

[26] C. Lunsford, A. Mundra, L. Audenaerd, J. Cheng, C. Devlin, A. Gross, R. Mayer, J. Sherry, W. Bryant, E. Johnson, and Others. Wind dependent concepts for wake avoidance: a comparative analysis of capacity benefits and implementation risks. In *Digital Avionics Systems Conference, 2005. DASC 2005. The 24th*, volume 1, 2005.
Referenced on page: 19

[27] Department For Transport. http://www.statistics.gov.uk/cci/nugget.asp?id=1104. Accessed 26 March 2010, 2009.
Referenced on page: 19, 19

[28] B. Landsberg. Wake Turbulence: Should You Worry? *AOPA Online*, 41(10), 1998.

Referenced on page: 20, 20

[29] Http://www.flightglobal.com/articles/2008/11/20/319106/mexican learjet-wake-vortex-crash-likened-to-us crash.html. Mexican Learjet wake vortex crash likened to US crash. Accessed 2010/06/08, 2008.

Referenced on page: 20

[30] J B Barlow, W H Rae, and A Pope. *Low-speed wind tunnel testing*. Wiley, third edition, 1999.

Referenced on page: 30, 30

[31] C Breitsamter. Wake vortex characteristics of transport aircraft. *Progress in Aerospace Sciences*, 47(2):89–134, 2011.

Referenced on page: 33, 34

[32] R.H. Liebeck. Design of subsonic airfoils for high lift. *Journal of Aircraft*, 15(9):547 to 561, 1978.

Referenced on page: 36, 46, 123, 123

[33] Edward A Whalen, Andy P Broeren, and Michael B Bragg. Considerations for Aerodynamic Testing of Scaled Runback Ice Accretions. *AIAA Paper*, 260, 2006.

Referenced on page: 42

[34] M Maureen Hand, D A Simms, L J Fingersh, D W Jager, and J R Cotrell. *Unsteady aerodynamics experiment phase V: test configuration and available data campaigns*. National Renewable Energy Laboratory, 2001.

Referenced on page: 42, 42

[35] I H Abbott and A E Von Doenhoff. *Theory of wing sections: including a summary of airfoil data*. Dover Pubns, 1959.

Referenced on page: 45

[36] Http://www.le.ac.uk/bl/gat/virtualfc/Stats/normal.htm. University of Leister Online Statistics - Normal Distributions.

Referenced on page: 70

[37] N Gregory, C L O'Reilly, and Aeronautical Research Council (Great Britain). *Low-speed aerodynamic characteristics of NACA 0012 aerofoil section, including the effects of upper-surface roughness simulating hoar frost*. National Physical Laboratory, 1970.

Referenced on page: 89, 89, 91, 92, 94, 129, 138

[38] Chris Rumsey (NASA). Langley Research Center. Turbulence Modeling Resource.

Referenced on page: 89

[39] S S Sathaye. *Lift Distributions on Low Aspect Ratio Wings at Low Reynolds Numbers*. PhD thesis, WORCESTER POLYTECHNIC INSTITUTE, 2004.

Referenced on page: 96, 97

Appendix A TE Flap Specifications

TRIDENT

PLANETARY GEARHEAD

Plastic Version

GPP22._ _ _ _

TRIDENT ENGINEERING LIMITED
Trident House, King Street Lane,
Winnersh, Wokingham,
Berkshire, RG41 5AS

Telephone: 0118 978 6444
Fax: 0118 977 6345
Email: sales@tridenteng.co.uk
www.tridenteng.co.uk

General data

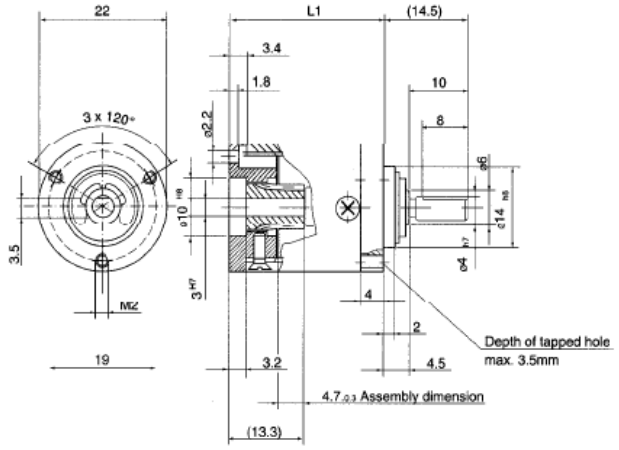
Planetary gearhead		straight teeth		
Bearing at output		sintered		
Max. permissible axial load		30	N	
Max. permissible force press fits		150	N	
Recommended input speed		6,000	rpm	
Recommended temperature range		-15/+65	°C	
Number of stages:	1	2	3	4
Max. radial load,				
10 mm from flange	15 N	30 N	45 N	60 N
Max backlash	1.5°	2.0°	2.5°	3.0°
Efficiency	80%	75%	70%	65%

Product combinations

2-22/02	(This catalogue)
22N_ _	(API Motion Catalogue)
22V_ _	
23V_ _	
26N_ _	
28L_ _	
28LT_ _	

Gearhead Order No	Reduction	Number of stages	Maximum torque continuous [Nm]	Maximum torque intermittent [Nm]	Sense of direction	Weight [g]	L1 [mm]
GPP22.0004	4:1	1	0.2	0.2	=	41	27.1
GPP22.0014	14:1	2	0.4	0.4	=	42	35.35
GPP22.0025	25:1	2	0.4	0.4	=	52	35.35
GPP22.0051	51:1	3	0.6	0.6	=	63	43.55
GPP22.0093	93:1	3	0.6	0.6	=	63	43.55
GPP22.0169	169:1	3	0.6	0.6	=	63	43.55
GPP22.0169	169:1	4	0.7	0.7	=	74	51.30
GPP22.0344	344:1	4	0.7	0.7	=	74	51.30
GPP22.0626	626:1	4	0.7	0.7	=	74	51.30
GPP22.1140	1140:1	4	0.7	0.7	=	74	51.30

The ratios shown are stock ratios, there are many more options available - please contact our technical department for more details.



Notes

TRIDENT

PLANETARY GEARHEAD

TRIDENT ENGINEERING LIMITED
Trident House, King Street Lane,
Winnersh, Wokingham,
Berkshire, RG41 5AS

Telephone: 0118 978 6444
Fax: 0118 977 6345
Email: sales@tridenteng.co.uk
www.tridenteng.co.uk

GP22._ _ _ _

General data

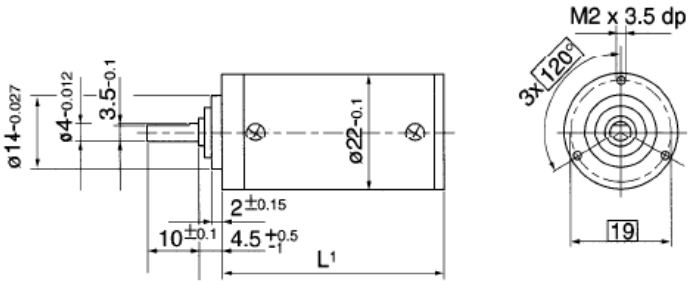
Planetary gearhead		straight teeth		
Bearing at output		ball bearing		
Radial play, 10mm from flange		max. 0.10	mm	
Axial play		max. 0.7	mm	
Max. permissible axial load		30	N	
Max. permissible force press fits		150	N	
Average backlash no load per stage		<0.9	°	
Recommended input speed		<4000	rpm	
Recommended temperature range		-15/+65	°C	
Number of stages:	1	2	3	4
Max. radial load, 10 mm from flange	15 N	30 N	45 N	60 N
Efficiency	80%	75%	70%	60%

Product combinations

2-22/02	(This catalogue)
22N_ _	(API Motion Catalogue)
22V_ _	
23V_ _	
26N	
28L_ _	
28LT_ _	

Gearhead Order No	Reduction	Number of stages	Maximum torque continuous [Nm]	Maximum torque intermittent [Nm]	Sense of direction	Weight [g]	L1 [mm]
GP22.0004	4:1	1	0.2	0.2	=	33	27.1
GP22.0014	14:1	2	0.4	0.4	=	43	35.35
GP22.0025	25:1	2	0.4	0.4	=	43	35.35
GP22.0051	51:1	3	0.6	0.6	=	54	43.55
GP22.0093	93:1	3	0.6	0.6	=	54	43.55
GP22.0169	169:1	3	0.6	0.6	=	54	43.55
GP22.0189	189:1	4	0.7	0.7	=	65	51.80
GP22.0344	344:1	4	0.7	0.7	=	65	51.80
GP22.0626	626:1	4	0.7	0.7	=	65	51.80
GP22.1140	1140:1	4	0.7	0.7	=	65	51.80

The ratios shown are stock ratios, there are many more options available - please contact our technical department for more details.



Notes

Specifications subject to change without notice

Precious Metal-Brush Motors

Typical Applications/Audio and Visual Equipments

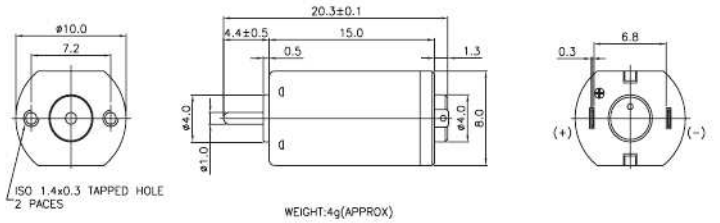
· Camcorder

Precision li

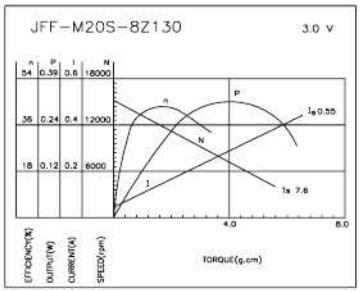
MODEL	VOLTAGE		NO LOAD		AT MAXIMUM EFFICIENCY					STALL
	OPERATING RANGE	NOMINAL	SPEED	CURRENT	SPEED	CURRENT	TORQUE	OUTPUT	EFF	TORQUE
			rpm	A	rpm	A	g.cm	W	%	g.cm
JFF-M20S-8Z130	2.0~3.0	3.0V CONSTANT	15200	0.045	11820	0.16	1.70	0.21	43.0	7.6
JFF-M20S-10100	1.2~3.5	2.4V CONSTANT	15800	0.056	12410	0.20	1.80	0.23	47.7	8.6
JFF-M20S-7Z170	2.0~4.0	2.0V CONSTANT	8000	0.025	6020	0.08	0.96	0.06	37.0	3.9
JFF-M20S-1260	1.5~3.5	1.5V CONSTANT	20000	0.120	13500	0.43	2.00	0.28	43.4	6.2

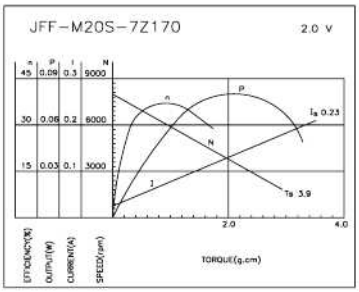
DIRECTION OF ROTATION

UNIT: MILLIMETERS



WEIGHT:4g(APPROX)





Appendix B Faulhaber Motor and Controller Data Sheets

FAULHABER

Linear DC-Servomotors

3,6 N

with Analog Hall Sensors
QUICKSHAFT® Technology

For combination with
Motion Controllers:
MCLM 3003/06 S, MCLM 3003/06 C

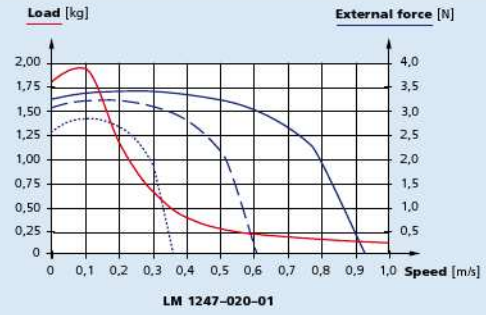
Series LM 1247 ... 01

		LM 1247–	020–01	040–01	060–01	080–01	100–01	120–01	
1	Continuous force [1]	$F_{e\,max.}$	3,6						N
2	Peak force [1] [2]	$F_{p\,max.}$	10,7						N
3	Continuous current [1]	$I_{e\,max.}$	0,55						A
4	Peak current [1] [2]	$I_{p\,max.}$	1,66						A
5	Back-EMF constant	k_E	5,25						V/m/s
6	Force constant [3]	k_F	6,43						N/A
7	Terminal resistance, phase-phase	R	13,17						Ω
8	Terminal inductance, phase-phase	L	820						µH
9	Stroke length	$s_{max.}$	20	40	60	80	100	120	mm
10	Repeatability [4]		40	40	40	40	40	40	µm
11	Precision [4]		120	140	160	180	200	220	µm
12	Acceleration [5]	$a_{e\,max.}$	198,0	148,5	127,3	101,8	91,4	82,9	m/s²
13	Speed [5] [6]	$v_{e\,max.}$	2,0	2,4	2,8	2,9	3,0	3,2	m/s
14	Thermal resistance	$R_{th\,1}$ / $R_{th\,2}$	3,2 / 20,0						K/W
15	Thermal time constant	τ_{w1} / τ_{w2}	11 / 624						s
16	Operating temperature range		– 20 ... +125						°C
17	Rod weight [7]	m_m	18	24	28	35	39	43	g
18	Total weight [7]	m_t	57	63	67	74	78	82	g
19	Magnetic pitch	τ_m	18						mm
20	Rod bearings		polymer sleeves						
21	Housing material		metal, non-magnetic						
22	Direction of movement		electronically reversible						

[1] thermal resistance $R_{th\,2}$ by 55% reduced
[2] for max. 1 second with a duty cycle of 20%
[3] with sine wave commutation
[4] typical values with integrated linear Hall sensors and Motion Controller MCLM 3003/06 S/C.
The values depend on conditions of use
[5] theorical value, referring only to the motor
[6] with a triangular speed profile and the max. stroke
[7] rounded value, for reference only

Notes: These motors are for operation with DC-voltage < 75 V DC.
The given values are for free standing motors.
The mounting with magnetic conductive metal can influence the characteristics of the motor.

Caution: Presence of strong magnetic fields. Static sensitive device.



LM 1247–020–01

Trapezoidal motion profile (t1 = t2 = t3)

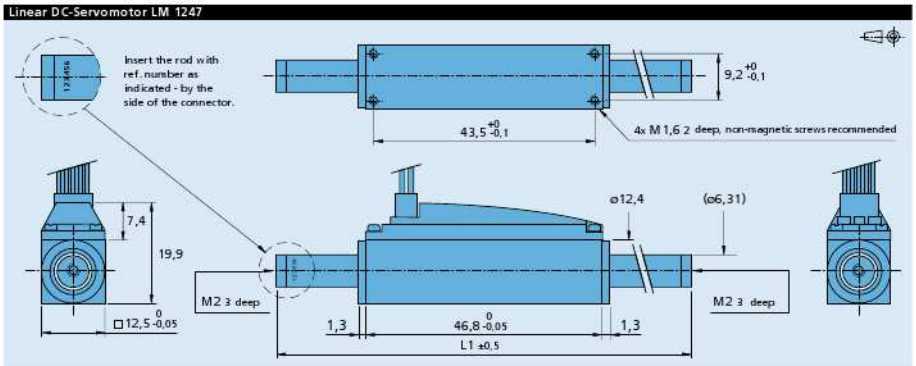
Displacement distance:	20 mm
Friction coefficient:	0,2
Slope angle:	0°
Rest time:	0,1 s

Load: The max. permissible load at a given speed with an external force of 0 N

External force: The max. permissible external force at a given speed with a load of:
- 0,1 Kg ——————
- 0,2 Kg — — — -
- 0,5 Kg ----------

© DR. FRITZ FAULHABER GMBH & CO. KG
Specifications subject to change without notice.
www.faulhaber.com

Linear DC-Servomotor LM 1247

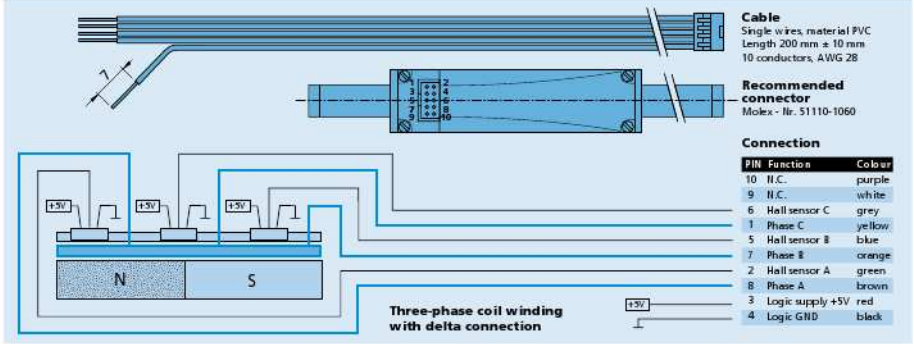


Ordering information

Linear DC-Servomotors Series	Stroke mm	Rod length L1 ±0,5 mm
LM 1247-020-01	0 −10 +10	82
LM 1247-040-01	−20 +20	109
LM 1247-060-01	−30 +30	127
LM 1247-080-01	−40 +40	154
LM 1247-100-01	−50 +50	172
LM 1247-120-01	−60 +60	190

Note: Single rod available on request.

Cable and connection information



Cable
Single wires, material PVC
Length 200 mm ± 10 mm
10 conductors, AWG 28

Recommended connector
Molex - Nr. 51110-1060

Connection

PIN	Function	Colour
10	N.C.	purple
9	N.C.	white
6	Hall sensor C	grey
1	Phase C	yellow
5	Hall sensor B	blue
7	Phase B	orange
2	Hall sensor A	green
8	Phase A	brown
3	Logic supply +5V	red
4	Logic GND	black

For notes on technical data and lifetime performance refer to "Technical Information".
Edition 2010 Jun. 14

© DR. FRITZ FAULHABER GMBH & CO. KG
Specifications subject to change without notice.
www.faulhaber.com

FAULHABER

Motion Controller

4-Quadrant PWM
with CAN interface

For combination with:
Linear DC-Servomotors
with Hall sensors

Series MCLM 3003/06 C

		MCLM 3003 C	MCLM 3006 C	
Power supply	U_B	12 ... 30	12 ... 30	V DC
PWM switching frequency	f_{PWM}	78,12	78,12	kHz
Efficiency	η	95	95	%
Max. continuous output current [1]	I_{dauer}	3	6	A
Max. peak output current	I_{max}	10	10	A
Total standby current	I_{el}	0,06	0,06	A
Speed range [2]		2 ... 10 000	2 ... 10 000	mm/s
Scanning rate	N	100	100	µs
Encoder resolution with Hall Sensors [3]		≤ 3 000	≤ 3 000	inc./τ_m
Resolution with external encoder [3]		≤ 65 535	≤ 65 535	inc./mm
Input/output (partially free configurable)		3	3	
Operating temperature range		0 ... + 70	0 ... + 70	°C
Storage temperature		– 25... + 85	– 25 ... + 85	°C
Housing material		without housing	zinc, black coated	
Weight		18	160	g

[1] at 22°C ambient temperature
[2] Speed in the range 1 ... 5 mm/s may have fluctuations due to the motor type, load characteristics and controller parameters
[3] τ_m is the magnetic pitch of the linear motor

Connection information				
Connection "CANH", "CANL":			CAN-High / CAN-Low	
Interface			CAN	
Communication protocol			CANopen	
Max. transfer speed rate			1	Mbit/s
Connection "AGND":				
– analog ground			analog GND	
– digital input	external encoder		channel B	
		R_{in}	10	kΩ
		f	≤ 400	kHz
Connection "Fault":				
– digital input		R_{in}	100	kΩ
– digital output (open collector)		U	≤ U_B	V
		I	≤ 30	mA
		clear	switched to GND	
		set	high-impedance	
	fault output	no error	switched to GND	
		error	high-impedance	
	signal output	f	≤ 2	kHz
		resolution	1...255	inc./τ_m
Connection "AnIn":			"AGND" as GND	
– analog input	set position value	U_{in}	± 10	V
– digital input	external encoder		channel A	
		f	≤ 400	kHz
	step frequency input	f	≤ 400	kHz
		R_{in}	5	kΩ
Connection "+24V":		U_B	12 ... 30	V DC
Connection "GND":			ground	
Connection "3. In":				
– digital input		R_{in}	22	kΩ
– electronic supply voltage [4]		U_B	12 ... 30	V DC

[4] Optional on request

© DR. FRITZ FAULHABER GMBH & CO. KG
Specifications subject to change without notice.
www.faulhaber.com

Connection information					
Phase connection "A", "B", "C":					
	A		Phase A	brown [1]	
	B		Phase B	orange [1]	
	C		Phase C	yellow [1]	
		U_{out}	0 ... U_B		V
PWM switching frequency		f_{PWM}	78,12		kHz
Hall Sensor connection "A", "B", "C":					
	A		Hall Sensor A	green [1]	
	B		Hall Sensor B	blue [1]	
	C		Hall Sensor C	grey [1]	
		U_{in}	≤ 5		V
Connection "SGND":					
Signal GND			Signal ground	black [1]	
Connection "+5V":					
Output voltage for external use [2]		U_{out}	5	red [1]	V DC
Load current		I_{out}	≤ 60		mA

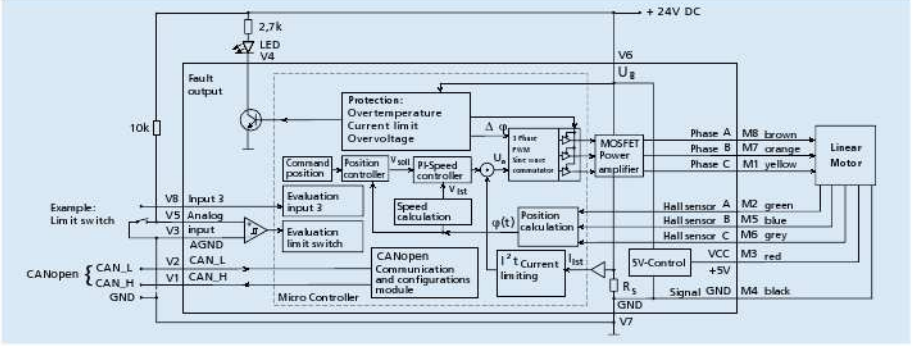
[1] Colour identification for linear DC-Servomotor
[2] E.g. Hall sensor

D-SUB-connector information			
Connection D-SUB-connector:			
Pin 2	CAN_L		CAN-Low
Pin 3	GND		Ground
Pin 7	CAN_H		CAN-High

Digital inputs general information			
- PLC, default	high	12,5 ... U_B	V
	low	0 ... 7	V
- TTL	high	3,5 ... U_B	V
	low	0 ... 0,5	V

The signal level (PLC or TTL) of the digital inputs can be set over the interface (see instruction manual).

Position control



© DR. FRITZ FAULHABER GMBH & CO. KG
Specifications subject to change without notice.
www.faulhaber.com

Appendix C C# Motor Control Code

```
using System;
using System.Collections.Generic;
using System.ComponentModel;
using System.Data;
using System.Drawing;
using System.Linq;
using System.Text;
using System.Windows.Forms;
using System.IO.Ports;

namespace WindowsFormsApplication1
{
    public partial class Form1 : Form
    {
        SerialPort sp = new SerialPort();

        double freq;    // Freq (Hz)
        double AmpPer;  // Percentage gurney flap extends
        double A;       // Amplitude
        double MaxPos;  // Max Displacement position
        double MinPos;  // Min Displacement position
        double omega;   // 2*pi*freq
        double disp;    // Sinusoidal Displacement
        double t;       // time
        double pos;     // Controller Position
        //string pos;     //controller position

        int i;          //loop variable
        int ft;
        int wt;



        public Form1()
        {
            InitializeComponent();
            sp.Open();
            sp.WriteLine("NET1" );
            sp.WriteLine("ANSW1" );
        }

        private void button1_Click(object sender, EventArgs e)
        {
            // start button

            i = 1;



            omega = 2 * Math.PI * freq;
            A = (MaxPos-MinPos)/2;  // 200 = 2 * 100 ie factor of 2 as a result of sine wave eqn


                t = 0;
                timer1.Start();


            while (i==1)

                {

                    disp = (-A * Math.Sin(omega * t - Math.PI / 2) + (MaxPos-A))*(AmpPer/100);
                    sp.WriteLine("LA" + disp);
                    sp.WriteLine("M");

                    label7.Text = "ON";
                    label7.BackColor = Color.Green;

                    Application.DoEvents();
                    if (i == 0)
                    { break; }

                }
```

```
            timer1.Stop();

        }
        private void button2_Click(object sender, EventArgs e)
        {
            // Stop button

            i = 0;

            label7.Text = "OFF";
            label7.BackColor = Color.Red;
        }

        private void textBox1_TextChanged(object sender, EventArgs e)
        {
            // freq input
        }

        private void textBox2_TextChanged(object sender, EventArgs e)
        {
            // percentage travel
        }

        private void Form1_Load(object sender, EventArgs e)
        {

        }

        private void label4_Click(object sender, EventArgs e)
        {

        }

        private void textBox3_TextChanged(object sender, EventArgs e)
        {
            // Max position number ie -1666 < x < 1666
        }

        private void label5_Click(object sender, EventArgs e)
        {

        }


        private void timer1_Tick(object sender, EventArgs e)
        {
            t += 0.015;
            //if (Math.IEEERemainder(Math.Floor(t * 1000), 500) == 0)
            //{
            //    label6.Text = Convert.ToString(t);
            //}
        }

        private void button3_Click(object sender, EventArgs e)
        {
            // Master controller Activate
            sp.WriteLine("EN");

            label6.Text = "FT Active";
            label6.BackColor = Color.Green;

            label5.Text = "WT Active";
            label5.BackColor = Color.Green;

        }

        private void button4_Click(object sender, EventArgs e)
        {
            // Master controller Deactivate
            sp.WriteLine("DI");

            label6.ForeColor = Color.White;
            label6.Font = new Font(label5.Font.FontFamily.Name, 16);
            label6.Text = "FT Inactive";
```

```
            label6.BackColor = Color.Red;

            label5.ForeColor = Color.White;
            label5.Font = new Font(label5.Font.FontFamily.Name, 16);
            label5.Text = "WT Inactive";
            label5.BackColor = Color.Red;

        }

        private void button5_Click(object sender, EventArgs e)
        {
            sp.WriteLine("HO"); //Defines zero position

        }

        private void button6_Click(object sender, EventArgs e)
        {
            sp.WriteLine("LA0");    //Centre Actuator
            sp.WriteLine("M");
        }

        private void label1_Click(object sender, EventArgs e)
        {

        }

        private void button10_Click(object sender, EventArgs e)
        {
            //FT Deactivate
            sp.WriteLine("1DI");
            ft = 0;
            label6.ForeColor = Color.White;
            label6.Font = new Font(label5.Font.FontFamily.Name, 16);
            label6.Text = "FT Inactive";
            label6.BackColor = Color.Red;


        }

        private void button8_Click(object sender, EventArgs e)
        {
            //FT Activate
            sp.WriteLine("1EN");
            ft = 1;
            label6.Text = "FT Active";
            label6.BackColor = Color.Green;
        }

        private void button7_Click(object sender, EventArgs e)
        {
            //WT Activate
            sp.WriteLine("2EN");
            wt = 1;
            label5.Text = "WT Active";
            label5.BackColor = Color.Green;
        }

        private void button9_Click(object sender, EventArgs e)
        {
            //WT Deactivate
            sp.WriteLine("2DI");
            wt = 0;
            label5.ForeColor = Color.White;
            label5.Font = new Font(label5.Font.FontFamily.Name, 16);
            label5.Text = "WT Inactive";
            label5.BackColor = Color.Red;

        }

        private void label5_Click_1(object sender, EventArgs e)
        {

        }
```

```
        private void label6_Click(object sender, EventArgs e)
        {

        }

        private void label7_Click(object sender, EventArgs e)
        {

        }

        private void textBox4_TextChanged(object sender, EventArgs e)
        {

        }

        private void label8_Click(object sender, EventArgs e)
        {

        }

        private void button11_Click(object sender, EventArgs e)
        {
            sp.WriteLine("LA" + MaxPos);
            sp.WriteLine("M");
        }

        private void button12_Click(object sender, EventArgs e)
        {
            sp.WriteLine("LA" + MinPos);
            sp.WriteLine("M");
        }

        private void textBox5_TextChanged(object sender, EventArgs e)
        {

        }

        private void button13_Click(object sender, EventArgs e)
        {

            sp.WriteLine("LA" + pos);
            sp.WriteLine("M");
        }

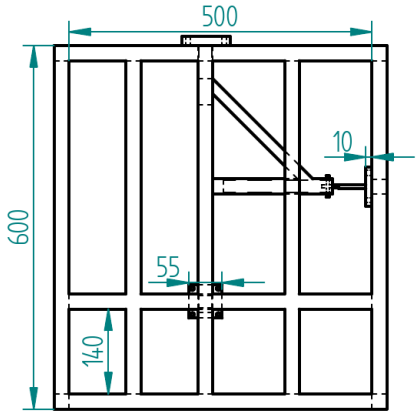
        private void button14_Click(object sender, EventArgs e) // Initialise All
        {
            freq = Convert.ToDouble(textBox1.Text); //converts the freq input to a double
            AmpPer = Convert.ToDouble(textBox2.Text); // converts the percentage travel to a double
            MaxPos = Convert.ToDouble(textBox3.Text); // converts the max displacement to a double
            MinPos = Convert.ToDouble(textBox4.Text); // converts the max displacement to a double
            pos = Convert.ToDouble(textBox5.Text); // converts the position displacement to a double
        }


    }
}
```

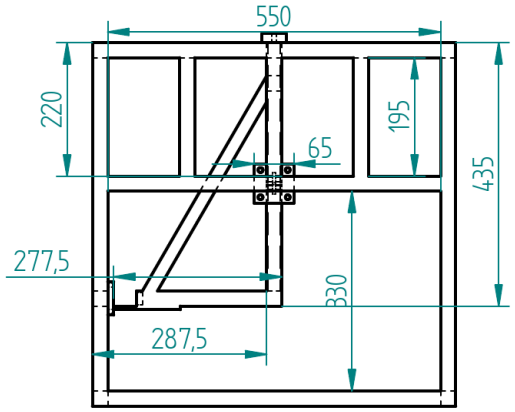
Appendix D Sting Balance Dimensions & Drawings

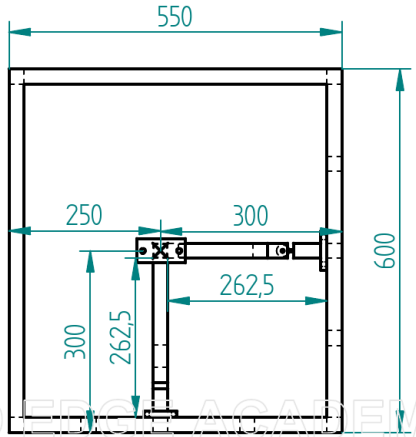
REVISION HISTORY			
REV	DESCRIPTION	DATE	APPROVED

Lift Arm



Drag Arm





SOLID EDGE ACADEMIC COPY

	NAME	DATE
DRAWN	ARWood	11/28/11
CHECKED		
ENG APPR		
MGR APPR		

UNLESS OTHERWISE SPECIFIED
DIMENSIONS ARE IN MILLIMETERS
ANGLES ±X.X°
2 PL ±X.XX 3 PL ±X.XXX

SOLID EDGE
UGS - The PLM Company

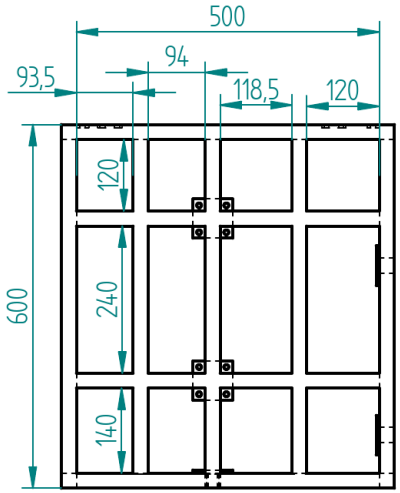
TITLE

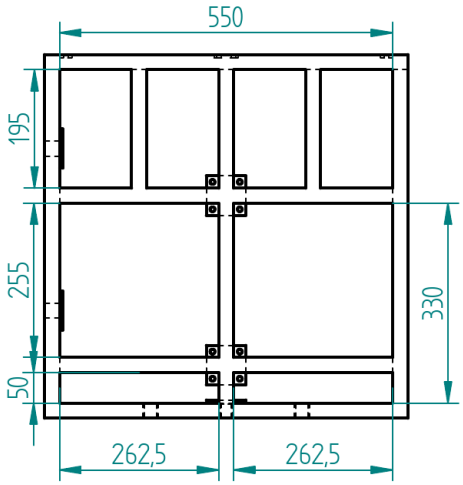
SIZE	DWG NO	REV
A4		

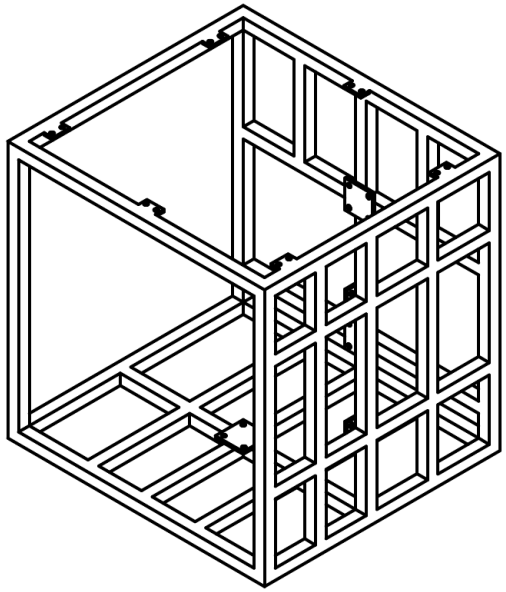
FILE NAME: Existing Cage Dimensions.dft

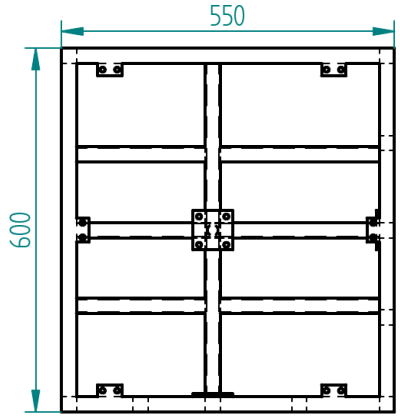
SCALE:	WEIGHT:	SHEET 1 OF 1

REVISION HISTORY			
REV	DESCRIPTION	DATE	APPROVED









	NAME	DATE
DRAWN	ARWood	12/05/11
CHECKED		
ENG APPR		
MGR APPR		

UNLESS OTHERWISE SPECIFIED
DIMENSIONS ARE IN MILLIMETERS
ANGLES ±X.X°
2 PL ±X.XX 3 PL ±X.XXX

SOLID EDGE
UGS - The PLM Company

TITLE: Sting Cage Overview

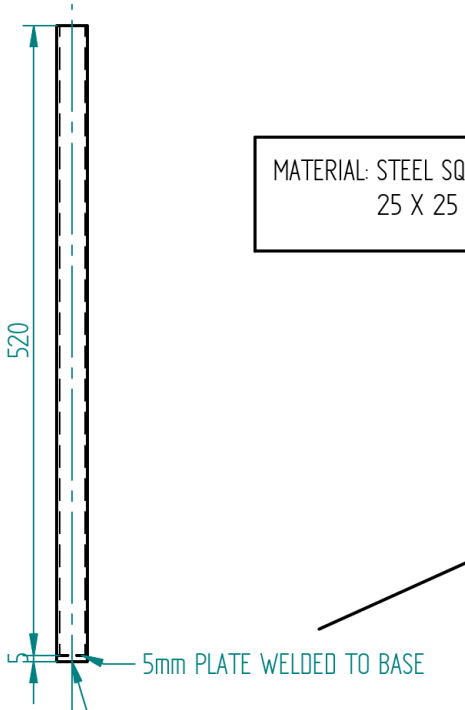
SIZE	DWG NO	REV
A4	072 592 5363	

FILE NAME: Frame no sting.dft

SCALE:	WEIGHT:	SHEET 1 OF 1

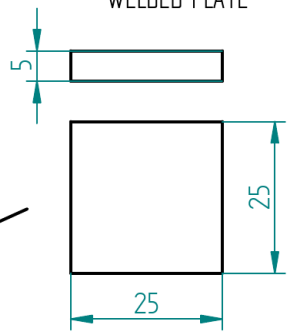
SOLID EDGE ACADEMIC COPY

REVISION HISTORY			
REV	DESCRIPTION	DATE	APPROVED



MATERIAL: STEEL SQUARE SECTION
25 X 25 X 2

WELDED PLATE



BEARING SEAT IS SEPERATE COMPONENT. JUST WELDING REQUIRED

	NAME	DATE
DRAWN	ARWood	12/12/11
CHECKED		
ENG APPR		
MGR APPR		

UNLESS OTHERWISE SPECIFIED
DIMENSIONS ARE IN MILLIMETERS
ANGLES ±X.X°
2 PL ±X.XX 3 PL ±X.XXX

SOLID EDGE
UGS - The PLM Company

TITLE

SIZE	DWG NO	REV
A4		

FILE NAME: Sting Upright.dft

SCALE:	WEIGHT:	SHEET 1 OF 1

SOLID EDGE ACADEMIC COPY

Appendix E Data Acquisition

Technical Sales
South Africa
0 800 203 199
ni.southafrica@ natinst.co.za

NI USB-6211

16-Bit, 250 kS/s M Series Multifunction DAQ, Bus-Powered

- 16 analog inputs (16-bit, 250 kS/s)
- 2 analog outputs (16-bit, 250 kS/s); 4 digital inputs; 4 digital outputs; 32-bit counters
- Bus-powered USB for high mobility; built-in signal connectivity
- NI signal streaming for sustained high-speed data streams over USB; OEM version available
- Compatible with LabVIEW, LabWindows™/CVI, and Measurement Studio for Visual Studio .NET
- NI-DAQmx driver software and NI LabVIEW SignalExpress LE interactive data-logging software



Overview

The National Instruments USB-6211 is a bus-powered USB M Series multifunction data acquisition (DAQ) module optimized for superior accuracy at fast sampling rates. It offers 16 analog inputs; 250 kS/s single-channel sampling rate; two analog outputs; four digital input lines; four digital output lines; four programmable input ranges (±0.2 to ±10 V) per channel; digital triggering; and two counter/timers.

The NI USB-6211 is designed specifically for mobile or space-constrained applications. Plug-and-play installation minimizes configuration and setup time, while direct screw-terminal connectivity keeps costs down and simplifies signal connections. This product does not require external power.

This module also features the new NI signal streaming technology, which gives you DMA-like bidirectional high-speed streaming of data across the USB bus. For more information about NI signal streaming, view the Resources tab.

Each module features an OEM version. Check the resources tab or use the left navigation to get pricing and technical information.

Driver Software

NI-DAQmx driver and measurement services software provides easy-to-use configuration and programming interfaces with features such as DAQ Assistant to help reduce development time. Browse the information in the Resources tab to learn more about driver software or download a driver. M Series devices are not compatible with the Traditional NI-DAQ (Legacy) driver.

Application Software

Every M Series data acquisition device includes a copy of NI LabVIEW SignalExpress LE data-logging software, so you can quickly acquire, analyze, and present data without programming. In addition to LabVIEW SignalExpress, M Series data acquisition devices are compatible with the following versions (or later) of NI application software – LabVIEW 7.1, LabWindows/CVI 7.x, or Measurement Studio 7.x. M Series data acquisition devices are also compatible with Visual Studio .NET, C/C++, and Visual Basic 6.

The mark LabWindows is used under a license from Microsoft Corporation.

Specifications

Specifications Documents

- Specifications
- Data Sheet

Specifications Summary

General	
Product Name	USB-6211
Product Family	Multifunction Data Acquisition
Form Factor	USB
Operating System/Target	Windows , Linux , Mac OS
DAQ Product Family	M Series
Measurement Type	Voltage
RoHS Compliant	Yes
Analog Input	
Channels	16 , 8
Single-Ended Channels	16
Differential Channels	8
Resolution	16 bits
Sample Rate	250 kS/s
Max Voltage	10 V
Maximum Voltage Range	-10 V , 10 V
Maximum Voltage Range Accuracy	2.69 mV
Maximum Voltage Range Sensitivity	91.6 µV
Minimum Voltage Range	-200 mV , 200 mV
Minimum Voltage Range Accuracy	0.088 mV
Minimum Voltage Range Sensitivity	4.8 µV
Number of Ranges	4
Simultaneous Sampling	No
On-Board Memory	4095 samples
Analog Output	
Channels	2
Resolution	16 bits

Technical Sales
South Africa
0 800 203 199
ni.southafrica@ natinst.co.za

NI USB-6225

16-Bit, 250 kS/s M Series Multifunction DAQ, External Power

- 80 analog inputs (16-bit, 250 kS/s)
- 2 analog outputs (16-bit, 833 kS/s); 24 digital I/O (8 clocked); 32-bit counters
- Use mass termination version with SCC signal conditioning
- NI signal streaming for sustained high-speed data streams over USB; OEM version available
- Compatible with LabVIEW, LabWindows™/CVI, and Measurement Studio for Visual Studio .NET
- NI-DAQmx driver software and NI LabVIEW SignalExpress LE interactive data-logging software



Overview

The National Instruments USB-6225 is a USB high-performance M Series multifunction data acquisition (DAQ) module optimized for superior accuracy at fast sampling rates. The NI USB-6225 is ideal for applications such as high-channel-count data logging and for sensor measurements when used with NI signal conditioning.

The USB-6225 is designed specifically for mobile or space-constrained applications. Plug-and-play installation minimizes configuration and setup time, while direct screw-terminal connectivity helps keep costs down and simplifies signal connections.

This module also features the new NI signal streaming technology, which gives you DMA-like bidirectional high-speed streaming of data across USB. For more information about NI signal streaming, check the Resources tab.

Each module also features an OEM version. Check the Resources tab or use the left navigation to get pricing and technical information.

Driver Software

NI-DAQmx driver and measurement services software provides easy-to-use configuration and programming interfaces with features such as DAQ Assistant to help reduce development time. Browse the information in the Resources tab to learn more about driver software or download a driver. M Series devices are not compatible with the Traditional NI-DAQ (Legacy) driver.

Application Software

Every M Series data acquisition device includes a copy of NI LabVIEW SignalExpress LE data-logging software, so you can quickly acquire, analyze, and present data without programming. In addition to LabVIEW SignalExpress, M Series data acquisition devices are compatible with the following versions (or later) of NI application software – LabVIEW 7.1, LabWindows™/CVI 7.x, or Measurement Studio 7.x. M Series data acquisition devices are also compatible with Visual Studio .NET, C/C++, and Visual Basic 6.

The mark LabWindows is used under a license from Microsoft Corporation.

Specifications

Specifications Documents

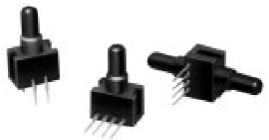
- Specifications
- Data Sheet

Specifications Summary

General	
Product Name	USB-6225 Screw Term
Product Family	Multifunction Data Acquisition
Form Factor	USB
Operating System/Target	Windows
DAQ Product Family	M Series
Measurement Type	Quadrature encoder , Voltage
RoHS Compliant	Yes
Product Name	USB-6225 Mass Term
Product Family	Multifunction Data Acquisition
Form Factor	USB
Operating System/Target	Windows
DAQ Product Family	M Series
Measurement Type	Voltage , Quadrature encoder
RoHS Compliant	Yes
Analog Input	
Channels	80 , 40
Single-Ended Channels	80
Differential Channels	40
Resolution	16 bits
Sample Rate	250 kS/s
Max Voltage	10 V
Maximum Voltage Range	-10 V , 10 V
Maximum Voltage Range Accuracy	3100 µV
Maximum Voltage Range Sensitivity	97.6 µV
Minimum Voltage Range	-200 mV , 200 mV
Minimum Voltage Range Accuracy	112 µV
Minimum Voltage Range Sensitivity	5.2 µV

Pressure Sensors
Gage and Differential/Unamplified-Noncompensated

Basic Sensors



FEATURES

- Lowest priced pressure sensor
- Miniature package
- Variety of gage pressure port configurations - easily and quickly modified for your special needs
- Choice of termination for gage sensors
- 2 mA constant current excitation significantly reduces sensitivity shift over temperature.*
- Can be used to measure with vacuum or positive pressure

24PC SERIES PERFORMANCE CHARACTERISTICS at 10.0 ±0.01 VDC Excitation, 25°C

	Min.	Typ.	Max.	Units
Excitation	—	10	12	VDC
Null Offset	–30	0	+30	mV
Null Shift, 25°C to 0°C, 25°C to 50°C	—	±2.0	—	mV
Linearity, P2 > P1, BFSL	—	±0.25	±1.0	%Span
Sensitivity Shift, 25°C to 0°C, 25°C to 50°C	—	±5.0*	—	%Span
Repeatability & Hysteresis	—	±0.15	—	%Span
Response Time	—	—	1.0	msec
Input Resistance	—	5.0 K	—	ohms
Output Resistance	—	5.0 K	—	ohms
Stability over One Year	—	±0.5	—	%Span
Weight	—	2	—	grams

ENVIRONMENTAL SPECIFICATIONS

Operating Temperature	–40°C to +85°C (–40°F to +185°F)
Storage Temperature	–55°C to +100°C (–67°F to +212°F)
Shock	Qualification tested to 150 g
Vibration	Qualification tested to 0 to 2 kHz, 20 g sine
Media (P1 & P2)	Limited only to those media which will not attack polyetherimide, silicon and fluorosilicone seal

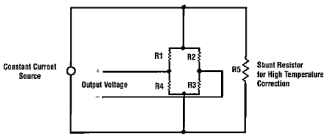
24PC SERIES ORDER GUIDE

Catalog Listing	Pressure Range psi	Span, mV			Sensitivity mV/psi Typ.	Overpressure psi Max.
		Min.	Typ.	Max.		
24PCE Type	0.5	24	35	46	70	20
24PCA Type	1.0	30	45	60	45	20
24PCB Type	5.0	85	115	145	23	20
24PCC Type	15	165	225	285	15	45
24PCD Type	30	240	330	420	11	60
24PCF Type	100	156	225	294	2.25	200
24PCG Type	250	145	212	280	0.85	500

*Non-compensated pressure sensors, excited by constant current instead of voltage, exhibit temperature compensation of Span. Application Note #1 briefly discusses current excitation.

Constant current excitation has an additional benefit of temperature measurement. When driven by a constant current source, a silicon pressure sensor's terminal voltage will rise with increased temperature. The rise in voltage not only compensates the Span, but is also an indication of die temperature.

Constant Current Excitation Schematic



Gage and Differential/Unamplified-Noncompensated

SENSOR SELECTION GUIDE

2 Product Family	4 Circuit Type	PC Pressure Transducer	A Pressure Range	F* Type of Seal	A Type of Port	2 Termination Style	G Pressure Measurement
2 20PC family	**4** Noncompensated		**A** 1 psi **B** 5 psi **C** 15 psi **D** 30 psi **E** 0.5 psi **F** 100 psi **G** 250 psi	**F** Fluorosilicone	**A** Straight **B** Barbed **C** Luer **D** Modular **H** M5 Thread **I** 90° Port **J** Needle **M** ¼ - 28 UNF Thread	**1** 1 x 4 **2** 2 x 2	**G** Gage **D** Differential

Example: 24PCAFA2G
Standard, non-compensated 1 psi sensor with fluorosilicone seal, straight port, 2 x 2 terminals, and Gage pressure measurement.
*Other media seal materials may be available.

ACCESSORIES SELECTION GUIDE

Catalog Listing	Description
PC10182	Steel lockring (Included with Port Style A, 1 x 4 terminals only)
PC10949	Single hole plastic bracket (Must be separately ordered)

Not all combinations are established. Contact 800 number before final design. The following listings are typically stocked in small quantities.

March 2000

National Semiconductor

LM134/LM234/LM334
3-Terminal Adjustable Current Sources

General Description

The LM134/LM234/LM334 are 3-terminal adjustable current sources featuring 10,000:1 range in operating current, excellent current regulation and a wide dynamic voltage range of 1V to 40V. Current is established with one external resistor and no other parts are required. Initial current accuracy is ±3%. The LM134/LM234/LM334 are true floating current sources with no separate power supply connections. In addition, reverse applied voltages of up to 20V will draw only a few dozen microamperes of current, allowing the devices to act as both a rectifier and current source in AC applications.

The sense voltage used to establish operating current in the LM134 is 64mV at 25˚C and is directly proportional to absolute temperature (˚K). The simplest one external resistor connection, then, generates a current with ≈+0.33%/˚C temperature dependence. Zero drift operation can be obtained by adding one extra resistor and a diode.

Applications for the current sources include bias networks, surge protection, low power reference, ramp generation, LED driver, and temperature sensing. The LM234-3 and LM234-6 are specified as true temperature sensors with guaranteed initial accuracy of ±3˚C and ±6˚C, respectively. These devices are ideal in remote sense applications because series resistance in long wire runs does not affect accuracy. In addition, only 2 wires are required.

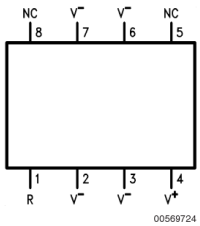
The LM134 is guaranteed over a temperature range of −55˚C to +125˚C, the LM234 from −25˚C to +100˚C and the LM334 from 0˚C to +70˚C. These devices are available in TO-46 hermetic, TO-92 and SO-8 plastic packages.

Features

- Operates from 1V to 40V
- 0.02%/V current regulation
- Programmable from 1µA to 10mA
- True 2-terminal operation
- Available as fully specified temperature sensor
- ±3% initial accuracy

Connection Diagrams

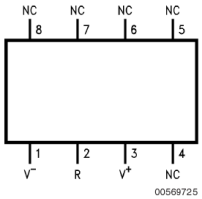
SO-8
Surface Mount Package



00569724

Order Number LM334M or LM334MX
See NS Package Number M08A

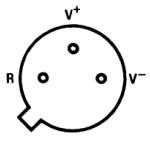
SO-8 Alternative Pinout
Surface Mount Package



00569725

Order Number LM334SM or LM334SMX
See NS Package Number M08A

TO-46
Metal Can Package

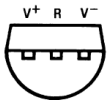


00569712

V⁻ Pin is electrically connected to case.

Bottom View
Order Number LM134H,
LM234H or LM334H
See NS Package
Number H03H

TO-92 Plastic Package



00569710

Bottom View
Order Number LM334Z, LM234Z-3 or LM234Z-6
See NS Package Number Z03A

© 2004 National Semiconductor Corporation

Absolute Maximum Ratings (Note 1)

If Military/Aerospace specified devices are required, please contact the National Semiconductor Sales Office/ Distributors for availability and specifications.

V^+ to V^- Forward Voltage	
LM134/LM234/LM334	40V
LM234-3/LM234-6	30V
V^+ to V^- Reverse Voltage	20V
R Pin to V^- Voltage	5V
Set Current	10 mA
Power Dissipation	400 mW
ESD Susceptibility (Note 6)	2000V
Operating Temperature Range (Note 5)	
LM134	−55˚C to +125˚C
LM234/LM234-3/LM234-6	−25˚C to +100˚C
LM334	0˚C to +70˚C
Soldering Information	
TO-92 Package (10 sec.)	260˚C
TO-46 Package (10 sec.)	300˚C
SO Package	
Vapor Phase (60 sec.)	215˚C
Infrared (15 sec.)	220˚C

See AN-450 "Surface Mounting Methods and Their Effect on Product Reliability" (Appendix D) for other methods of soldering surface mount devices.

Electrical Characteristics (Note 2)

Parameter	Conditions	LM134/LM234			LM334			Units
		Min	Typ	Max	Min	Typ	Max	
Set Current Error, V^+=2.5V,	10µA ≤ I_{SET} ≤ 1mA			3			6	%
(Note 3)	1mA < I_{SET} ≤ 5mA			5			8	%
	2µA ≤ I_{SET} < 10µA			8			12	%
Ratio of Set Current to	100µA ≤ I_{SET} ≤ 1mA	14	18	23	14	18	26	
Bias Current	1mA ≤ I_{SET} ≤ 5mA		14			14		
	2 µA≤I_{SET}≤100 µA		18	23		18	26	
Minimum Operating Voltage	2µA ≤ I_{SET} ≤ 100µA		0.8			0.8		V
	100µA < I_{SET} ≤ 1mA		0.9			0.9		V
	1mA < I_{SET} ≤ 5mA		1.0			1.0		V
Average Change in Set Current	2µA ≤ I_{SET} ≤ 1mA							
with Input Voltage	1.5 ≤ V^+ ≤ 5V		0.02	0.05		0.02	0.1	%/V
	5V ≤ V^+ ≤ 40V		0.01	0.03		0.01	0.05	%/V
	1mA < I_{SET} ≤ 5mA							
	1.5V ≤ V ≤ 5V		0.03			0.03		%/V
	5V ≤ V ≤ 40V		0.02			0.02		%/V
Temperature Dependence of	25µA ≤ I_{SET} ≤ 1mA	0.96T	T	1.04T	0.96T	T	1.04T	
Set Current (Note 4)								
Effective Shunt Capacitance			15			15		pF

Note 1: ."Absolute Maximum Ratings" indicate limits beyond which damage to the device may occur. Operating Ratings indicate conditions for which the device is functional, but do not guarantee specific performance limits.

Note 2: Unless otherwise specified, tests are performed at T_j = 25˚C with pulse testing so that junction temperature does not change during test

Note 3: Set current is the current flowing into the V^+ pin. For the Basic 2-Terminal Current Source circuit shown on the first page of this data sheet. I_{SET} is determined by the following formula: I_{SET} = 67.7 mV/R_{SET} (@ 25˚C). Set current error is expressed as a percent deviation from this amount. I_{SET} increases at 0.336%/˚C @ T_j = 25˚C (227 µV/˚C).

National Semiconductor

February 25, 2011

LM117/LM317A/LM317

3-Terminal Adjustable Regulator

General Description

The LM117 series of adjustable 3-terminal positive voltage regulators is capable of supplying in excess of 1.5A over a 1.2V to 37V output range. They are exceptionally easy to use and require only two external resistors to set the output voltage. Further, both line and load regulation are better than standard fixed regulators. Also, the LM117 is packaged in standard transistor packages which are easily mounted and handled.

In addition to higher performance than fixed regulators, the LM117 series offers full overload protection available only in IC's. Included on the chip are current limit, thermal overload protection and safe area protection. All overload protection circuitry remains fully functional even if the adjustment terminal is disconnected.

Normally, no capacitors are needed unless the device is situated more than 6 inches from the input filter capacitors in which case an input bypass is needed. An optional output capacitor can be added to improve transient response. The adjustment terminal can be bypassed to achieve very high ripple rejection ratios which are difficult to achieve with standard 3-terminal regulators.

Besides replacing fixed regulators, the LM117 is useful in a wide variety of other applications. Since the regulator is "floating" and sees only the input-to-output differential voltage, supplies of several hundred volts can be regulated as long as the maximum input to output differential is not exceeded, i.e., avoid short-circuiting the output.

Also, it makes an especially simple adjustable switching regulator, a programmable output regulator, or by connecting a fixed resistor between the adjustment pin and output, the LM117 can be used as a precision current regulator. Supplies with electronic shutdown can be achieved by clamping the adjustment terminal to ground which programs the output to 1.2V where most loads draw little current.

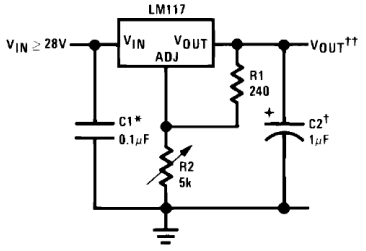
For applications requiring greater output current, see LM150 series (3A) and LM138 series (5A) data sheets. For the negative complement, see LM137 series data sheet.

Features

- Guaranteed 1% output voltage tolerance (LM317A)
- Guaranteed max. 0.01%/V line regulation (LM317A)
- Guaranteed max. 0.3% load regulation (LM117)
- Guaranteed 1.5A output current
- Adjustable output down to 1.2V
- Current limit constant with temperature
- P+ Product Enhancement tested
- 80 dB ripple rejection
- Output is short-circuit protected

Typical Applications

1.2V–25V Adjustable Regulator



906301

Full output current not available at high input-output voltages

*Needed if device is more than 6 inches from filter capacitors.

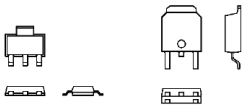
†Optional—improves transient response. Output capacitors in the range of 1μF to 1000μF of aluminum or tantalum electrolytic are commonly used to provide improved output impedance and rejection of transients.

$$\dagger\dagger V_{OUT} = 1.25V\left(1 + \frac{R2}{R1}\right) + I_{ADJ}(R_2)$$

LM117/LM317A/LM317 Package Options

Part Number	Suffix	Package	Output Current
LM117, LM317	K	TO-3	1.5A
LM317A, LM317	T	TO-220	1.5A
LM317	S	TO-263	1.5A
LM317A, LM317	EMP	SOT-223	1.0A
LM117, LM317A, LM317	H	TO-39	0.5A
LM117	E	LCC	0.5A
LM317A, LM317	MDT	TO-252	0.5A

SOT-223 vs. TO-252 (D-Pak) Packages



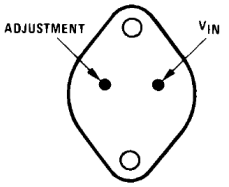
906354

Scale 1:1

© 2011 National Semiconductor Corporation

Connection Diagrams

TO-3 (K)
Metal Can Package

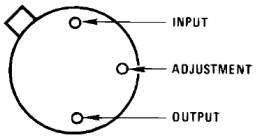


906330

CASE IS OUTPUT

Bottom View
Steel Package
NS Package Number K02A or K02C

TO-39 (H)
Metal Can Package

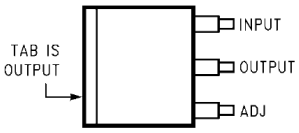


906331

CASE IS OUTPUT

Bottom View
NS Package Number H03A

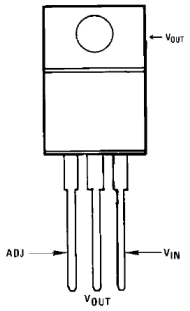
TO-263 (S)
Surface-Mount Package



906335

Top View

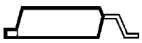
TO-220 (T)
Plastic Package



906332

Front View
NS Package Number T03B

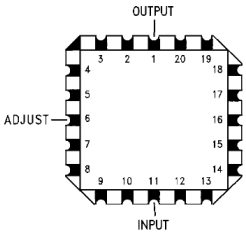
TO-263 (S)
Surface-Mount Package



906336

Side View
NS Package Number TS3B

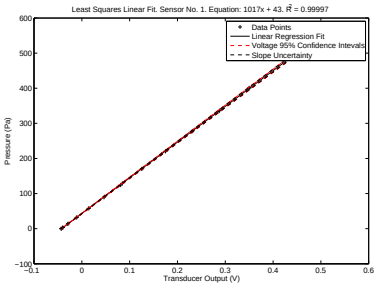
Ceramic Leadless
Chip Carrier (E)

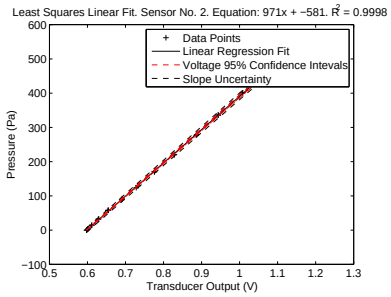


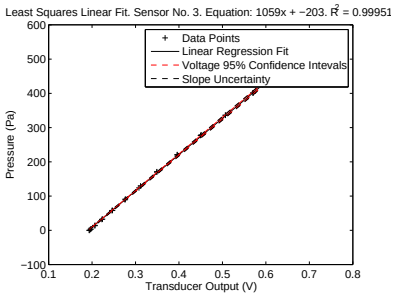
906334

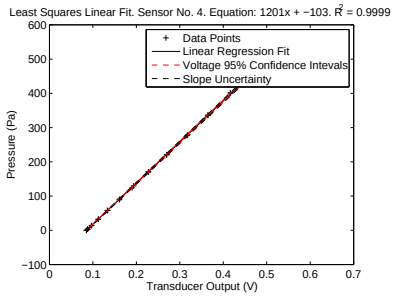
Top View
NS Package Number E20A

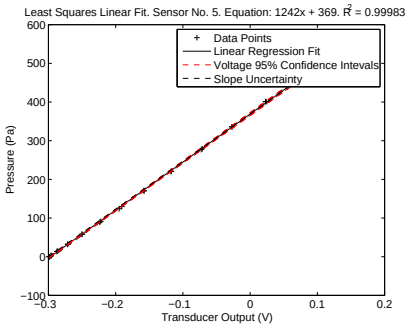
Appendix F Pressure Calibration

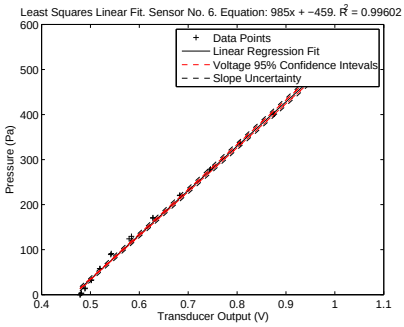


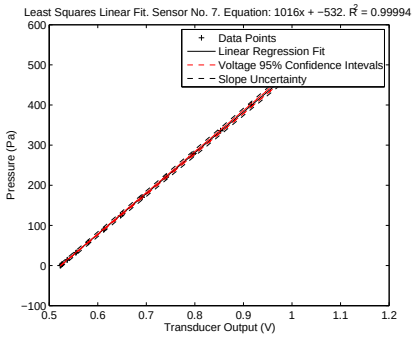


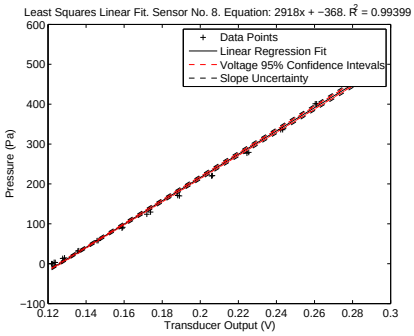


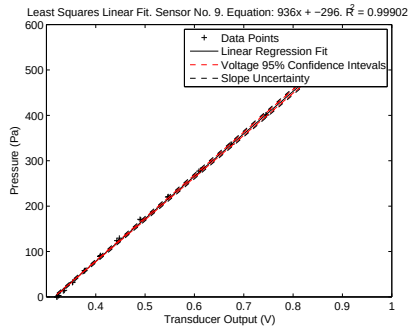


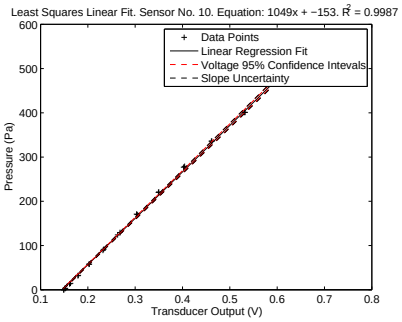


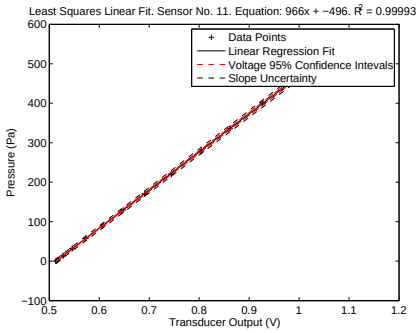


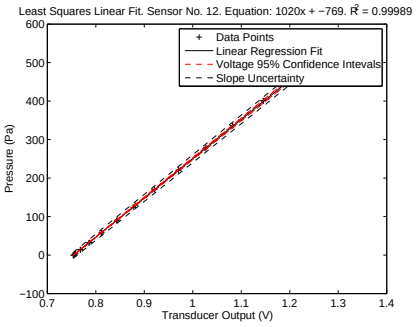

Least Squares Linear Fit. Sensor No. 7. Equation: 1016x + −532. R^2 = 0.99994
Data Points
Linear Regression Fit
Voltage 95% Confidence Intevals
Slope Uncertainty
Pressure (Pa)
Transducer Output (V)

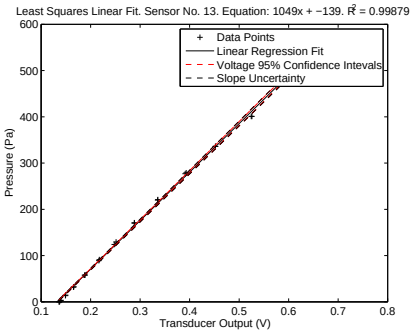

Least Squares Linear Fit. Sensor No. 8. Equation: 2918x + −368. R^2 = 0.99399
Data Points
Linear Regression Fit
Voltage 95% Confidence Intevals
Slope Uncertainty
Pressure (Pa)
Transducer Output (V)

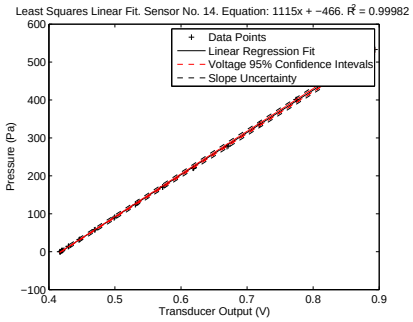

Least Squares Linear Fit. Sensor No. 9. Equation: 936x + −296. R^2 = 0.99902
Data Points
Linear Regression Fit
Voltage 95% Confidence Intevals
Slope Uncertainty
Pressure (Pa)
Transducer Output (V)

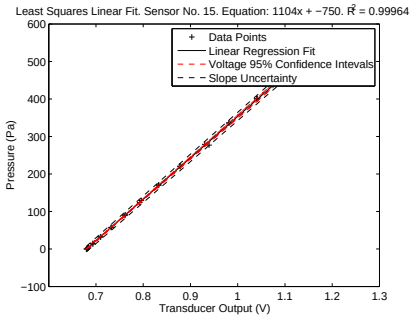

Least Squares Linear Fit. Sensor No. 10. Equation: 1049x + −153. R^2 = 0.9987
Data Points
Linear Regression Fit
Voltage 95% Confidence Intevals
Slope Uncertainty
Pressure (Pa)
Transducer Output (V)

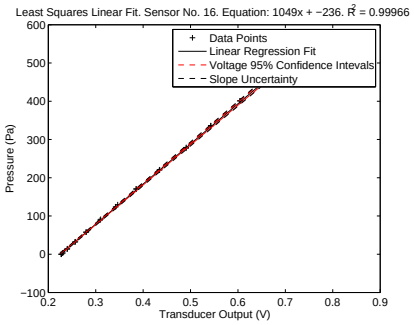

Least Squares Linear Fit. Sensor No. 11. Equation: 966x + −496. R^2 = 0.99993
Data Points
Linear Regression Fit
Voltage 95% Confidence Intevals
Slope Uncertainty
Pressure (Pa)
Transducer Output (V)

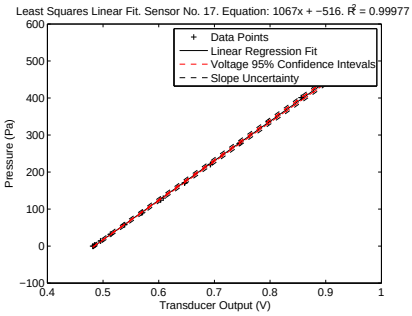

Least Squares Linear Fit. Sensor No. 12. Equation: 1020x + −769. R^2 = 0.99989
Data Points
Linear Regression Fit
Voltage 95% Confidence Intevals
Slope Uncertainty
Pressure (Pa)
Transducer Output (V)

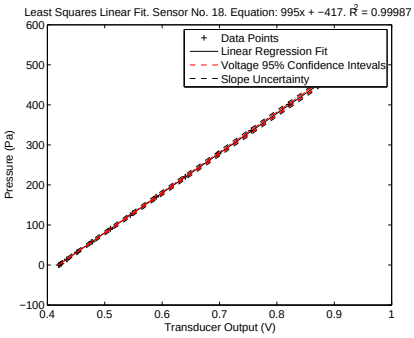

Least Squares Linear Fit. Sensor No. 13. Equation: 1049x + −139. R^2 = 0.99879
Data Points
Linear Regression Fit
Voltage 95% Confidence Intevals
Slope Uncertainty
Pressure (Pa)
Transducer Output (V)

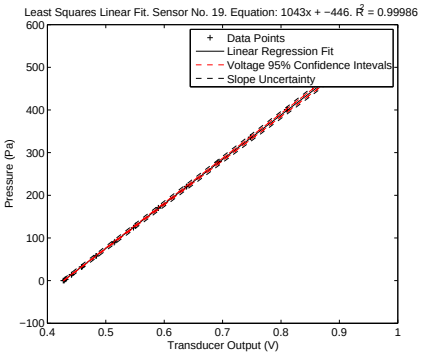

Least Squares Linear Fit. Sensor No. 14. Equation: 1115x + −466. R^2 = 0.99982
Data Points
Linear Regression Fit
Voltage 95% Confidence Intevals
Slope Uncertainty
Pressure (Pa)
Transducer Output (V)

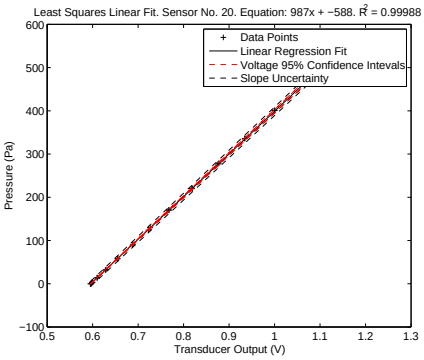

Least Squares Linear Fit. Sensor No. 15. Equation: 1104x + −750. R² = 0.99964
Data Points
Linear Regression Fit
Voltage 95% Confidence Intevals
Slope Uncertainty
Pressure (Pa)
Transducer Output (V)

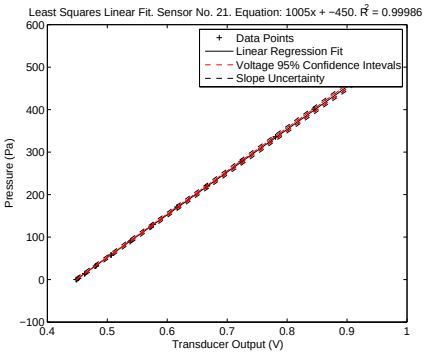

Least Squares Linear Fit. Sensor No. 16. Equation: 1049x + −236. R² = 0.99966
Data Points
Linear Regression Fit
Voltage 95% Confidence Intevals
Slope Uncertainty
Pressure (Pa)
Transducer Output (V)

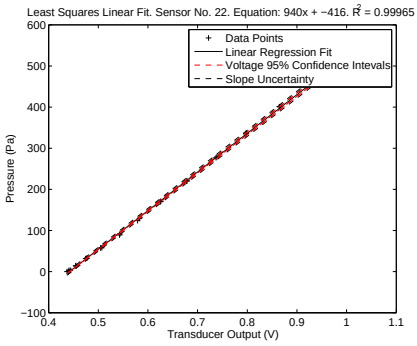

Least Squares Linear Fit. Sensor No. 17. Equation: 1067x + −516. R² = 0.99977
Data Points
Linear Regression Fit
Voltage 95% Confidence Intevals
Slope Uncertainty
Pressure (Pa)
Transducer Output (V)

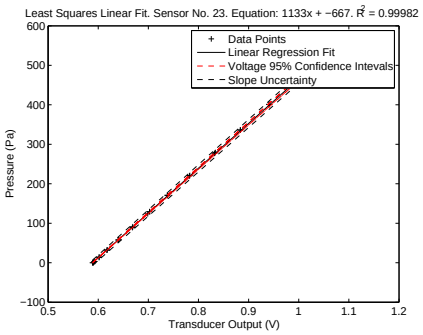

Least Squares Linear Fit. Sensor No. 18. Equation: 995x + −417. R² = 0.99987
Data Points
Linear Regression Fit
Voltage 95% Confidence Intevals
Slope Uncertainty
Pressure (Pa)
Transducer Output (V)

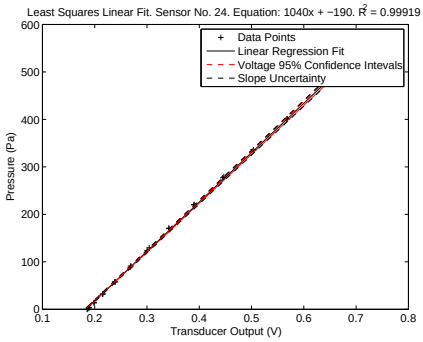

Least Squares Linear Fit. Sensor No. 19. Equation: 1043x + −446. R² = 0.99986
Data Points
Linear Regression Fit
Voltage 95% Confidence Intevals
Slope Uncertainty
Pressure (Pa)
Transducer Output (V)


Least Squares Linear Fit. Sensor No. 20. Equation: 987x + −588. R² = 0.99988
Data Points
Linear Regression Fit
Voltage 95% Confidence Intevals
Slope Uncertainty
Pressure (Pa)
Transducer Output (V)


Least Squares Linear Fit. Sensor No. 21. Equation: 1005x + −450. R² = 0.99986
Data Points
Linear Regression Fit
Voltage 95% Confidence Intevals
Slope Uncertainty
Pressure (Pa)
Transducer Output (V)


Least Squares Linear Fit. Sensor No. 22. Equation: 940x + −416. R² = 0.99965
Data Points
Linear Regression Fit
Voltage 95% Confidence Intevals
Slope Uncertainty
Pressure (Pa)
Transducer Output (V)


Least Squares Linear Fit. Sensor No. 23. Equation: 1133x + −667. R^2 = 0.99982
Data Points
Linear Regression Fit
Voltage 95% Confidence Intevals
Slope Uncertainty
Pressure (Pa)
Transducer Output (V)


Least Squares Linear Fit. Sensor No. 24. Equation: 1040x + −190. R^2 = 0.99919
Data Points
Linear Regression Fit
Voltage 95% Confidence Intevals
Slope Uncertainty
Pressure (Pa)
Transducer Output (V)

DP MEASUREMENT
Unit 11, Top Angel, Buckingham Industrial Park, Buckingham. MK18 1TH
Tel/Fax: 01280 817122 e-mail: dpm@ttseries.com www.ttseries.com

CALIBRATION CERTIFICATE

CALIBRATION DETAILS:
Date Of Calibration: 11/01/2012
Due Date: 11/01/2013

INSTRUMENT DETAILS:
Model: ST650 M
Serial Number: 236

TEST ROOM CONDITIONS:
Temperature: 21°C ± 2°C
Manufacturer: DP Measurement

Specification
Pressure & Velocity: Readings < 100 counts ± 2 counts. Readings > 100 counts ± 1% of reading ± 1 count.
Temperature: Instrument only ± 2°C

TEST RESULTS:

Calibration Points Pa:	0	40.0	160.0	800.0	4000	-40.0	-160.0	-800.0	-4000
Indicated Readings:	0	39.9	160.0	800.0	4001	-40.1	-160.0	-803.0	-4020
Error:	0	-0.3%	0.0%	0.0%	0.0%	0.3%	0.0%	0.4%	0.5%
Calibration Points mbar:	0	0.400	1.60	8.00	40.0	-0.400	-1.60	-8.00	-40.0
Indicated Readings:	0	0.402	1.60	8.00	40.1	-0.398	-1.59	-8.00	-40.2
Error:	0	0.5%	0.0%	0.0%	0.3%	-0.5%	-0.6%	0.0%	0.5%
Calibration Points mmH_2O:	0	4.08	16.3	81.6	408	-4.08	-16.3	-81.6	-408
Indicated Readings:	0	4.07	16.3	81.6	409	-4.09	-16.3	-81.6	-410
Error:	0	-0.2%	0.0%	0.0%	0.2%	0.2%	0.0%	0.0%	0.5%
Calibration Points mmHg:	0	0.299	1.20	5.98	29.9	-0.299	-1.20	-5.98	-29.9
Indicated Readings:	0	0.298	1.20	6.00	30.1	-0.298	-1.20	-6.00	-30.1
Error:	0	-0.3%	0.0%	0.3%	0.7%	-0.3%	0.0%	0.3%	0.7%
Calibration Points m/sec:	0	5.00	8.16	11.5	15.0	16.3	25.8	36.5	50.0
Indicated Readings:	0	5.02	8.11	11.5	15.0	16.3	25.8	36.5	50.0
Error:	0	0.4%	-0.6%	0.0%	0.0%	0.0%	0.0%	0.0%	0.0%

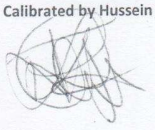
Calibration Points °C	0.0	20.0	50.0	100.0	250.0	400.0	500.0
Indicated Readings:	0.5	20.0	49.6	99.8	249.4	400.5	499.5
Error:	0.5	0.0	-0.4	-0.2	-0.6	0.5	-0.5

Traceablity:
Equipment: The instrument detailed above the pressure range has been calibrated against equipment whose serial number 0047381 which in turn has been calibrated against instruments and equipment that are traceable to National Standards.
(UKAS Calibration Laboratory N° 0157)

Velocity Range: Is calibrated for the ellipsoidal nose (NPL Type) Pitot Static Tubes used at air density 1.20kg/m³. 16°C, 1000 mbar.

Temperature Range: Is calibrated against equipment whose serial number is 13724. Which in turn has been calibrated against instruments and equipment that are traceable to National or International Standards. (K026-10P4495)

Calibrated by Hussein Khimji:



Associated Instrument Repairs Ltd. Trading as DP Measurement.
Company Reg. No: 3485904 VAT No: 685 868 755
Registered Office: Ebenezer House, Poole Road, Bournemouth, Dorset. BH2 5QJ.

Appendix G Pressure Sensor Uncertainty Calibration

The uncertainty calculation of the pressure sensors is based on the uncertainty of the manometer used to measure the pressure as well as the variability in the output voltage from the pressure sensors.

$$P = C\Delta V \tag{G.1}$$

$$C = P\Delta V^{-1} \tag{G.2}$$

Where:
P Gauge Pressure determined by Manometer [Pa]
ΔV Pressure Sensor Voltage (Measured Voltage - Zero Voltage) [V]
C Pressure/Voltage Slope

The uncertainty of the measurement has the following form.

$$\sigma_C = \left(\left(\frac{dC}{dP} \right)^2 \sigma_P^2 + \left(\frac{dC}{d\Delta V} \right)^2 \sigma_{\Delta V}^2 \right)^{0.5} \tag{G.3}$$

Where:
σ_c Uncertainty in Slope
σ_P Uncertainty in the Pressure Measurement
$\sigma_{\Delta V}$ Uncertainty in the Voltage Output

The derivatives are given in the following form:

$$\frac{dC}{dP} = \frac{1}{\Delta V} \tag{G.4}$$

$$\frac{dC}{d\Delta V} = \frac{-P}{\Delta V^2} \tag{G.5}$$

Therefore the uncertainty is:

$$\sigma_C = \left(\left(\frac{1}{\Delta V} \right)^2 \sigma_P^2 + \left(\frac{-P}{\Delta V^2} \right)^2 \sigma_{\Delta V}^2 \right)^{0.5} \tag{G.6}$$

A worked example based on a typical data set from Sensor No. 5 is given now. The following values are given to the variables:

ΔV	0.0808
P	100
σ_P	1
$\sigma_{\Delta V}$	0.001
C	1242

Substituting these values into Equation G.6 results in the uncertainty in the slope being calculated as:
$\sigma_c = 12.4$.

The slope uncertainty error is thus given as:

$$\frac{\sigma_C}{C} = \frac{12.4}{1242} = 0.01 = 1\% \tag{G.7}$$